ANALYSIS OF THE NONLINEAR BEHAVIOR OF FLOODWALL STRUCTURES

By

ISSAM S. HALLAL

Bachelor of Science
Oklahoma State University
Stillwater, Oklahoma
1981

Master of Science
Oklahoma State University
Stillwater, Oklahoma
1982

Submitted to the Faculty of the
Graduate College of the
Oklahoma State University
in partial fulfillment of
the requirements for
the Degree of
DOCTOR OF PHILOSOPHY
July, 1988

ANALYSIS OF THE NONLINEAR BEHAVIOR

OF FLOODWALL STRUCTURES

Thesis Approved:

Mete Oner

Thesis Adviser

W. M. Dawkins

A. Ekuly

J. K. Good

G. Steven Gipson

Norman N. Durham

Dean of the Graduate College

ACKNOWLEDGMENTS

Of the many people deserving acknowledgment, it is appropriate that the first to receive thanks is Dr. Mete Oner my major adviser and chairman of my committee. He never ceased to amaze me by his imaginative thinking and his diversified knowledge that taught me a lot of things. I thank Dr. W. P. Dawkins, a committee member and an important part of this research. I thank him for providing continual advice and information in every step of the work. I thank the other committee members, Dr. A. Kelly, Dr. G. S. Gipson, and Dr. K. Good, for their valuable assistance and guidance.

I thank the U.S. Army Engineers for funding this study. I sincerely hope this work will provide long-term benefits for them.

Finally, I thank my family for their love, support, and sacrifices that helped immensely in my being able to progress through the formal education process and kept me going toward achieving this goal.

TABLE OF CONTENTS

LIST OF TABLES

LIST OF FIGURES

CHAPTER I

INTRODUCTION

A floodwall structure consists of a sheetpile driven into a levee to gain the needed height for flood protection (Fig. 1). The depth of penetration is currently found using conventional active/passive pressure theories with some modifications to take the levee slopes into account. While systems designed on this basis have performed successfully, uncertainties in the calculation of soil pressures and in predicting displacement of the wall have necessitated a conservative approach.

In a typical application where the levee is not compacted and rests on soft ground, there are considerable difficulties in design which are amplified by uncertainties as to the applicability of the conventional analysis procedures. Without detailed analyses it is difficult to know precisely how such a complex soil-structure system would behave. A good understanding of the mechanisms involved and the soil behavior around the sheetpile are needed for resolving these uncertainties so that good engineering judgments can be made in the design process and, hopefully, result in more economical designs.

This research effort aims at clarifying some of the uncertainties involved in floodwall structures by developing and applying a comprehensive analysis procedure based on the plane strain finite element method and the modern understanding of the mechanical soil

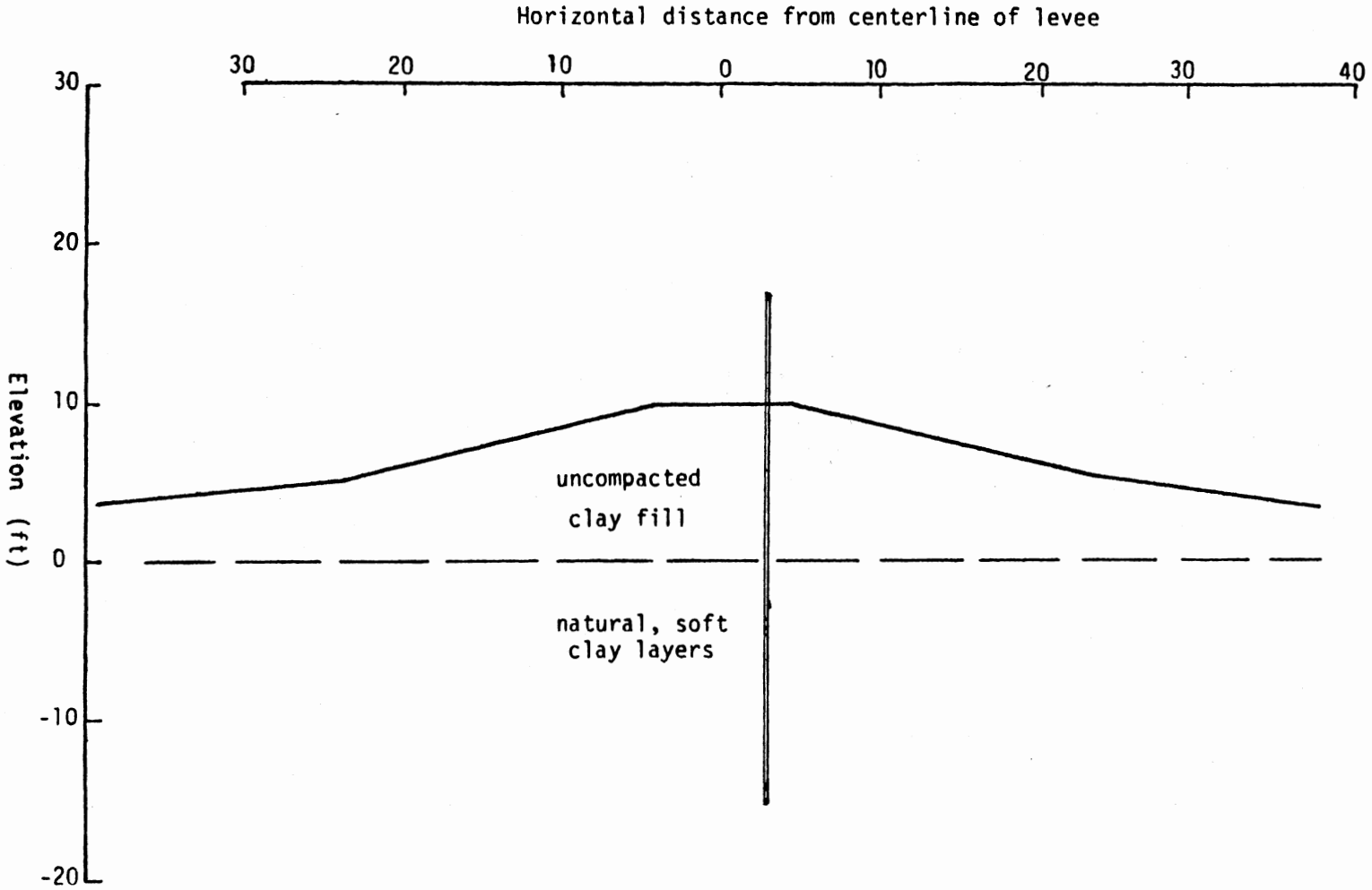

Fig. 1 Cross section of a typical floodwall

behavior. The details of this procedure are presented in chapter II. With this tool it is possible to study the deformation patterns that should be expected in typical configurations, the effects of the sheetpile penetration on the stability of the structure, and on the stresses and deformations in the soil, and the development of soil failure patterns.

A full scale test performed by New Orleans District, Corps of Engineers, on a test section near E99 East Atchafalaya Basin Flood Protection Levee offers a unique opportunity for verification of the analytical tool developed. Important aspects and results of the E99 wall test are briefly presented in chapter III of this report. Although the geometry of the system tested deviates somewhat from that of a typical floodwall, the soil types involved and the nature and sequence of loading imposed closely resemble typical conditions. Therefore the results of this test were used in the second part of this study for verification and fine tuning of the method. This has completed the tool-development stage of the research.

After this development effort has been completed, the typical soil and structure characteristics of the existing floodwalls have been examined and a number of idealized cases have been established. The procedure developed has been applied to these cases. The effects of the sheet pile penetration and soil strength on the floodwall performance have been investigated. The documentation of this analysis is shown in chapter IV. Finally, the conclusion of this research effort and further recommendations are discussed in chapter V.

CHAPTER II

METHOD OF ANALYSIS

A comprehensive numerical procedure tailored to the modeling requirements of the floodwall problem has been developed as the first step of this study. It is based on the plane strain finite element method which incorporates the following features (Fig.2):

1. Beam-column elements.
2. Soil elements.
3. Frictional/adhesive soil-structure interface elements.
4. Simulation of sequential construction and stepwise loading.
5. Consideration of soil drainage conditions.
6. A nonlinear constitutive model for the soil.

The basic techniques of the methodology used bears the contribution of many research efforts during the past decade or so in relation to foundations, dams, excavations, and certain types of retaining walls (e.g., Refs. 1, 3, 4, 5, 9, 12, 15). However, the program's capabilities (Ref. 10) exceeds by far the current needs required for the analysis of flood walls. Therefore, only an overview is presented in the following paragraphs where emphasis is placed on the special aspects of the current application.

Beam-Column Elements

Isoparametric quadrilateral elements could have been used to model

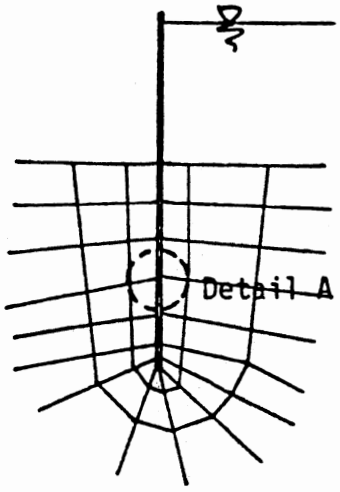

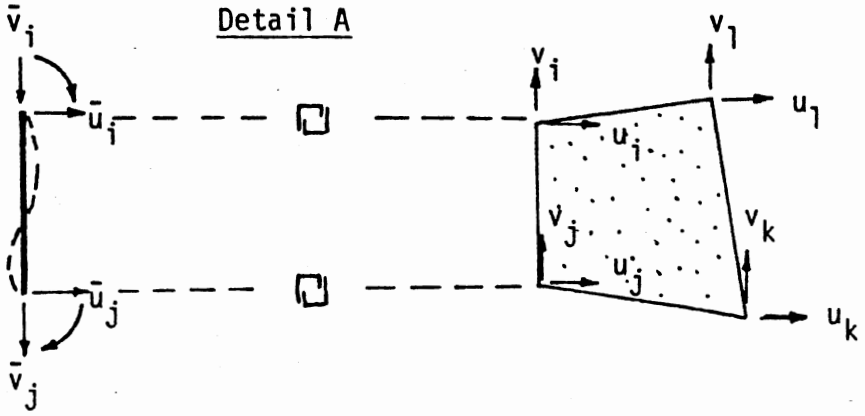

Wall element

(bending)

Soil element

(quadrilateral)

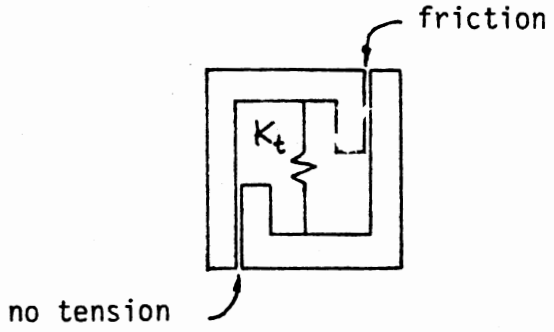

Interface element

Figure 2. Details of the element types used in FE model.

the sheet pile. However, to preserve a reasonable aspect ratio, the use of quadrilateral elements to accurately represent the slender pile would have substantially increased the number of soil nodes and soil elements in the vicinity of the wall. In spite of the increased complexity in coding and program logic inherent in mixing diverse elements in the model, beam bending elements were employed to simulate the flexural capability of the sheet pile. These elements are assumed to be linear elastic.

Soil Elements

Four node isoparametric plane strain elements are used to model the soil. Four point Gaussian quadrature was used to perform the integration necessary for evaluating the element stiffness matrices. Although the state of stress varies throughout each element, the soil shear modulus (discussed later) was only evaluated at the centroid of the element. As demonstrated by the close comparisons of measured and calculated system response, this simplified approach is considered to be sufficiently accurate.

Interface Model

The interface elements are concentrated nonlinear springs that are used to represent the boundary between the sheetpile and the soil. These elements allow separation of the soil from the sheetpile when tension tends to develop in the direction normal to the sheetpile surface. Also sliding at the interface is allowed whenever the friction or adhesion capacity of the interface is exceeded. These elements are necessary to correctly model the formation of tension cracks in active

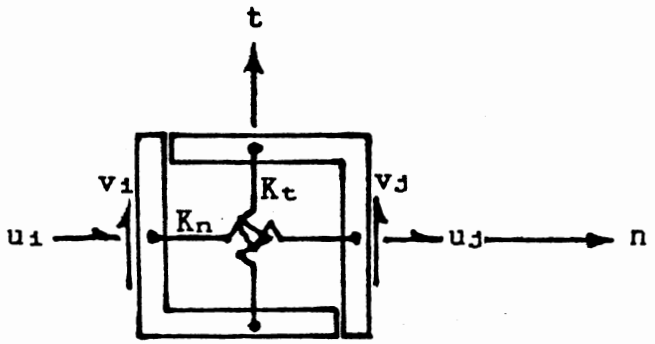

Figure 3(a). Typical interface element.

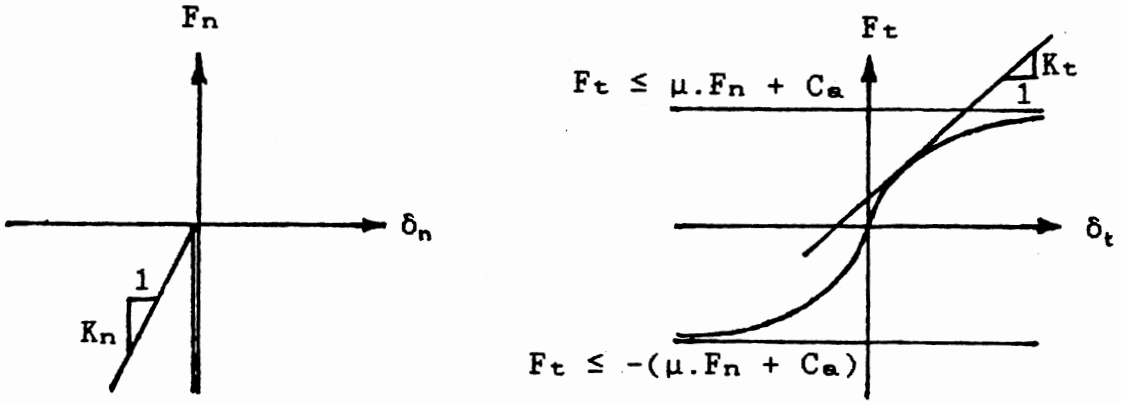

Case I. $\delta_n < 0$ (Compression)

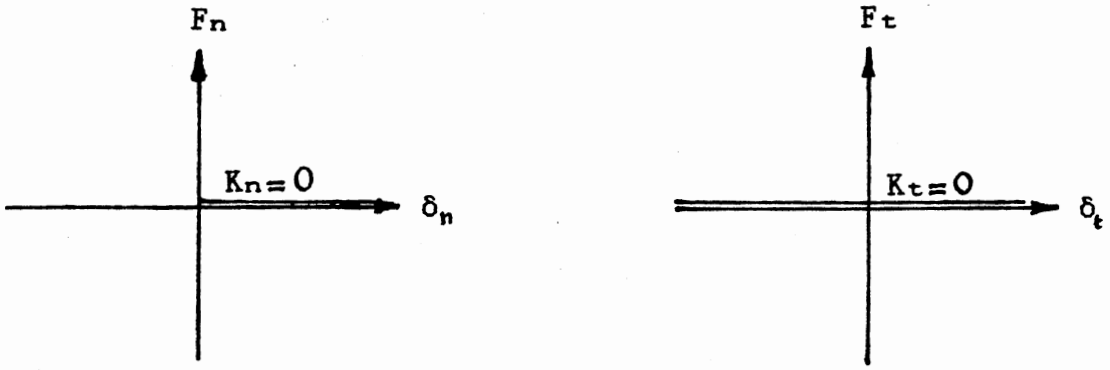

Case II. $\delta_n > 0$ (tension)

Figure 3(b). Various force-displacement relations at the interface in normal and tangential directions.

failure regions in cohesive soils in an undrained condition. A typical interface element consists of two nodes occupying the same geometrical location. These nodes are interconnected by two concentrated springs in the normal and the tangential direction to the interface as shown in Figure 3(a). The stiffness formulation of the interface element in the N-T system (Normal/Tangential) may be written as

$$\begin{bmatrix} K_n & 0 & -K_n & 0 \\ 0 & K_t & 0 & -K_t \\ -K_n & 0 & K_n & 0 \\ 0 & -K_t & 0 & K_t \end{bmatrix} \begin{Bmatrix} u_i \\ v_i \\ u_j \\ v_j \end{Bmatrix} = \begin{Bmatrix} -P_n \\ -P_t \\ P_n \\ P_t \end{Bmatrix} \qquad (2.1)$$

where u and v are the displacements in the normal and tangential directions, respectively; K_n and K_t are the stiffness values in the normal and tangential directions, respectively; and P_n and P_t are the forces in the normal and tangential directions, respectively.

Various load-displacement relations can take place at the interface and are shown in Figure 3(b). In this figure, δ_n and δ_t correspond to the relative normal and the relative tangential displacements between nodes i and j, respectively. Both the tangential and normal stiffnesses are totally lost when the structure and the soil separate. When they are in contact, the normal stiffness becomes infinite. Naturally a large but finite number must be used in the computer program. Experience shows that if the stiffness value is not large enough, an undesirable overlapping occurs. On the other hand, the use of a very large stiffness value creates numerical instability in the solution

process. This can be explained using the example shown in Fig. 4.

After eliminating the fixed/known boundary conditions (u_1 and u_4), the equilibrium equations of the system are written in matrix form as

$$\begin{bmatrix} (K_1+K_n) & -K_n \\ -K_n & (K_2+K_n) \end{bmatrix} \begin{Bmatrix} u_2 \\ u_3 \end{Bmatrix} = \begin{Bmatrix} F_2 \\ F_3 \end{Bmatrix} \tag{2.2}$$

where

$k_i = E.A_i/L_i$, $i = 1,2$.

Using a very large value for K_n introduces numerical instability since K_1 and K_2 are very small relative to K_n which makes the determinant of the equation system nearly zero.

In order to mend this type of numerical instability, Wilson (15) proposed a method in which the stiffness matrix is formulated based on one absolute and one relative displacement instead of two absolute displacements. In the previous example u_3 could be written as

$$u_3 = u_2 + \delta \tag{2.3}$$

where u_2 and u_3 are defined as the independent and the dependent degree-of-freedom respectively. δ is the relative displacement between node 2 and 3. Based on the above assumption we can write

$$\begin{Bmatrix} u_2 \\ u_3 \end{Bmatrix} = \begin{bmatrix} 1 & 0 \\ 1 & 1 \end{bmatrix} \begin{Bmatrix} u_2 \\ \delta \end{Bmatrix} \tag{2.4}$$

After some manipulation it can be shown that Eq. (2.2) becomes

$$\begin{bmatrix} (K_1+K_2) & K_2 \\ K_2 & (K_2+K_n) \end{bmatrix} \begin{Bmatrix} U_2 \\ \delta \end{Bmatrix} = \begin{Bmatrix} (F_2+F_3) \\ F_3 \end{Bmatrix} \tag{2.5}$$

Hence, the above system of equations (2.5) is solvable and K_n can assume any value to yield a numerically stable solution. Effectively, the above change of variable simply lumps the force and the column and row corresponding to the dependent degree-of-freedom to those of the independent one.

To incorporate this procedure in a general two-dimensional finite element problem, it must be ensured that the normal stiffness (K_n) only appears on the main diagonal in the global stiffness formulation. This is possible only when the degrees of freedom of all the nodes existing on the interface are expressed in normal and tangential directions to the interface, hence avoiding the projection of the normal stiffness (K_n) in more than one direction.

For incorporation of stiffness matrices expressed in such local coordinates in the global equations of the finite elements, some transformations are necessary. To illustrate this concept, consider the portion of a finite element mesh shown in figure 5. For a typical isoparametric quadrilateral element (or any two-dimensional finite element), the stiffness matrix relates the global displacements to the global forces on the nodes through the equilibrium equations expressed in matrix form as follows:

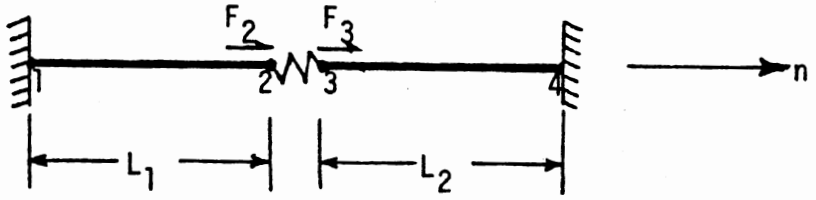

Figure 4. Example used in illustrating Ill-Conditioning.

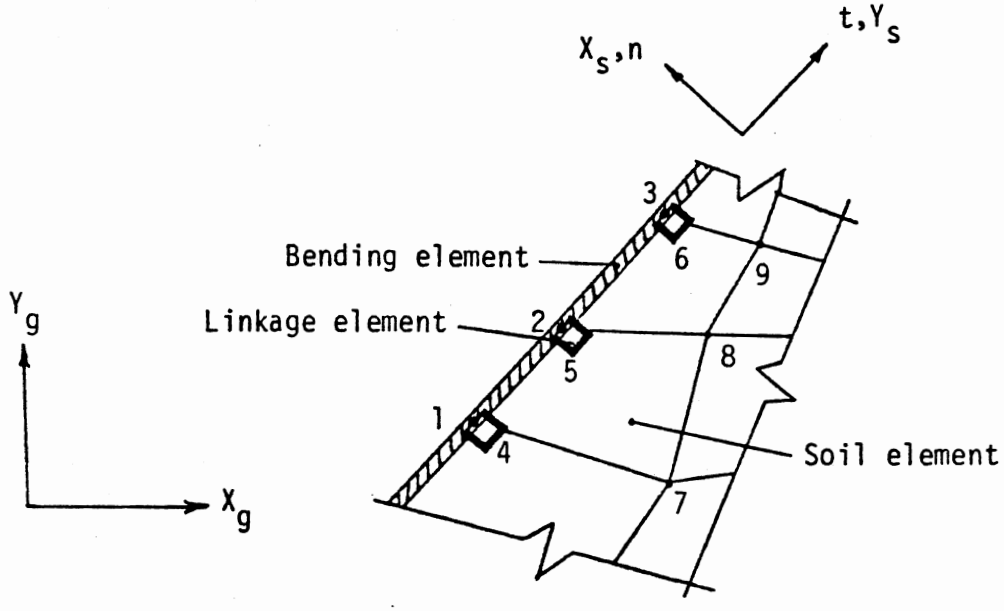

Figure 5. Finite element section used to illustrate the use of different coordinate systems.

$$K.U_g = F_g \tag{2.6}$$

where K is the 8x8 element stiffness matrix, and

$$U_g = < u_i \; v_i \; u_j \; v_j \; u_k \; v_k \; u_l \; v_l >^T$$

$$F_g = < P_i \; Q_i \; P_j \; Q_j \; P_k \; Q_k \; P_l \; Q_l >^T$$

Let the sets of displacements, or forces, at nodes i, j, k, and l rotate by arbitrary positive rotations β_i, β_j, β_k, and β_l, respectively, as shown in Fig. 6. The old set of displacements (global, unprimed) is related to the new set of displacements (primed) at each node by the following:

$$u = \cos(\beta).u' - \sin(\beta).v'$$

$$v = \sin(\beta).u' + \cos(\beta).v'$$

or

$$U_g = R.U_m \tag{2.7}$$

where

$$U_g = < u \; v >^T \; , \; U_m = < u' \; v' >^T$$

and

$$R = \begin{bmatrix} \cos(\beta) & -\sin(\beta) \\ \sin(\beta) & \cos(\beta) \end{bmatrix}$$

Similar arguments hold for nodes i, j, k, and l. Thus,

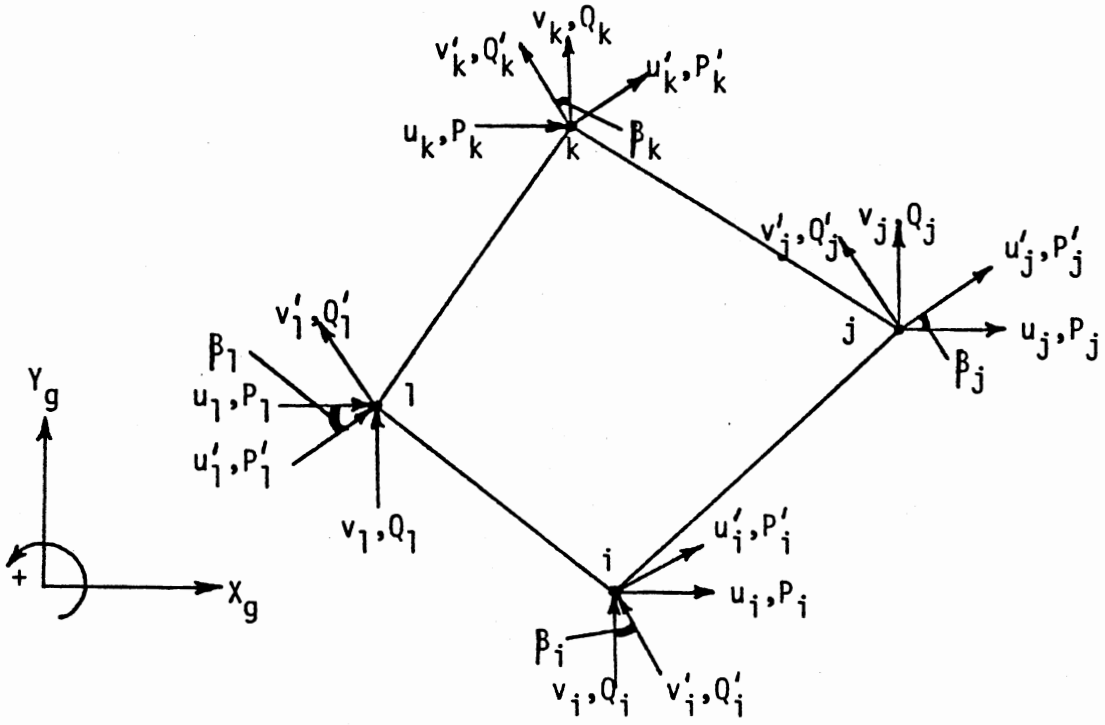

Figure 6. General representation of the degrees-of-freedom for a typical quadrilateral element.

$$\begin{Bmatrix} u_i \\ v_i \\ u_j \\ v_j \\ u_k \\ v_k \\ u_l \\ v_l \end{Bmatrix} = \begin{bmatrix} c_i & -s_i & 0 & 0 & 0 & 0 & 0 & 0 \\ s_i & c_i & 0 & 0 & 0 & 0 & 0 & 0 \\ 0 & 0 & c_j & -s_j & 0 & 0 & 0 & 0 \\ 0 & 0 & s_j & c_j & 0 & 0 & 0 & 0 \\ 0 & 0 & 0 & 0 & c_k & -s_k & 0 & 0 \\ 0 & 0 & 0 & 0 & s_k & c_k & 0 & 0 \\ 0 & 0 & 0 & 0 & 0 & 0 & c_l & -s_l \\ 0 & 0 & 0 & 0 & 0 & 0 & s_l & c_l \end{bmatrix} \begin{Bmatrix} u_i \\ v_i \\ u_j \\ v_j \\ u_k \\ v_k \\ u_l \\ v_l \end{Bmatrix}$$

or

$$U_g = R.U_e \tag{2.8}$$

With this transformation matrix the element stiffness and force vector can be expressed in local coordinates as

$$K_e.U_e = F_e \tag{2.9}$$

where

$$K_e = R^T.K.R \ , \quad F_e = R^T.F_g$$

For a beam element a similar transformation is performed.

In this manner we obtain a generalized form of the regular global assembly utilized in the finite element method where the degrees of freedom of each node could be described in a special system of coordinates.

To incorporate this formulation in a finite element code the algorithm used is:

a. Find K_e for each element except for interface elements.

b. Assemble the global stiffness matrix.

c. Find the overall load vector, F_s.

d. For each of the interface elements,

   (1) Add the tangential stiffness matrix to the global stiffness matrix in the proper locations.

   (2) Establish a dependent and an independent node; then add the force, and the global stiffness row and column corresponding to the dependent degree-of-freedom in the normal direction to those of the independent one.

   (3) Finally, add the normal stiffness K_n to the diagonal term, in the global stiffness matrix, corresponding to the dependent degree of freedom.

e. Apply the known boundary conditions and solve for the displacements U_s.

f. Transform the dependent displacements back to absolute displacements.

g. If necessary, transform all displacements and forces to the global system.

Simulation of Sequential Construction

This capability is an important ingredient of the method. The stress distribution in the soil as the water level changes can be calculated reliably only if the initial stresses are known reasonably accurately. Both the levee construction and water level change are imposed step-by-step. In addition, nonlinear soil modeling also dictates the step-by-step modification of loading and geometry.

Consideration of Soil Drainage Conditions

Because of the strong dependence of the soil shear strength and stress-strain relationship on the drainage conditions, careful attention must be paid to the soil drainage aspect. The program developed is capable of treating drained or undrained loading; in the case of undrained loading analysis can be performed either in terms of total or effective stresses. In order to use the effective stress approach, however, pore pressure parameters are necessary which are not routinely determined. Whether a total stress analysis or an effective stress analysis should be performed for an undrained problem depends mainly on the soil types involved and availability of soil test data. In the cases reported in the following paragraphs total stress analysis was used.

Constitutive Model

The numerical method incorporates a simple but adequate nonlinear constitutive model. The importance of this is clear because significant portions of the levee and its foundation may reach limiting equilibrium (or failure) in an economically designed system. A linear analysis would have no practical value in this particular problem. Some linear analyses, however, were performed in early stages of the research for specific purposes such as testing various components of the computer program.

It is well known that a vast array of constitutive models are available today for use in predicting soil behavior. Some of these models have been incorporated into finite element codes with varying degrees of success; others are either too complicated or require the

determination of up to 15 parameters which renders them impractical. Clearly, what is required in the present research is a nonlinear soil model that represents the essential characteristics of soil behavior. These characteristics can be summarized as:

a. Strain-softening as the material approaches failure.

b. Increase in rigidity parallel to an increase in either confining pressure or shear strength.

c. Returning to a high rigidity upon load reversal (unloading).

d. Failure upon an extended load reversal (as in passive failure).

It is essential that the model predict the typical soil behavior under stress paths encountered in the problem being analyzed. But it is also important that the number of parameters required be kept at a minimum and that parameters have physical meaning.

The hyperbolic model (e.g. Ref. 5), and the "degree of mobilization" model (e.g. Refs. 7, 11), which have successfully been applied to many soil and SSI problems, were considered at the beginning of this study. It is observed from the comparisons given in Fig. 7 that there is no "overshoot" in the degree of mobilization model whereas in the hyperbolic model the curve must be truncated to avoid exceeding the failure stress.

The hyperbolic model, in its published form, does not have a provision for the passive stress path because it reverts to linearity upon unloading or reloading. The passive stress path is a critical one in the floodwall problem. Based on these observations the degree of mobilization model ("f" model) was chosen for the finite element analyses in this study. However, the "f" model needs to be modified to account for non-monotonic loading. The modification of the model was

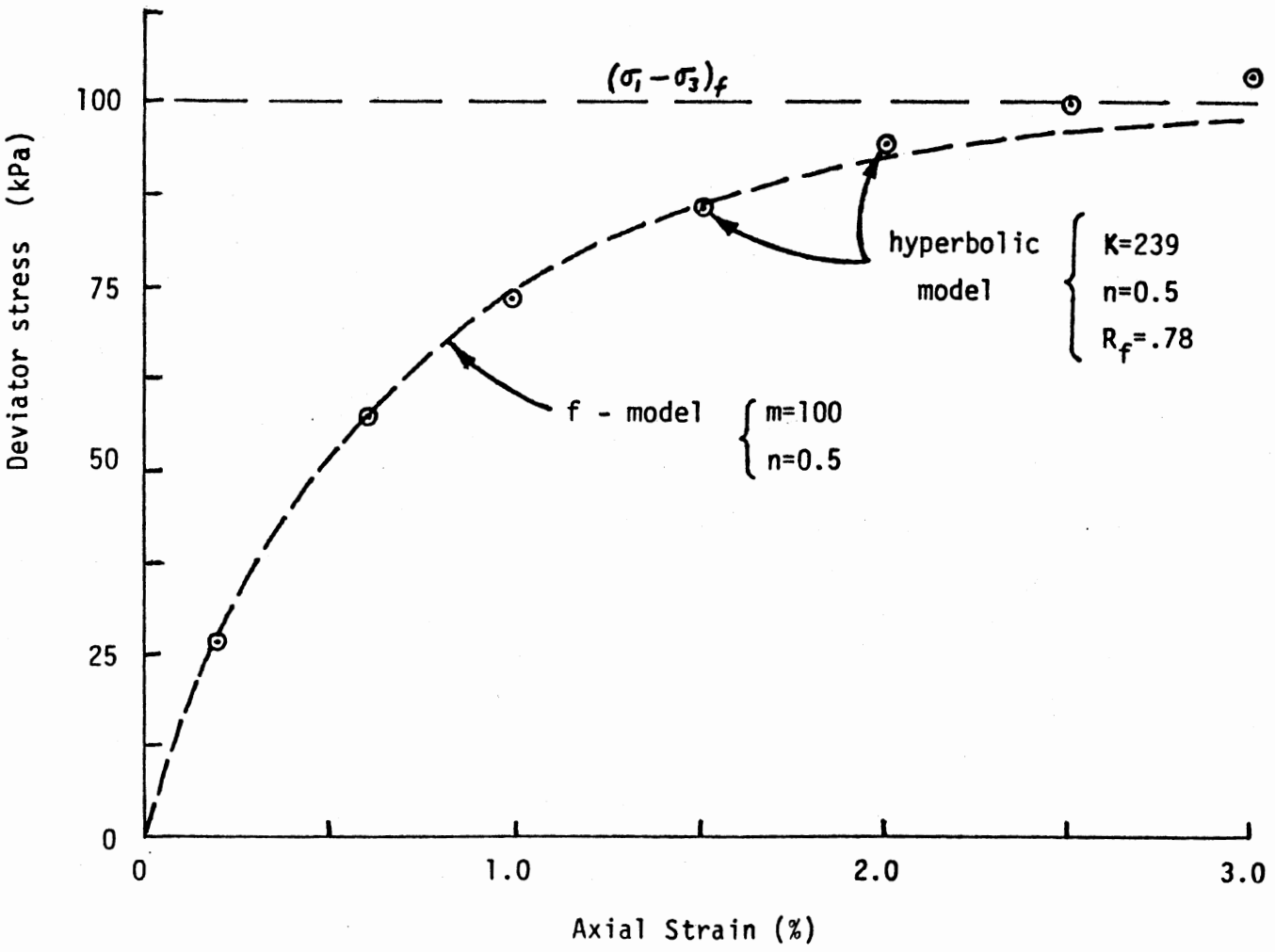

Figure 7. Typical stress-strain curve from the f-model compared with the hyperbola.

accomplished in this study. For the sake of completeness the generalized form of the "f" model is presented below.

The "f" model uses a modified form of the stress-strain matrix:

$$\begin{Bmatrix} \sigma_x \\ \sigma_y \\ \tau_{xy} \end{Bmatrix} = \begin{bmatrix} M & M-2G & 0 \\ M-2G & M & 0 \\ 0 & 0 & 2G \end{bmatrix} \begin{Bmatrix} \epsilon_x \\ \epsilon_y \\ \epsilon_{xy} \end{Bmatrix} \tag{2.10}$$

where the constrained modulus, M, and shear modulus, G, are related to Young's modulus, E, and Poisson's ratio, v, as follows:

$$M = \frac{E\ (1 - v)}{(1-2v)(1+v)} \tag{2.11}$$

$$G = \frac{E}{2(1+v)} \tag{2.12}$$

The constrained modulus at the K_o condition, M_o, is given by the empirical relationship (Ref. 7):

$$M_o = m\ p_a\ (\sigma_1/p_a)^n \tag{2.13}$$

where σ_1 is the major principal stress, p_a is atmospheric pressure, and m and n are empirical constants.

The strain softening effect is given by a factor of (1 - f) where f is called "degree of mobilization" which is the inverse of factor of safety:

$$f = \tan \phi_d / \tan \phi \qquad \text{for} \quad \phi > 0 \tag{2.14a}$$

$$f = \tau_{max}/c_u \qquad \text{for} \quad \phi = 0 \tag{2.14b}$$

where ϕ_d is the mobilized friction angle, ϕ is the maximum angle of friction, τ_{max} is the mobilized shear stress, and c_u is the soil cohesion.

Failure in the "f" model (f=1) is based on Mohr-Coulomb failure criteria; f is the ratio of slopes as shown in Fig. 8, and it is measured from the isotropic point (ϕ_d=0).

At any stress level, shear modulus is given by:

$$G = G_o\,(1 - f)/(1 - f_o) \tag{2.15}$$

in which f_o is the degree of mobilization at K_o condition which can readily be determined from the definition of f (Eq. 2.14(a) or (b)), and G_o is the shear modulus value at K_o condition. Alternatively, Eq. 2.15 can be re-written as

$$G = G_i\,(1 - f) \tag{2.16}$$

in which G_i is the shear modulus value at f=0, or the "initial modulus."

As the soil approaches failure the shear modulus decreases to zero whereas the constrained modulus, M, is kept constant at its initial value in a drained situation. However, in an undrained condition Poisson's ratio is kept constant; concequently, M varies along with G as indicated in Eq. 2.11.

The degree of mobilization model involves only the initial modulus

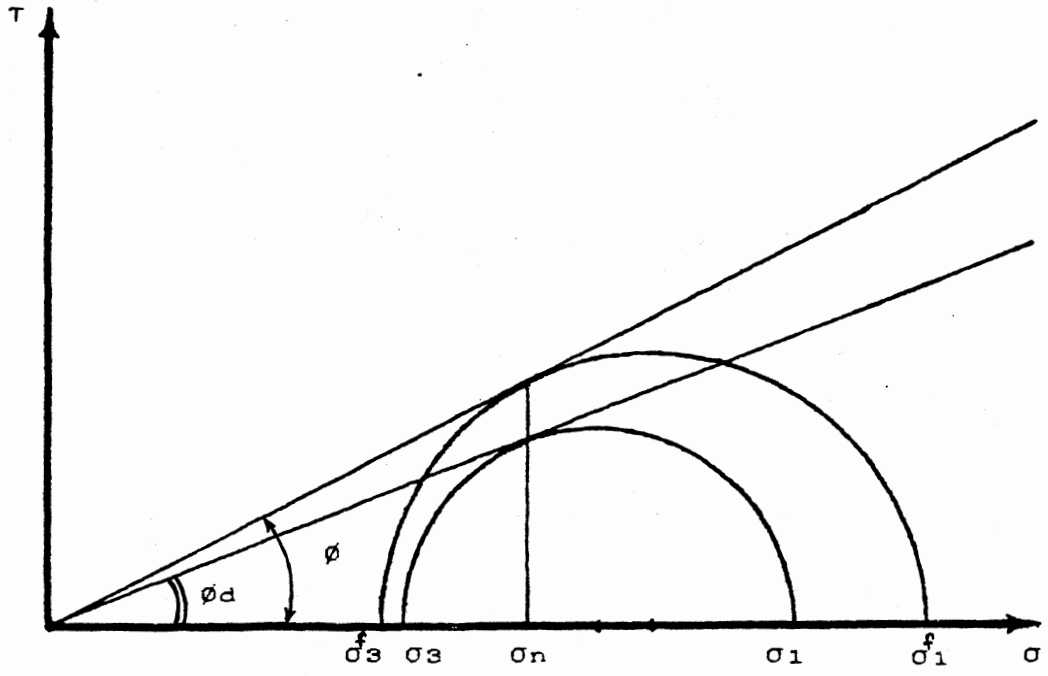

Figure 8. Representation of the degree of mobilization in Mohr diagram.

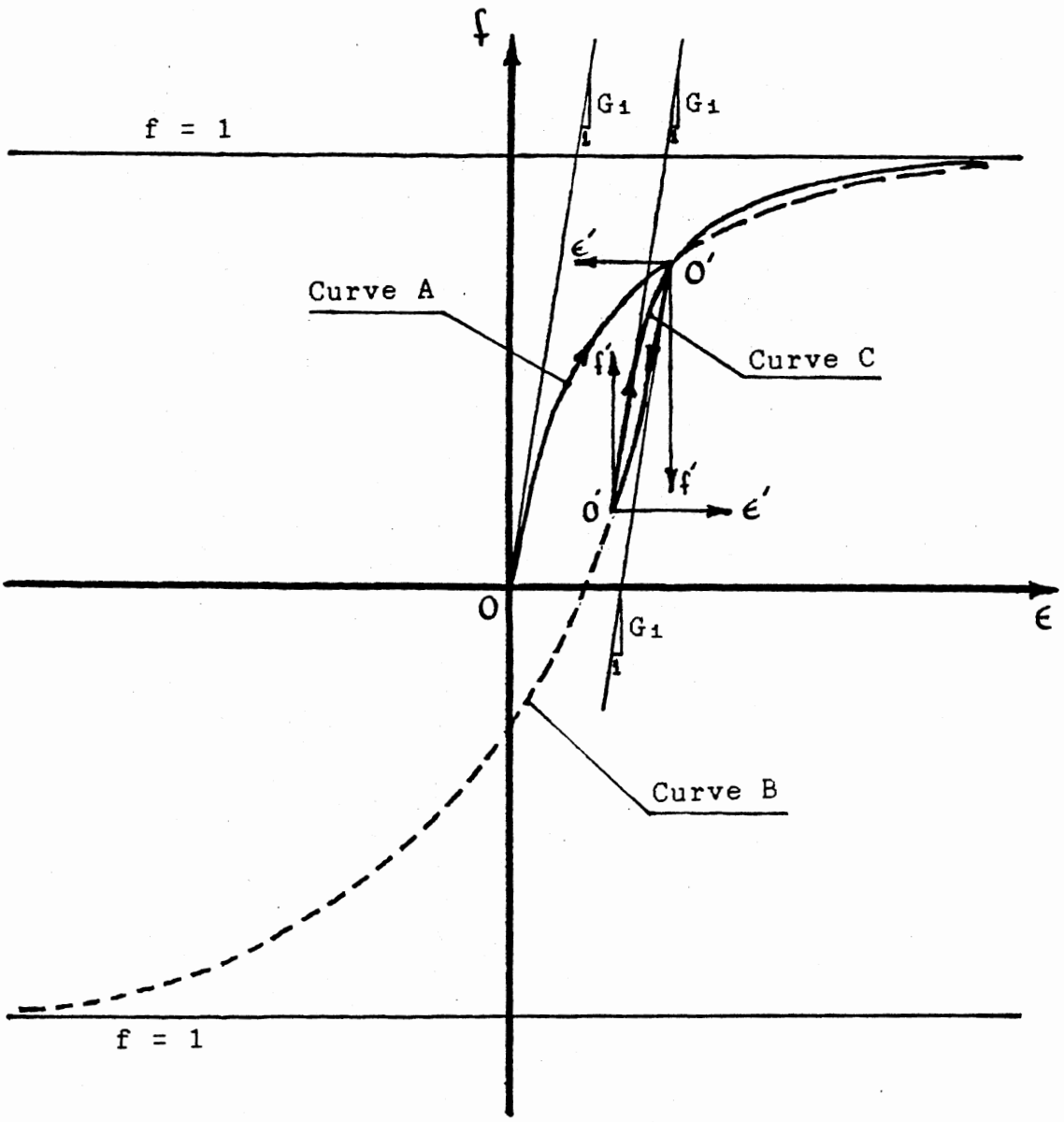

Figure 9. Generelization of the f-model for unloading and reloading on different paths.

parameters, m and n, in addition to the shear strength parameters of the soil and K_o. For drained conditions, the constrained modulus can be related to the well known consolidation "e-log p" curve parameters. For normally consolidated clays, a straight-line e-log p curve corresponds to n = 1. Also, it can be shown that, for analyses in terms of effective stresses, m is related to the compression index as:

$$m = \frac{(1+e)\ \ln 10}{C_c} \tag{2.17}$$

where e is the void ratio, and C_c is the compression index. The physical meaningfulness of the model parameters, and the relationships such as Eq. 2.17 make parameter estimation easier for the f model.

In its earlier form, the "f" model considers only one stress path with a center at f=0 as shown in the σ-ϵ domain by curve A in Fig. 9. The earlier definition of "f" (Eq. 2.14(a) and (b)) should be adjusted to accommodate the direction of the loading. This is done by introducing a relative degree of mobilization factor "f′". The significance of f′ is that it incorporates at the same time the effect of loading direction (loading, unloading) and the proximity of the state of stress to the failure envelope. These cases could not be acknowledged in the original "f" model.

Unloading behavior of the soil is modeled by employing the method generally known as the "Masing′s criterion." According to this criterion, the material regains its initial stiffness upon unloading. The shape of the stress-strain curve is constructed using the initial loading curve (in this case Eq. 2.15 or 2.16) by simply changing the scale. This scale change is accomplished in the "f" model as

$$G = G_i (1 - f') \tag{2.18}$$

where f' is defined as

$$f' = (f_c + s.f)/(f_c + t) \tag{2.19}$$

where f_c is the degree of mobilization at the unloading point, and s and t are given in Table I below. The two cases of unloading, denoted by (a) and (b) in Table I (curve B, Fig. 9), correspond to short and long unloading situations, respectively. A short unloading is one where the two normal stress components retain their relative position (i.e., the smaller one remains the smaller), and a long unloading is one where the relative position of the two normal stress components switch (i.e., the one that was greater becomes smaller).

TABLE I

POSSIBLE S-T COMBINATIONS

Loading condition	s	t	Fig. 9 Curve
Loading	+1	+1	A
Unloading (a)	-1	+1	B
Unloading (b)	+1	-1	B
Reloading	-1	-1	C

The validity of the generalized "f" model in active and passive stress paths was checked using data from published test results. It is shown in Appendix A that the model is capable of representing the soil stress-strain relationship very accurately for these stress paths.

Undrained Stress-Strain Model Parameters

In the special case of $\phi = 0$ (c_u analysis) the basic f model equation remains the same (See Eq. 2.16). However, f is calculated as the ratio of maximum shear stress in the element to the undrained shear strength (Eq. 2.14b). Since test results are normally given as the axial (major principal) stress versus axial strain, it is more convenient to determine E_i (Young's modulus), and use the elasticity relationship with $v = 1/2$ for the undrained condition,

$$G_i = E_i / 2(1 + v_i) = E_i/3 \qquad (2.20)$$

where the index i corresponds to the initial conditions.
There are various sources of information that should be considered when the undrained initial modulus is selected, such as: laboratory (unconfined compression, UU and CU type triaxial) test results; and, values backfigured from foundation settlement measurements.

Laboratory test results can be interpreted in various ways to obtain the initial modulus. Since the origin of the experimental stress-strain curves is not very clear, it is desirable to fit a curve and use its initial slope at the origin. In order to fit the f-model curve, Eq. (2.16) may be integrated, for the c_u case, to obtain

$$\epsilon = A \ln (1- \tau/c_u) \qquad (2.21)$$

with $A = -2\, c_u/E_i$. Thus, any value of f may be used to determine E_i.

A well-defined procedure is to measure the strain at half way to failure (f=1/2), the inverse of which gives the average <u>secant</u> modulus

of the soil. This modulus is called "E_{50}" in the literature, and will be used here. For f=1/2, Eq. (2.21) gives

$$\epsilon_{50} = -2 \, (c_u/E_i) \, \ln \, (1/2) = c_u/E_{50} \qquad (2.22)$$

after some manipulation Eq. (2.22) can be written as

$$E_i/E_{50} = -2 \, \ln \, (1/2) = 1.386 \qquad (2.23)$$

In interpreting the results reported in the literature, the differences in definition of terms should be considered. The term "E_u" used in earlier finite element studies refers to a bi-linear stress-strain curve. This value seems to be intended to represent the initial modulus, but it is very likely that it is closer numerically to E_{50}.

Nonlinear Analysis Scheme

The initial slope method is used in the finite element program to account for nonlinearity. Initial slope method tends to be inaccurate if stress increments due to loading or geometry changes are large. Since relatively large loading steps are necessary in a finite element analysis to keep computing resource requirements within reasonable limits, a stable acceleration scheme was devised for the "f" model to minimize the errors due to the use of initial slope method. The details of this scheme are presented in Appendix A.

CHAPTER III

ANALYSIS OF E99 I-WALL TEST SECTION

E99 Test Results

A full scale test, which will be referred to as "E99 Wall" test in the following paragraphs, was performed on a 200 ft long sheet pile wall constructed on the landside berm of the Item E99 East Atchafalaya Basin Protection Levee located on Avoca Island just south of Morgan City, LA (Fig. 10). Water was ponded between the sheet pile and the levee in four stages over a period of two months. The sheet pile had a free height of 10.8 ft, and penetrated 23 ft into the ground. The sheet pile section used was PZ-27.

Some of the information presented in the report on the test (Ref. 14) are reproduced here for reference. Data for the idealized soil profile (unit weight and undrained shear strength) are given in Table II below. Other critical results of the measurements are in the form of moment diagrams (Fig. 11), and deflection of the pile at four sections labeled A through D (Figs. 12 and 13). It should be noted that, probably due to the unevenness of the ground surface, the final 8 ft water head on various sections of the wall appear as 7.8 to 8.3 ft on these graphs. From the moment diagrams shown in Fig. 11, it may be concluded that the maximum moment at 8 ft head should have been about 20 k-ft, and it occurred at about elevation -5 ft. In Fig. 12, only two of the four deflection shapes are reproduced; the other two are similar but

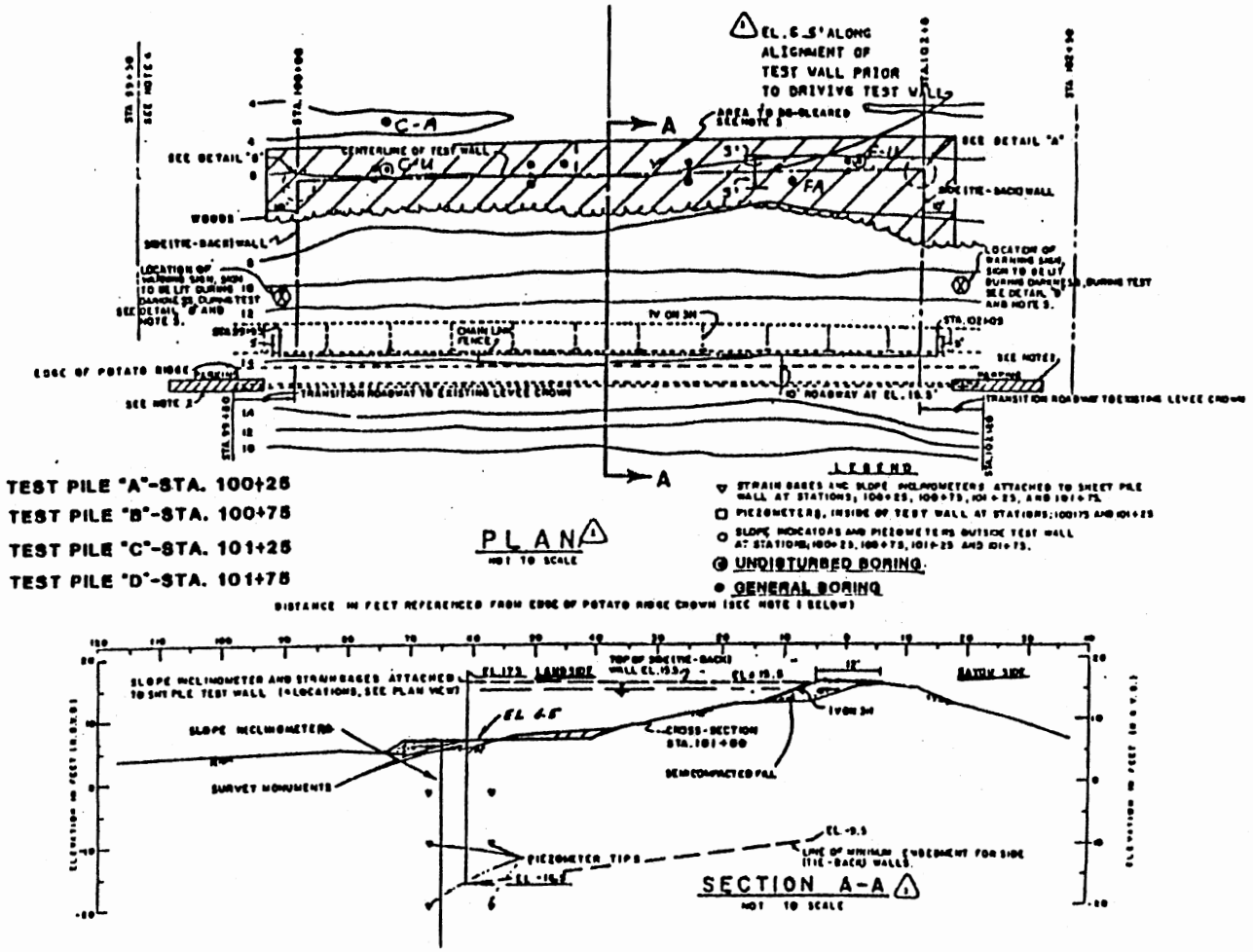

Figure 10. Plan and Profile of E98 wall (Ref. 14)

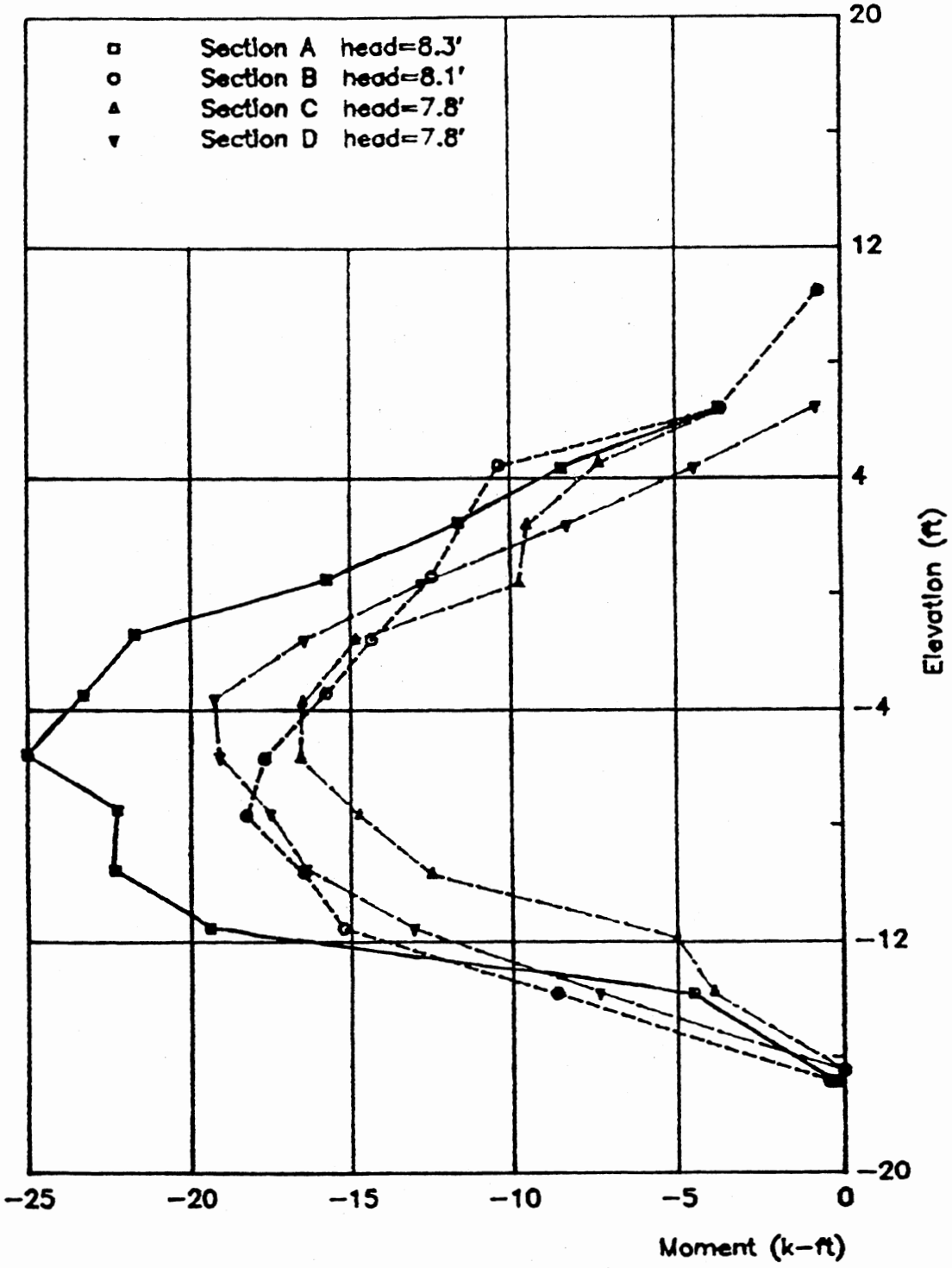

Figure 11. E99 wall: Measured moments.

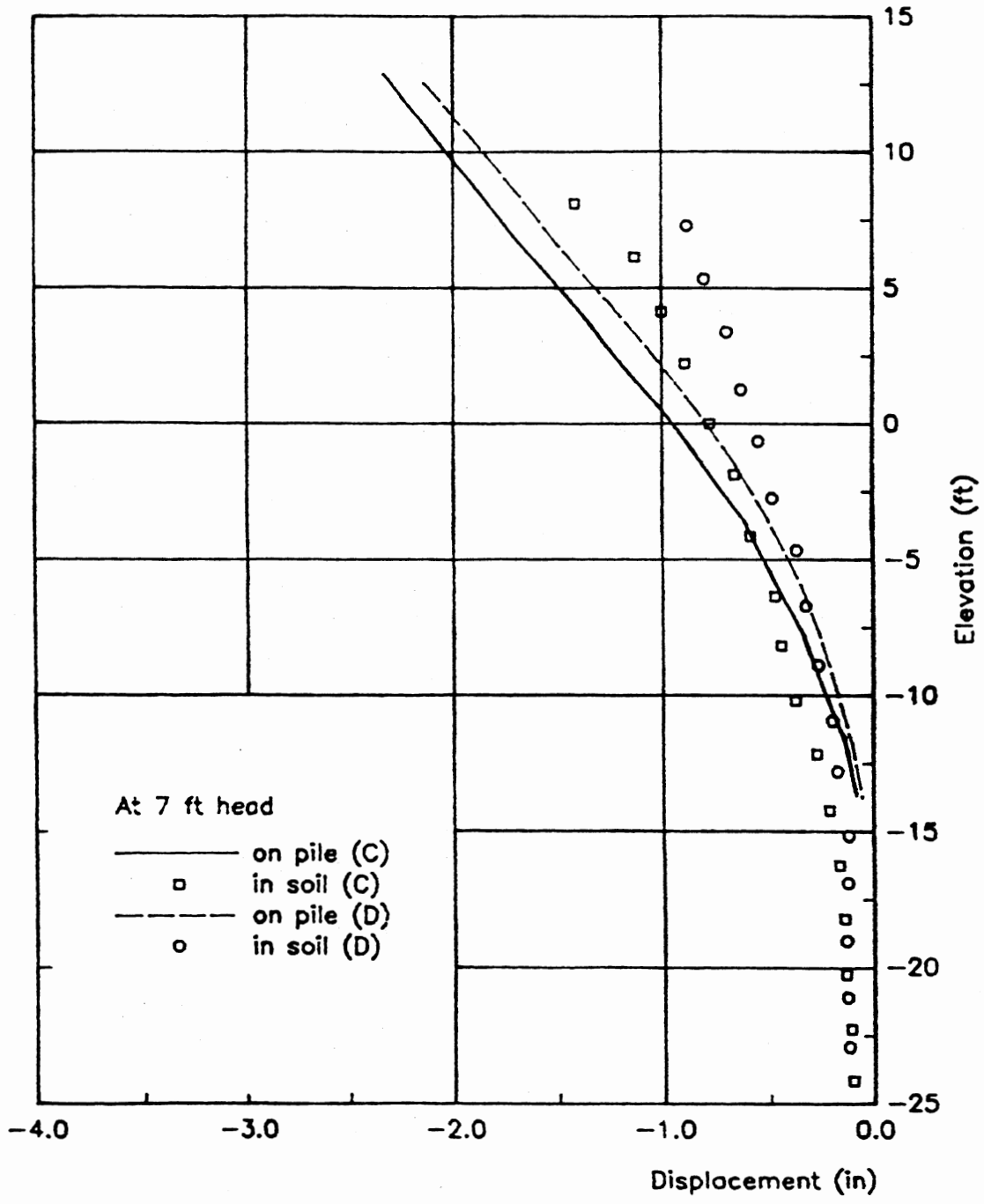

Figure 12. Measured lateral displacements on pile and in the soil 4 ft in front.

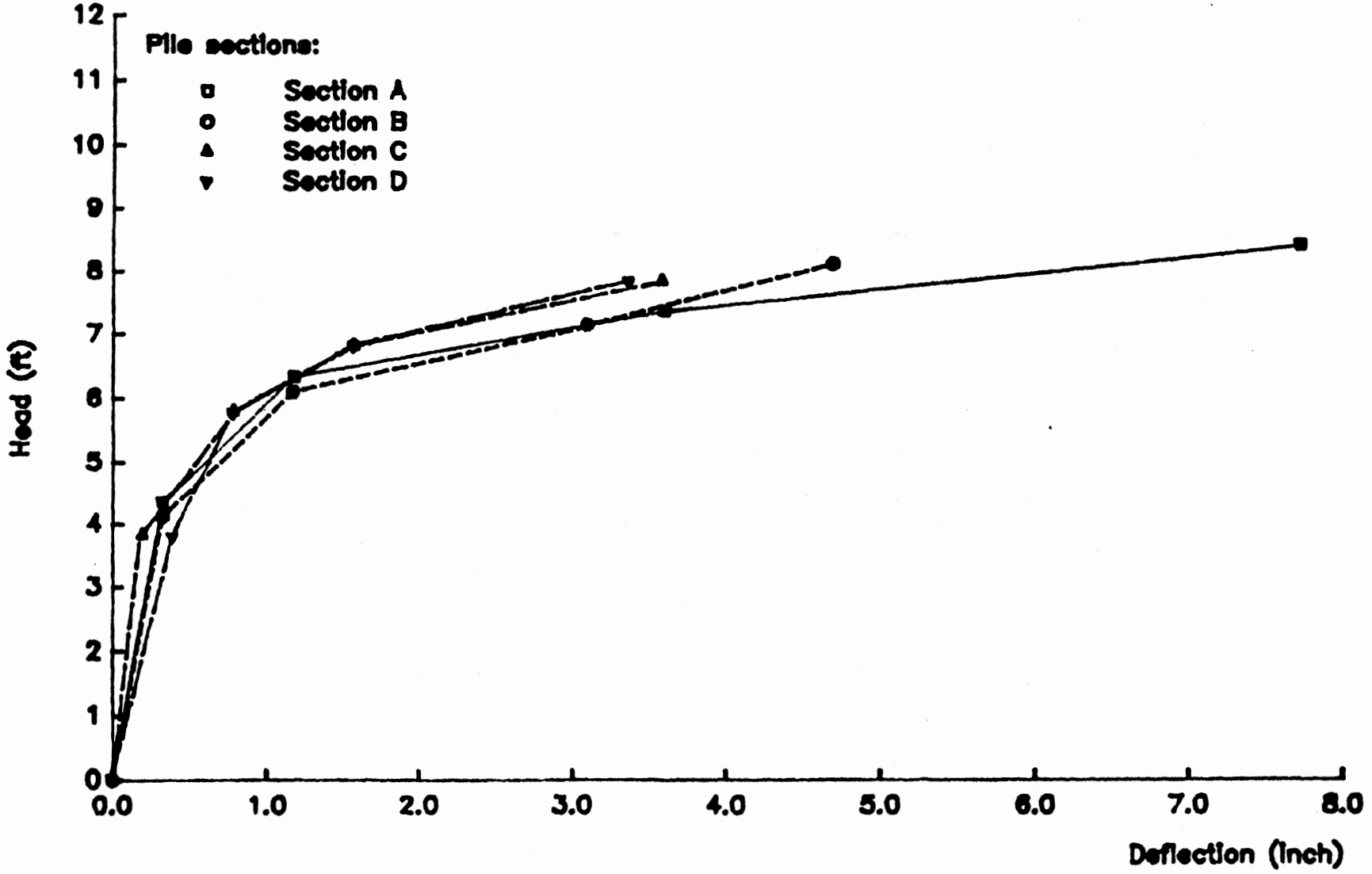

Figure 13. E99 wall: Measured top deflection.

appear somewhat irregular. The conclusion of the report on the test (Ref. 14) is that the soil displacements are in the order of 60% to 100% of those of the pile.

TABLE II

IDEALIZED SOIL PROFILE AT E99 WALL SITE

Elevations (ft)		Layer thickness (ft)	c_u (psf)	Unit weight (pcf)
6.5	-1	7.5	200	104
-1	-5	4.0	500	107
-5	-14	9.0	350	106
-14	-19	6.0	500	104
-19	-29	10.0	500	101
-29	-44	15.0	550	100

Soil Evaluation

Soil stress strain properties are not available for the soils at the E99 wall test section. Therefore the required model parameter has been estimated based on the "E_{50}/c_u" values obtained from published results. Holtz and Kovacs (Ref. 8) have collected data from the literature and have shown a correlation between the E_{50}/c_u ratio versus PI. This correlation, given in Fig. 14, shows that for soft clays with PI of 50 to 100, the E_{50}/c_u ratio is likely to be between 50 and 500. Figures 15 and 16, reproduced from various references (2, 6) show similar data.

Fig. 15 shows that for CH clays E_u/c_u lies between 50 and 1000 depending on the plasticity of the soil and the initial stress ratio

(which is the same as f here). Among CH clays in this figure, Atchafalaya clays have the smallest E_u/c_u ratio: for low initial-f (0.2-0.4) it is in the range of 200 to 400; for high initial-f (0.6-0.8) it drops to a range of 50-100. Initial-f is related to the OCR of the soil (Fig. 16(a)). For normally and slightly overconsolidated (OCR=1.5) soils, initial-f is 0.4 to 0.7; Fig. 15(a) gives E_u/c_u ratios in 80-200 range for this f range. Also, the data given in Fig. 15(b) shows that the E_u/c_u ratio for Atchafalaya clays is about 100 for higher initial-f values, and about 300 for lower initial-f values.

Based on the above information and tests on other soils in the area (furnished by the U.S. Army Corps of Engineers, Appendix B), the classification of the soils at the E99 site has been established. Important points may be summarized as

a. The soils in the area are generally classified as CH.

b. Soils are usually fully saturated and have high void ratios.

c. Undrained shear strengths are low.

d. E_{50}/c_u ratio varies in a wide band of about 50 to 350.

The properties of the typical soils of the area are such that they would clearly be in an undrained condition during the E99 wall test. Because of the uncertainty of the modulus parameter, a range was selected, and analyses were repeated for various values.

Although the term "prediction" may be used in the following, clearly the intent here is not to show how good the test results could have been predicted. Because the stress-strain relationship has only been estimated, the purpose in this work has been to calibrate or "fine tune" the analytical tools.

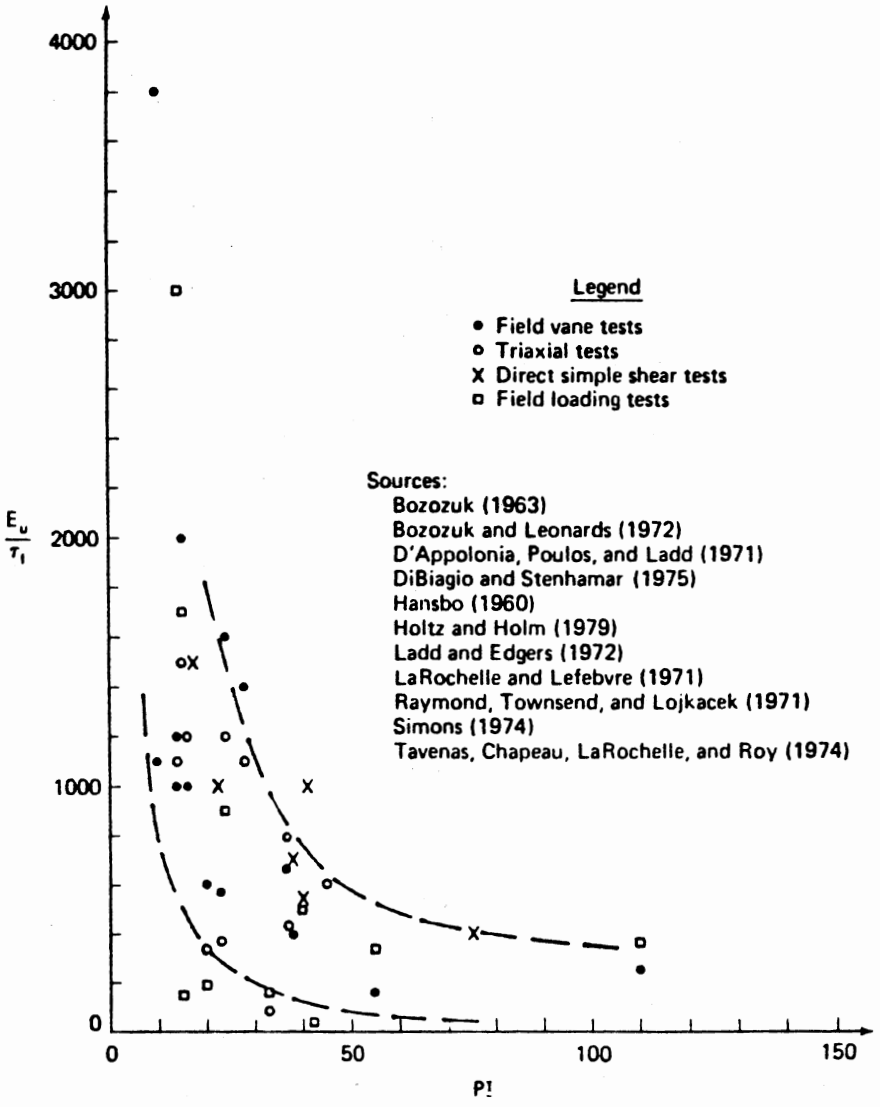

Figure 14. Ratio of E_u/τ_f versus plasticity index, as reported by several authors (after Holtz and Kovacs (8)).

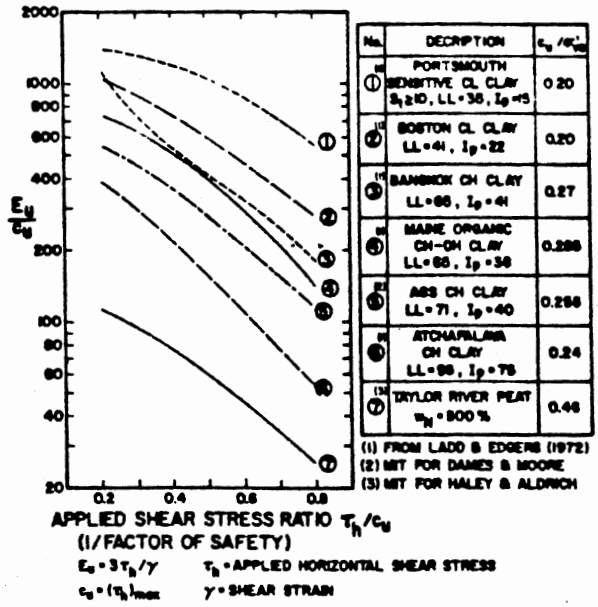

(a) NORMALIZED SECANT MODULUS VS. STRESS LEVEL FOR NORMALLY CONSOLIDATED SOILS

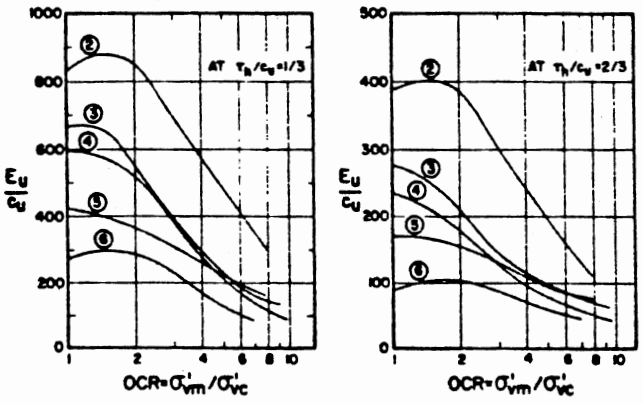

(b) NORMALIZED SECANT MODULUS VS. OVERCONSOLIDATION RATIO

Figure 15. Normalized Modulus Data from Ko-Consolidated Undrained Direct Simple Shear Tests (after Foott and Ladd (6)).

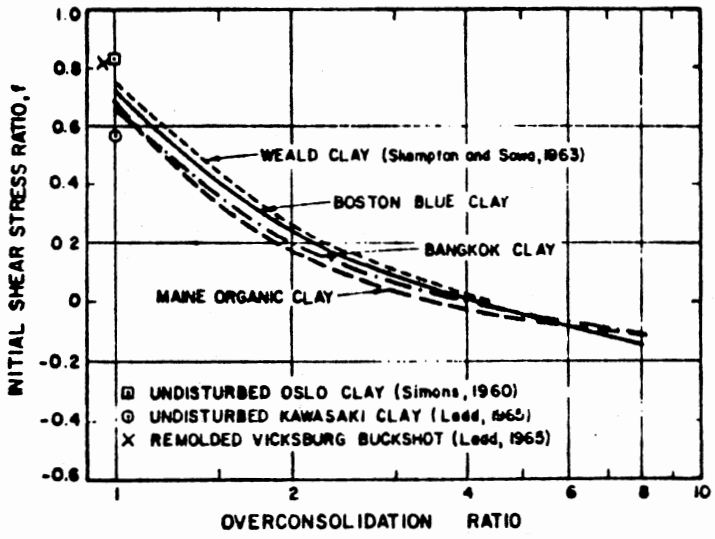

Figure 16(a). Relationship between initial shear stress ratio and overconsolidated ratio (after D'Appolonia et. al. (2)).

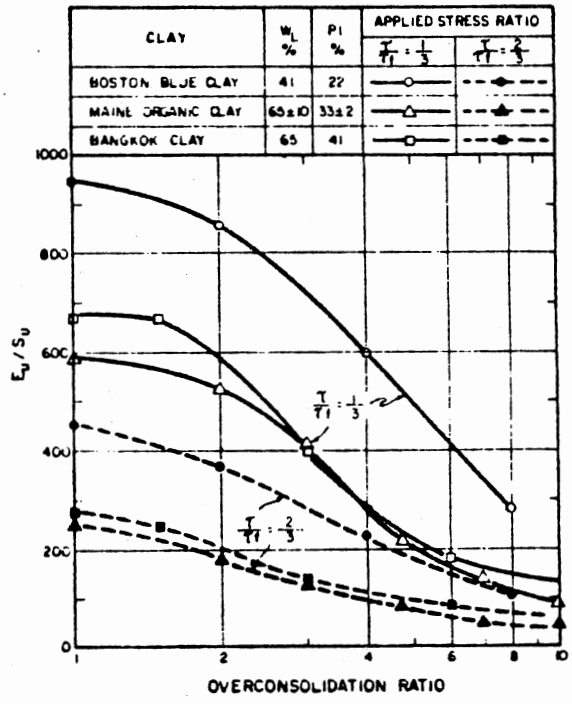

Figure 16(b). Relationship between E_u/s_u and OCR from CU tests on three clays (after D'Appolonia, et. al.(2))

Soil and Interface Parameters

Some of the input parameters values used in the analyses are listed in Table III.

TABLE III

SOIL AND INTERFACE INPUT PARAMETERS

K_t (lbs/ft/ft)	20000
μ	0.1
C_a (lbs/ft)	0
m	200,300
n	0
ϕ (degrees)	0

In the above table, K_t is the tangential stiffness at the interface, μ is the friction coefficient at the interface, C_a is the adhesion at the interface (between soil and wall), m and n are the "f model" parameters; m is equal to E_{50}/c_u, and finally, ϕ is the soil angle of friction which is equal to zero in this case (undrained).

Because of the lack of experimental results on interface behavior, three preliminary cases were analyzed to study the effect of K_t. In one case, K_t was assumed to vary linearly with depth. In the other cases, it was assumed to be constant along the depth. However, these trials show no significant effect of K_t on the obtained results. Hence, a constant value was assigned to K_t of the above magnitude.

The limiting value for the tangential force at the interface is shown in Fig. 3b ($F_t \leq \mu.F_n + C_a$). Two cases were considered (1) frictional interface ($C_a = 0$), and (2) adhesive interface ($\mu = 0$). Again, the results of both cases were identical ($\mu = 0.1$ and $C_a = 1000$). Hence, $\mu = 0.1$ and $C_a = 0$ were assumed.

Simulation of E99 Wall Test

The finite element grid used for analyzing the E99 wall test consists of 343 elements joined at 386 nodes. The grid (Fig. 17(a)) is unsymmetric because of the necessity of representing the levee behind the wall to account for its effects on initial stresses. Initial stresses were obtained by first calculating the K_o stresses for the natural ground using "gravity-turn-on" and then adding the levee in a second step. In all analyses Poisson's ratio equal to 0.49 was used to represent the undrained incompressible condition.

In the E99 wall system, the rising water level produces several loading effects. Most apparent is the hydrostatic pressure on the exposed wall above the ground surface. This part of the loading is independent of the deformation of the system. Water loading is also imposed on the ground surface between the wall and the face of the levee. This part of the loading applies both vertical and horizontal components to the soil mass. This part of the loading is also independent of system deformations. As the water level rises, the loading is sufficient to cause separation of the soil from the face of the wall on the flooded side (i.e., a "tension crack" develops behind the wall). This allows free water to enter the crack and to produce hydrostatic pressures on the wall and on the soil on both faces of the

tension crack. This part of the loading (i.e., the depth of the tension crack) is dependent on the water level as well as the deformation of the system.

In the analyses the water level change was represented in 17 steps, with 1 ft increments up to a 4 ft height, 0.5 ft up to 5.5, and 0.25 ft afterwards up to the highest level of 8 ft.

Results of Analyses

Deformations

Figures 17(a) and 17(b) show the deformed shape of the finite element grid at 8-ft water load for E_{50}/c_u = 200 (unless otherwise stated all results are for this value). The deformed shape is obtained by adding the nodal displacements to the coordinates of the nodes. In order to see the deformation clearly, nodal displacements are exaggerated by a factor (typically 20 as noted in the figures). Therefore, the node locations after deformation are not true and may create the illusion that some parts of the grid intrude on other parts. Fig. 17(a) shows the entire grid and Fig. 17(b) shows the details of the deformation pattern in the vicinity of the pile. The heave observed in front of the wall and on the far side of the levee are the result of the undrained (high Poisson's ratio) assumption. The settlement of the soil under water for this case is approximately 1.5 inches, and the heave in front of the pile is about 1 inch. It is also observed that the pile tends to retard the heave of the soil in the immediate vicinity of the front of the wall.

The calculated lateral displacements of the pile and the soil 4 ft in front of the pile are plotted in Fig. 17(c). These displacements are

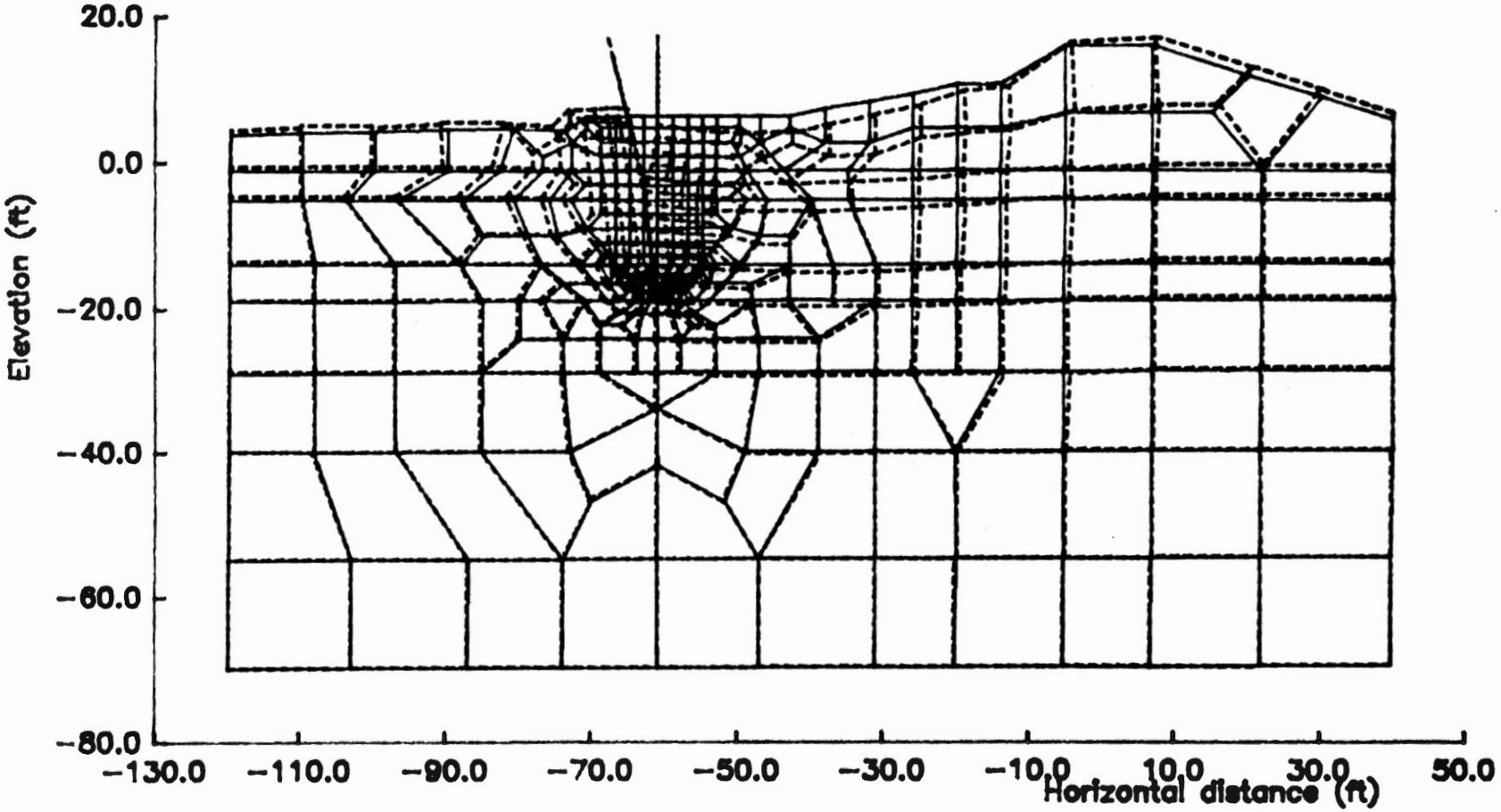

Figure 17(a). E99 wall grid deformed shape [20x] at 8 ft head.

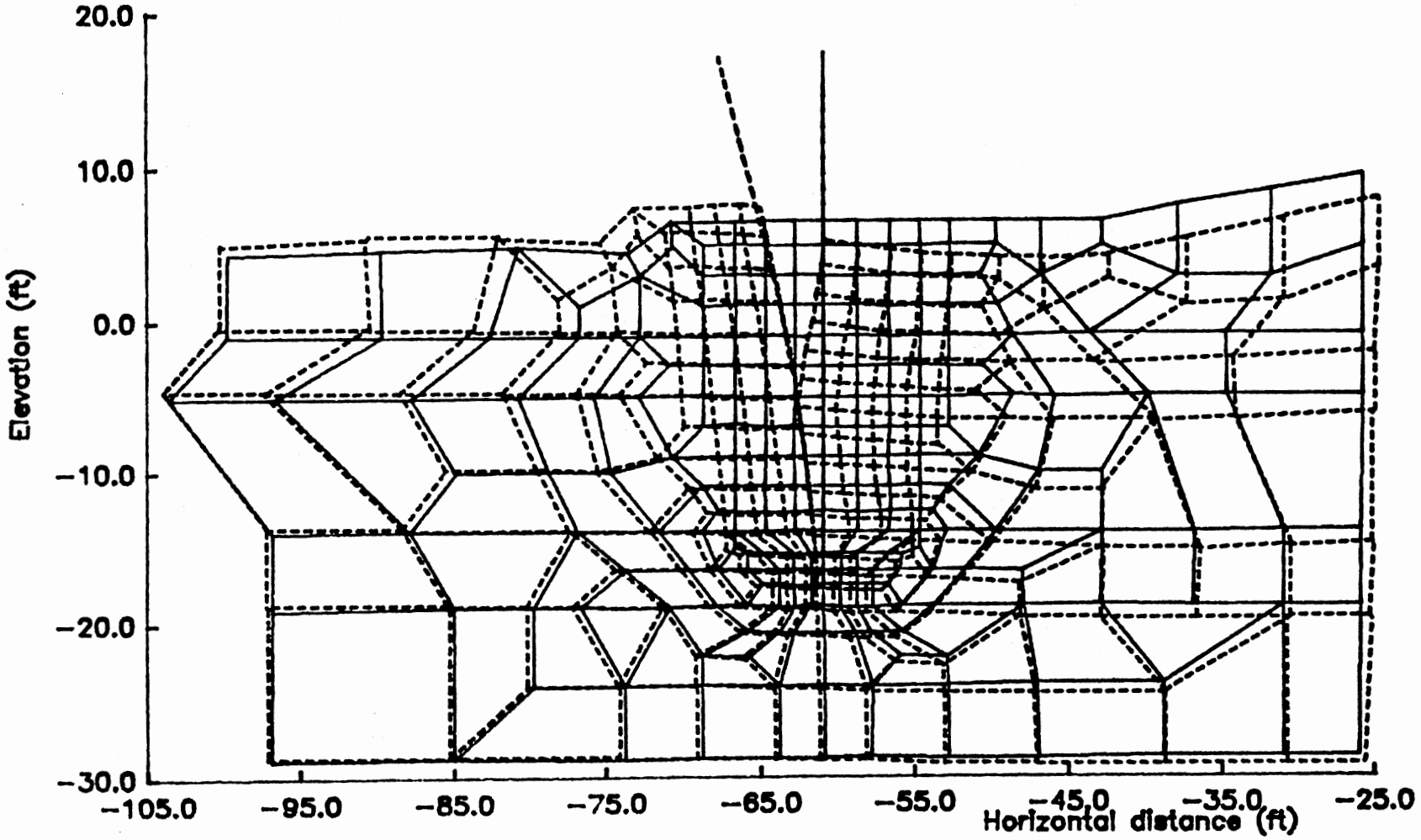

Figure 17(b). E99 wall deformation [20x] in the pile vicinity at 8 ft head.

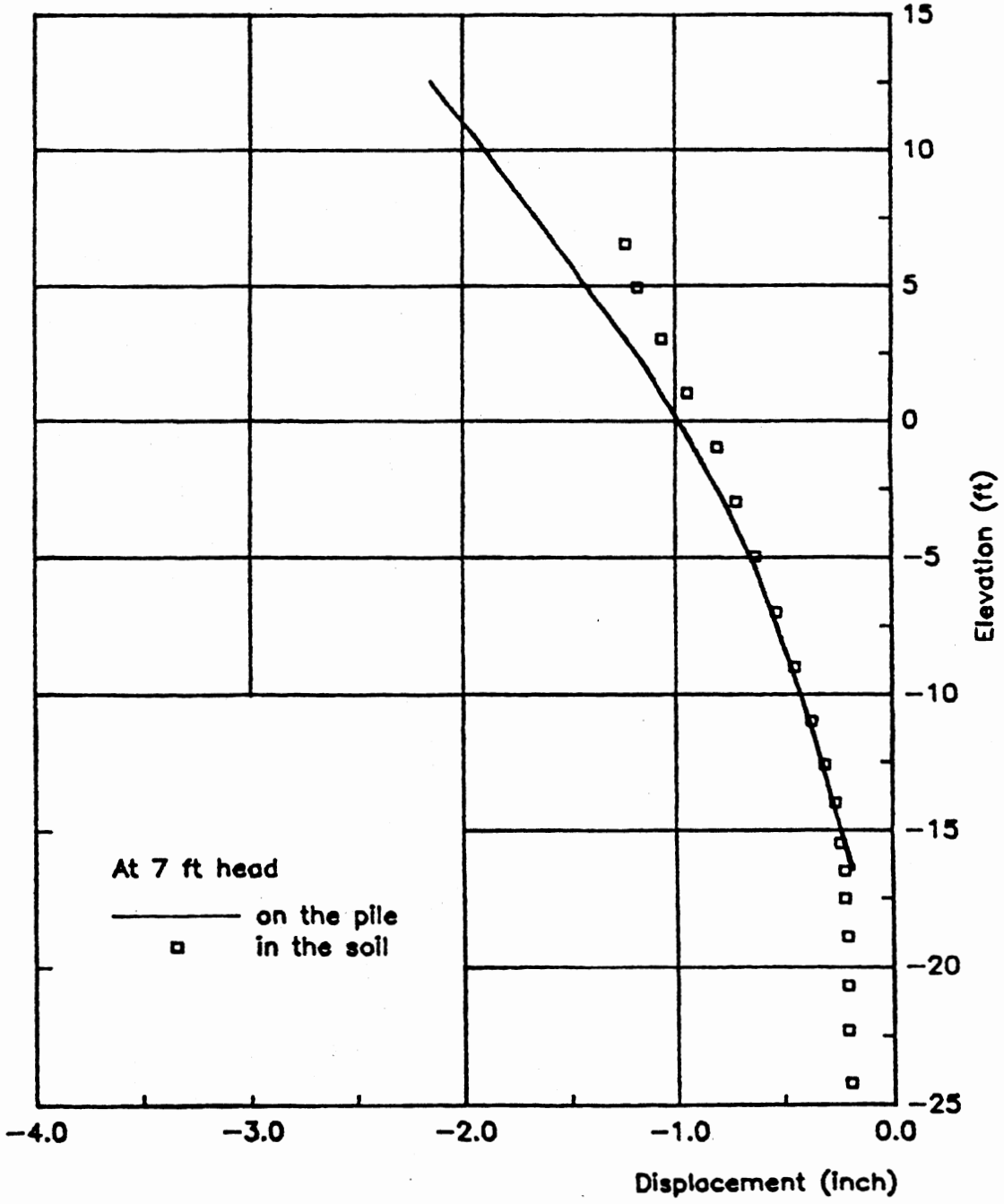

Figure 17(c). Calculated lateral displacements of the pile and the soil 4 ft in front.

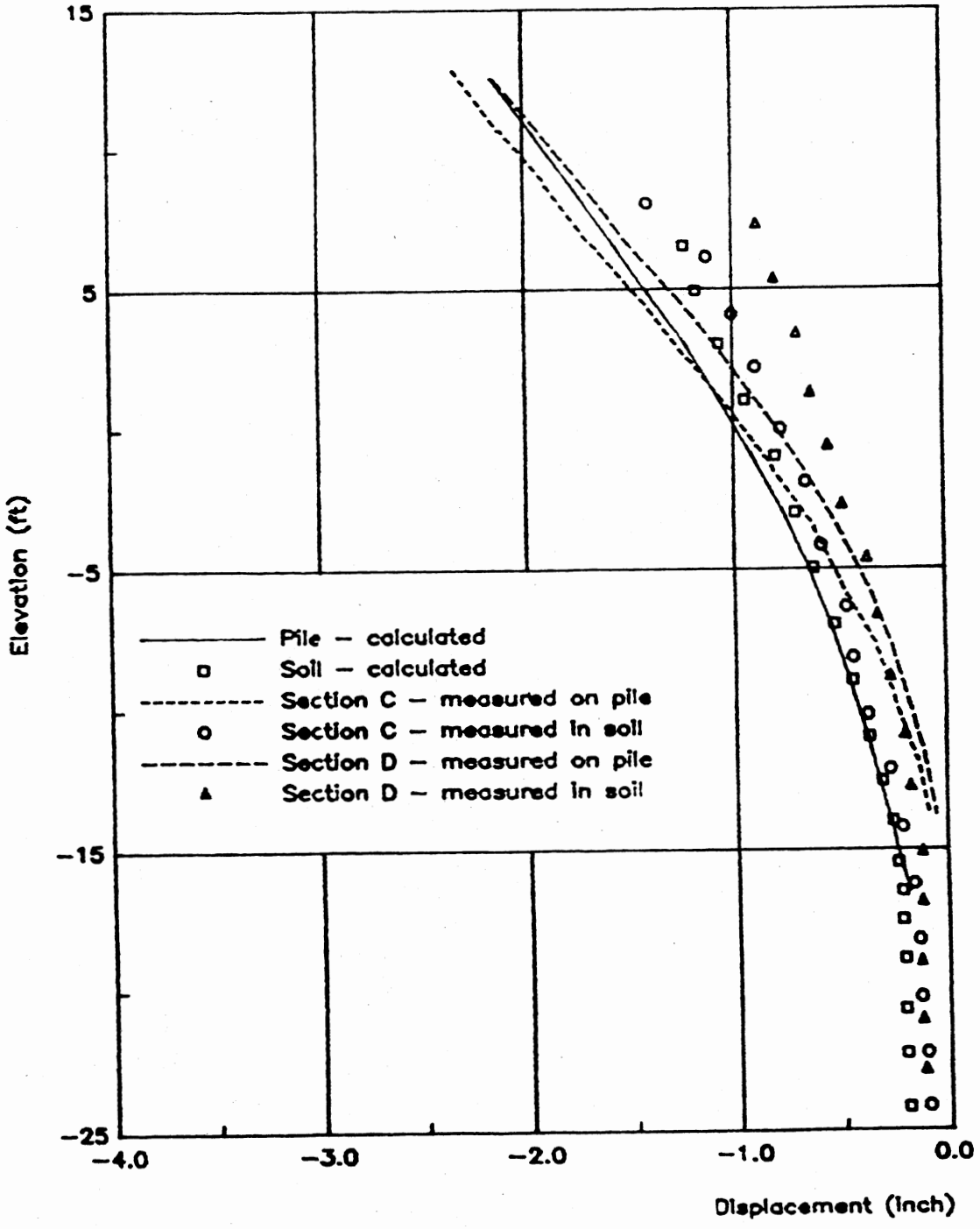

Figure 17(d). Comparison of measured and calculated lateral displacements at 7 ft head.

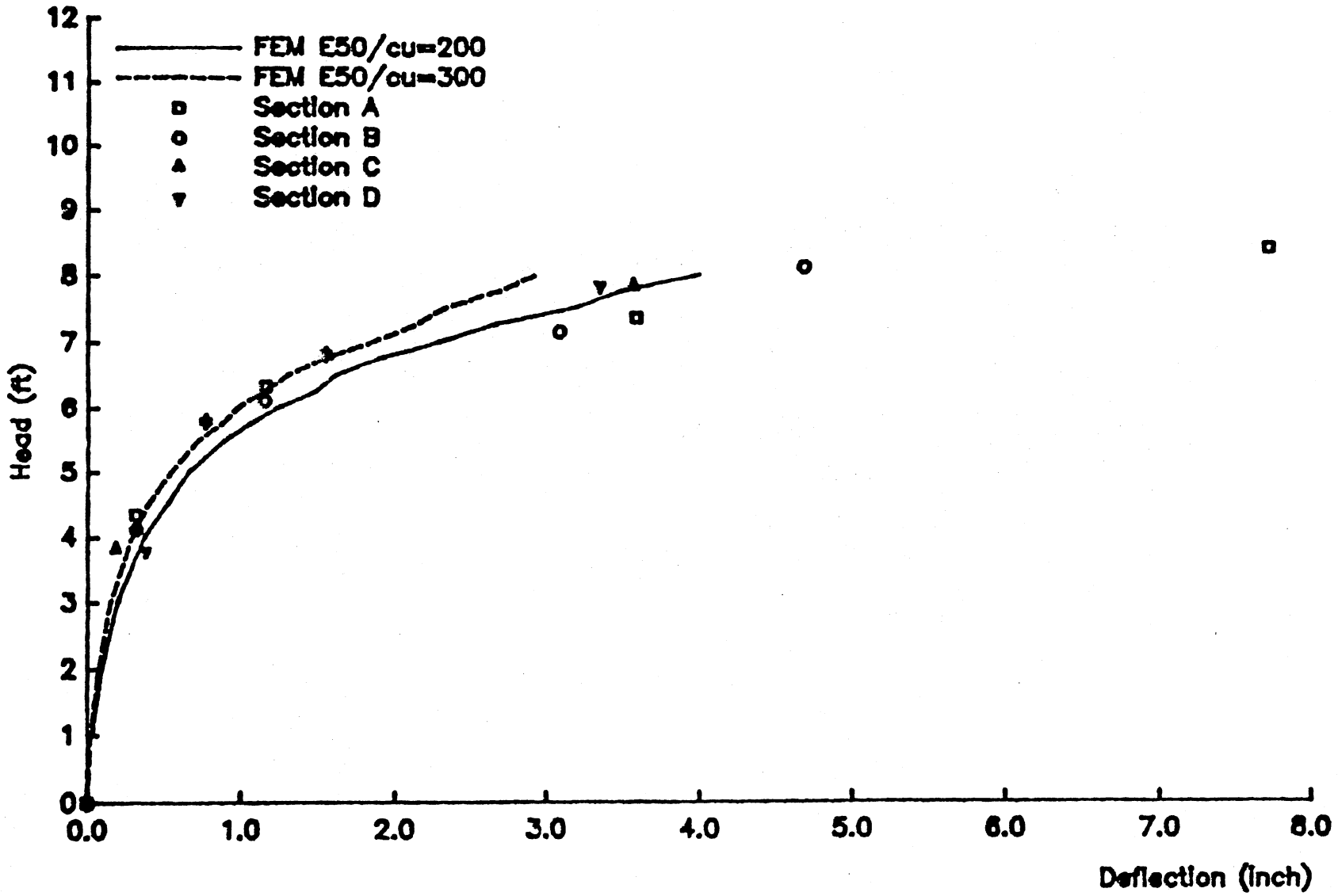

Figure 18. E99 wall: Top deflection versus water head.

compared with the results obtained from the test shown in Fig. 17(d). It is observed that the soil displacement lags behind the wall in the upper half of the embedded depth, indicating that the soil is under lateral compression in that area. At the ground surface level the calculated soil displacement is approximately 68% of that of the pile. In the lower half the difference between the displacements of the soil and pile is negligible except near the pile tip where the pile displacement is backward relative to the soil. This deformation pattern is compatible with test observations.

Figure 18 shows the predicted evolution of pile deflection as the water level is increased for two E_{50}/c_u values used in the soil model. Measured deflections for four sections on the test wall are presented for comparison. For consistency in reporting measured data, the displacement of the pile tip has been subtracted from the displacement of the top of the pile before plotting. Figure 18 shows that the characteristic shape of the water head versus top deflection curve can be predicted closely with the analytical method used. It appears that the appropriate value of E_{50}/c_u for the soils at this site is in the range of 200 to 300. The difference between the results of the two cases is less than the scatter range of the experimental data.

Moment in Sheet Pile

Figure 19 shows moment diagrams for the sheet pile at three water levels (6, 7 and 8 ft) as calculated by the finite element analysis. A comparison with measured moments, Fig. 19(b), indicates that both the location and the magnitude of the maximum moment are predicted reasonably accurately. These are indicative of the reliability of the

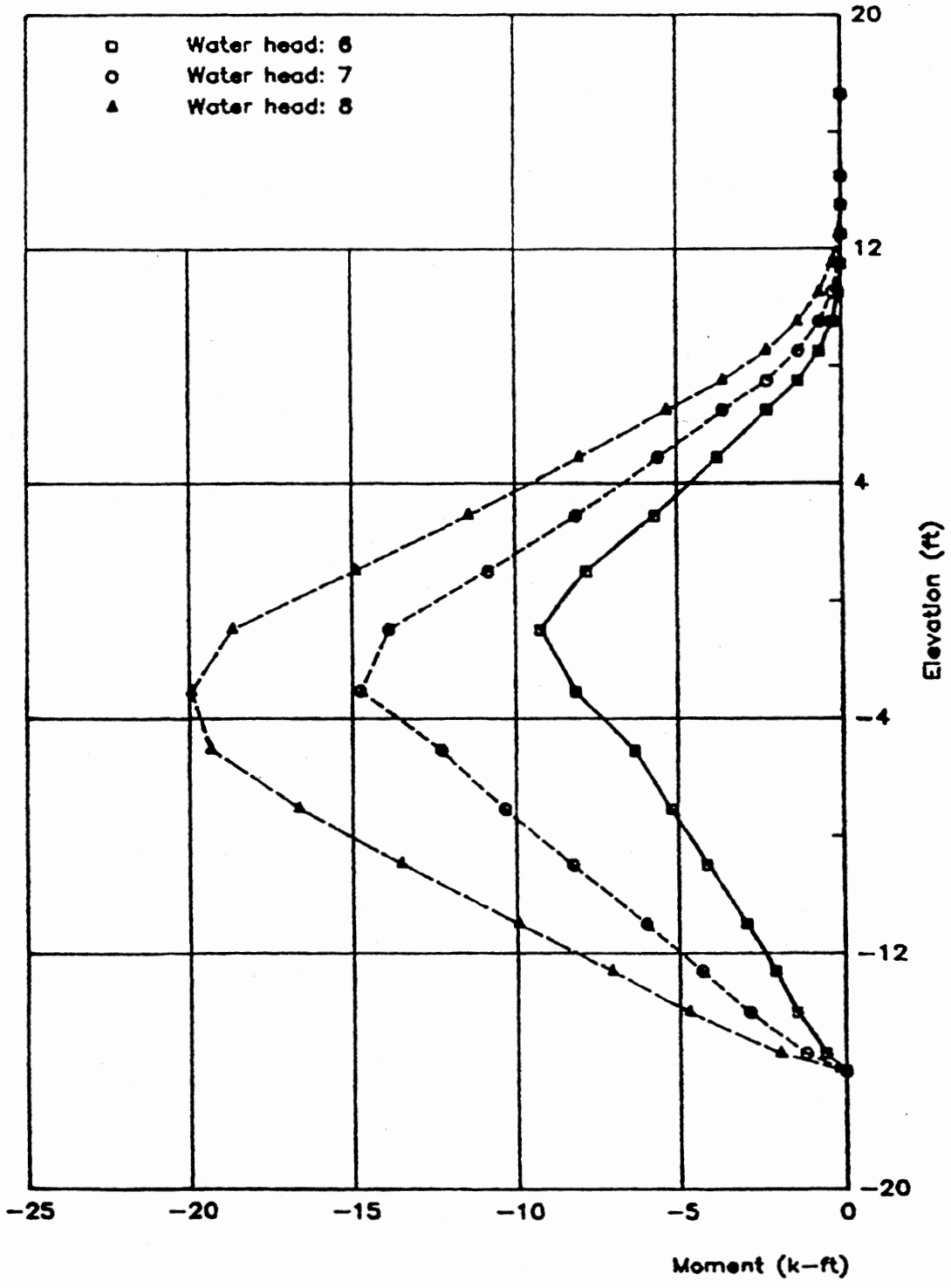

Figure 19(a). E99 wall: Calculated bending moments.

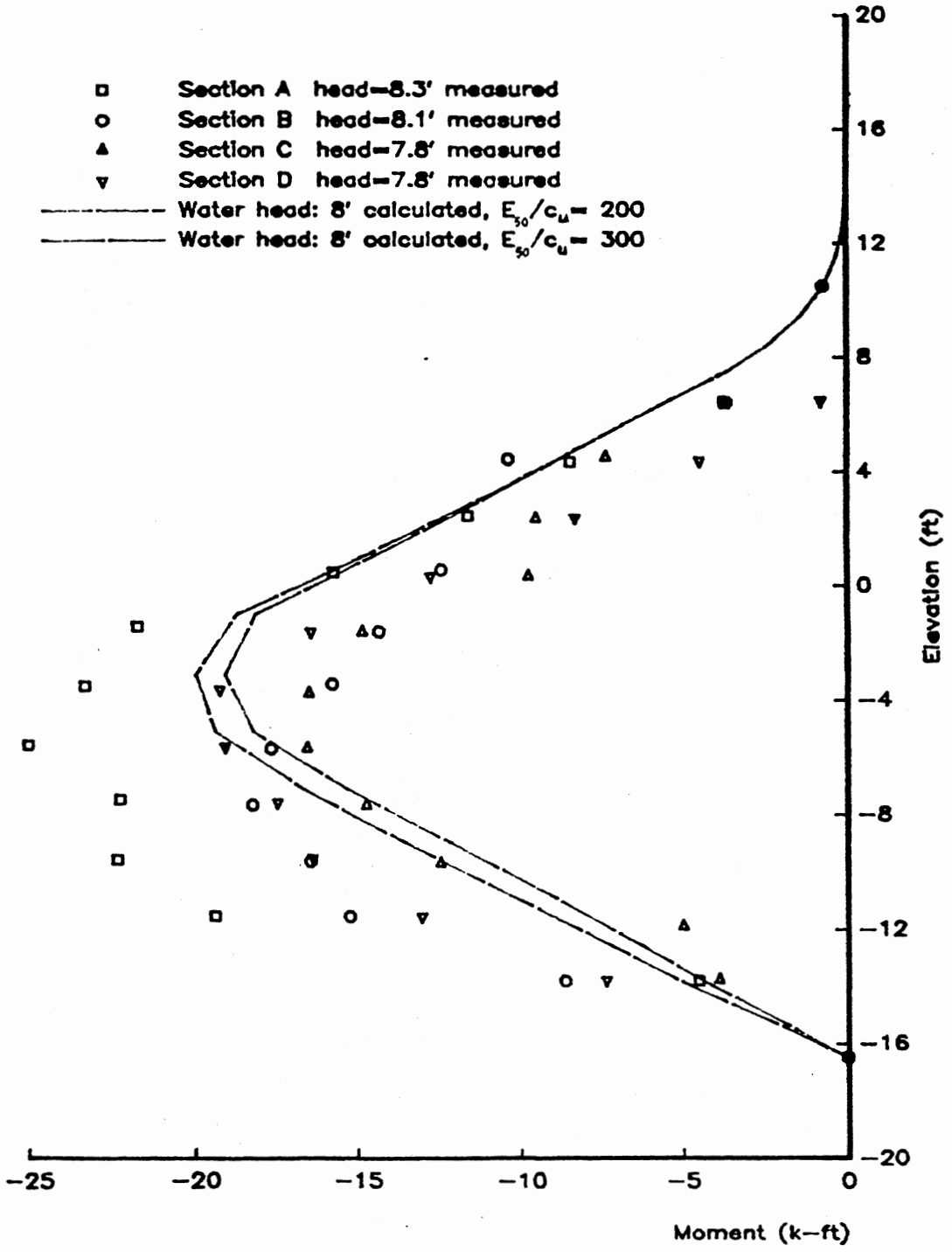

Figure 19(b). Comparison of calculated and measured moments.

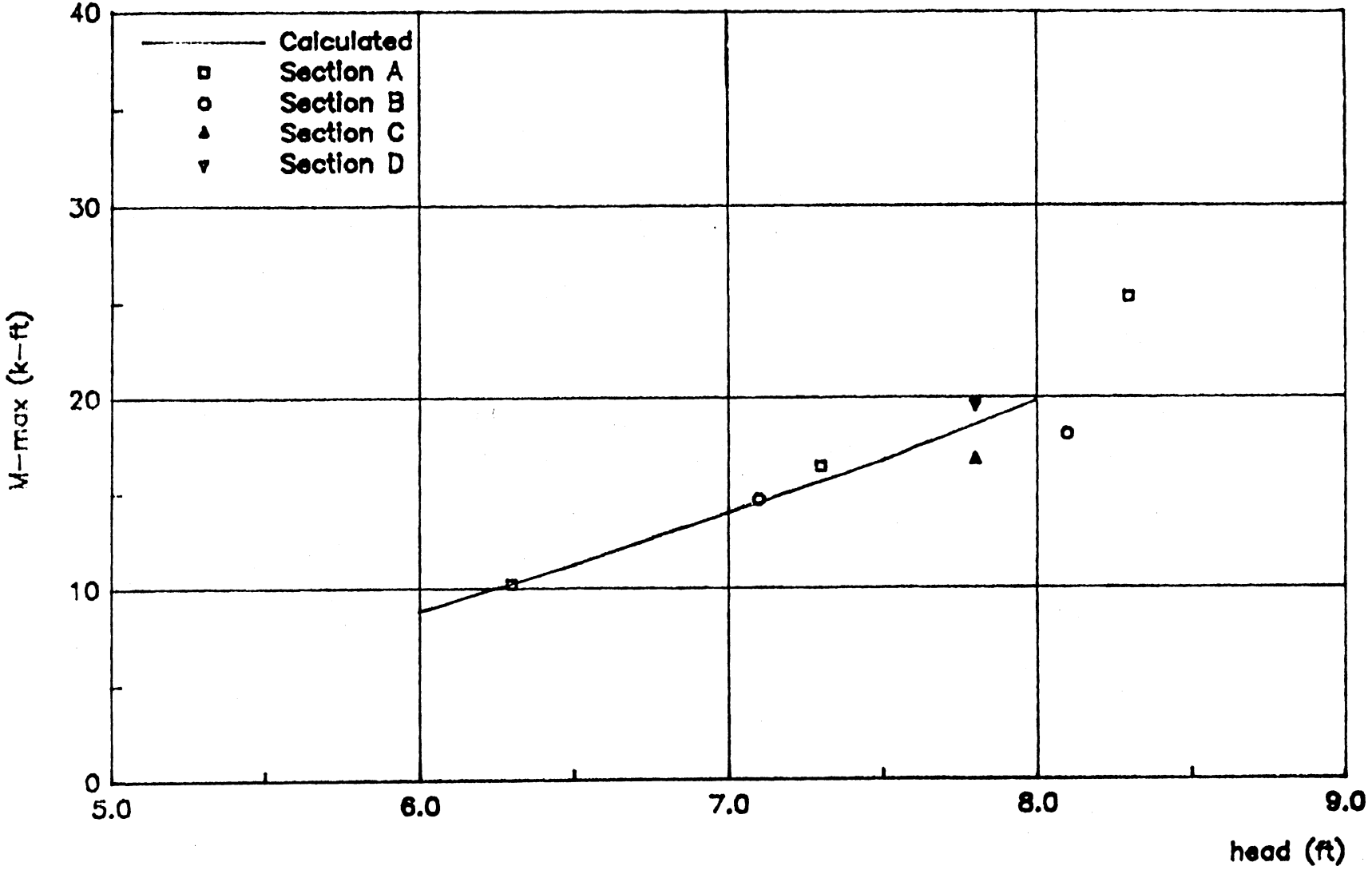

Figure 20. E99 wall: Maximum bending moments.

finite element model in revealing the lateral earth pressure distribution on the sheet pile. The variation of the maximum moment with loading (water head) is shown in Fig. 20 along with the measured values extracted from Fig. 11. Once again, the correlation of calculated and measured values is found to be satisfactory for the same E_{50}/c_u value that also yields the correct pile deflections.

Stresses in Soil

Figures 21, 22, and 23 depict the stress distribution in soil at 8 ft water head. In Fig. 21(a) it is observed that the vertical stress contours are essentially horizontal lines almost perfectly parallel to the ground surface except in the shallow region behind the wall (pond side). This effect of the weight of water can be seen more clearly in Fig. 21(b) where the stresses are shown normalized with respect to the initial overburden pressure. The contour lines labeled "100%" mean that the vertical stress is the same as the overburden. Vertical stresses higher than the overburden occur below the pond due to the weight of the water, and in the shallow region in front of the wall where the wall friction tends to keep the soil from moving upward relative to the pile.

Horizontal stresses, again at the end of the last loading step (8 ft), are plotted in Figs. 22(a) and (b). Higher lateral stresses in front of the wall, in the shallower region, are due to wall movement. The higher stresses in the top 10 ft behind the wall are due to the hydrostatic force of the water in the tension crack.

Shear stresses are plotted in Fig. 23. The highest shear stresses occur around the tip of the pile as should be expected. The stress concentration in front of the wall at about elevation -3 is the effect

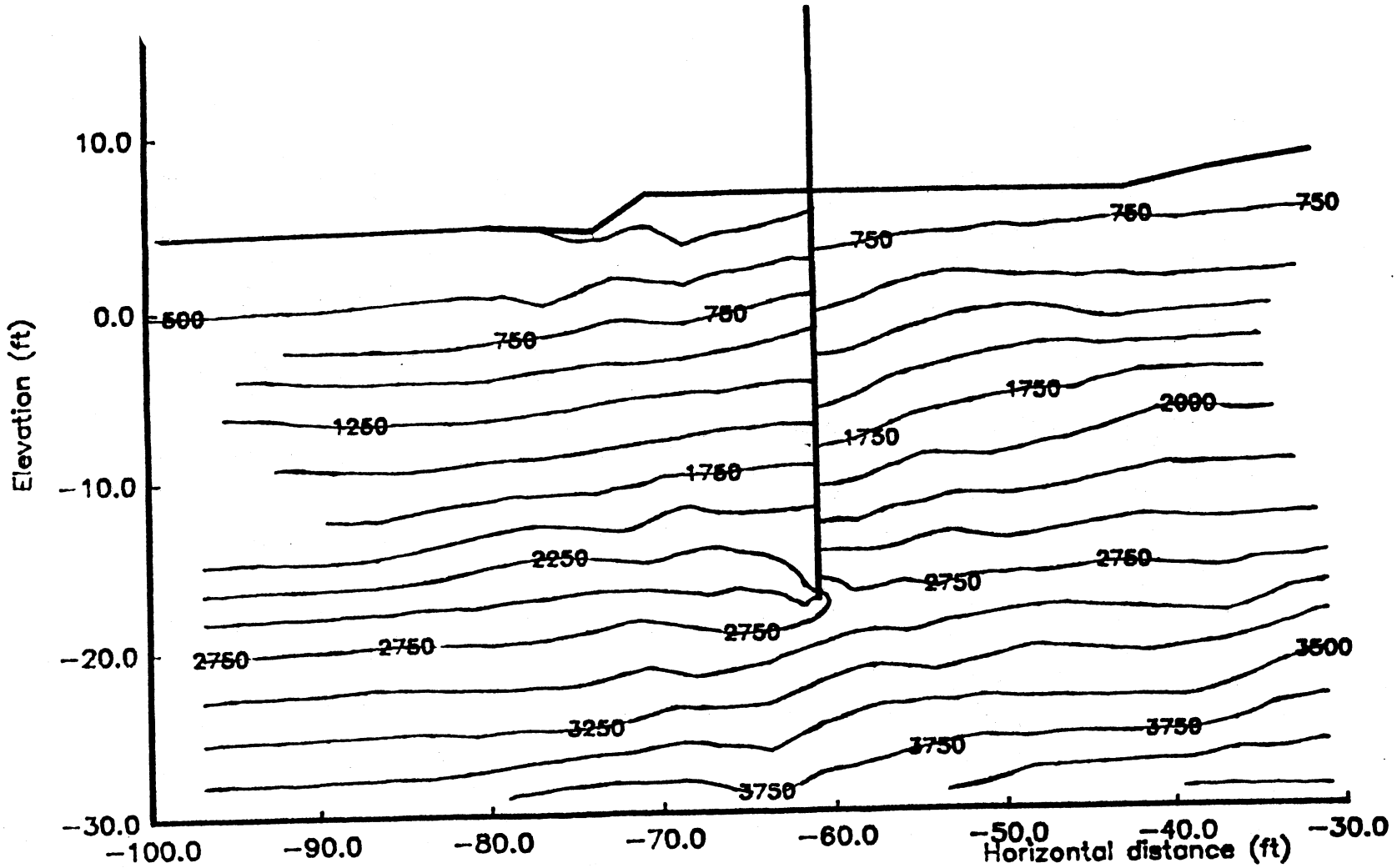

Figure 21(a). Vertical stress contours in the pile vicinity.

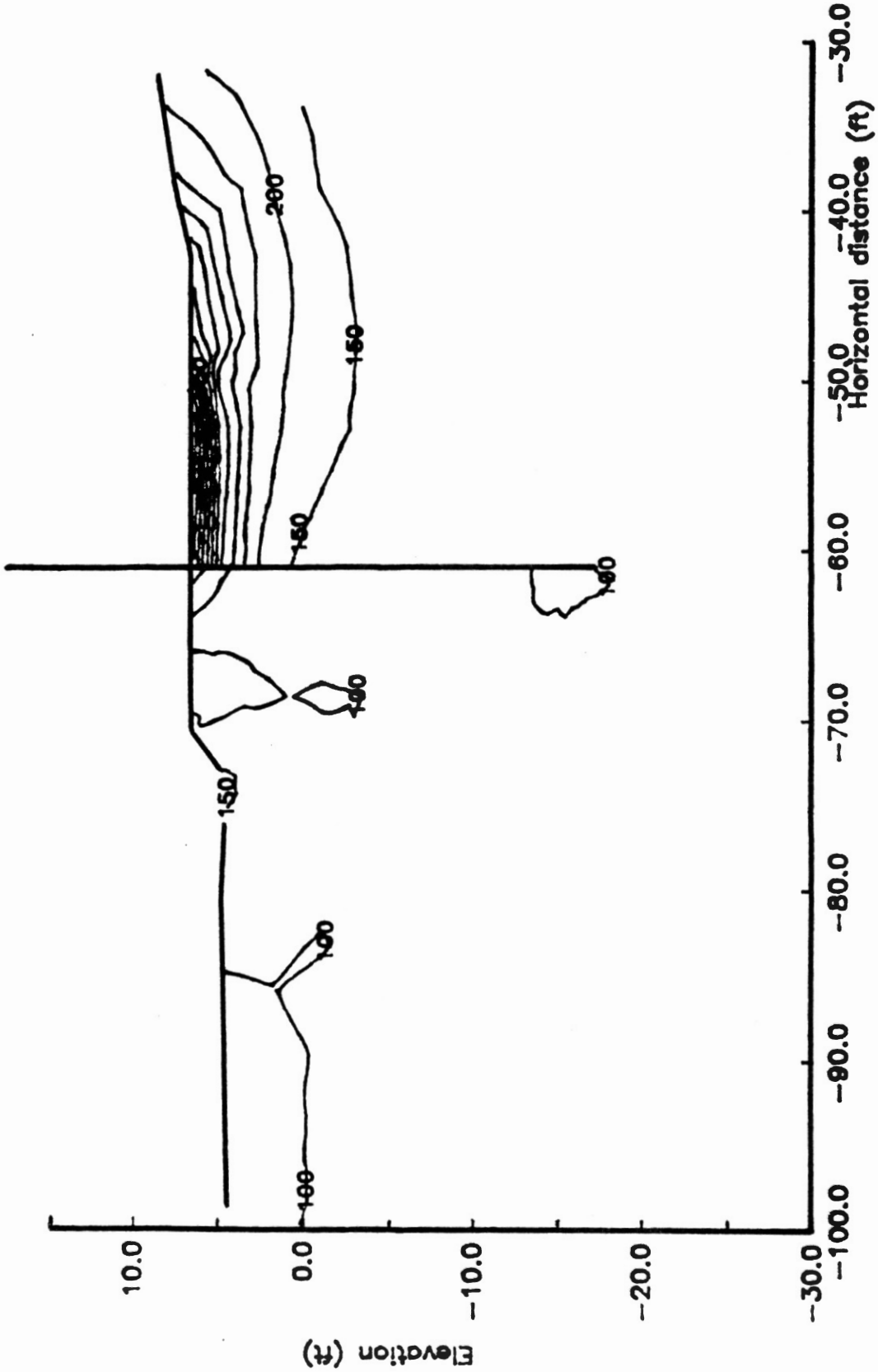

Figure 21(b). Vertical/Overburden stress contours (%).

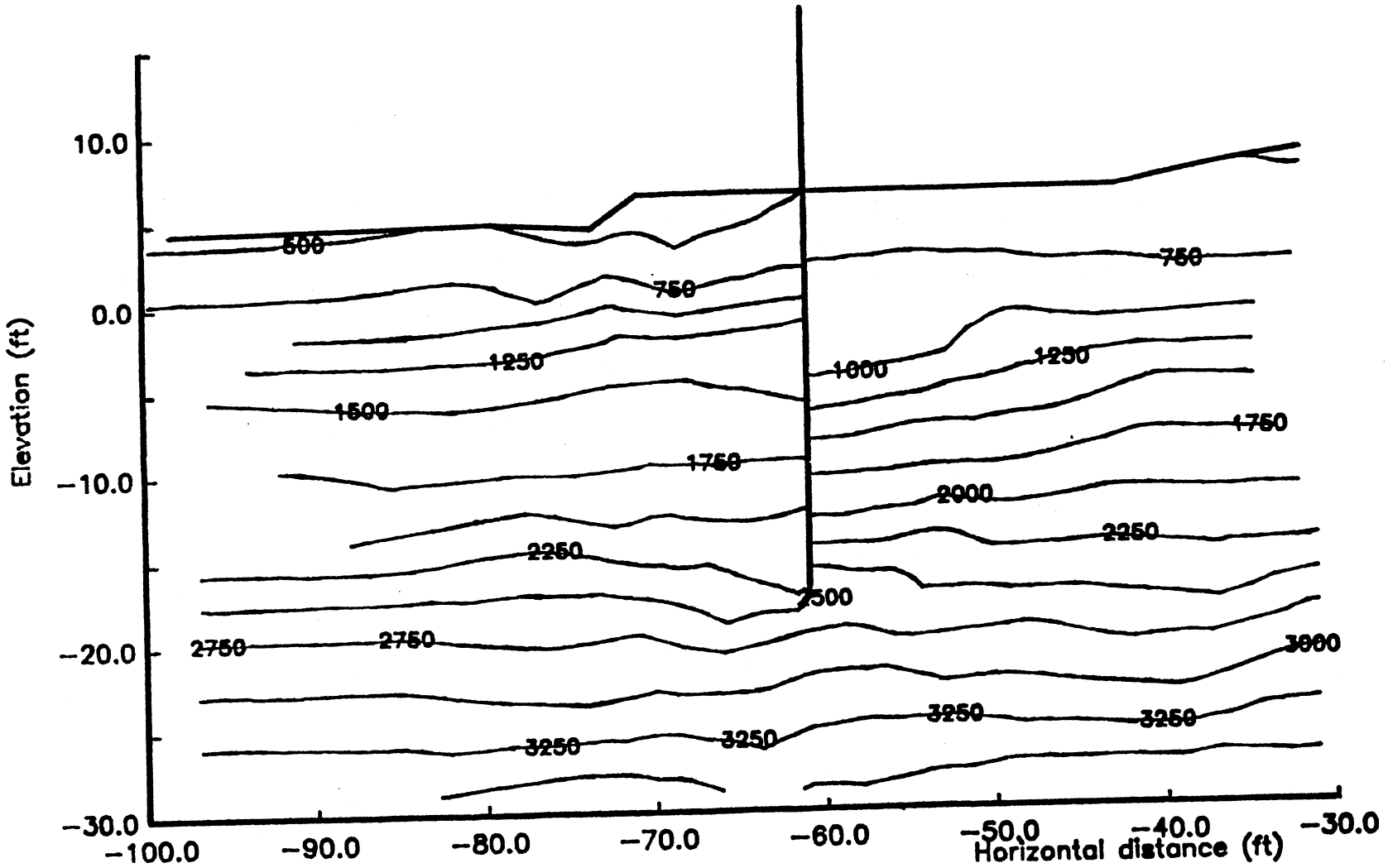

Figure 22(a). Horizontal stress contours in the pile vicinity.

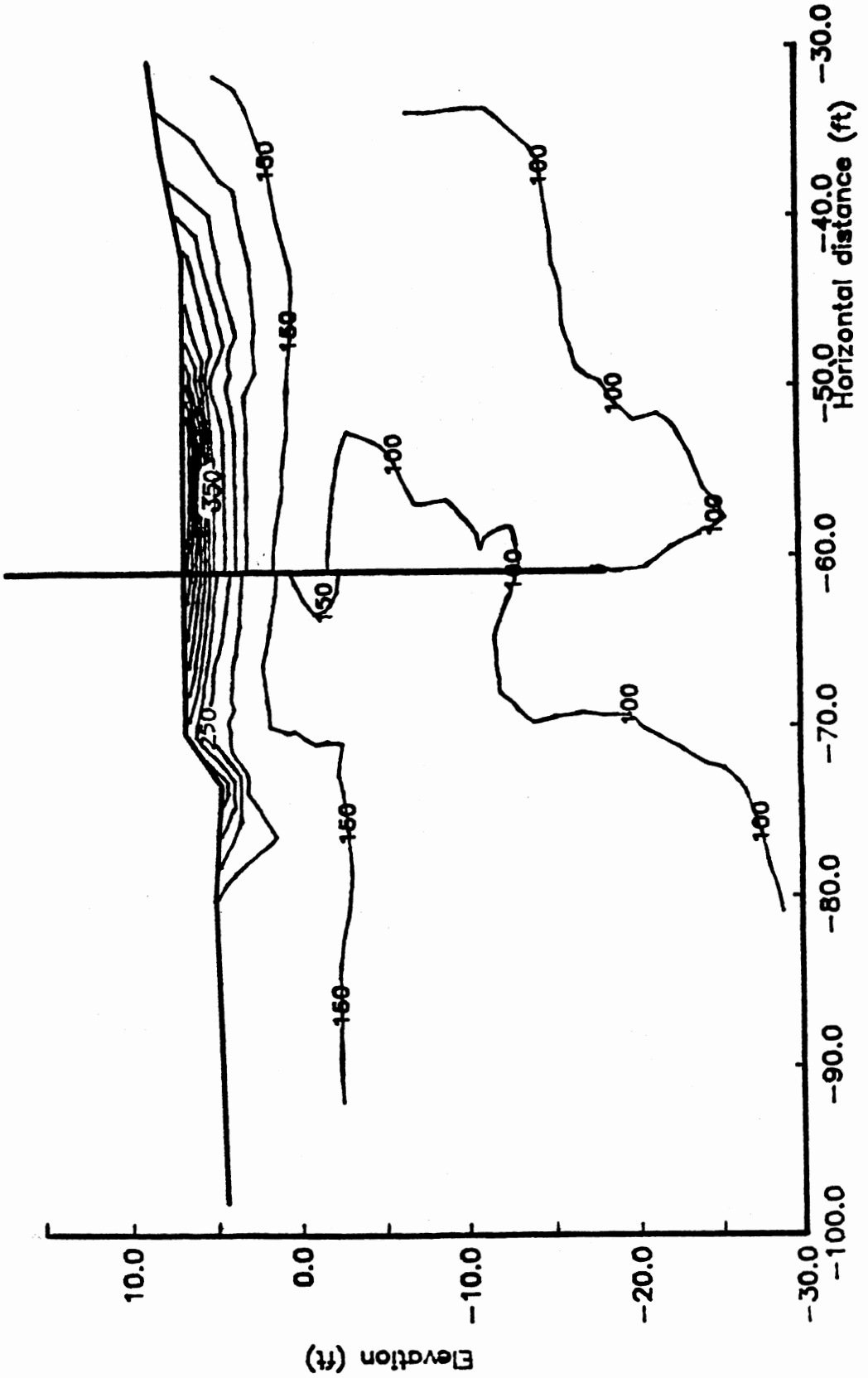

Figure 22(b). Horizontal/Overburden stress contours (%).

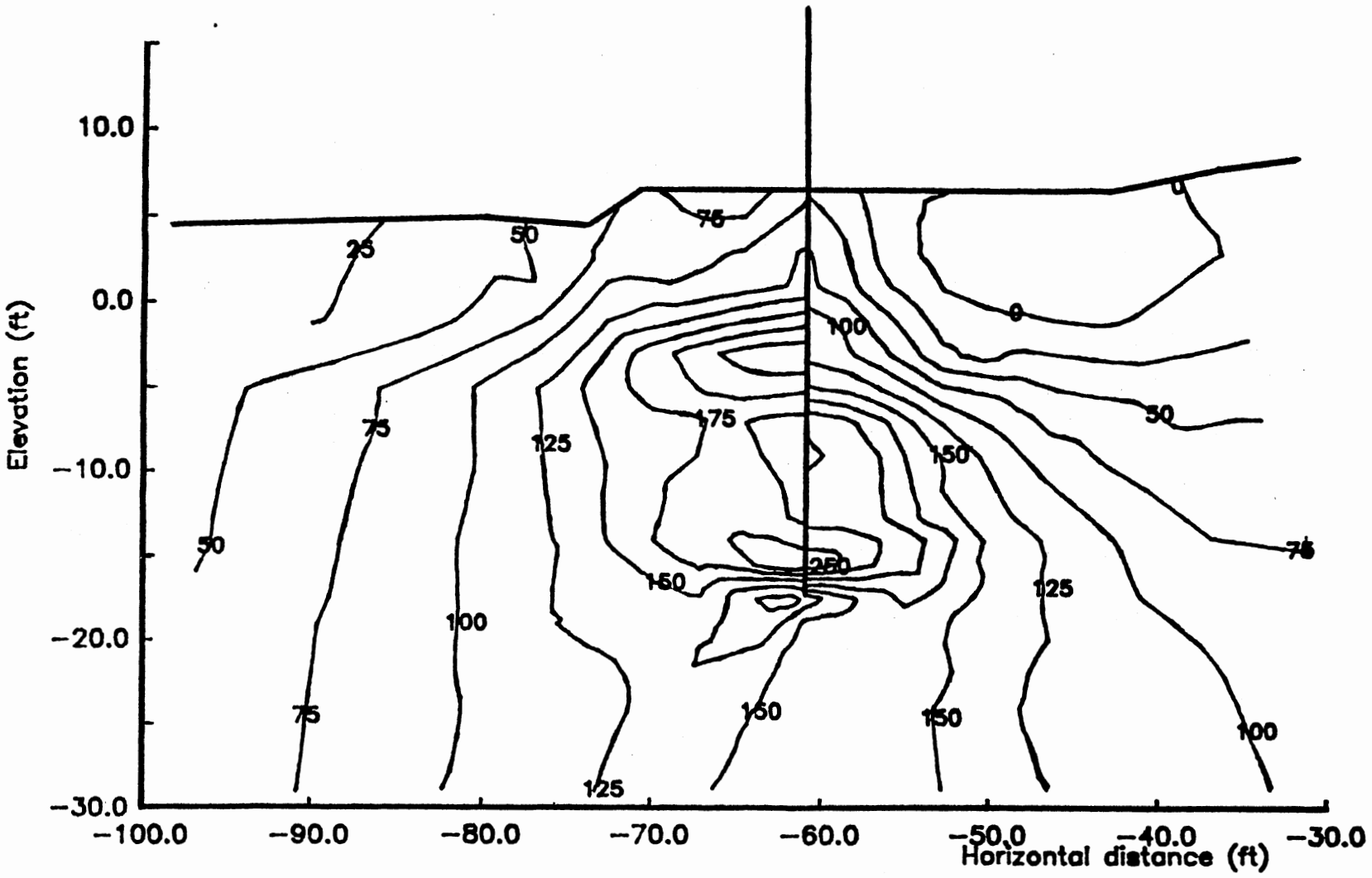

Figure 23. Shear stress contours in the pile vicinity.

of the relatively higher stiffness of the soil layer at that depth (between elevations -1 and -5). There is a region behind the wall near the ground surface where the soil is isotropically loaded. Closer to the wall, at about mid-depth, the shear stress increases at a high rate; this is due to the hydrostatic pressure in the crack. However, these stress concentrations are not as pronounced as the one near the pile tip.

Degree of Mobilization

One parameter that is of considerable significance is the variation in degree of mobilization of the soil shear strength, f, which indicates failure patterns in the soil. Figures 24 (a) through (h) show the evolution of f as the loading progresses. Recalling that a value of 100% in an area means local failure, it is interesting to observe that at the final (8 ft) water level, extensive areas of the soil have not reached failure. Until the ponding water level reaches about 4 ft, f remains below 30%; f values exceeding 50% begin to appear after 7-ft level. Drastic changes only occur during the final stages of loading, from 7 to 8 ft, and a few elements approach failure at the very end.

Referring to the last load step, it is observed that the zones where the soil approaches a critical stage are:

a. In the front (land) side of the wall near the ground surface; this is the expected "passive" pressure zone.
b. In front of the wall, below approximately elevation -10 ft; this is the region where the front soil tends to convert from passive to active.
c. In the back (flood) side of the wall, below approximately

elevation -10 ft; in this area the soil moves towards a passive failure condition.

An interesting point the f distribution reveals is that the expected active-passive reversal around the tip of the pile does not take place until the later stages of loading. It also starts at a very low level, at about 5 to 6 ft above the pile tip; the remaining part of the pile remains relatively inactive until the last loading stage. Even then, lateral pressures near the tip are far from failure. Based on these results, the imminent total collapse displayed by the top deflection curve is mainly due to the passive failure of the soil in near the surface in front of the wall.

Stress Paths

To examine the behavior of the soil in the critical regions around the sheet pile, stress paths may be used. The type of stress path used in this study may be described as the trace of the top point of the conventional Mohr's circle as the state of stress changes, i.e., a plot of p versus q, where

$$p = (\sigma_1 + \sigma_3)/2, \quad q = (\sigma_1 - \sigma_3)/2$$

A sequence of stress paths have been plotted in Fig. 25(a) through (m). The sequence followed in this figure is from top to bottom of the pile. In each of these figures there are two stress paths: one is for the element in "front" of the pile (i.e., the dry side), and the other is for the element on the "back" side of the wall (i.e. the water side) at the same elevation.

In the stress paths corresponding to the front side, there is a tendency to move into the passive failure mode which is more pronounced in the elements close to the ground surface. In these elements, the stress paths have roughly 45° inclinations, indicating an increasing horizontal stress while the vertical stress remains essentially constant. The deviations from 45° slope are a result of changing vertical stress due to wall friction. It should be noted that the stress paths begin at load step 1, when water head was 1 ft, and "q" has been calculated as the Mohr circle radius (i.e., always positive). As depth increases gradually the situation reverses. However, clear movements into the active condition are not apparent until the last elements around the pile tip (Figs. 25(l) and (m)) where the horizontal stress begins to decrease after 5-ft water head.

The stress paths for the back side at lower depths indicate the effect of the tension zone development. Figures 25(a) and (b) show that the top two elements are almost isotropically loaded after the pile and soil separate. The next three elements (Figs. 25(c), (d), (e)) display an interesting story in three parts: (1) during the early stages of loading these elements felt mainly a vertical loading due to the weight of the water; (2) this was followed by a lateral relaxation (wall moving away and causing an active-like condition); (3) but as separation propagated downward the trend reversed because of the hydrostatic pressure that increased the horizontal (as well as vertical) stresses. At larger depths (elevations -4 to -8, Figs. 25(f), (g), (h)) only the first two parts--vertical loading first and then lateral unloading--are observed. The third part is missing here because of the diminishing effect of the tension crack at larger depths. The next

depth range, from -10 to -13.3 (Figs. 25(i) - (k)), appears to be a transition region. In the lowest depth range close to the pile tip (Figs. 25(l) and (m)) no reversal occurs. The slope of the stress paths in this region are less than 45°, indicating that the horizontal stress begins to chase the vertical stress, a tendency toward the passive condition. However, failure is still not imminent.

Wall Pressure Development

Pressure distributions on the sheet pile at the last loading step (water head 8 ft) are shown in Fig. 26. Pressures shown are the horizontal stresses in the elements adjacent to the wall, except in the region where the soil is separated from the pile (tension zone behind the wall) where the hydrostatic pressures are plotted on the right side. The net pressure distribution is also shown in the figure. The reversal of net pressure near the tip of the pile indicates the closeness of the wall pressures to the conventional assumption. Full active and passive pressures, however, are not realized at this point.

One difficulty in comparing the wall pressures with conventional lateral earth pressures is the effect of the water weight on vertical (consequently horizontal) stresses. This effect is not taken into account in conventional design procedures since this effect does not exist in regular sheet piles. For an SSI method to simulate finite element results, some procedure should be devised to estimate these lateral pressures.

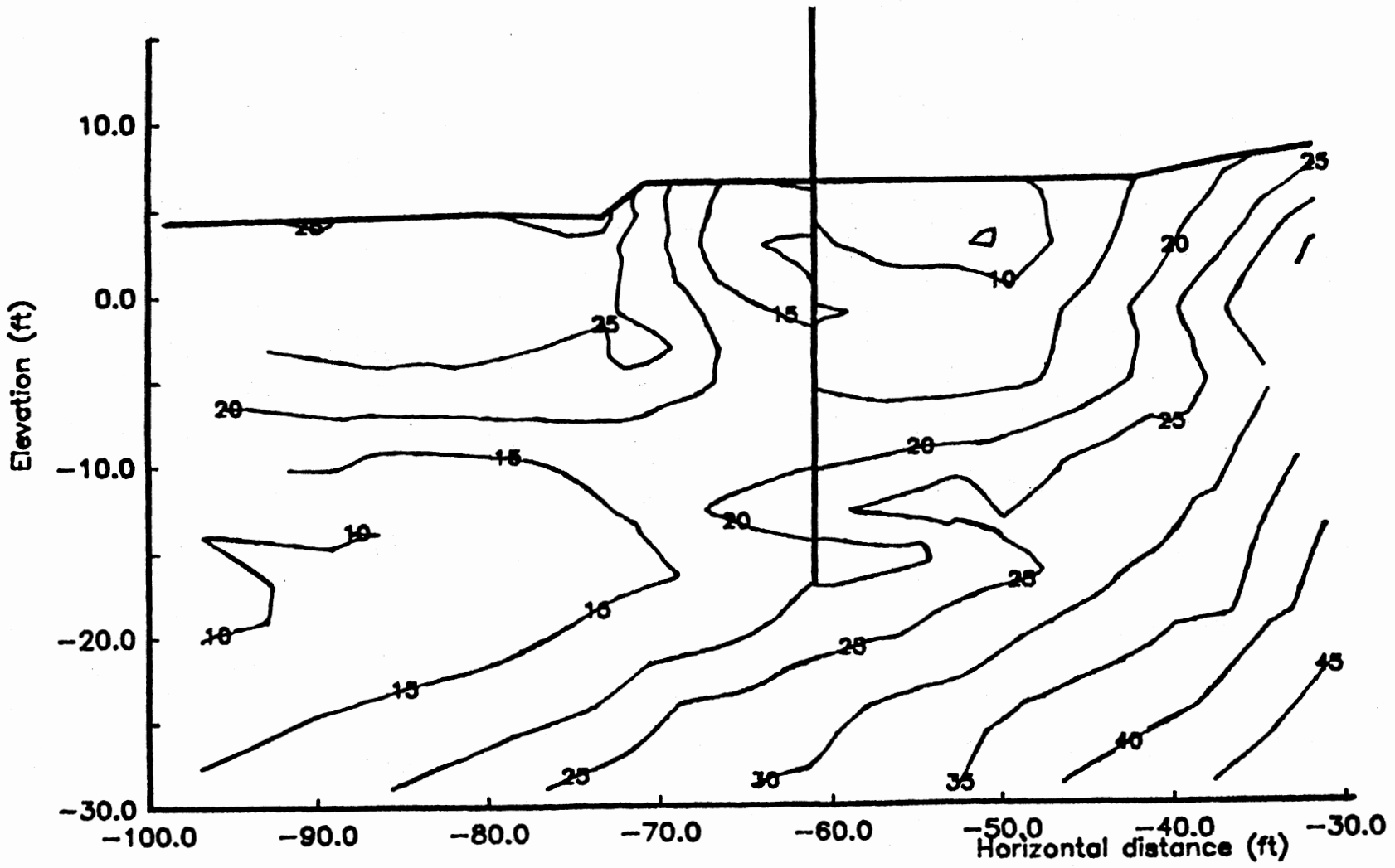

Figure 24(a). f contours (%) in the pile vicinity, head = 1 ft.

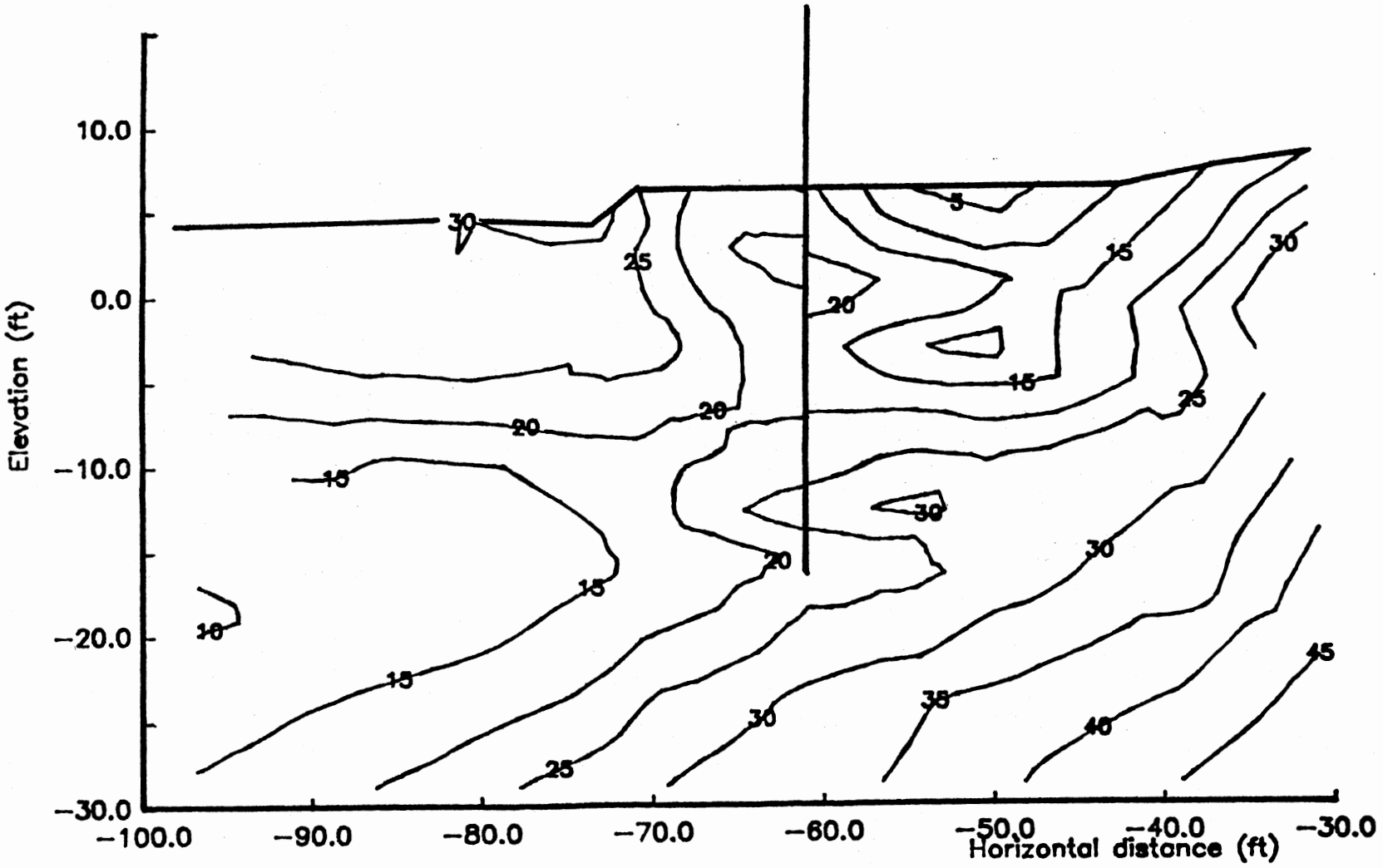

Figure 24(b). f contours (%) in the pile vicinity, head = 2 ft.

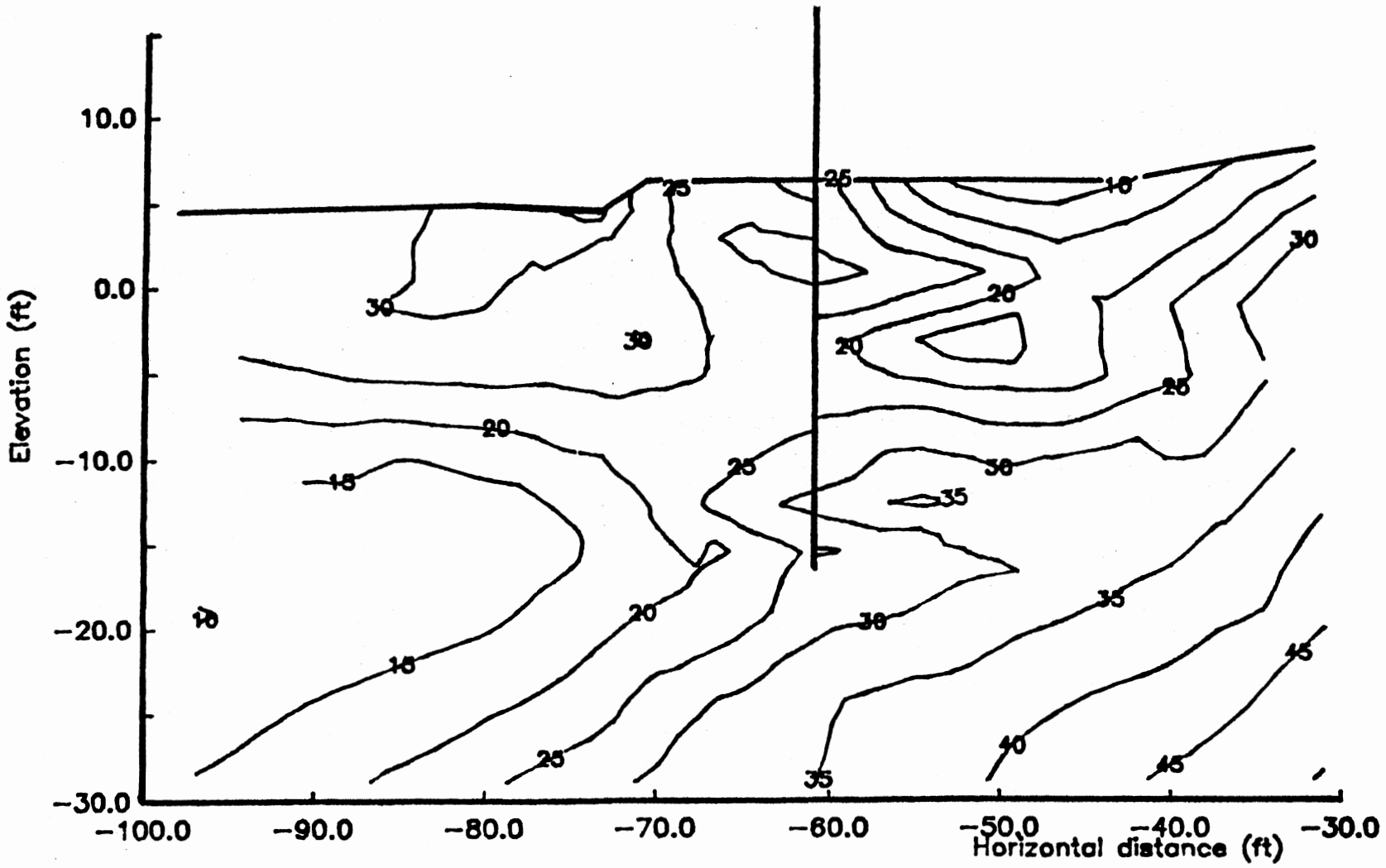

Figure 24(c). f contours (%) in the pile vicinity, head = 3 ft.

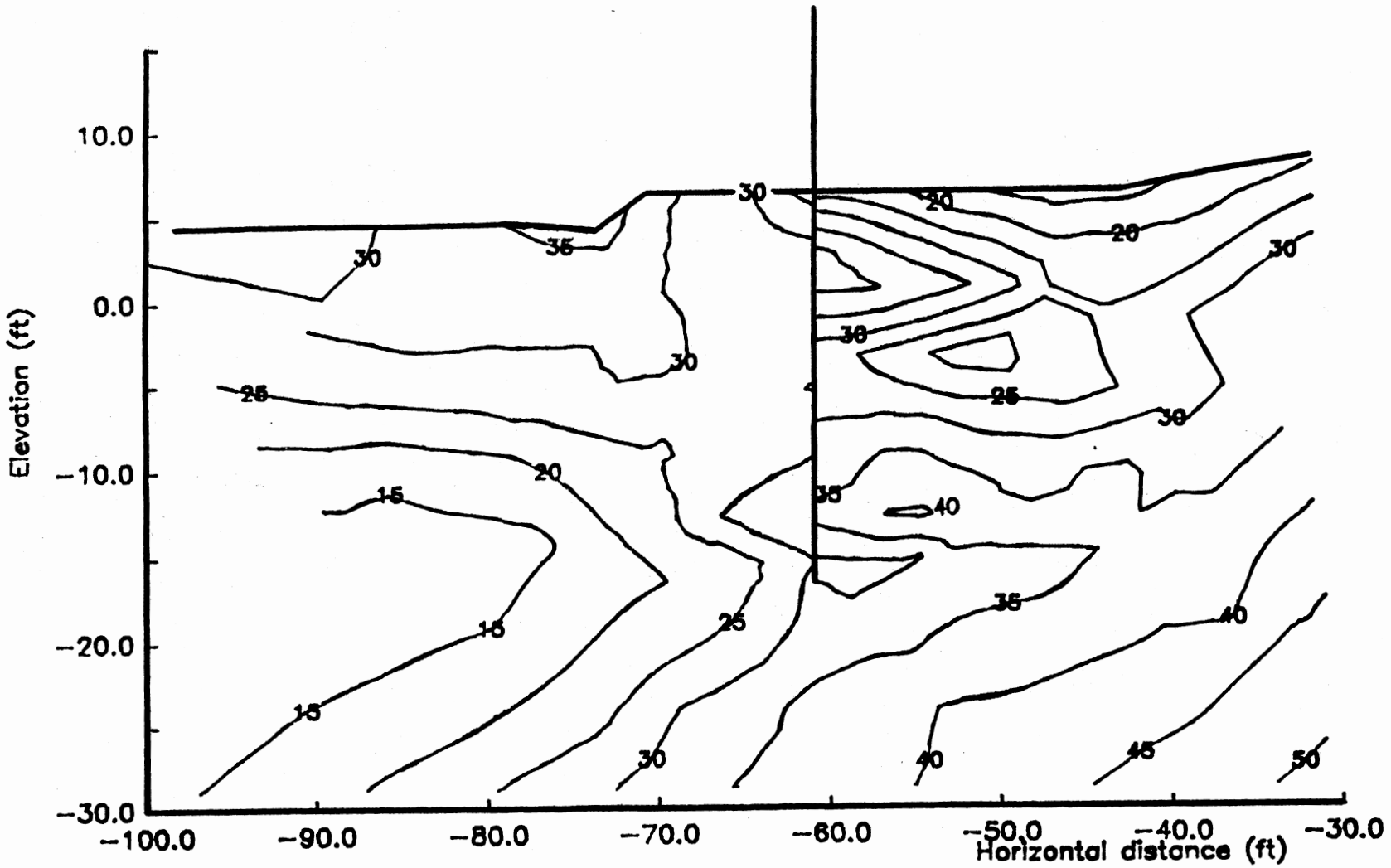

Figure 24(d). f contours (%) in the pile vicinity, head = 4 ft.

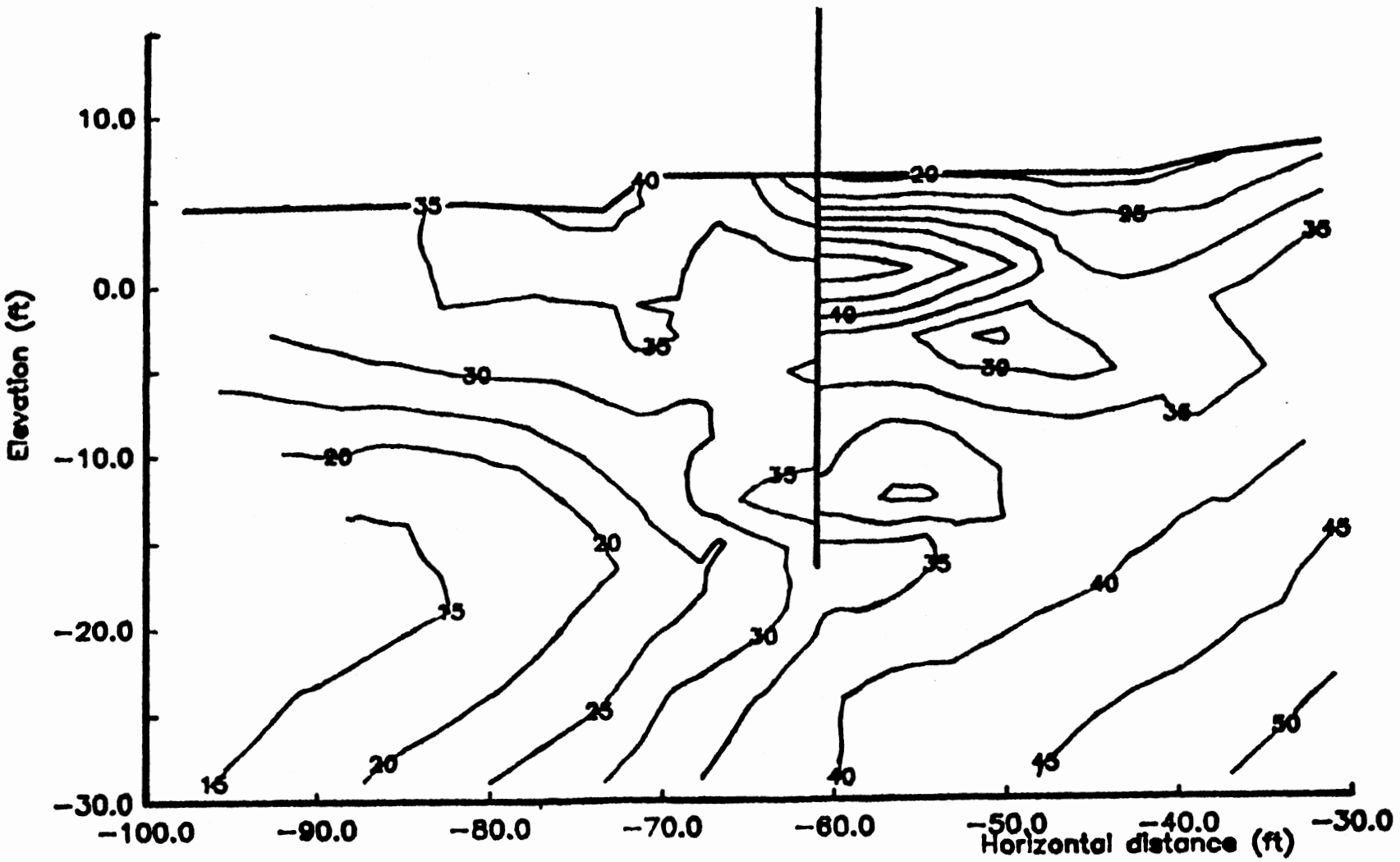

Figure 24(e). f contours (%) in the pile vicinity, head = 5 ft.

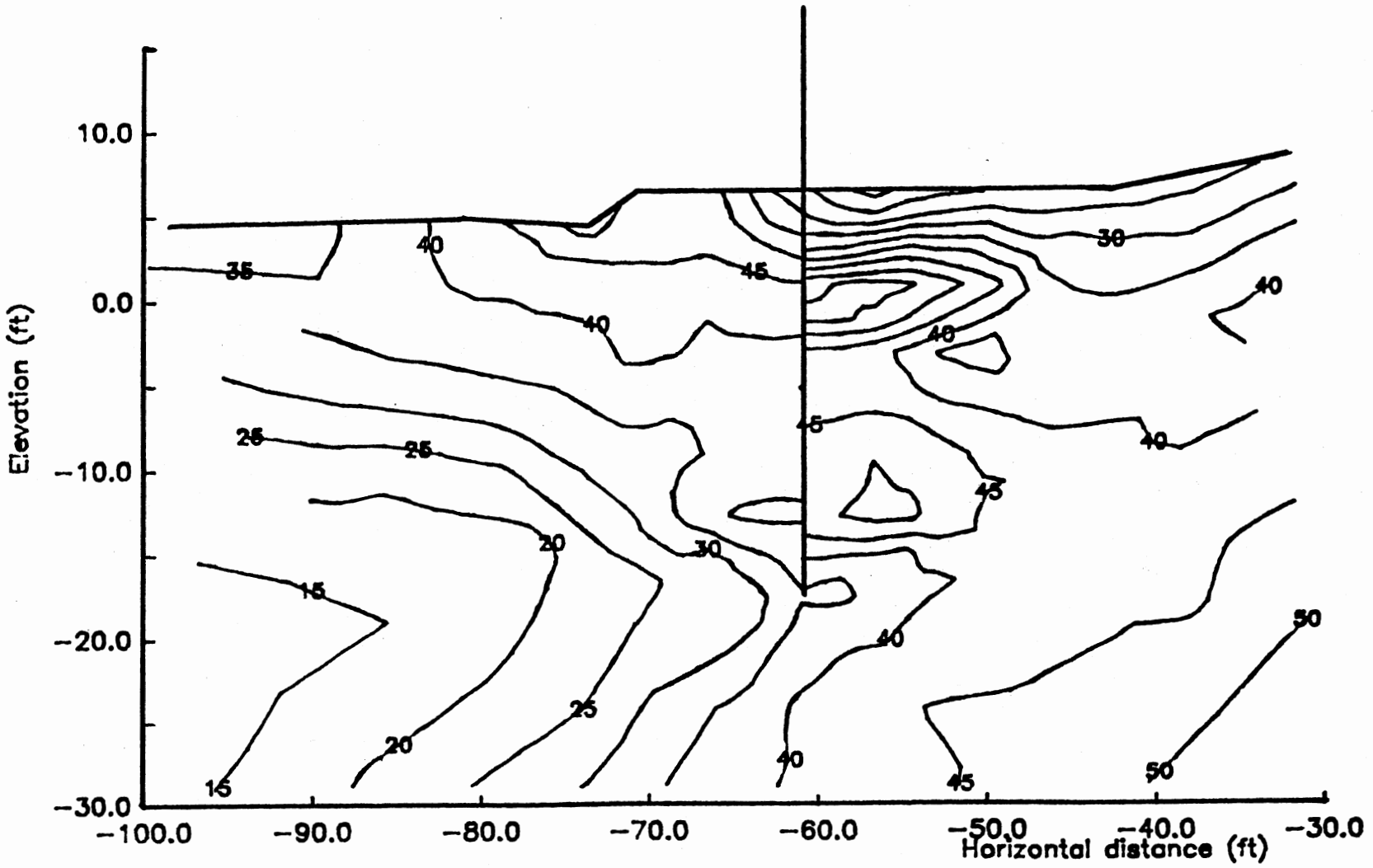

Figure 24(f). f contours (%) in the pile vicinity, head = 6 ft.

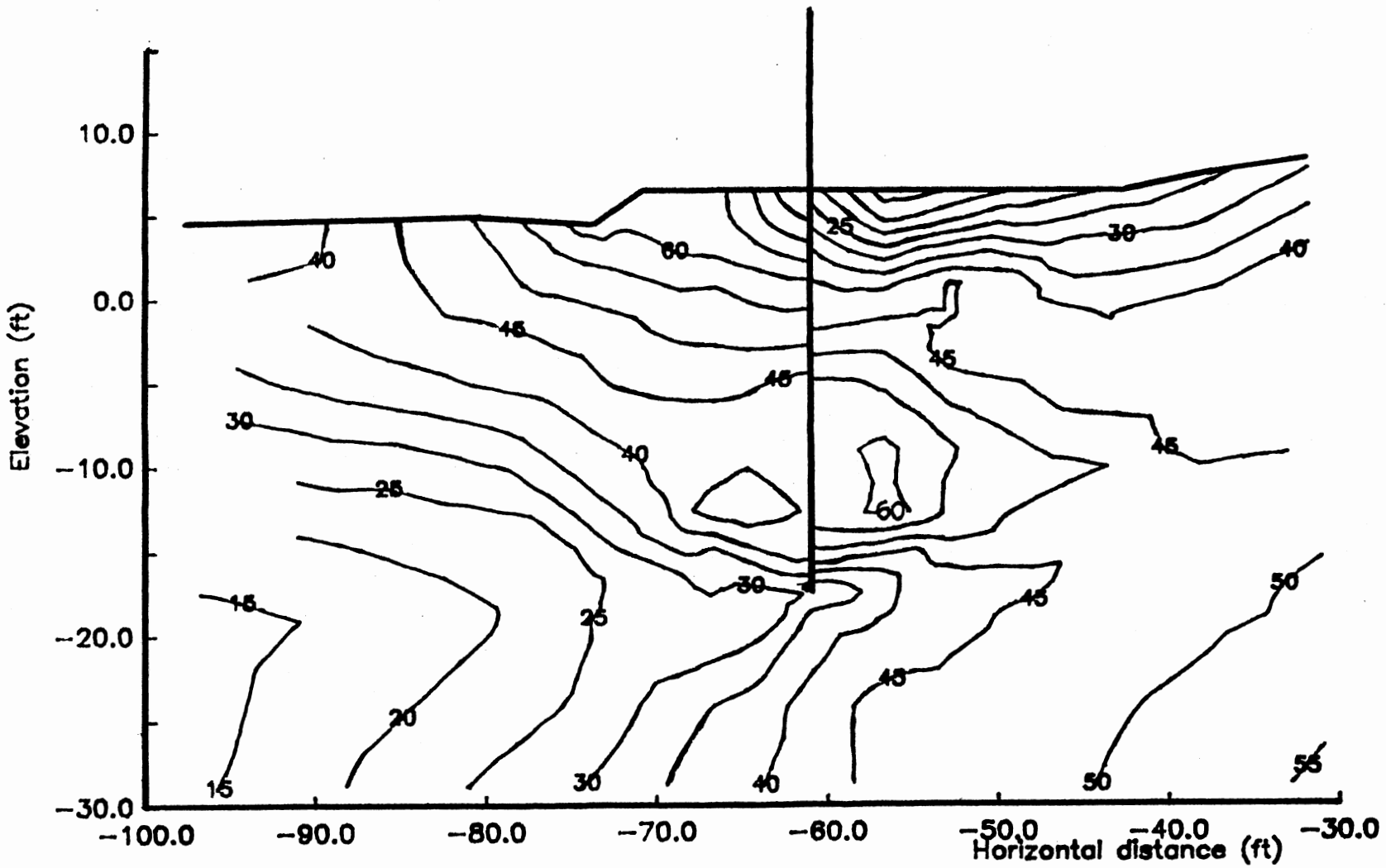

Figure 24(g). f contours (%) in the pile vicinity, head = 7 ft.

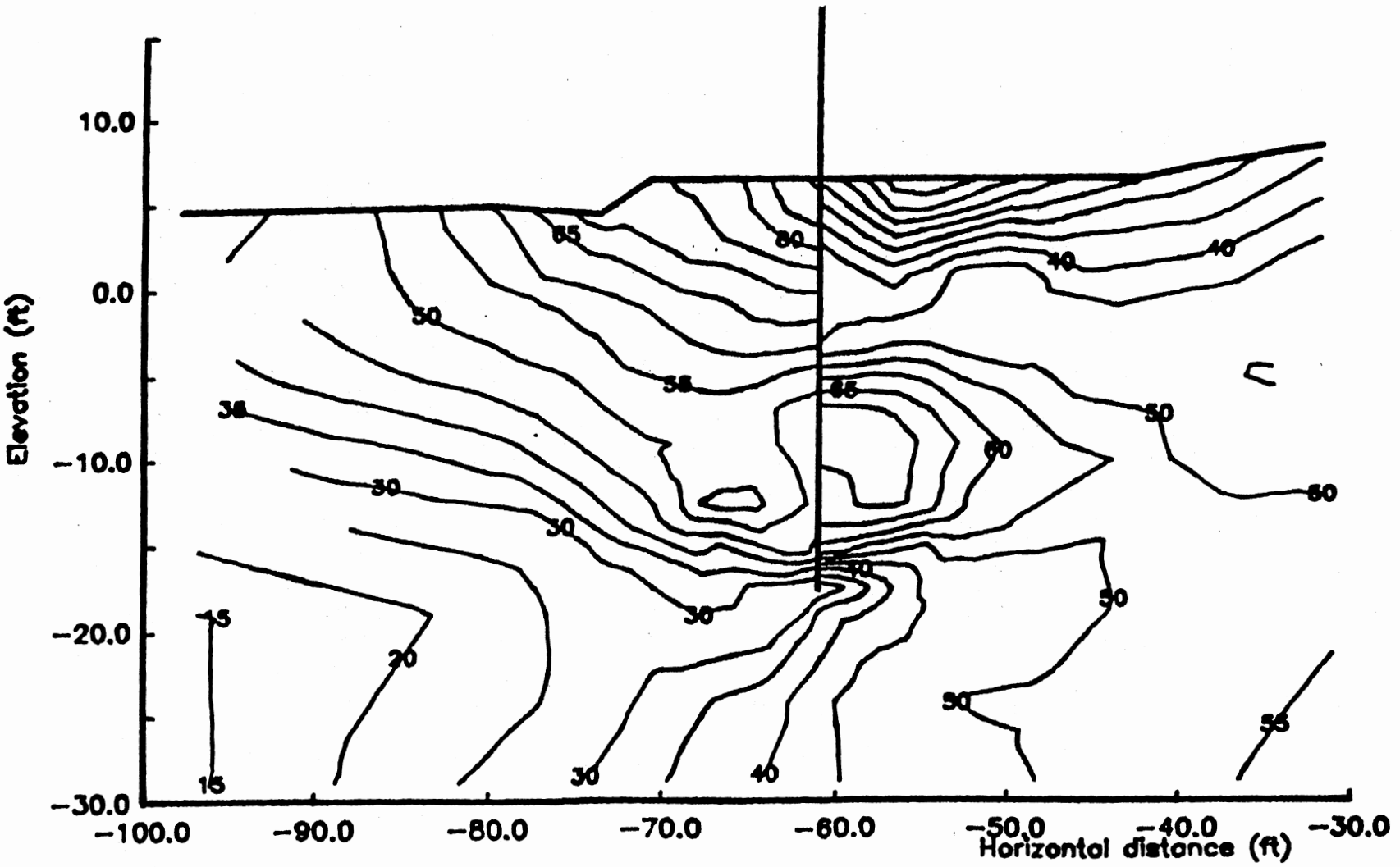

Figure 24(h). f contours (%) in the pile vicinity, head = 8 ft.

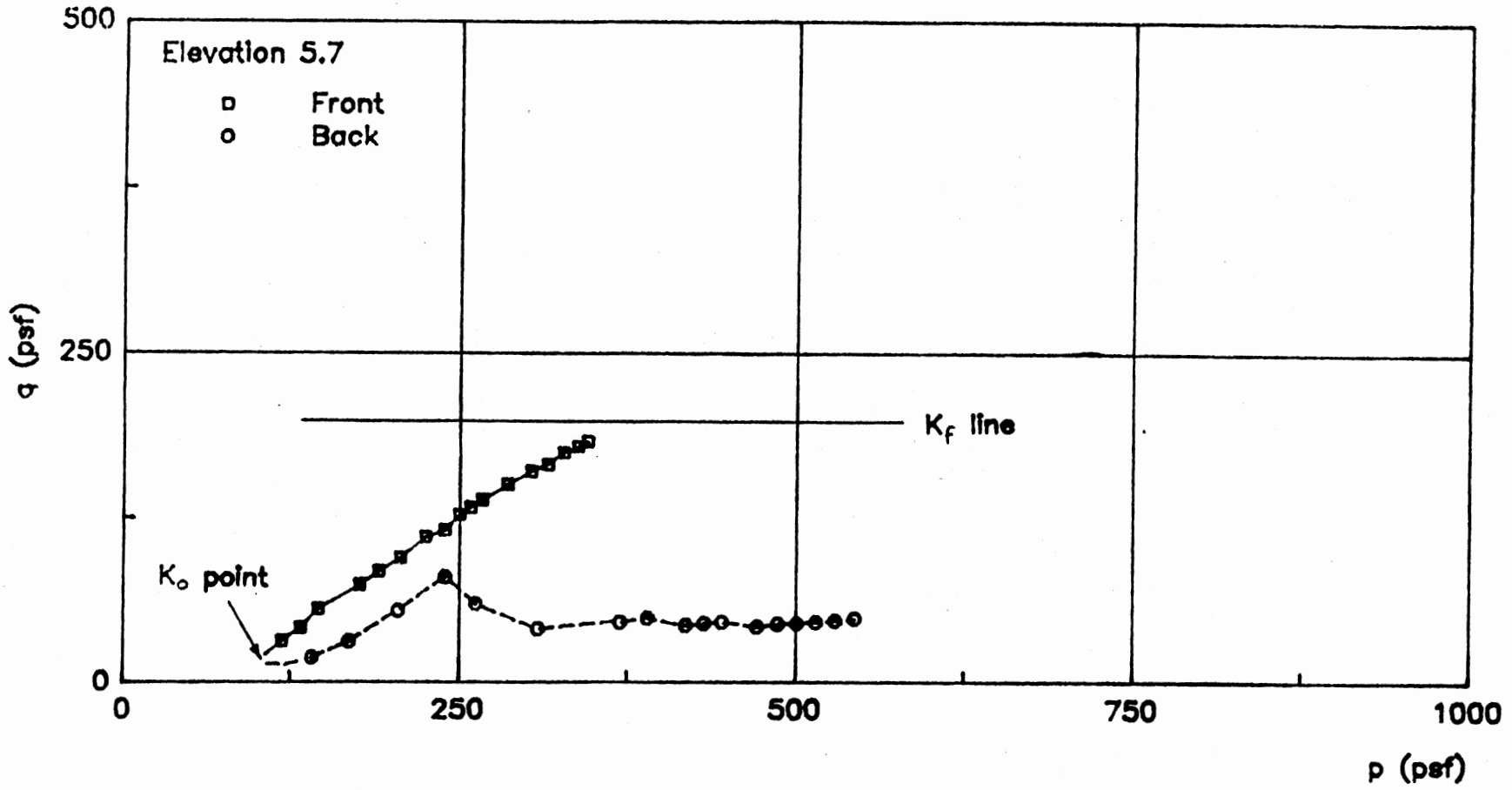

Figure 25(a). Stress paths at 5.7 ft elevation.

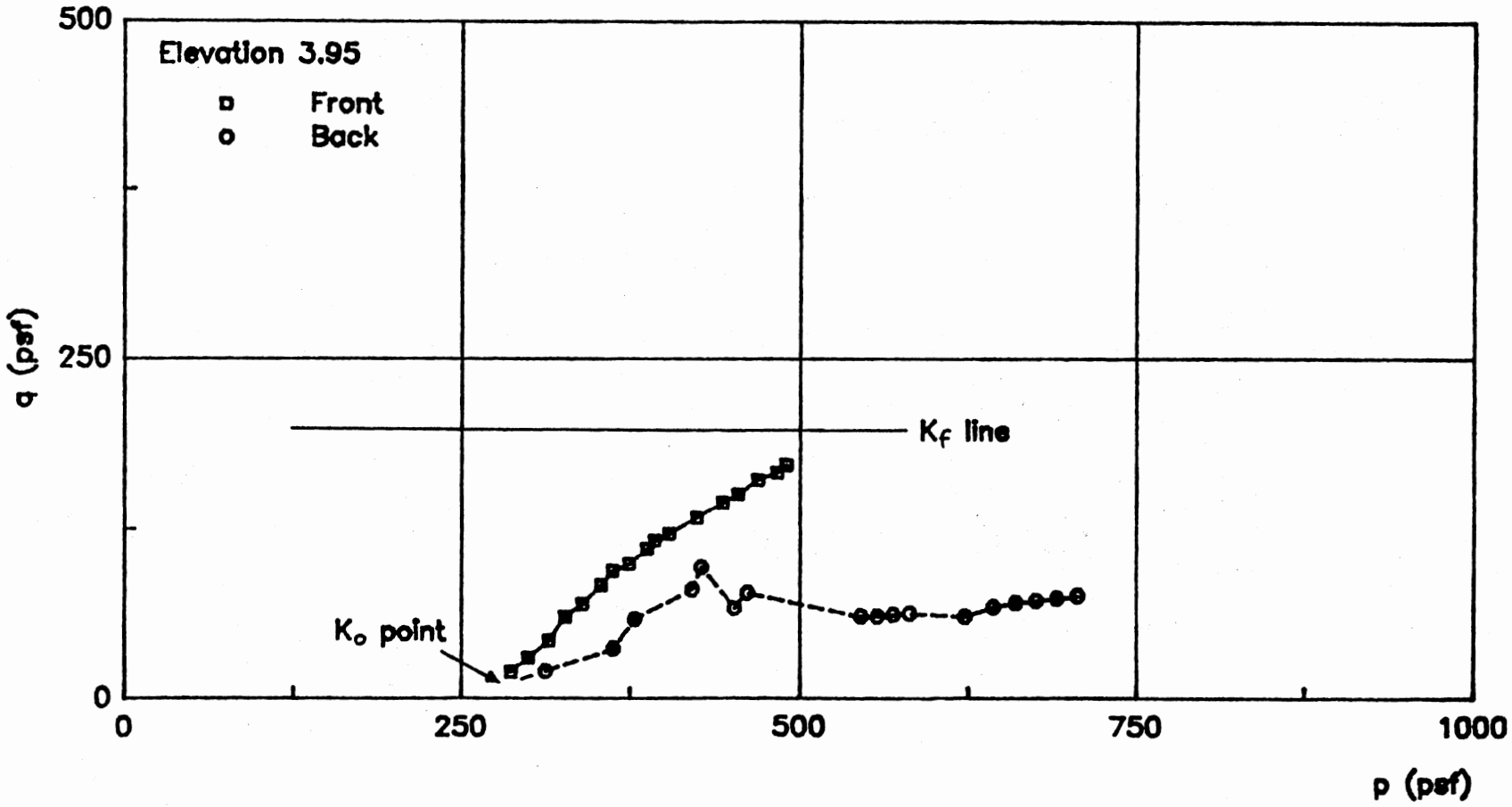

Figure 25(b). Stress paths at 3.95 ft elevation.

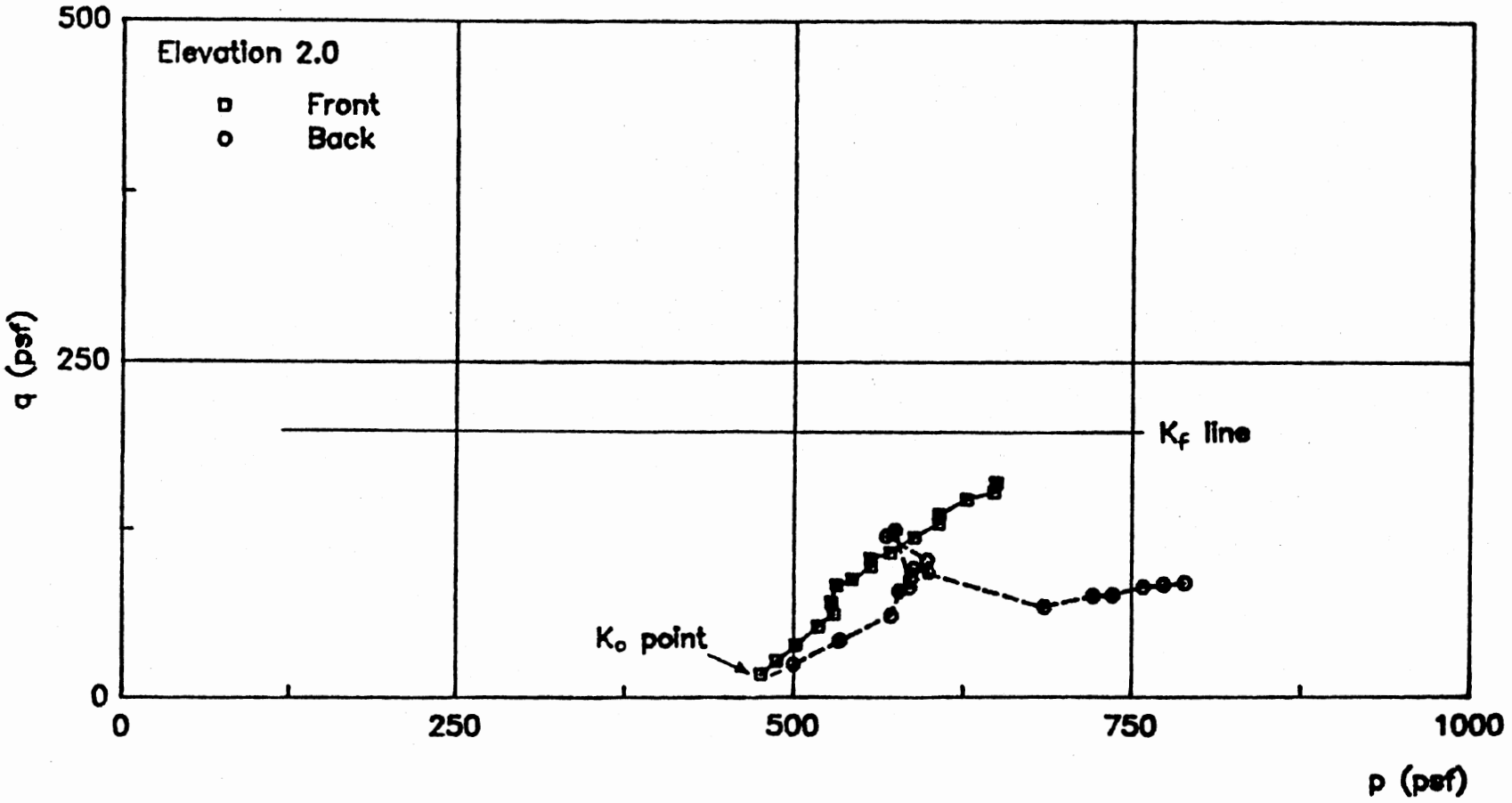

Figure 25(c). Stress paths at 2.0 ft elevation.

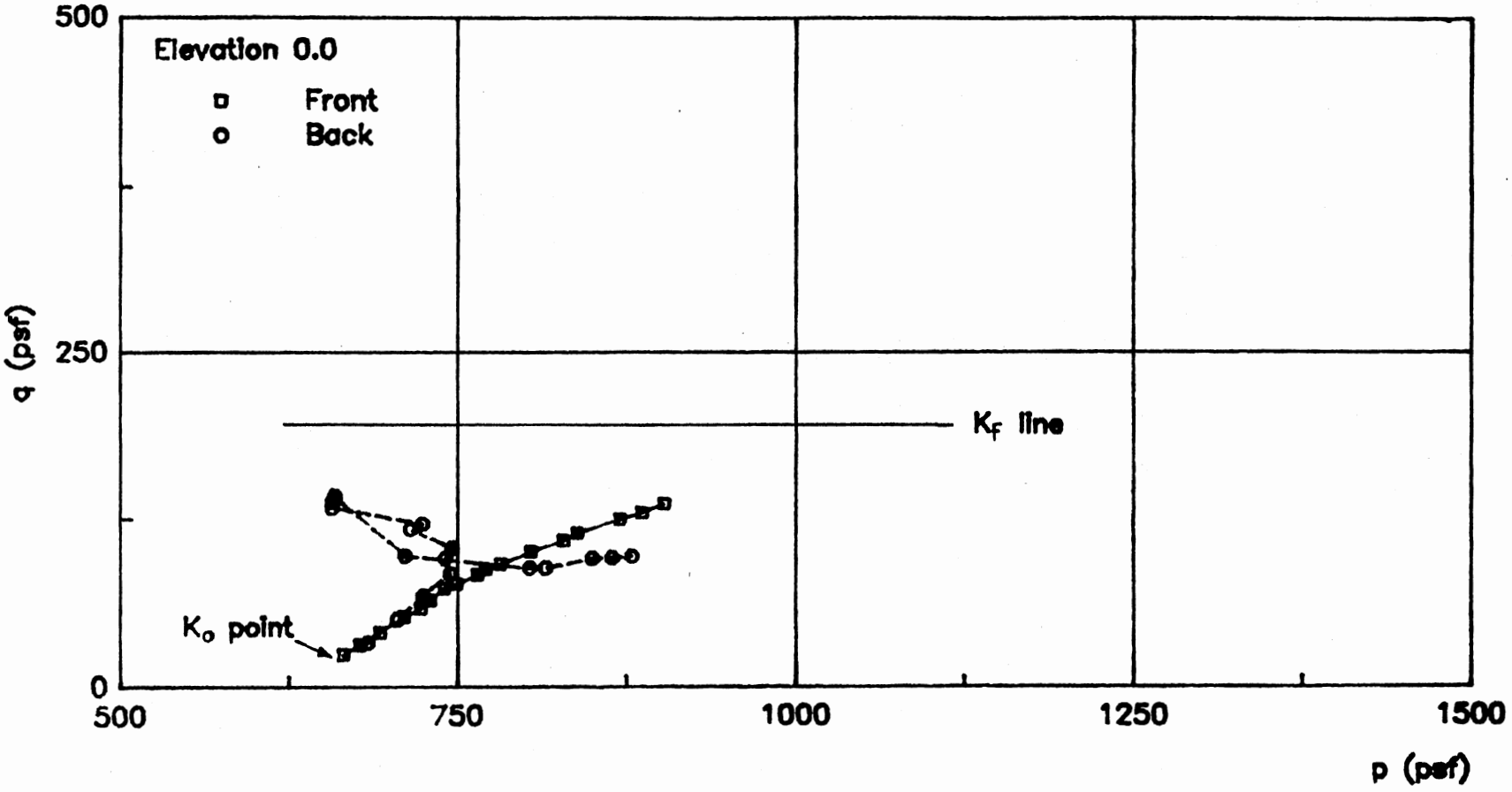

Figure 25(d). Stress paths at 0.0 ft elevation.

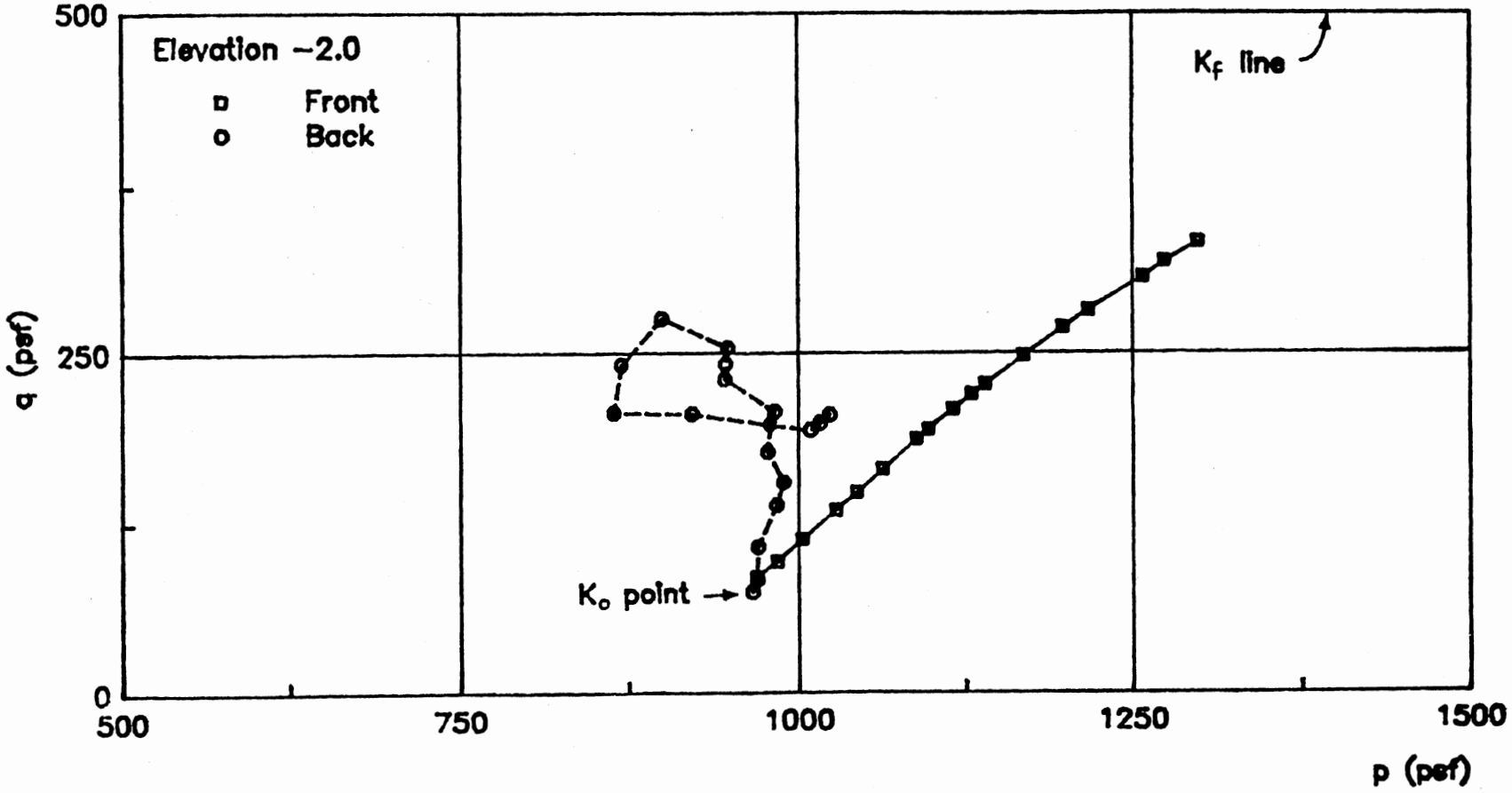

Figure 25(e). Stress paths at -2.0 ft elevation.

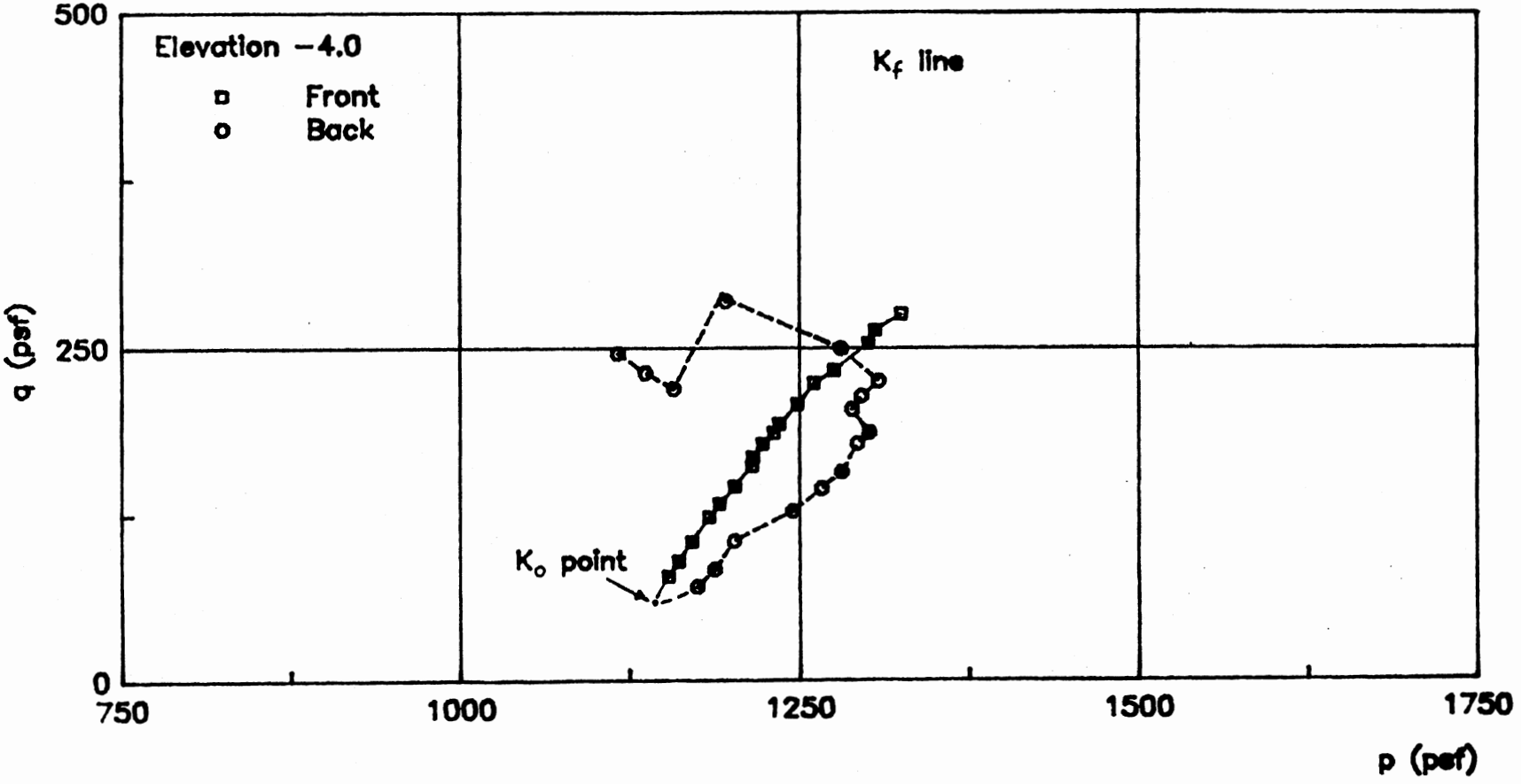

Figure 25(f). Stress paths at -4.0 ft elevation.

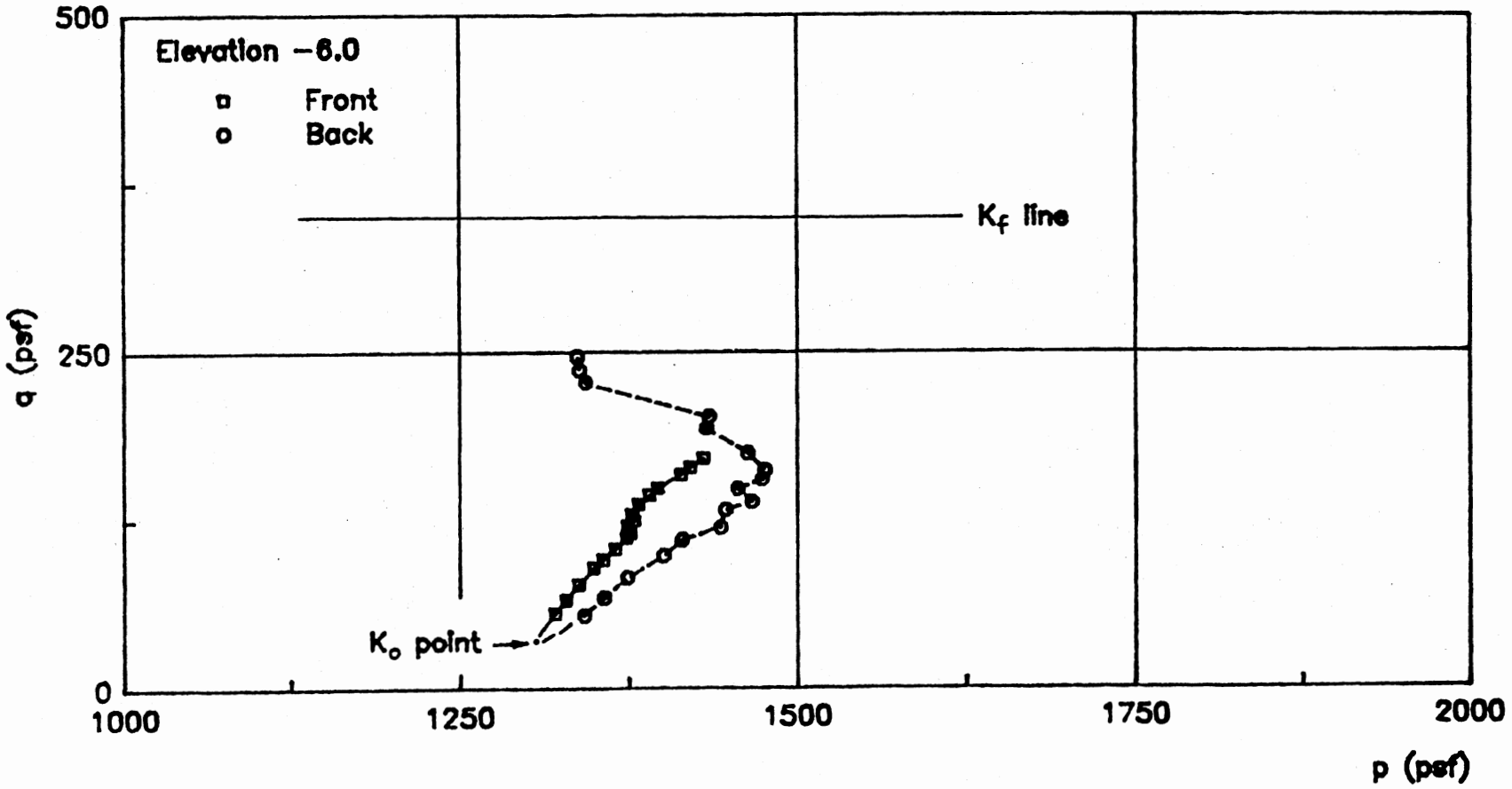

Figure 25(g). Stress paths at -6.0 ft elevation.

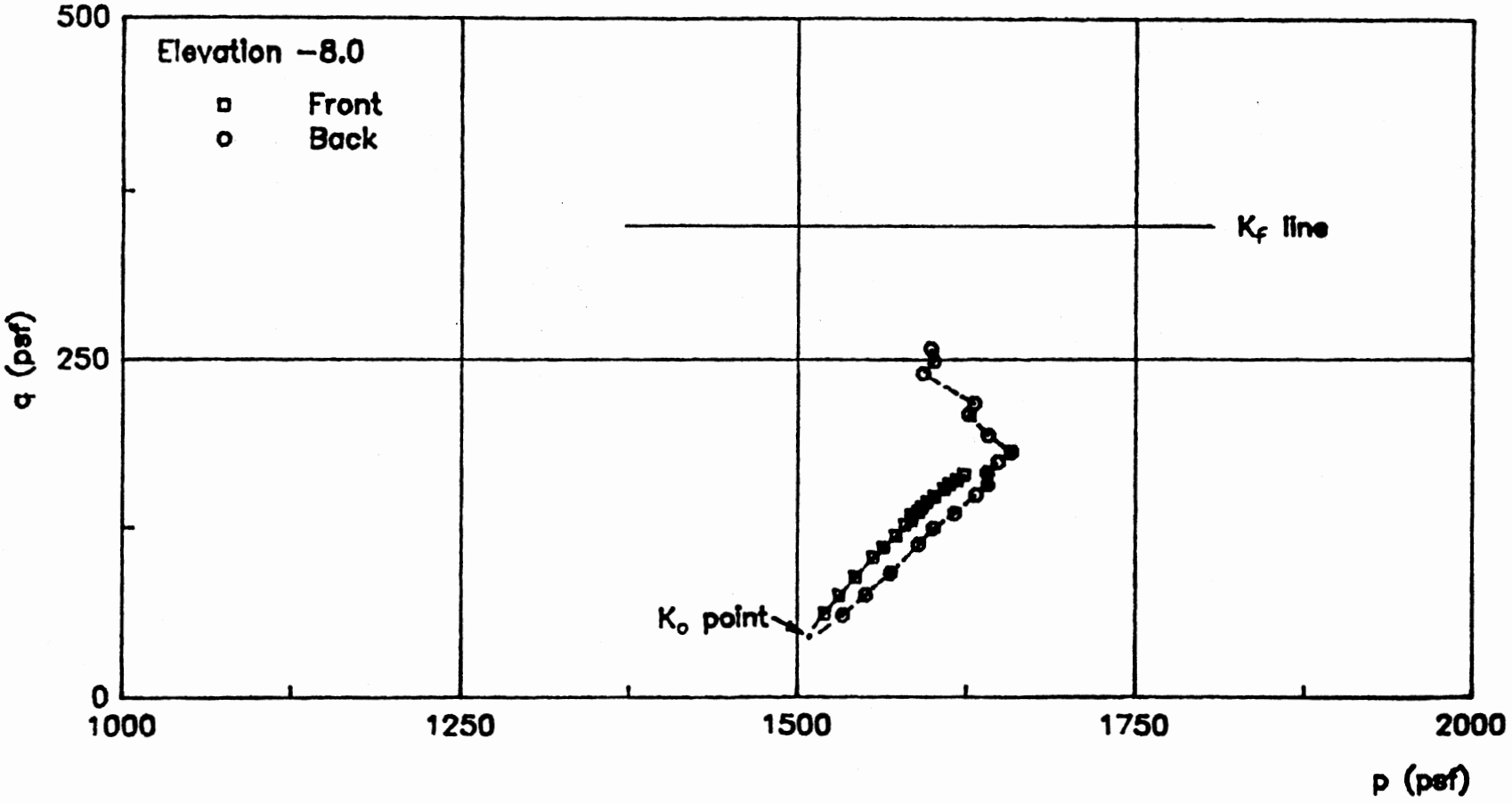

Figure 25(h). Stress paths at -8.0 ft elevation.

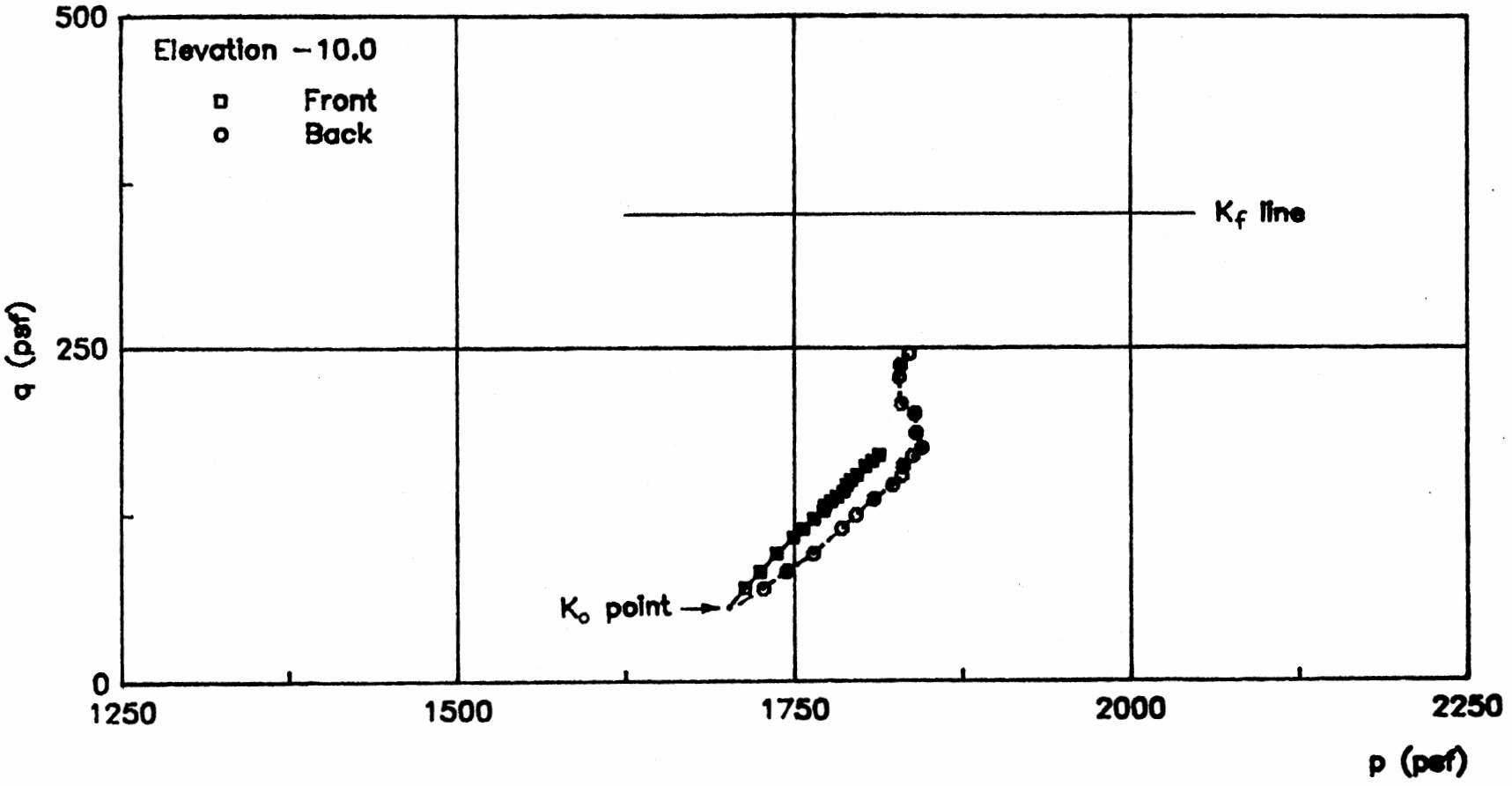

Figure 25(i). Stress paths at -10.0 ft elevation.

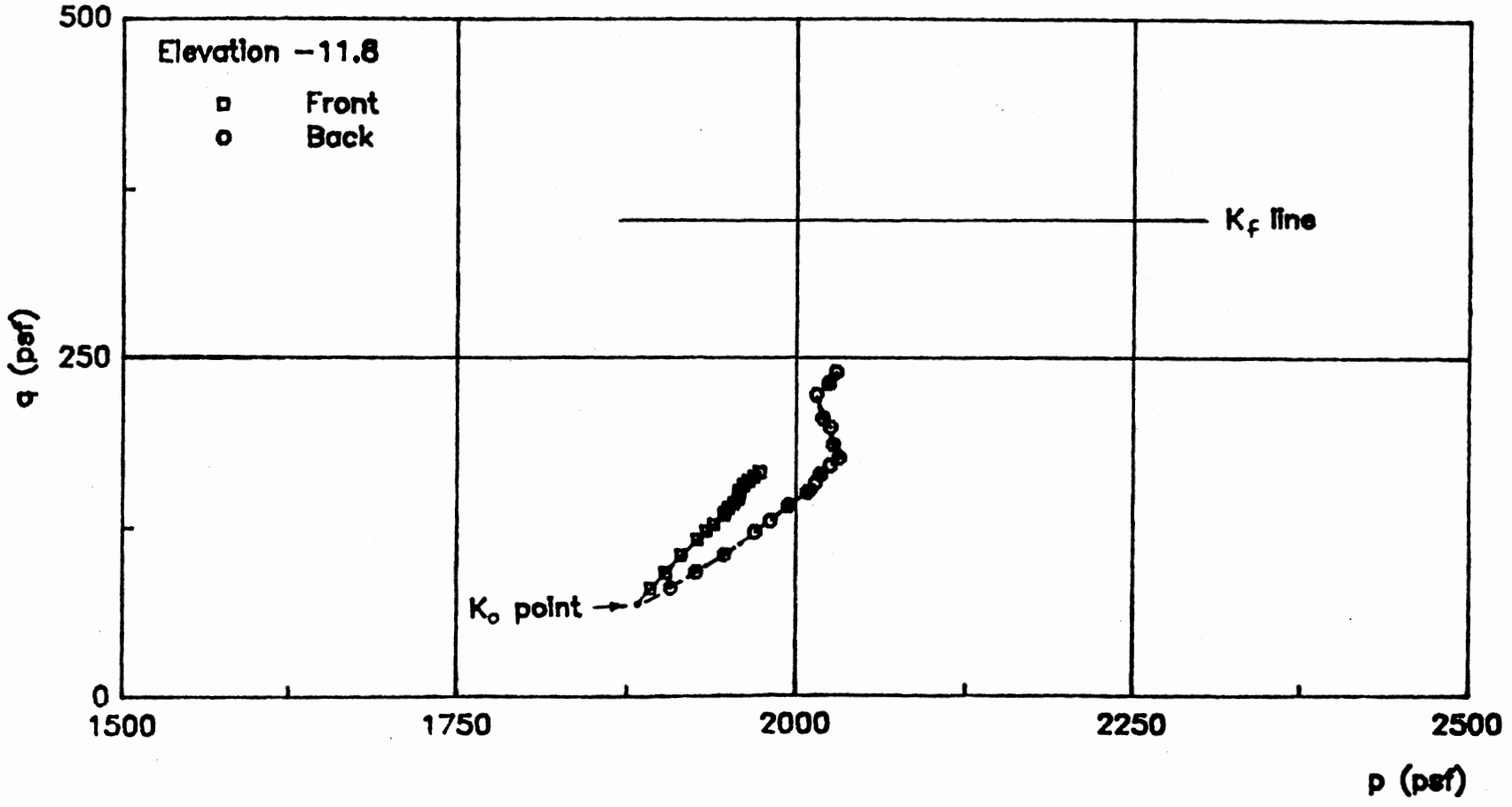

Figure 25(j). Stress paths at -11.8 ft elevation.

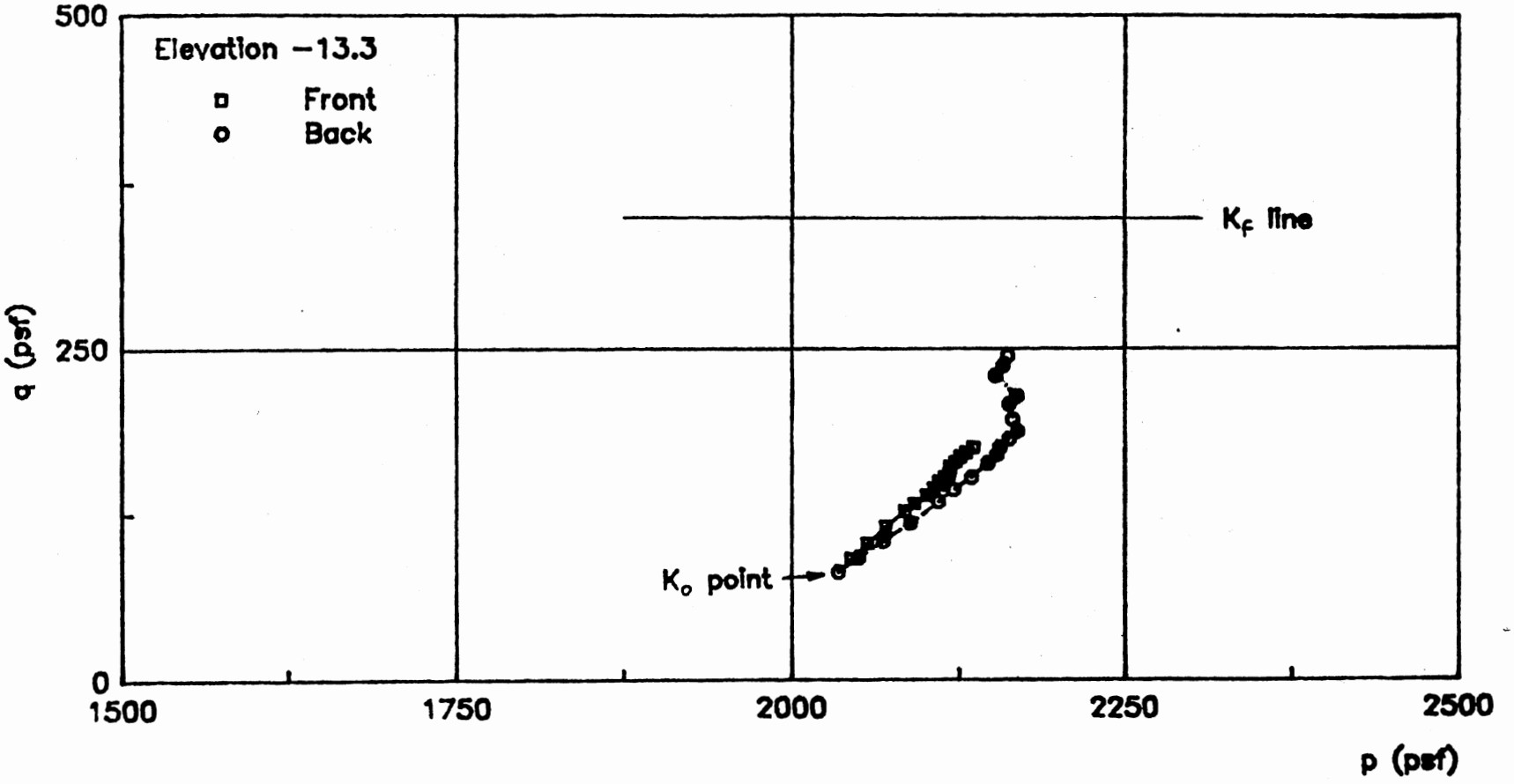

Figure 25(k). Stress paths at -13.3 ft elevation.

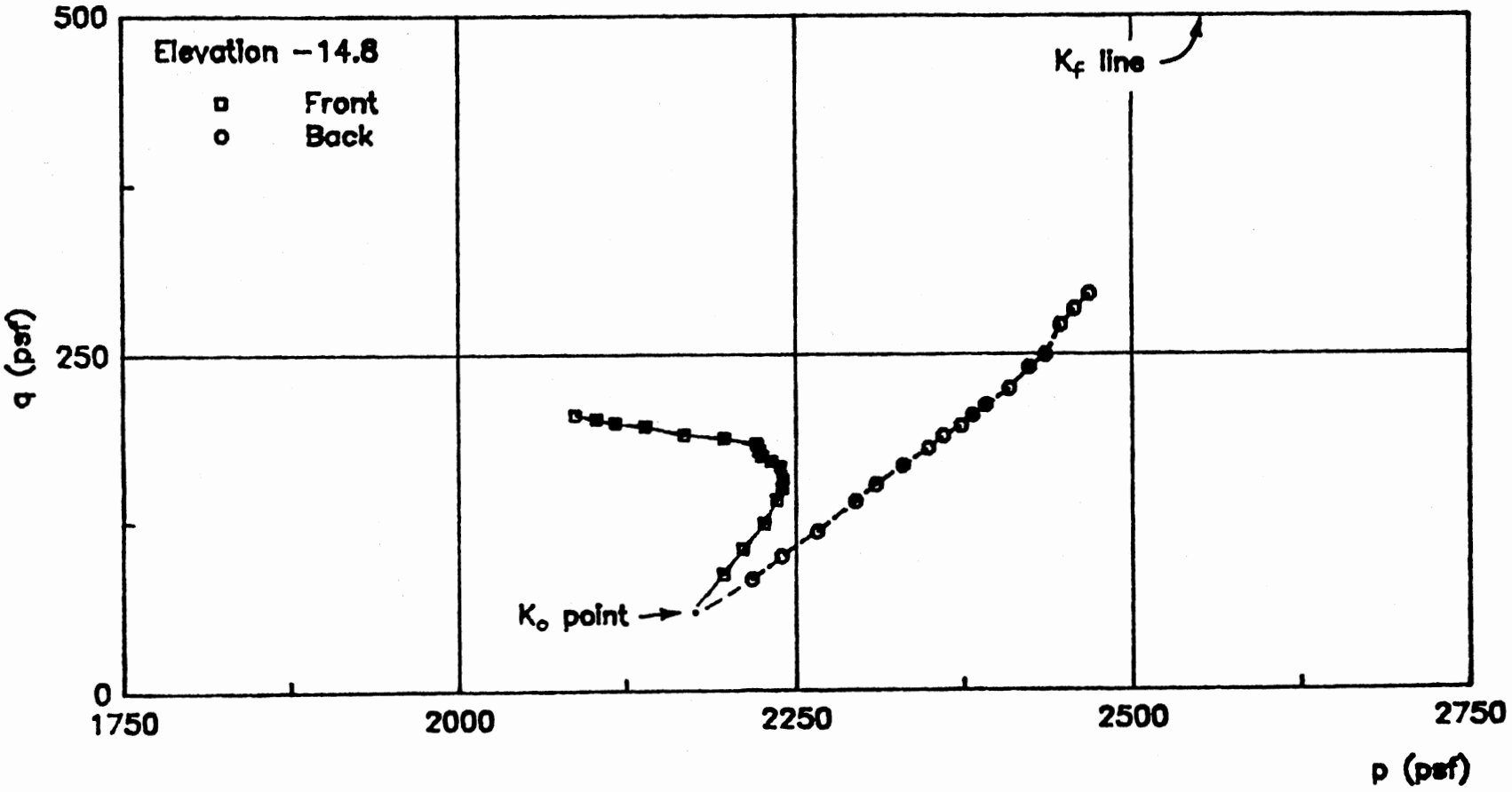

Figure 25(1). Stress paths at -14.8 ft elevation.

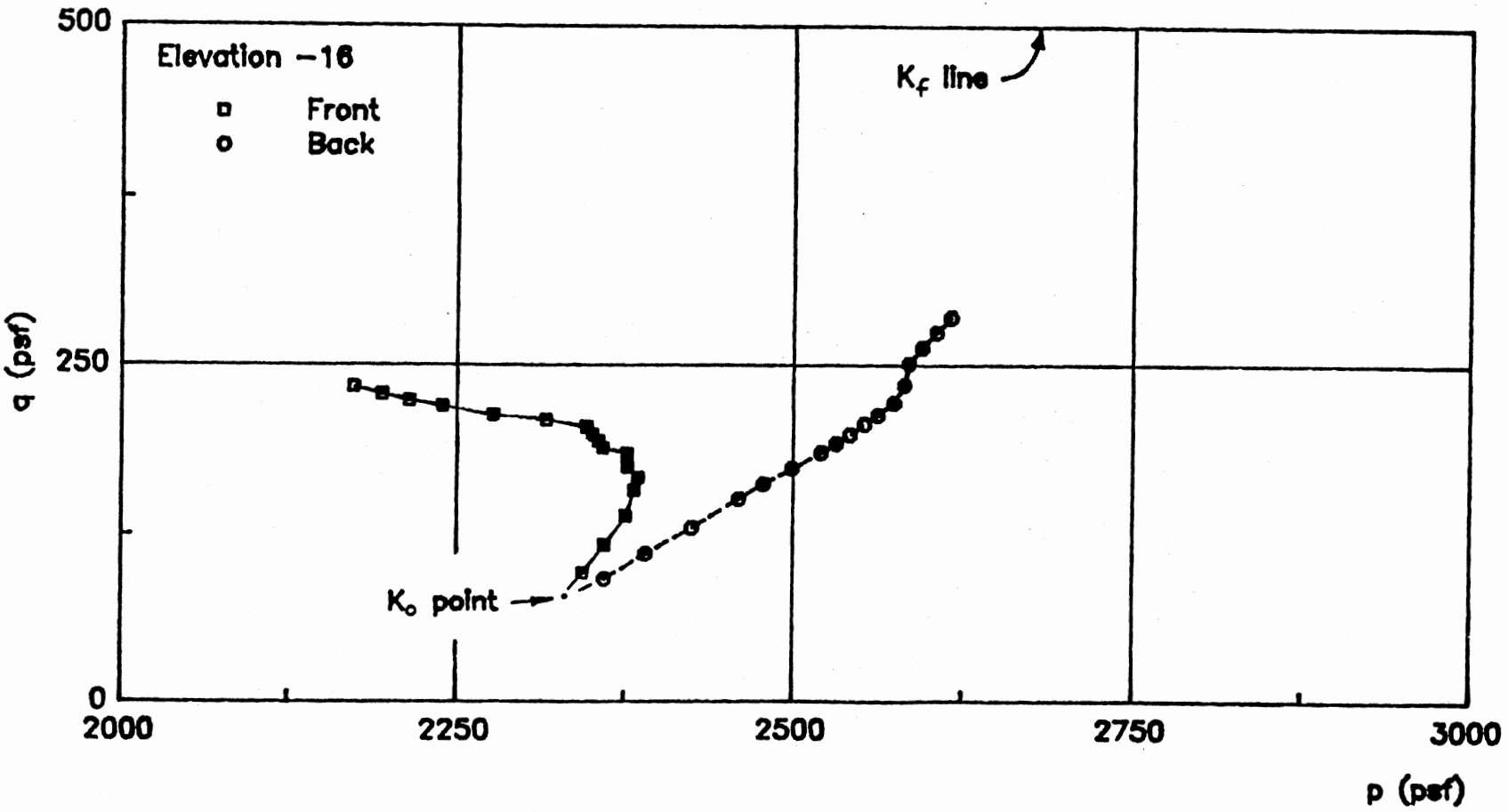

Figure 25(m). Stress paths at -16.0 ft elevation.

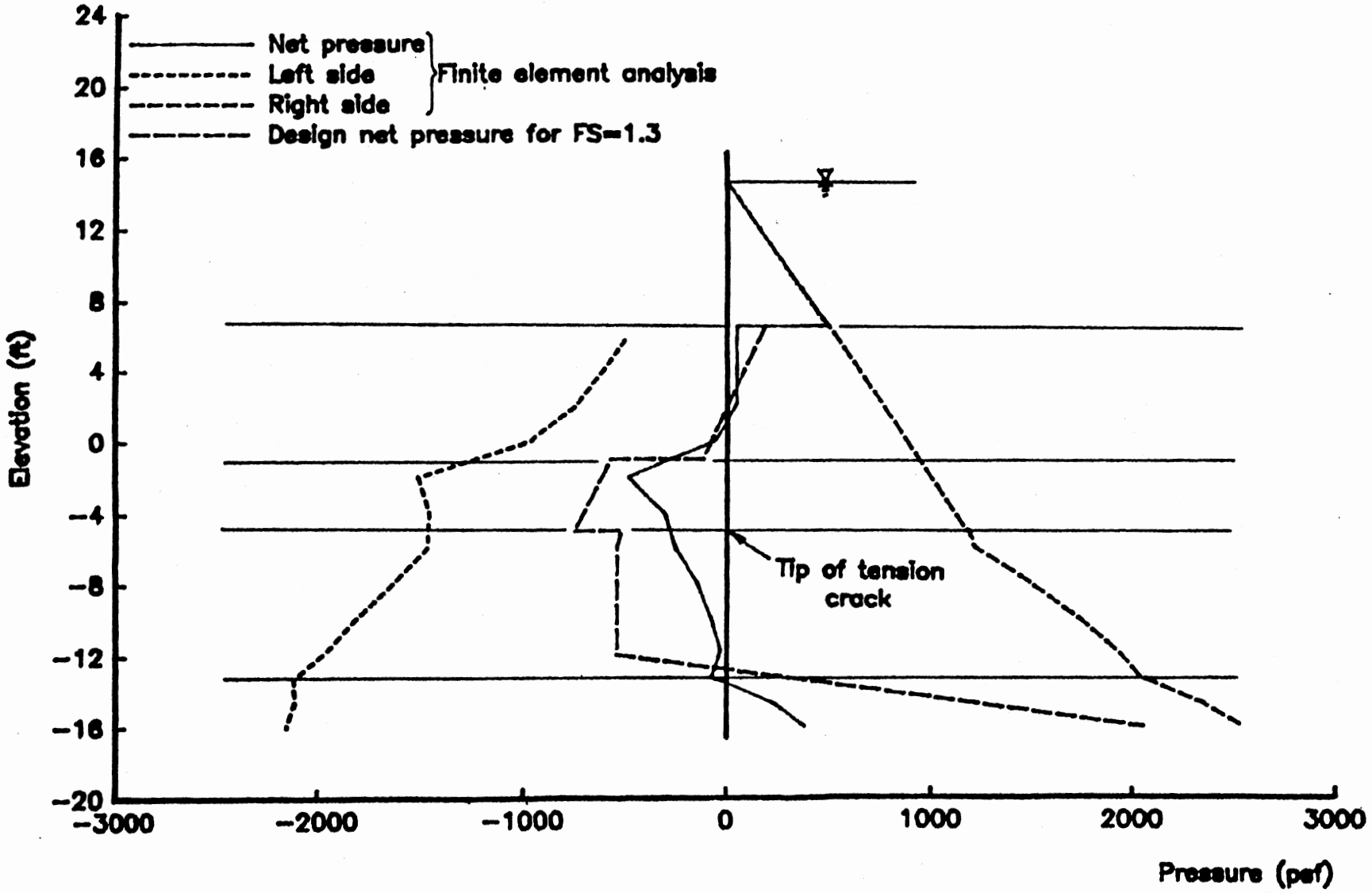

Figure 26. E99 wall: calculated lateral pressures.

CHAPTER IV

ANALYSIS OF TYPICAL SECTIONS

It has been demonstrated in the previous sections that the analytical model adequately predicts the behavior of a floodwall. As a prelude to this phase of the research, preliminary analyses of floodwall and levee systems typical of those found along the lower Mississippi River have been performed.

Soils data and design calculations for representative sections were provided by the U.S.A.E Waterways Experiment Station, Vicksburg, MS. A detailed analysis of the soils data extracted from these documents is given in Appendix B. It was found that the soils in the area exhibit undrained shear strengths which vary with depth as shown in Fig. 27. Two idealized strength profiles, a "medium" strength and a "high" strength profile, were chosen for illustrative analyses. However, the intention at the beginning was to select an additional "low" strength profile; but this was later aborted since a major portion of the soil failed under the weight of the levee in the "gravity-turn-on" stage of the analysis.

Geometry and Finite Element Grid

A typical levee height of 10 ft above natural ground with a crest width of 10 ft and side slopes of 1:4 was selected. A PZ-27 sheetpile driven 2 ft from the flood side of the crest was assumed as shown in

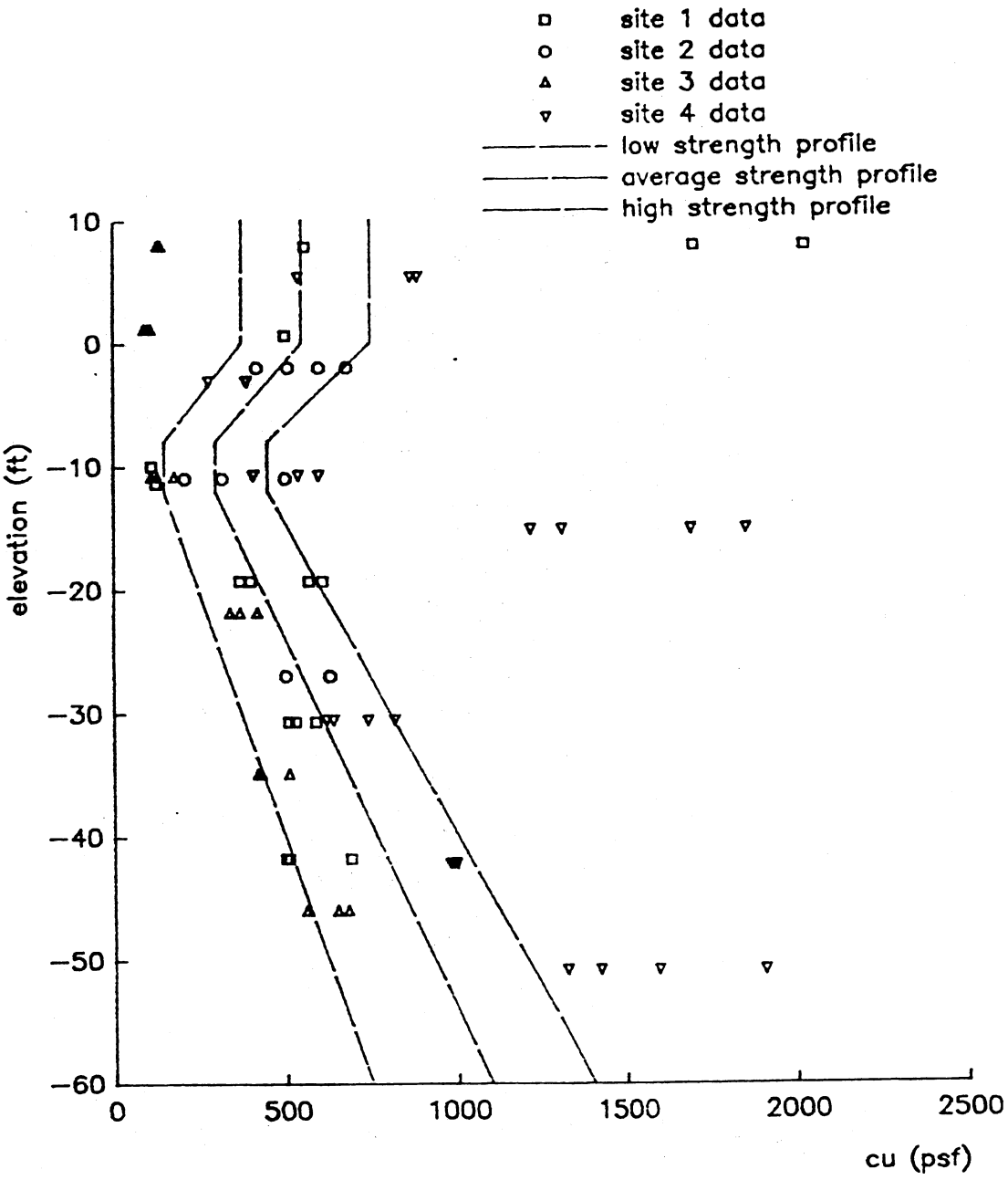

Figure 27. Idealized soil profile with data from typical sites superposed.

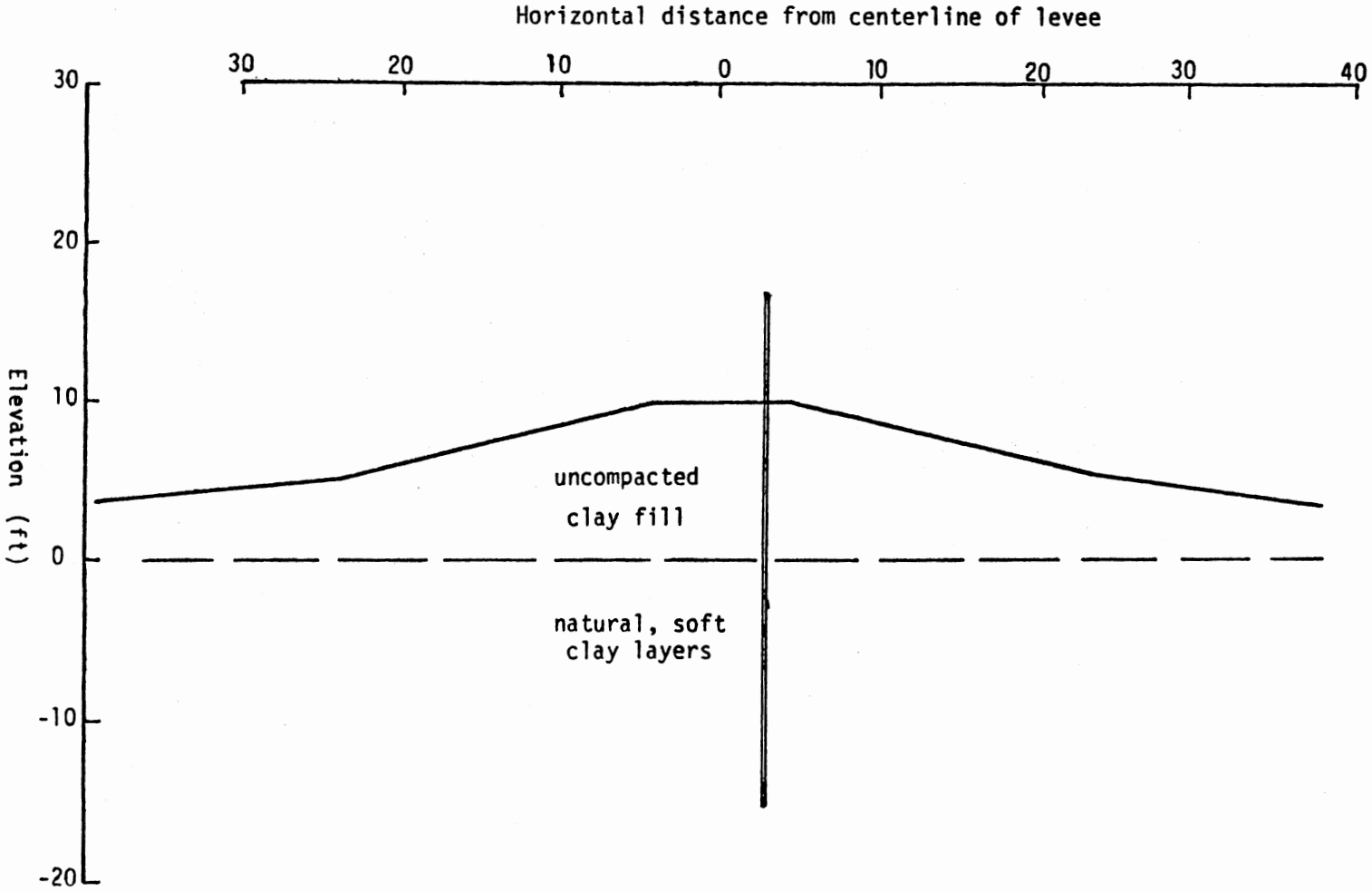

Figure 28. Typical floodwall cross section.

figure 28. For each of the strength profiles indicated above, analyses were performed for pile penetrations of 10, 20, and 30 ft below the levee crest. Thus in the first case the pile remains in the levee, and in the second and third cases it penetrates into the natural soil.

The finite element model of this system is shown in Fig. 29. The finite element grid consists of 542 elements and 539 nodes. Mesh fineness and lateral grid dimensions (from -105 ft to 165 ft) appeared to be satisfactory. This was confirmed by the degree of mobilization distribution, "f distribution", at various water heads (Figs. 31(a-h), 32(a-h), 33(a-h)). These plots reveal the areas of localized stress or stress concentrations and stress gradients. It is also shown in Fig. 30 that the f-contours tend to orient horizontally away from the levee; an indication of the diminishing effect of the levee.

As far as the overall depth of the grid is concerned, two depths (-90 ft and -150 ft) were analyzed for the "high" strength profile and 20 ft penetration depth. A comparison between the two cases showed that the moments in the pile and the stresses in the soils in the pile vicinity remain unchanged. However, the absolute displacements of the system are different. This is due to the fact that the soil medium is almost incompressible (Poisson's ratio, $v = 0.49$). Since the behavior of the pile and soils in the vicinity are of concern, a depth of -90 ft is considered satisfactory.

Initial Stresses and Loading

To determine the initial states of stress in the soil the "gravity-turn-on" analysis was done in three steps. In the first step, stresses were found for the horizontal surface at ground level as if the levee

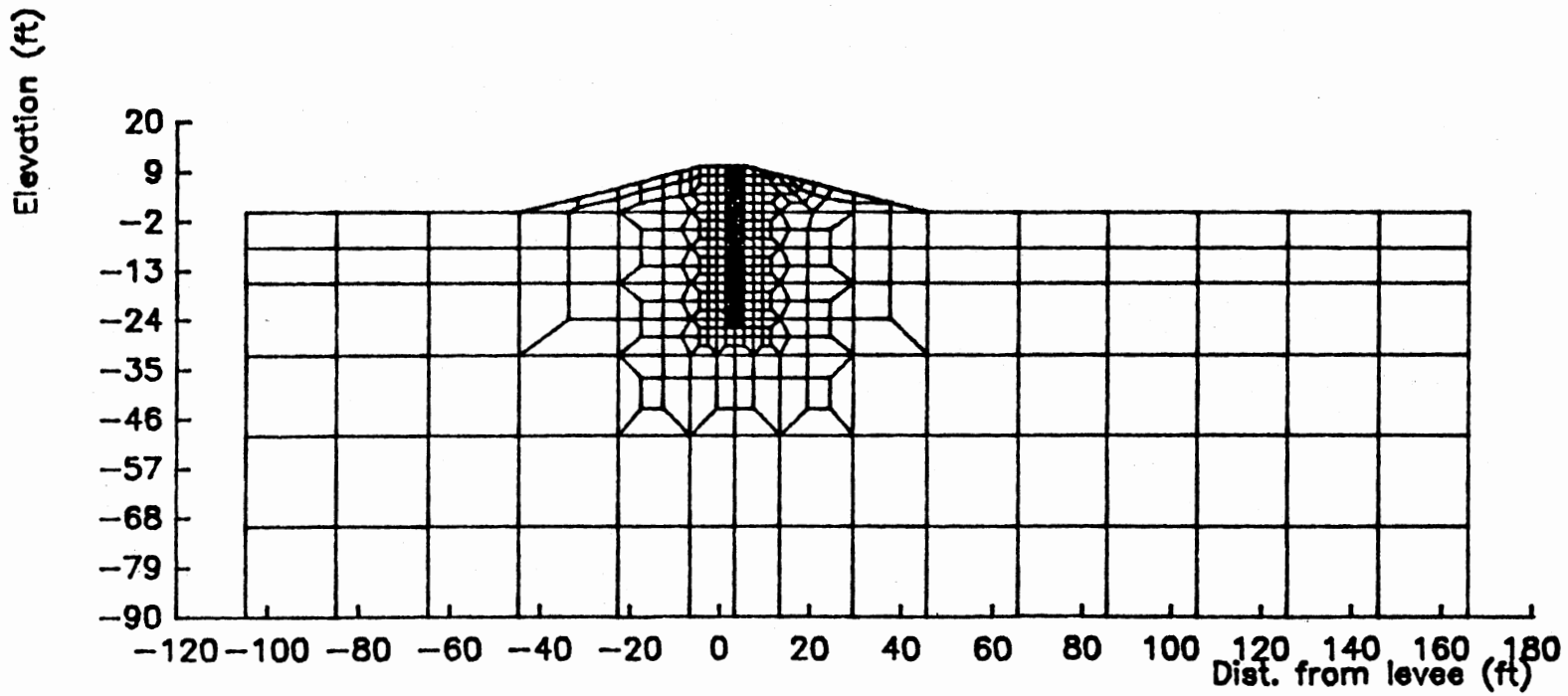

Figure 29(a). Grid for typical floodwall analyses.

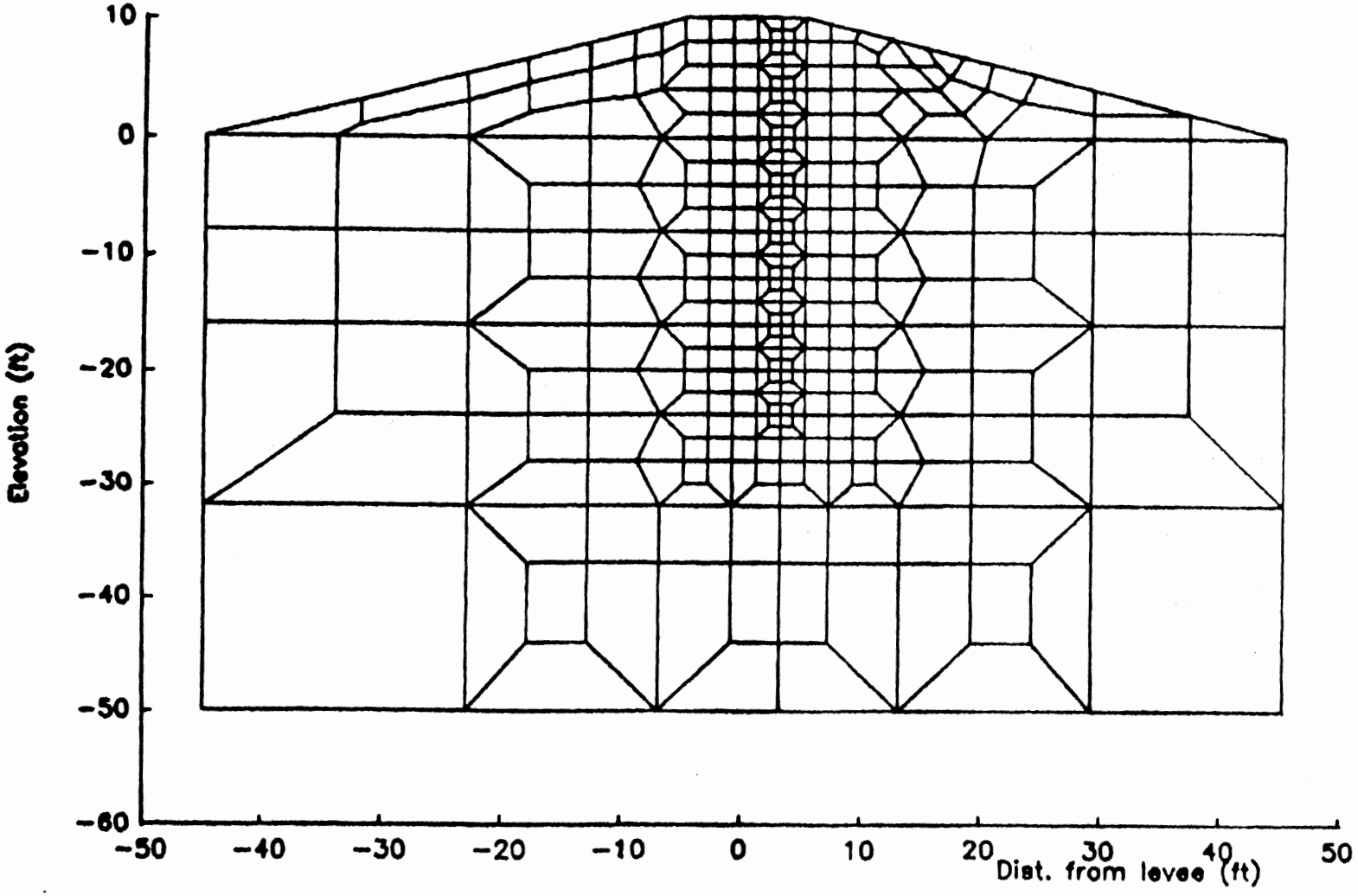

Figure 29(b). Details of the grid in the pile vicinity.

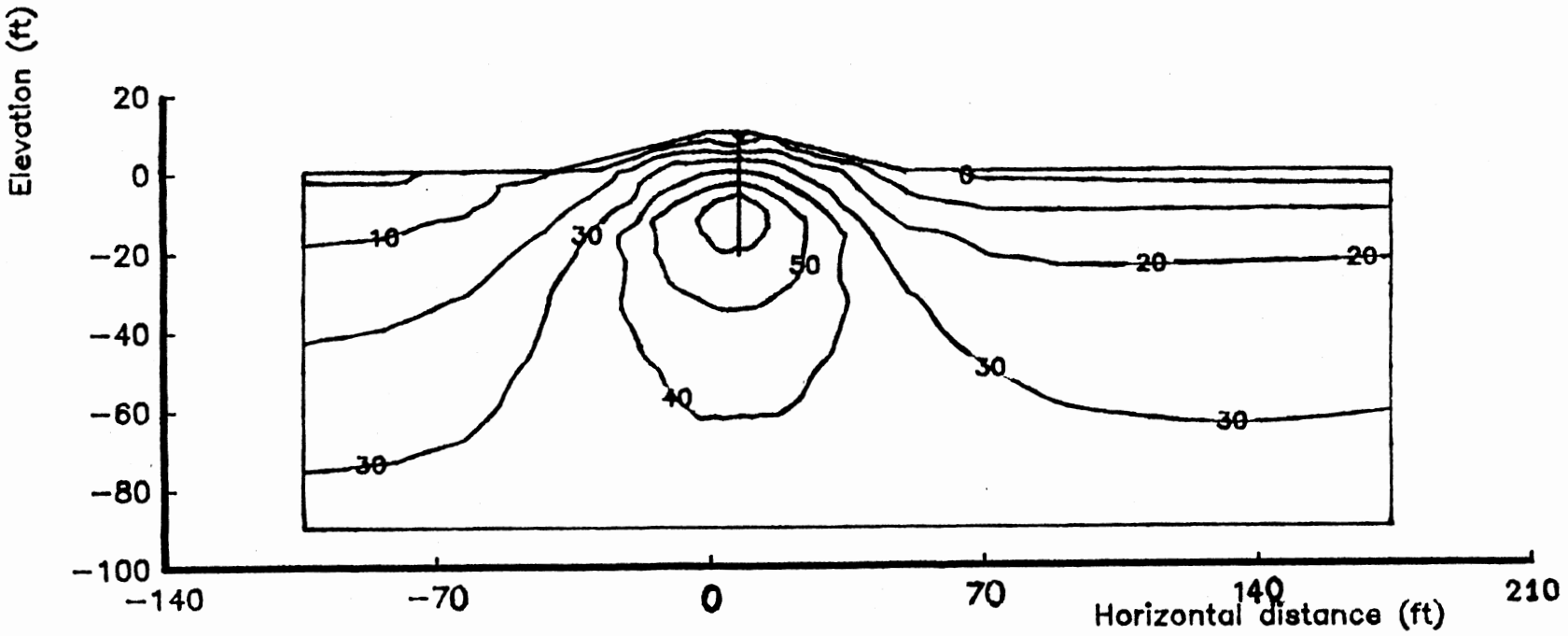

Figure 30. f contours at 2 ft head, high strength profile, 30 ft pile penetration.

did not exist. The levee then was built in two steps.

In loading the system, the water head was increased in 2-ft increments up to 10 ft above natural ground (levee crest) and in 1-ft increment thereafter up to 16 feet of head above natural ground.

Soil and Interface Parameters

The input parameters for the soils and the interface used in the analyses of typical cases are shown in the table below.

TABLE IV

SOIL AND INTERFACE INPUT PARAMETERS

K_t (lbs/ft/ft)	20000
μ	0.1
C_a (lbs/ft)	0
m	200
n	0
v	0.49
ϕ (degrees)	0

The input parameters in the above table are the same as those used in the E99 analysis (Table III). It should be noted that Fig. 55 in APPENDIX B shows that the variation of E_{50}/c_u varies between a minimum of 50 to a maximum of 350 with an average value of 200.

Results of Analyses for the High Strength Profile

Degree of Mobilization

The degrees of mobilization for the high strength profile and for water heads of 2, 4, 6, 8, 10, 12, and 16-ft are shown in figures 31(a) through (h), 32(a) through (h), and 33(a) through (h) for 10, 20, and 30-ft pile penetration, respectively. The initial f contours are symmetric, as expected, around the levee center line. The magnitudes of these contours vary between 0 % at the levee surface and 60 % in the soft layer (between El. -5 ft and El. -20 ft) under the center of the levee (Figs. 31a, 32a, and 33a). The reason for this increase is due to the decrease in soil strength on one hand and to the decrease in the confining stress (σ_x) on the other. The decrease in confining stress is due to the tendency of the levee to flow laterally away from the levee center line.

When loading progresses up to the levee crest (from 2 ft to 10 ft head; that is, before loading the pile directly) the contours tend to shift to the right, toward the loaded area. Also, this loading helps increase the confining stress (σ_x) in the soils directly underneath the levee center, hence stabilizing them. This is noticed from the decrease in the f magnitudes as shown in figures 31(a-e), 32(a-e), and 33(a-e). This behavior is similar for the three cases (10, 20, 30 ft penetrations). However, at higher loading when the pile is directly loaded (water head is above 10 ft), the distribution of the degree of mobilization is different in the three cases. The exception to that is the passive region in the upper part of the levee just in front of the wall where f reaches 50 % of the passive strength at 16-ft water

elevation. In this region, the f contours show similar behavior irrespective of the depth of penetration. For the 10-ft case, the soils at the back of the wall at El. 0-ft (pile tip) have an f value of 50 % of the active strength (Fig. 31(h)) and are being loaded in the passive direction; that is if these soils are still loaded in the same direction (passive), the f magnitude is going to decrease to 0 % (isotropic state) then increase toward the passive limit. However, for the 20-ft and 30-ft penetration cases, the f magnitudes in these soils decrease to 40 % of the active strength and remain loaded in the same direction (Figs. 32(h), 33(h)). This decrease is the result of the increase in embedment length where the pile tends to redistribute the stresses on a larger soil portion as shown in the net pressure distribution diagrams (Figs. 38(a), (b), and (c)). For the 20-ft case, the soils at the back of the pile at -10 ft elevation (pile tip) are in active condition with an f magnitude of 80% of the active capacity at 16 ft of water head (Fig. 32(h)). On the other hand, for the 30-ft case, these soils are loaded in the passive direction with f= 60 % of the active capacity (the state of stress still on the active side) as shown in Fig. 33(h). Finally, for the 30-ft case, the soils at the back of the pile at -30 ft elevation (pile tip) are in active state with f=70 % of the active strength at 16 ft of water head (Fig. 33(h)).

The above information reveals an interesting observation. That is for the soil strength profile assumed, the usual belief in "the deeper the pile the safer the system" is not valid when comparing the three pile penetration cases. This is manifested in the comparison between the 10-ft case and the 20-ft case. In the 20-ft case, the soils at the back of the pile at -10 ft elevation (in the weak layer) are in an

active state at f= 80 % of the active capacity (Fig. 32(h)) whereas in the 10-ft case, these soils are also in active state with only 60 % of the active capacity (Fig. 31(h)). The increase in the f magnitude in this region as the pile depth is increased is a special but critical case. As contradictory as this might seem at first sight, the explanation becomes evident under deeper reflection and careful interpretation.

The above mentioned behavior is due to the following reasons:

a. When the levee system is loaded, the soft (weak) layer, between -5 ft and -15 ft elevation, is excessively sheared.

b. In addition to the shearing of the weak layer, there is a clockwise rotation of the levee and the soil medium mainly above this layer.

c. As the pile penetrates this layer, it tries to resist the effects described in (a) and (b). In trying to do so, it encounters a reaction in the vicinity of its tip from the soils in front. This explains the existence of a passive zone at that particular location in front of the pile and, by the same token, an active zone behind it. Since the soil in front of the pile can do little in preventing the displacement of the pile due to the large discrepancy between the relative stiffnesses, this will aggravate the already existing active zone at the back of the pile.

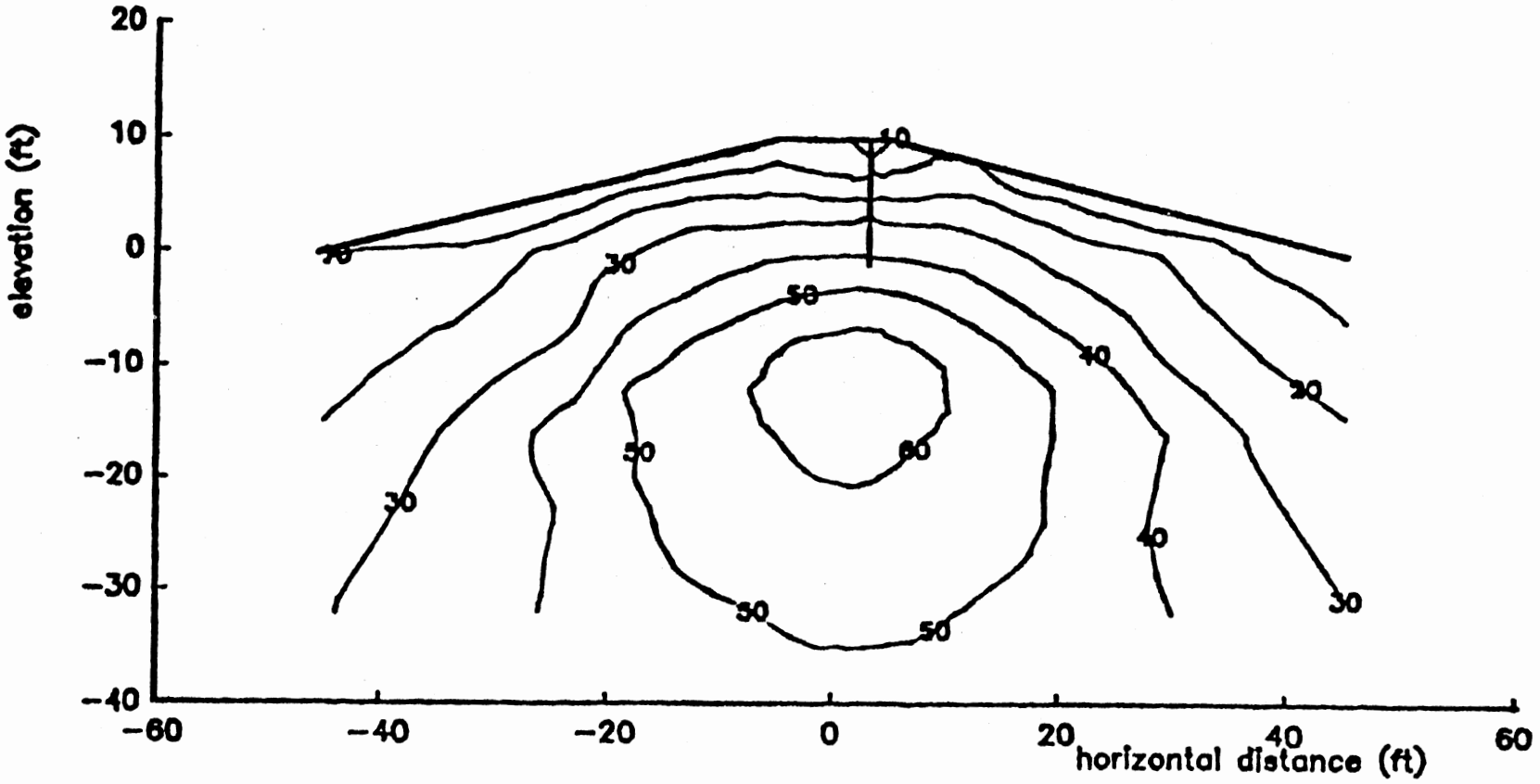

Figure 31(a). f contours at 2 ft head, high strength profile, 10 ft pile penetration.

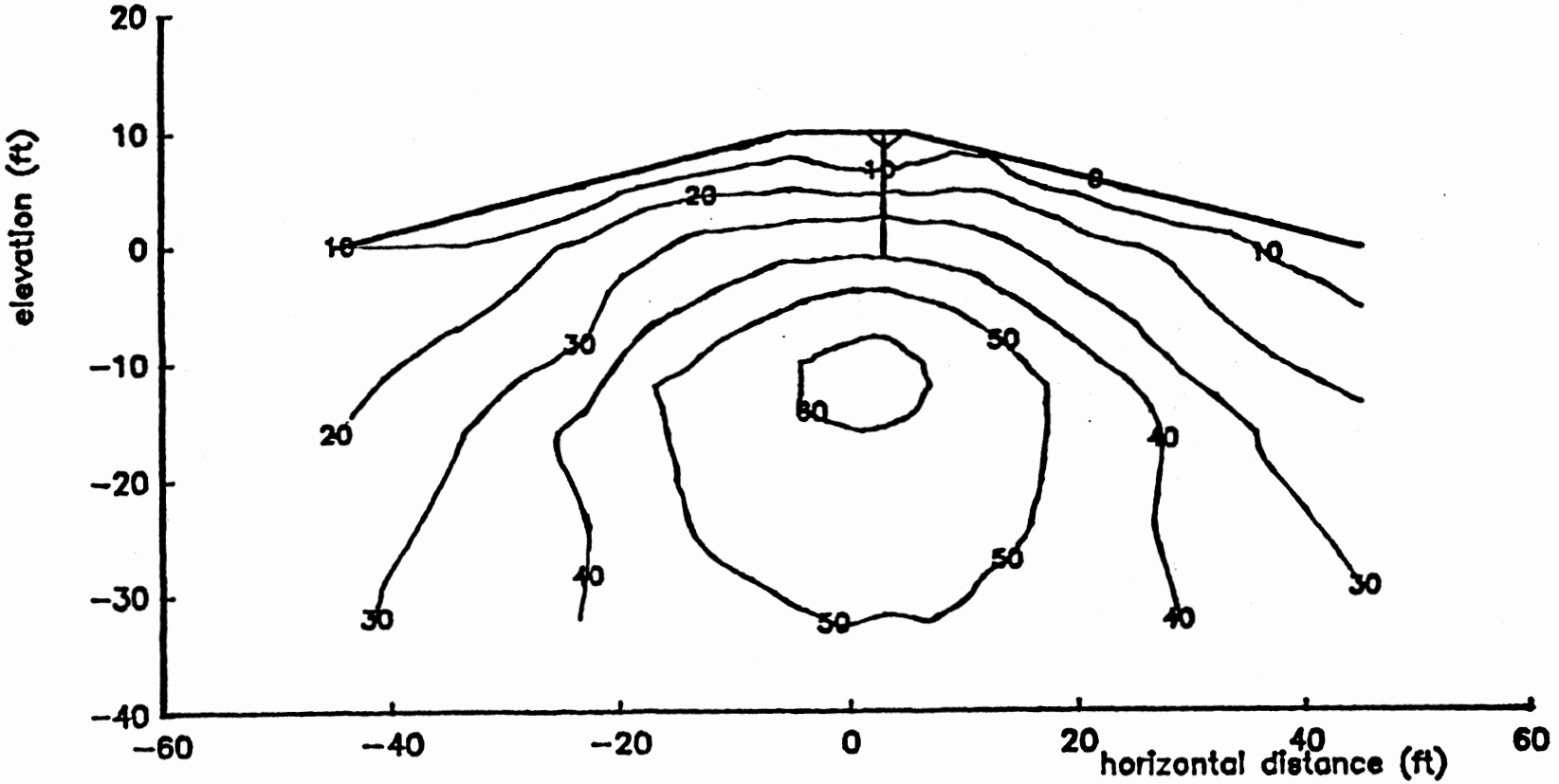

Figure 31(b). f contours at 4 ft head, high strength profile, 10 ft pile penetration.

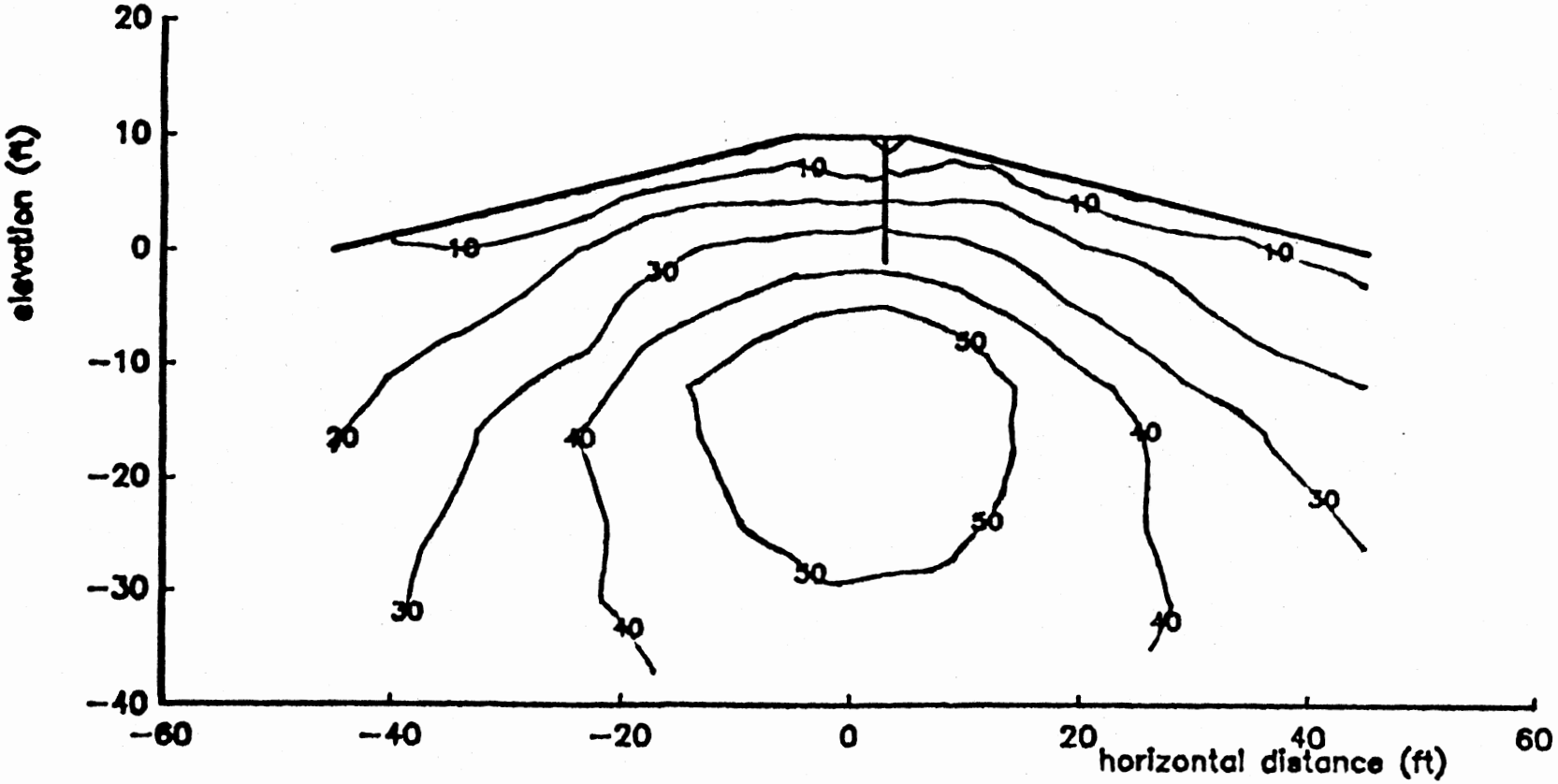

Figure 31(c). f contours at 6 ft head, high strength profile, 10 ft pile penetration.

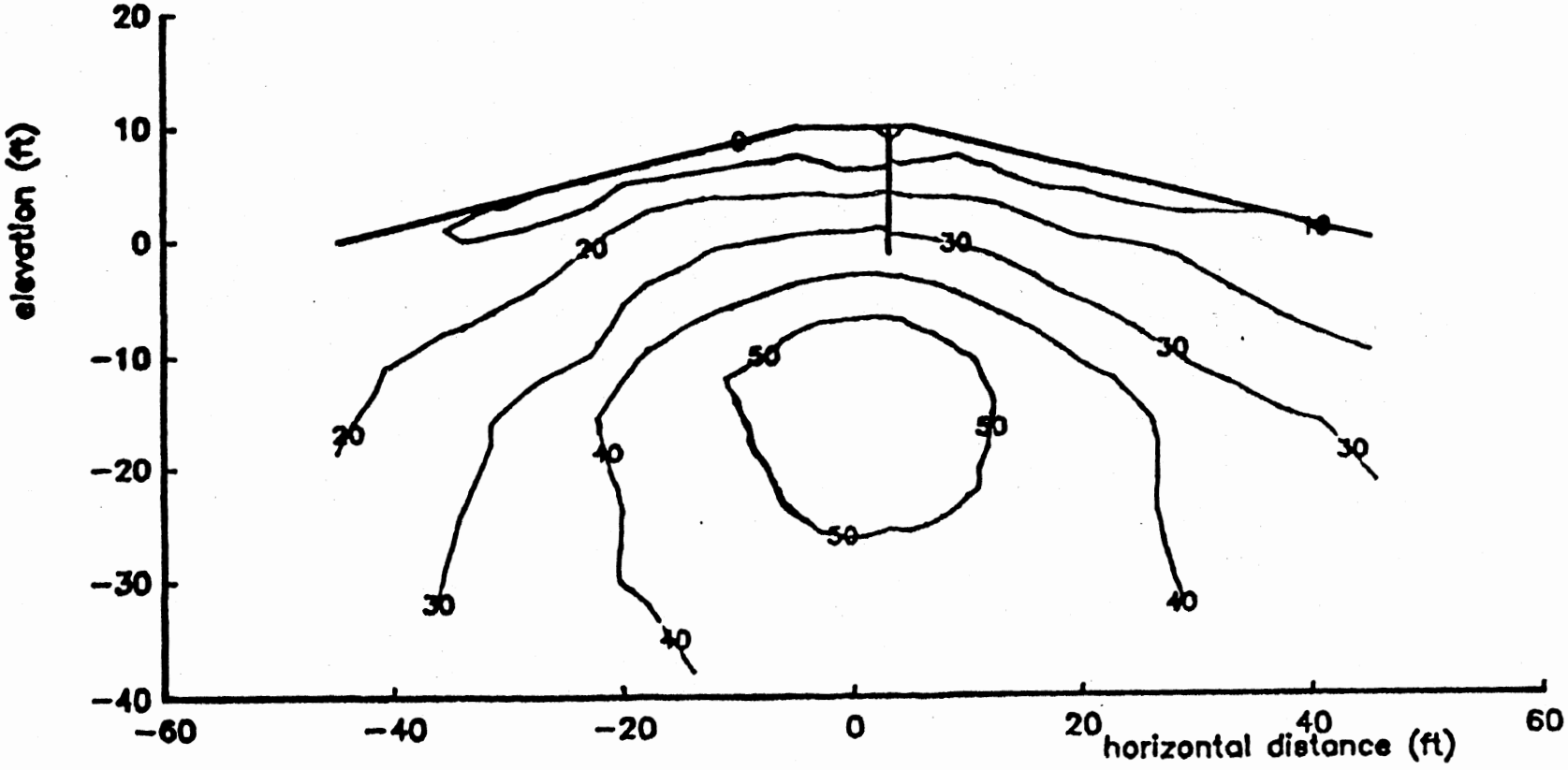

Figure 31(d). f contours at 8 ft head, high strength profile, 10 ft pile penetration.

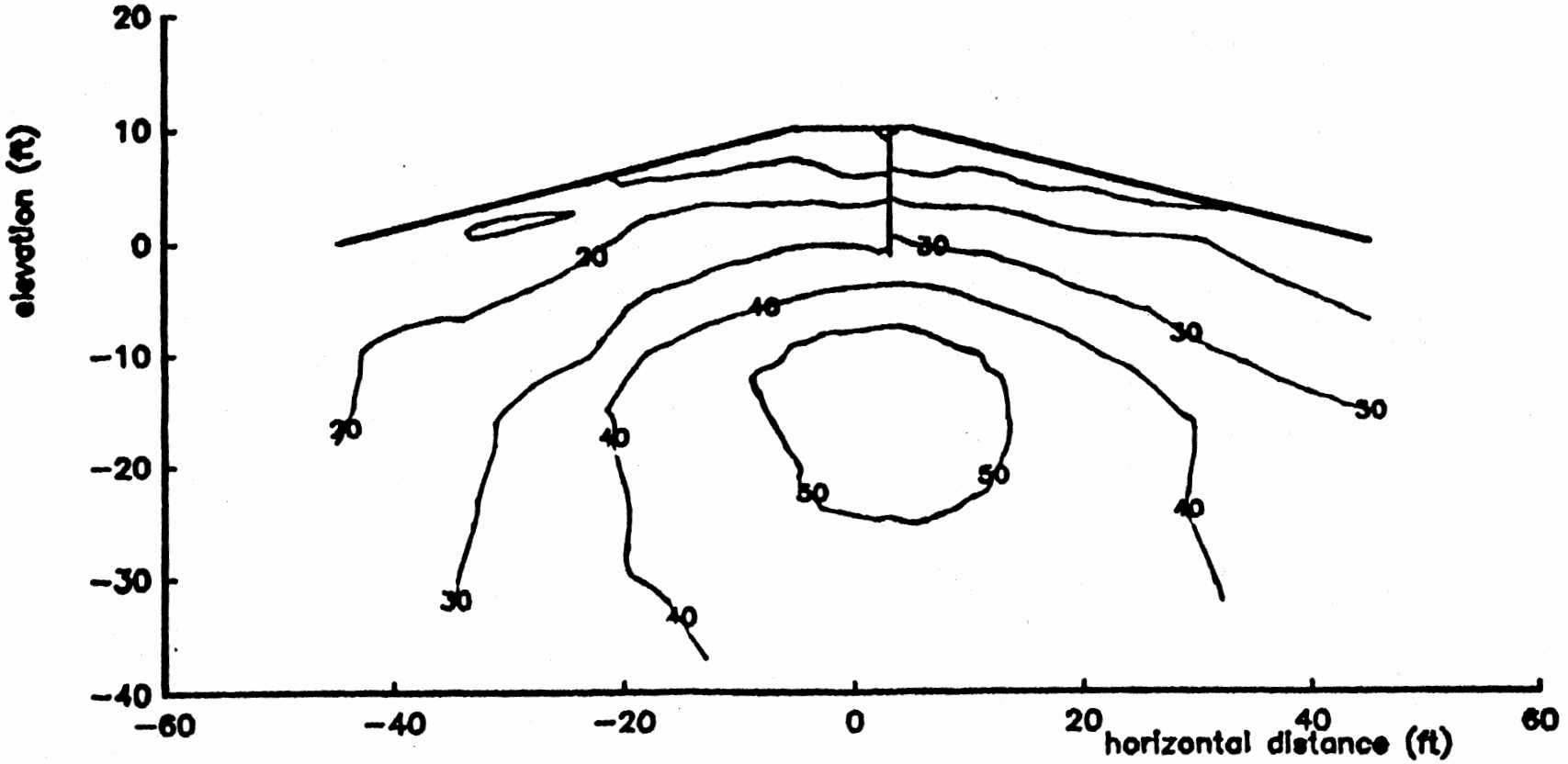

Figure 31(e). f contours at 10 ft head, high strength profile, 10 ft pile penetration.

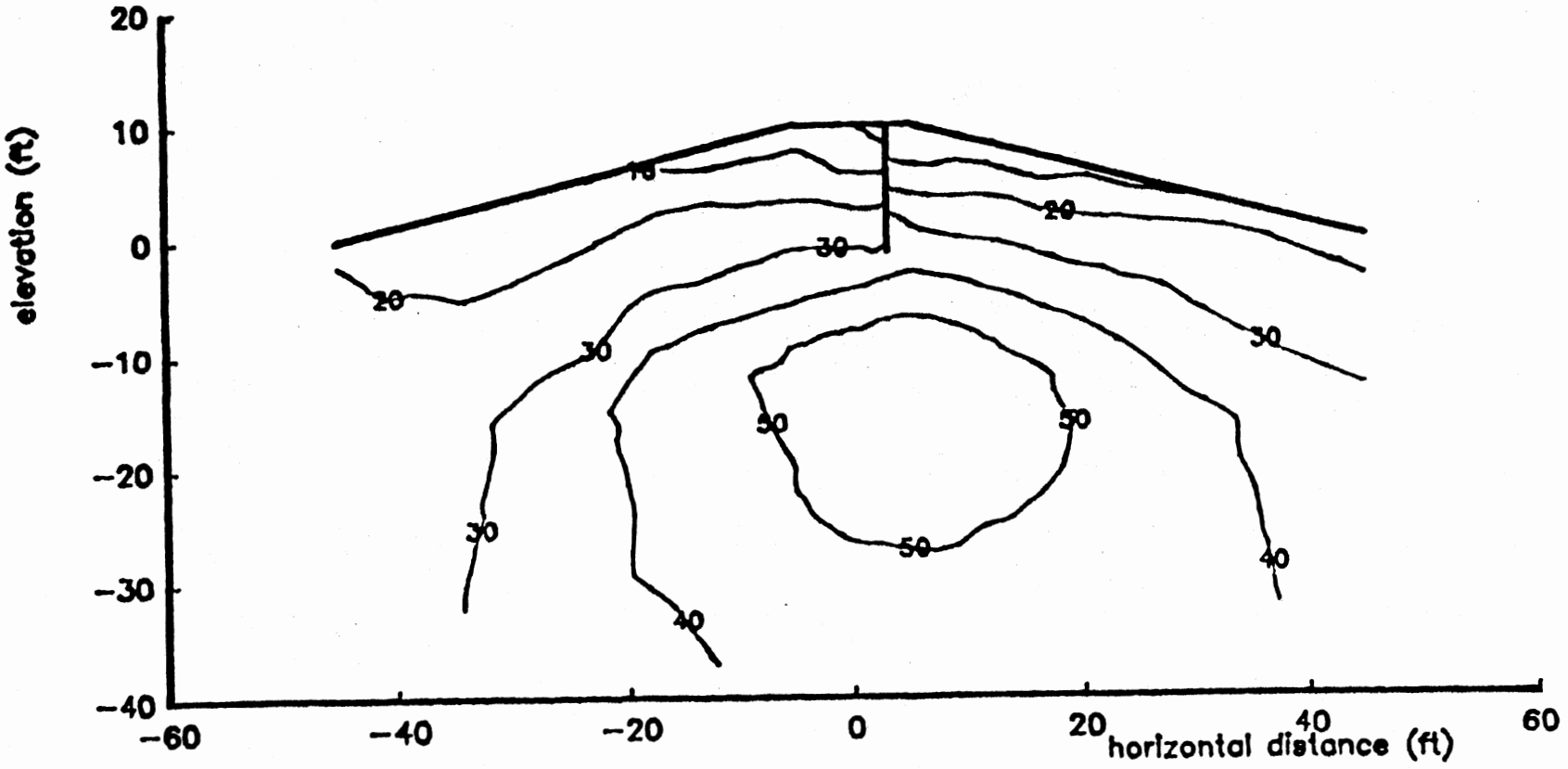

Figure 31(f). f contours at 12 ft head, high strength profile, 10 ft pile penetration.

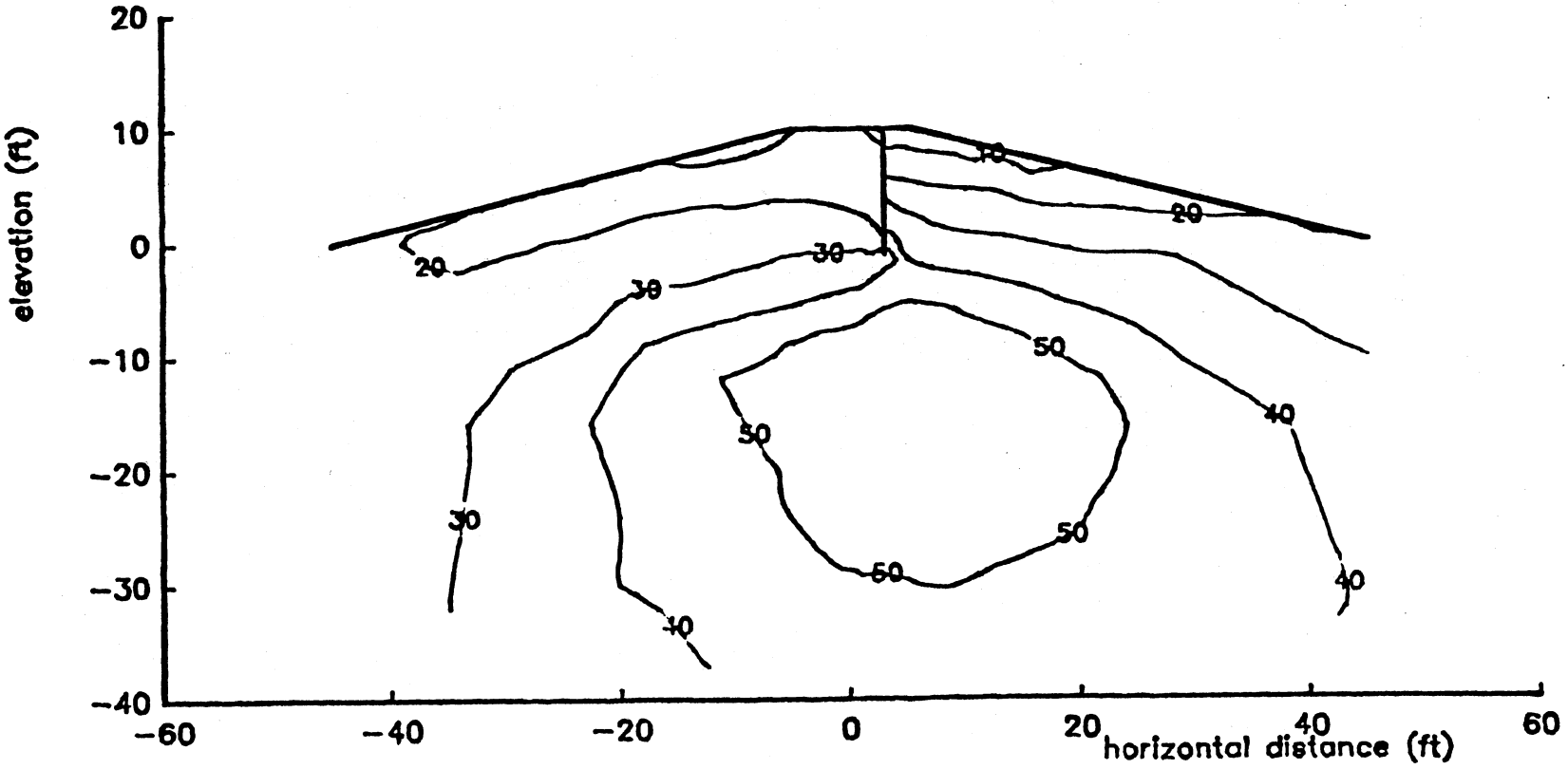

Figure 31(g). f contours at 14 ft head, high strength profile, 10 ft pile penetration.

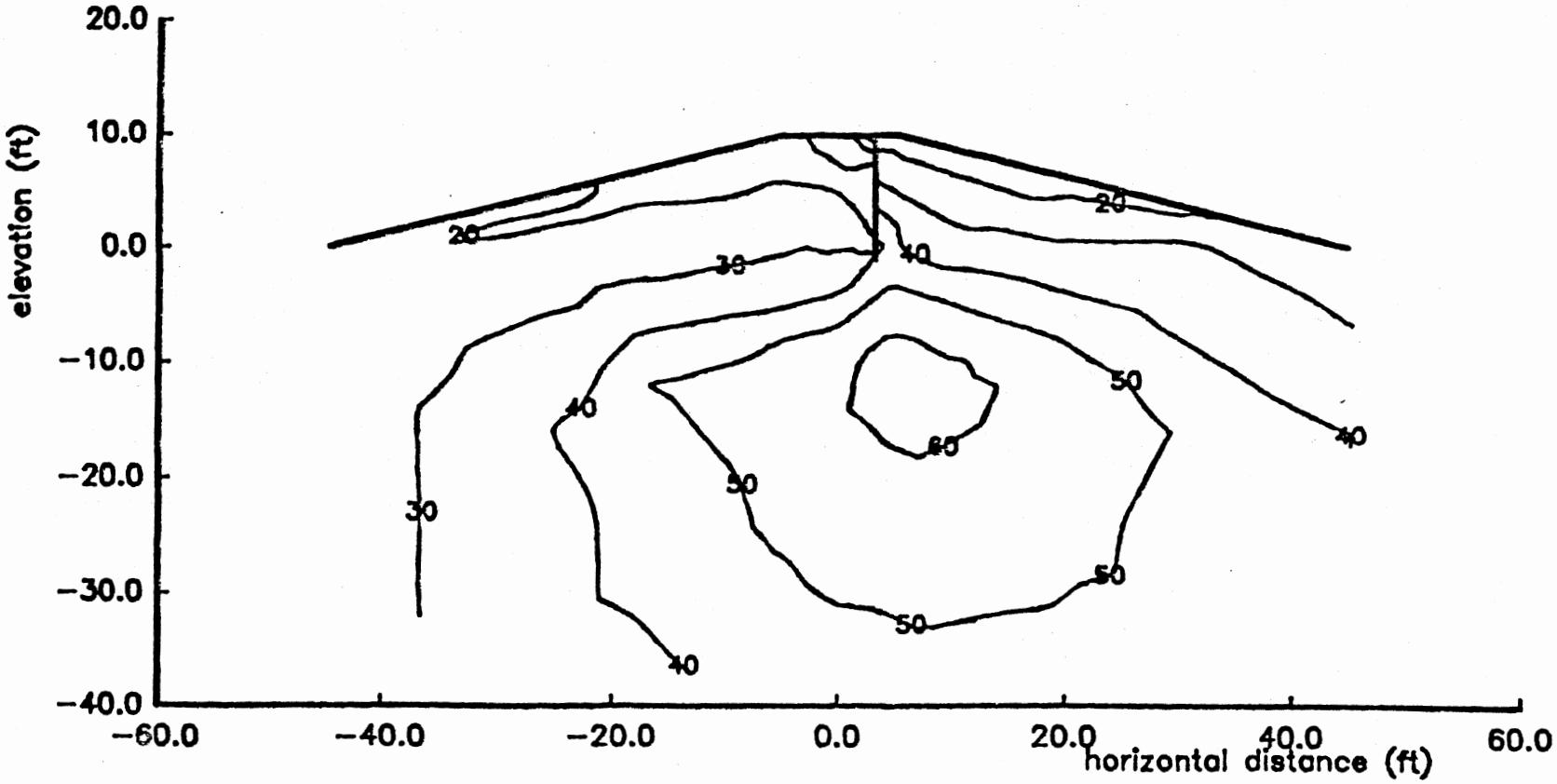

Figure 31(h). f contours at 16 ft head, high strength profile, 10 ft pile penetration.

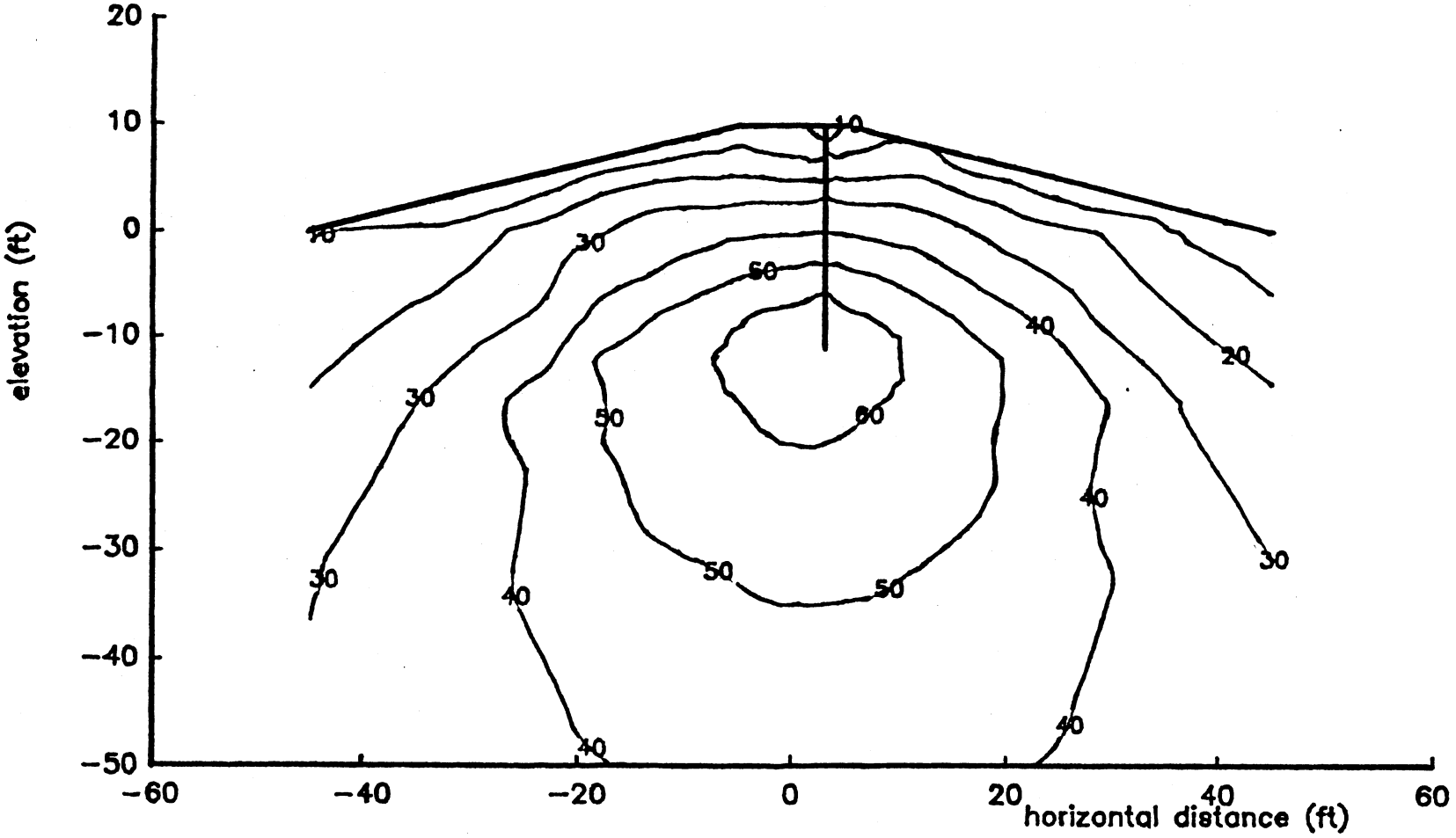

Figure 32(a). f contours at 2 ft head, high strength profile, 20 ft pile penetration.

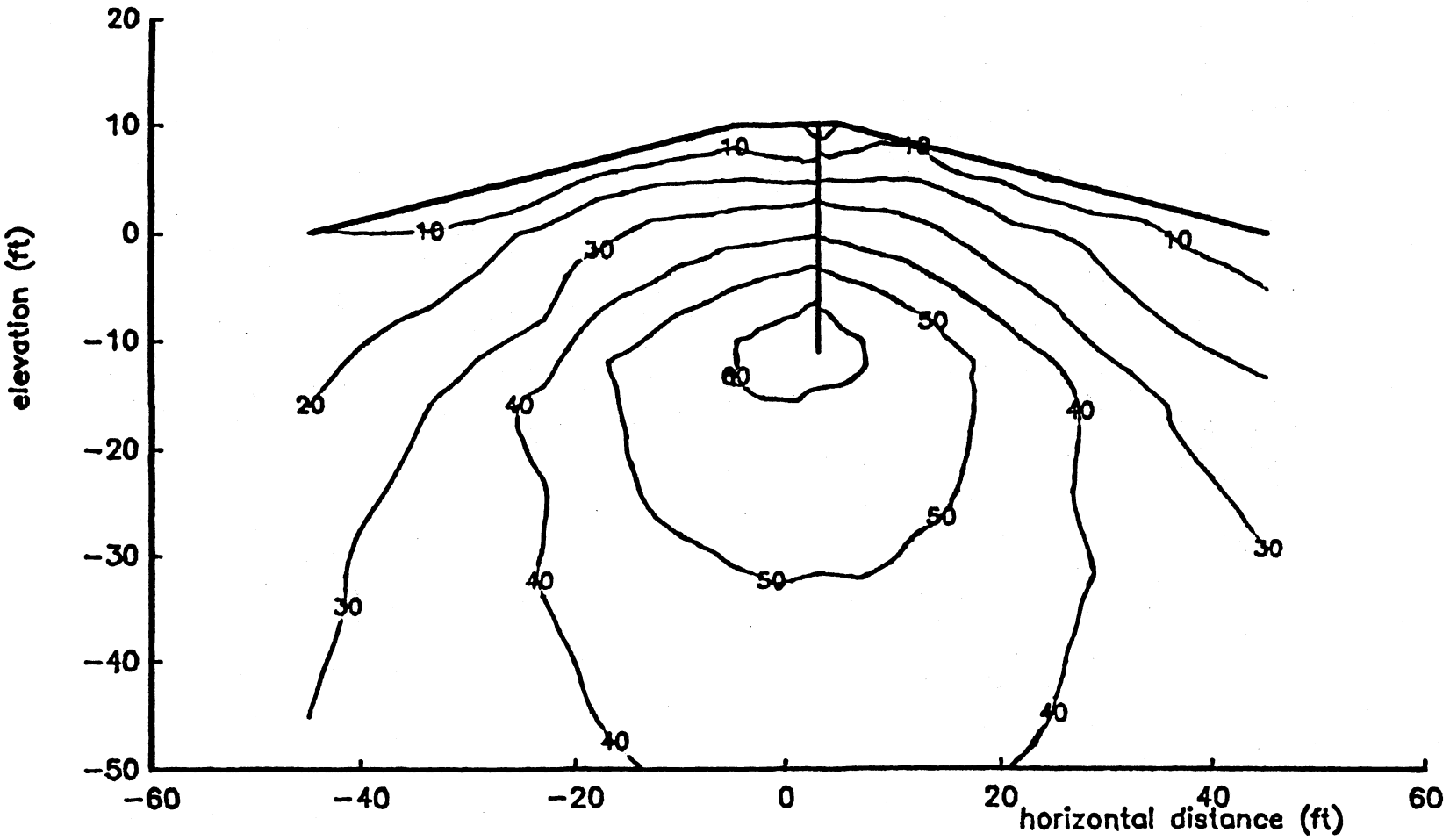

Figure 32(b). f contours at 4 ft head, high strength profile, 20 ft pile penetration.

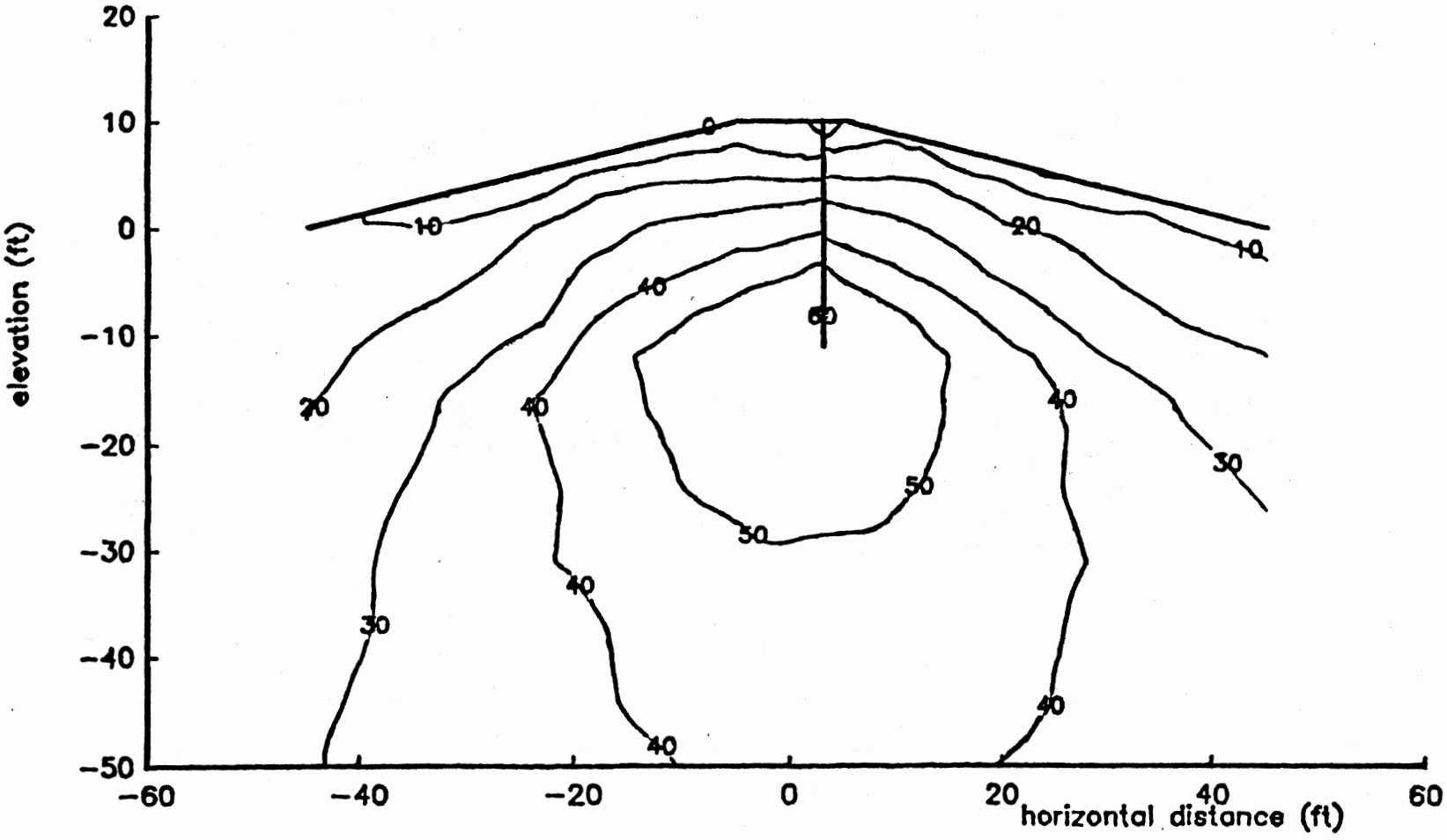

Figure 32(c). f contours at 6 ft head, high strength profile, 20 ft pile penetration.

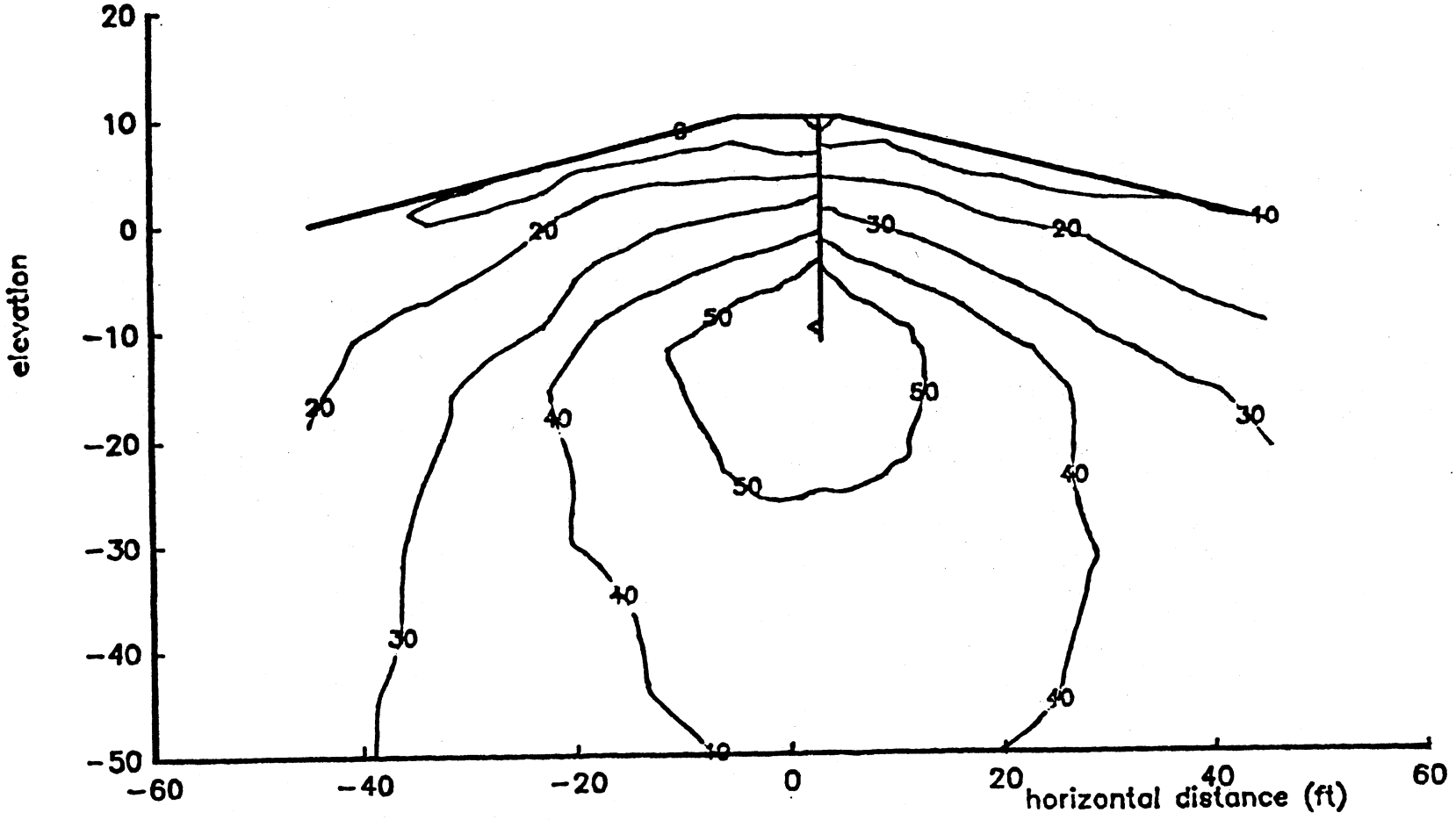

Figure 32(d). f contours at 8 ft head, high strength profile, 20 ft pile penetration.

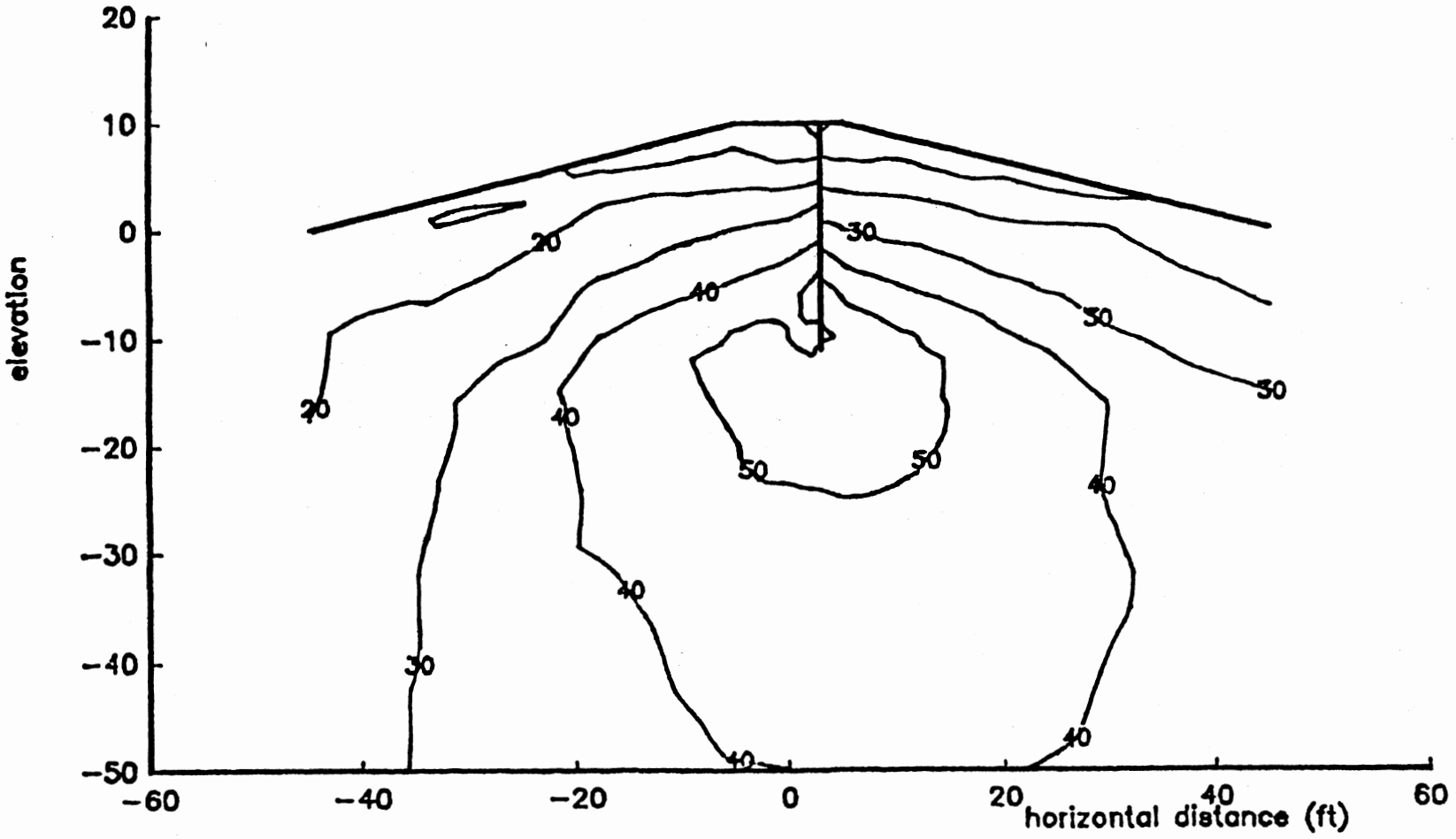

Figure 32(e). f contours at 10 ft head, high strength profile, 20 ft pile penetration.

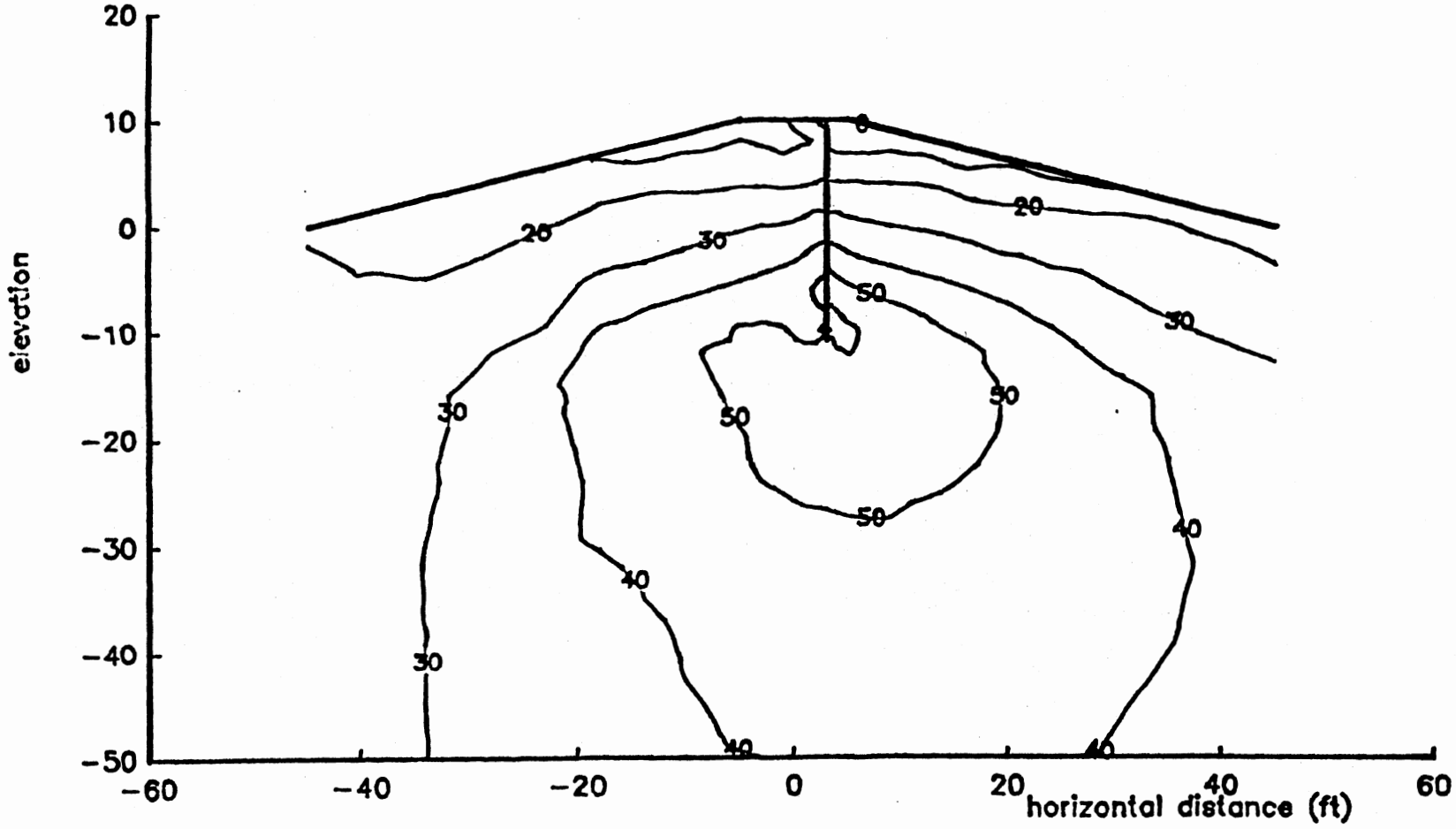

Figure 32(f). f contours at 12 ft head, high strength profile, 20 ft pile penetration.

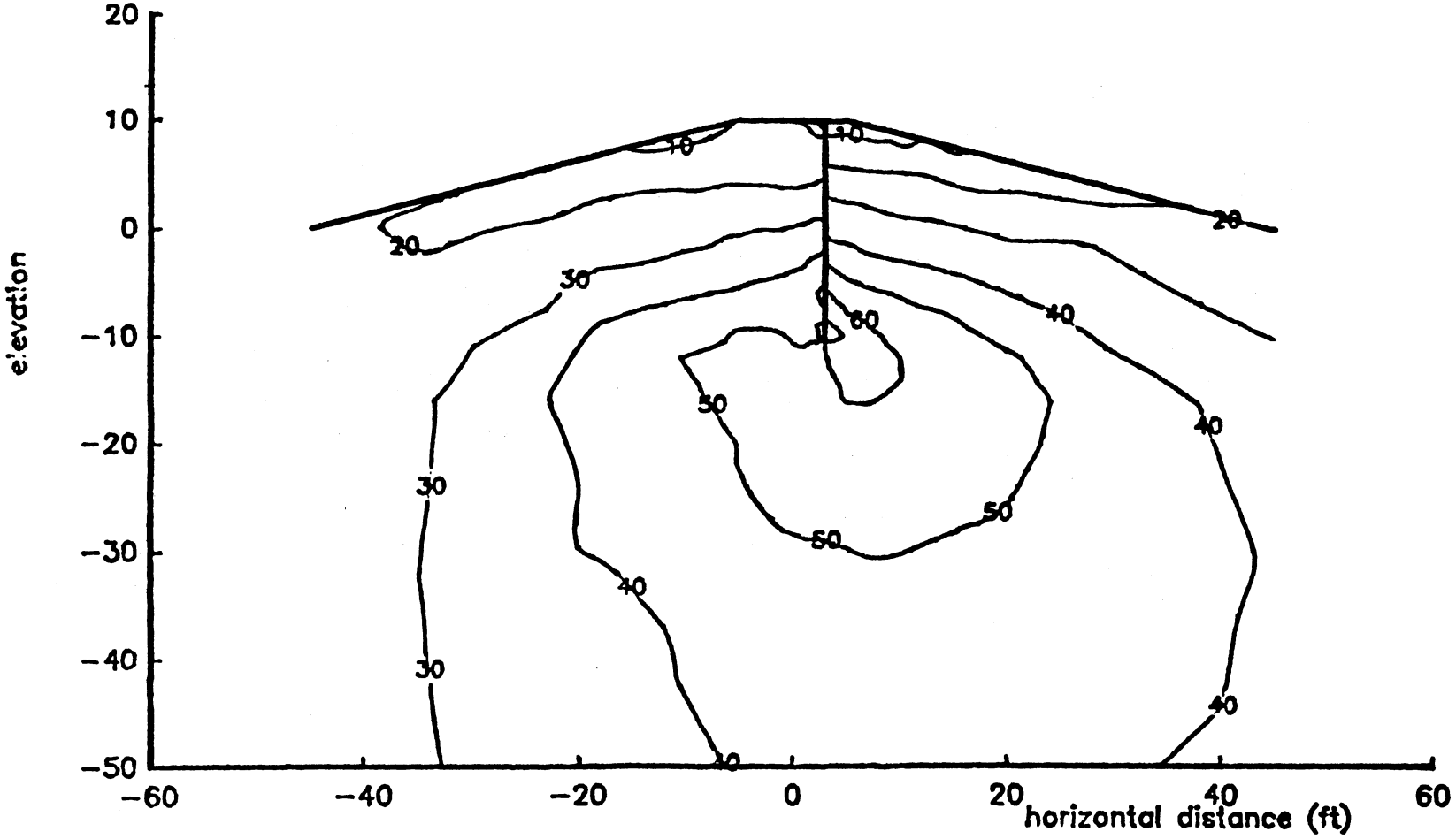

Figure 32(g). f contours at 14 ft head, high strength profile, 20 ft pile penetration.

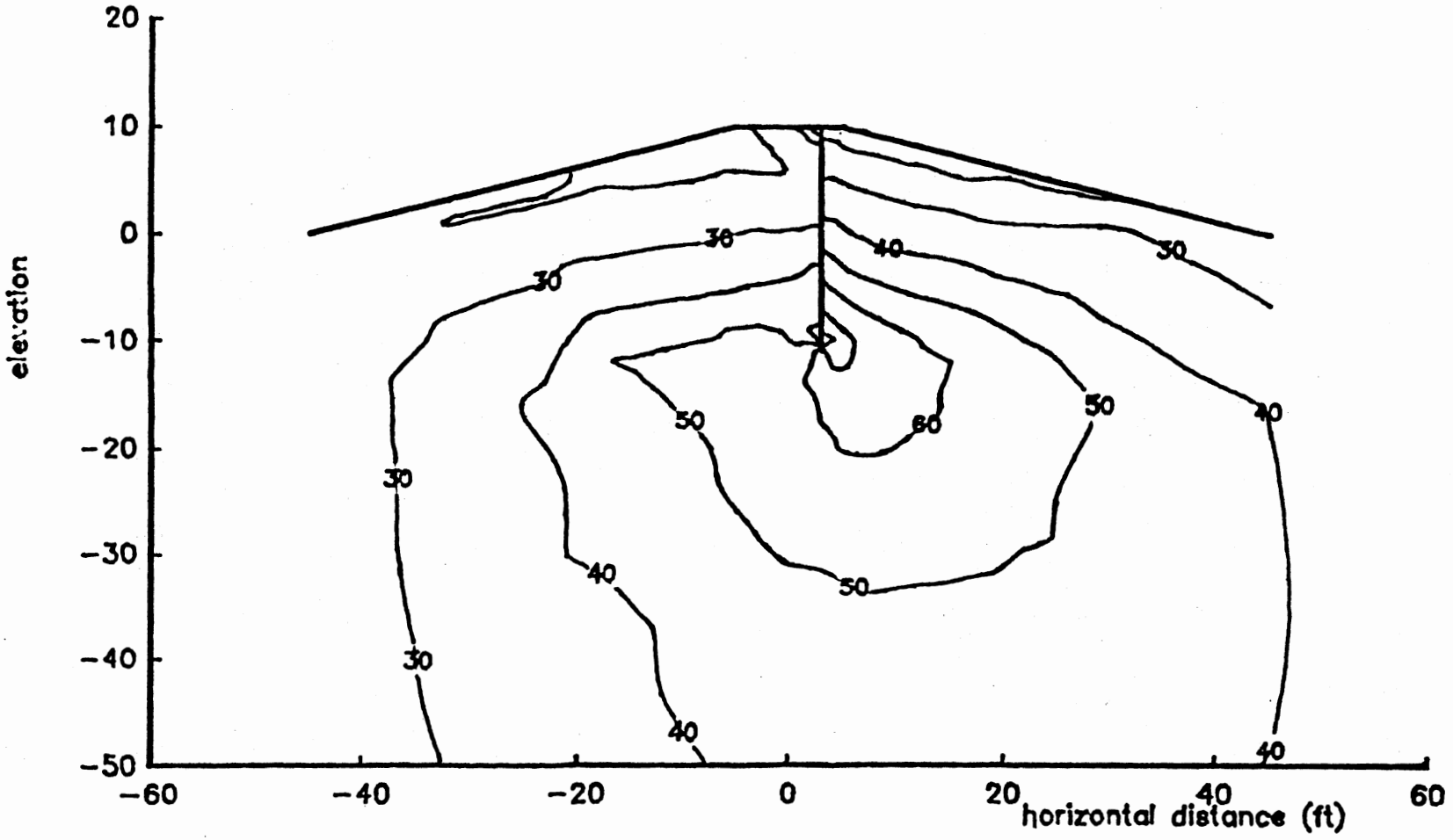

Figure 32(h). f contours at 16 ft head, high strength profile, 20 ft pile penetration.

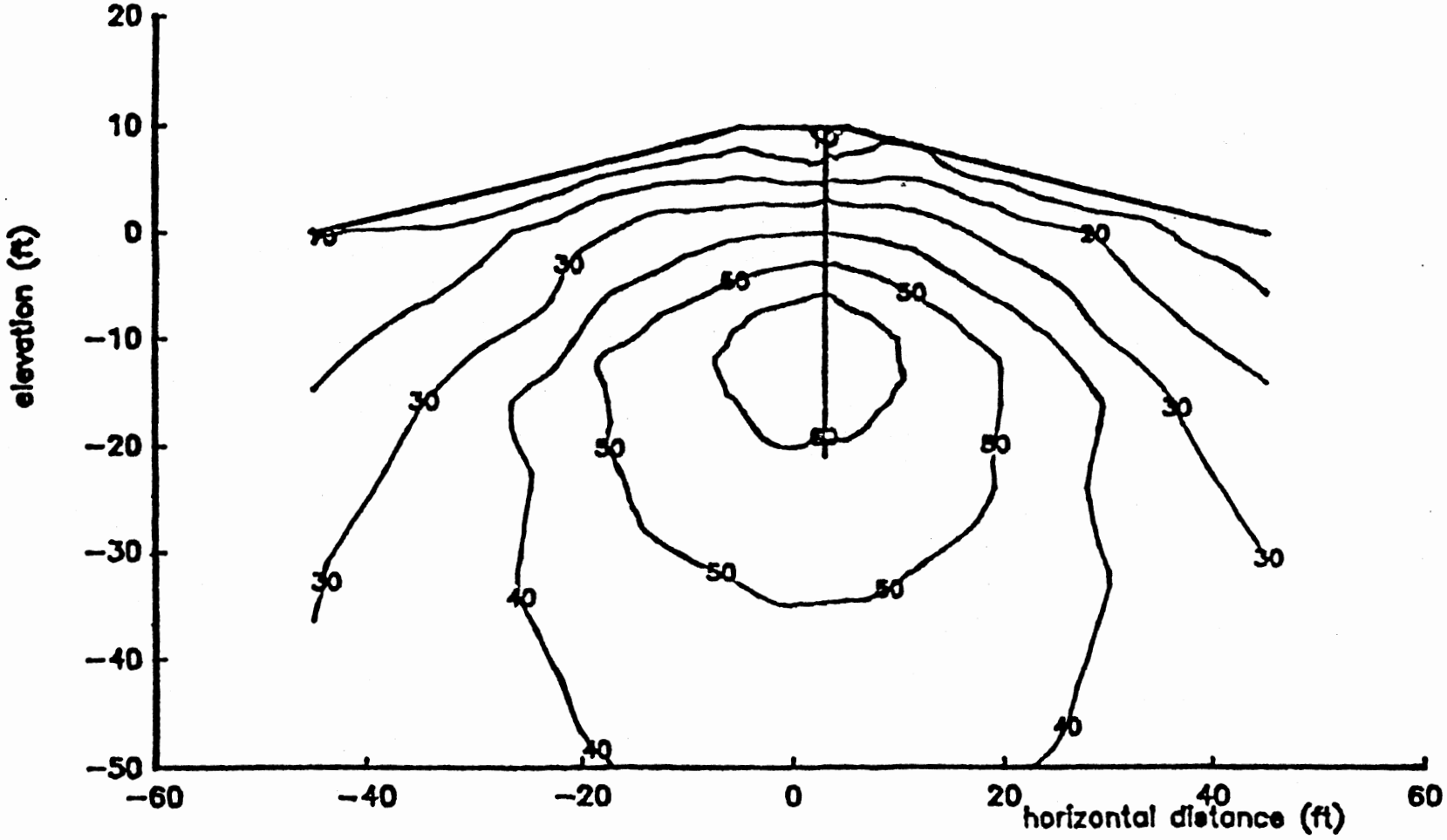

Figure 33(a). f contours at 2 ft head, high strength profile, 30 ft pile penetration.

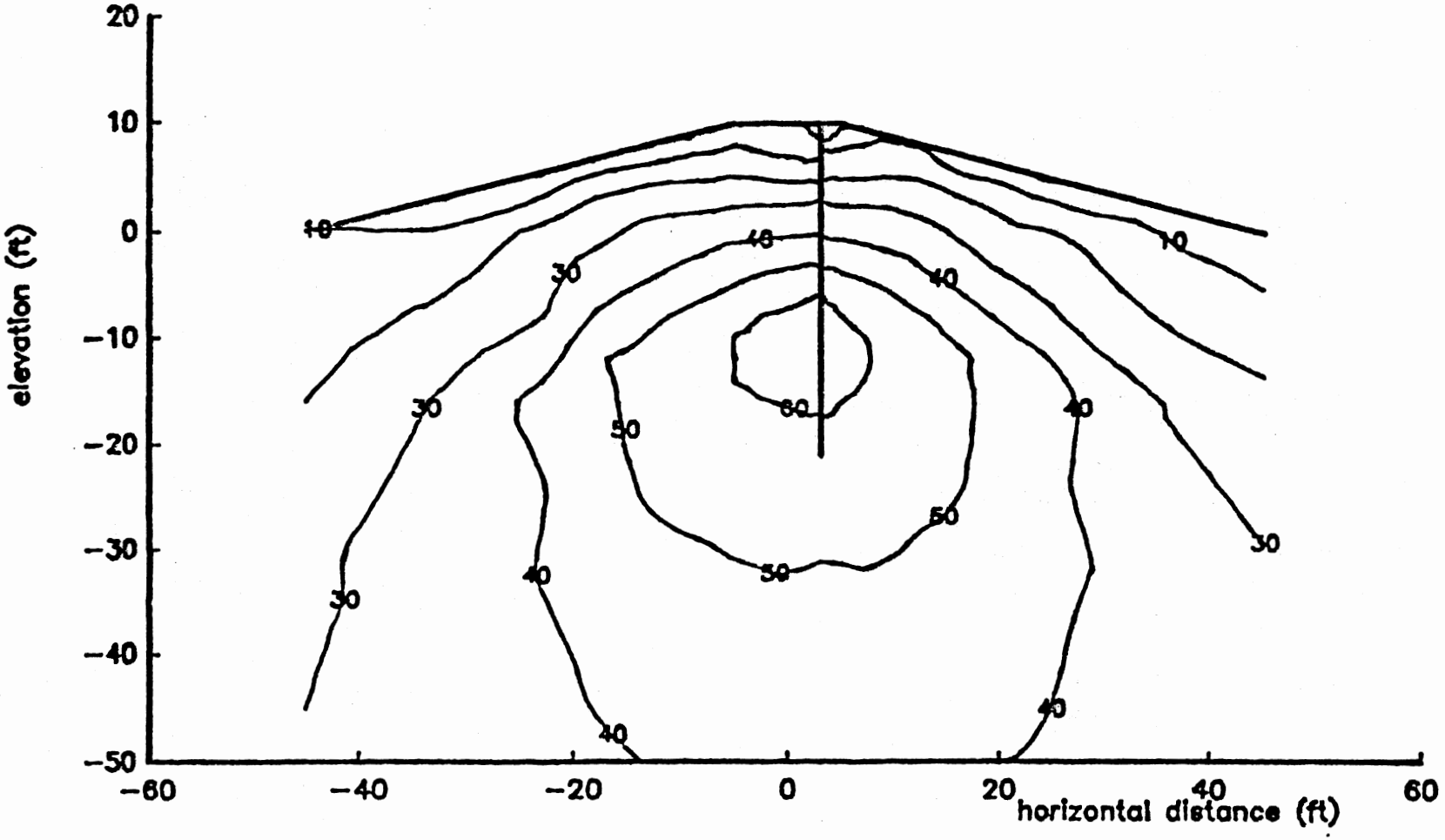

Figure 33(b). f contours at 4 ft head, high strength profile, 30 ft pile penetration.

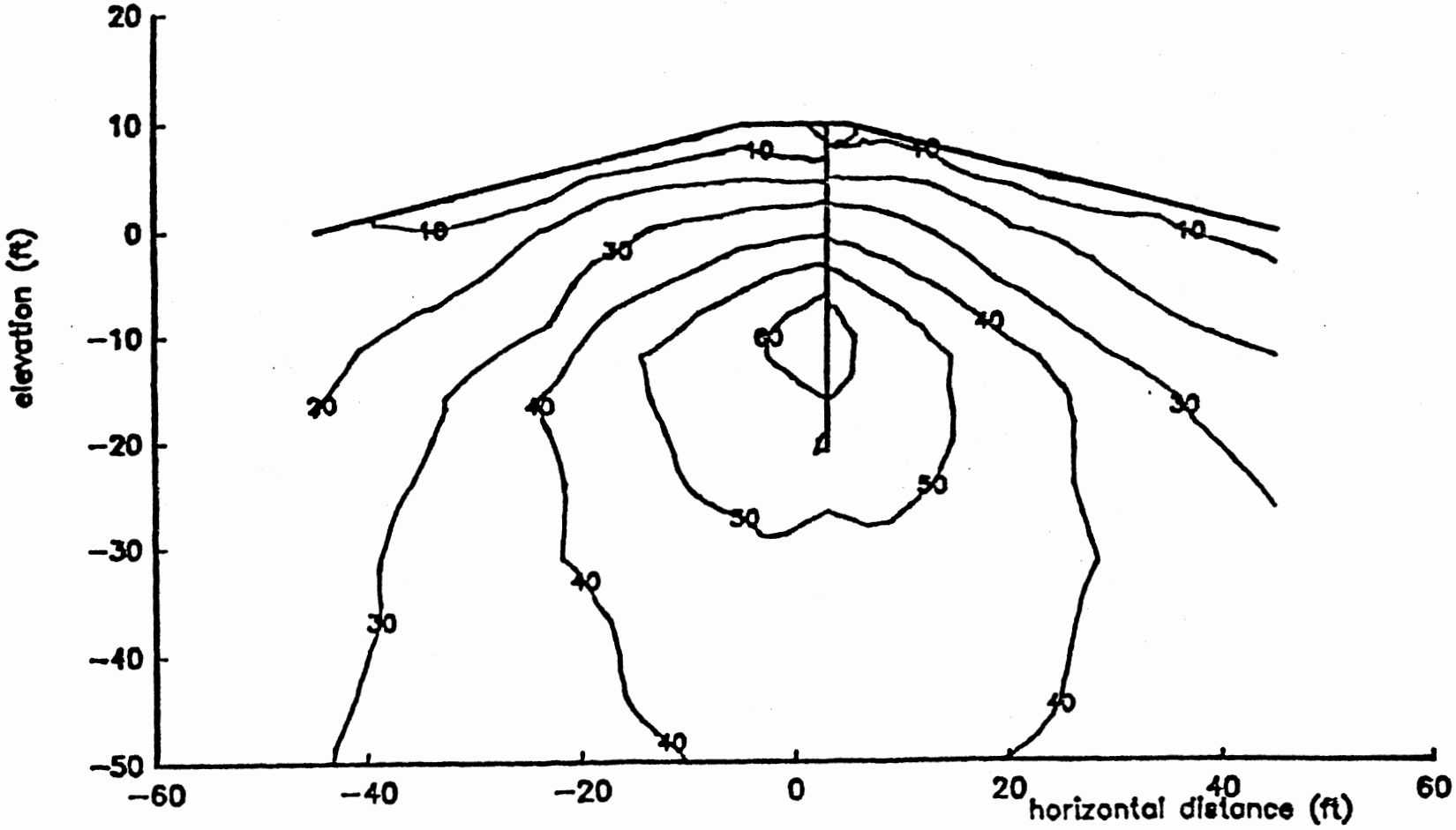

Figure 33(c). f contours at 6 ft head, high strength profile, 30 ft pile penetration.

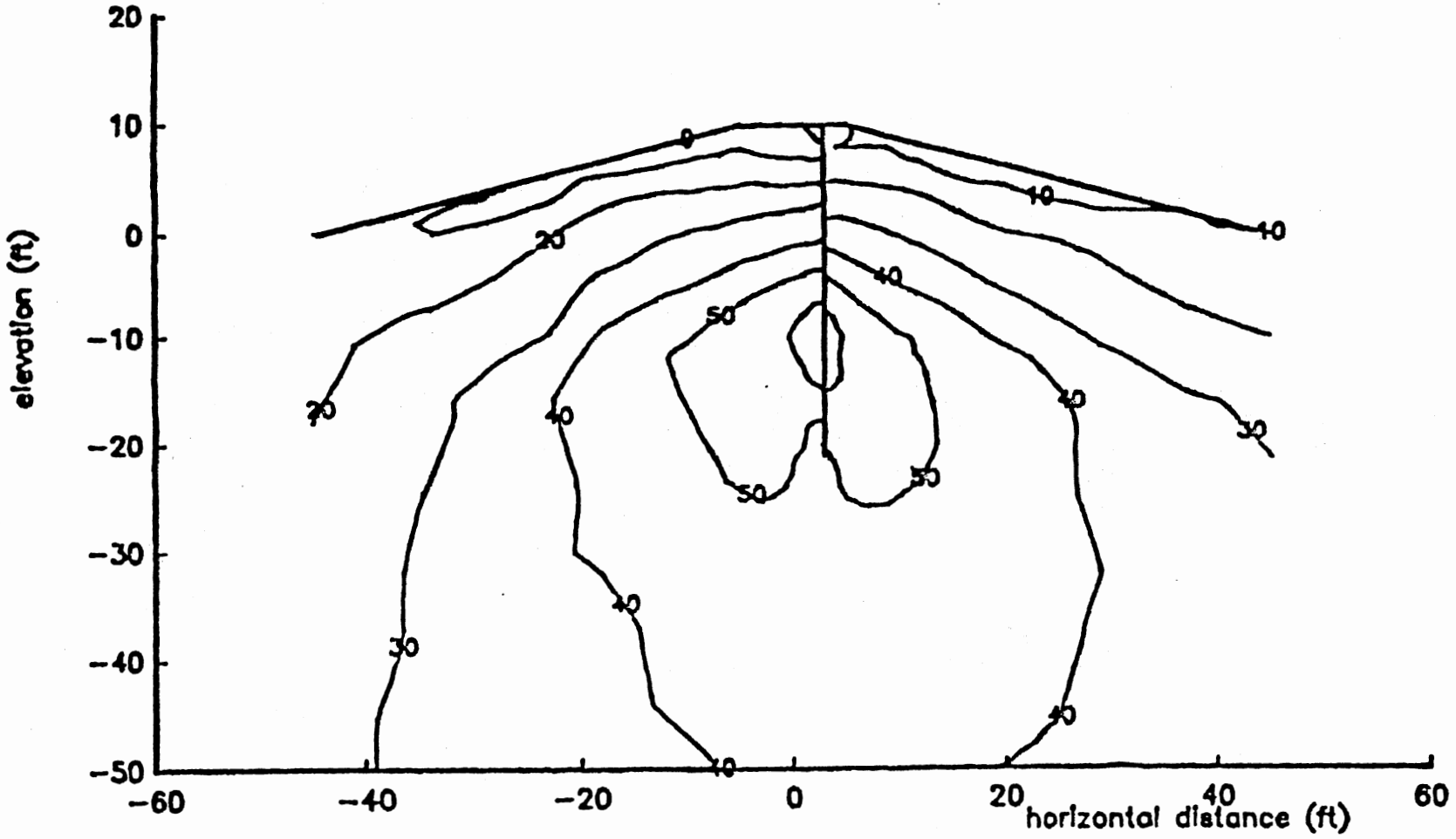

Figure 33(d). f Contours at 8 ft head, high strength profile, 30 ft pile penetration.

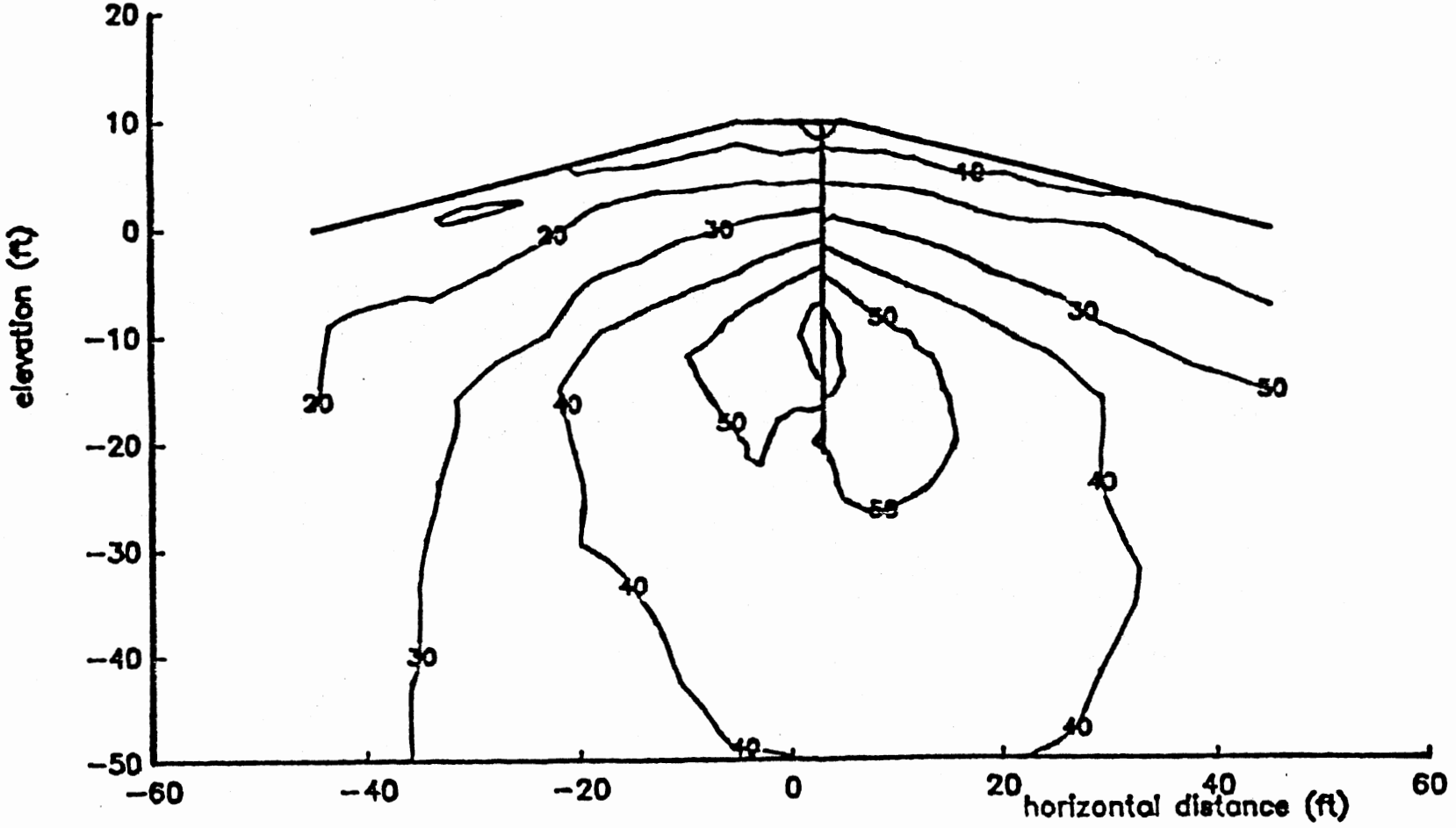

Figure 33(e). f contours at 10 ft head, high strength profile, 30 ft pile penetration.

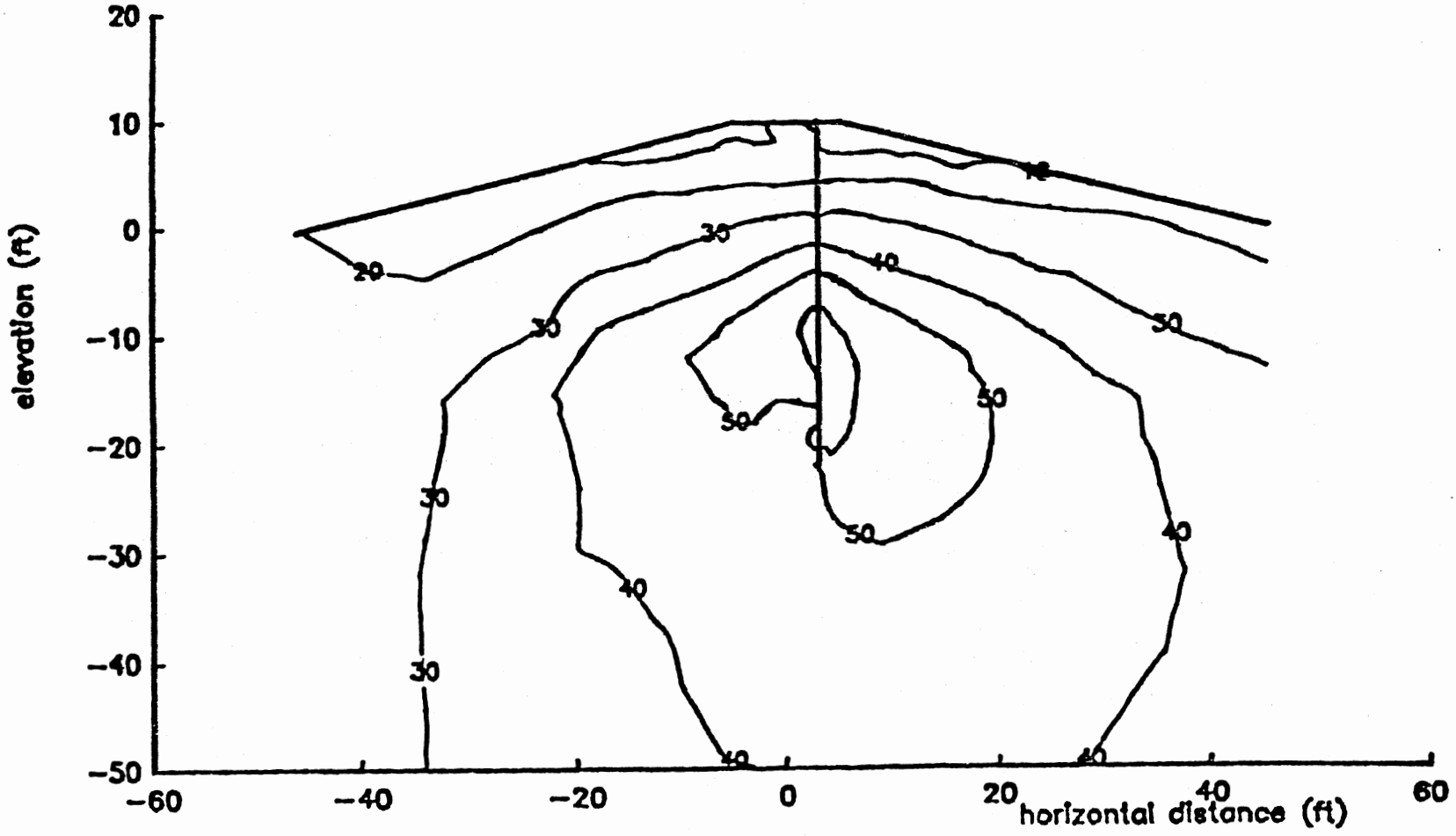

Figure 33(f). f contours at 12 ft head, high strength profile, 30 ft pile penetration.

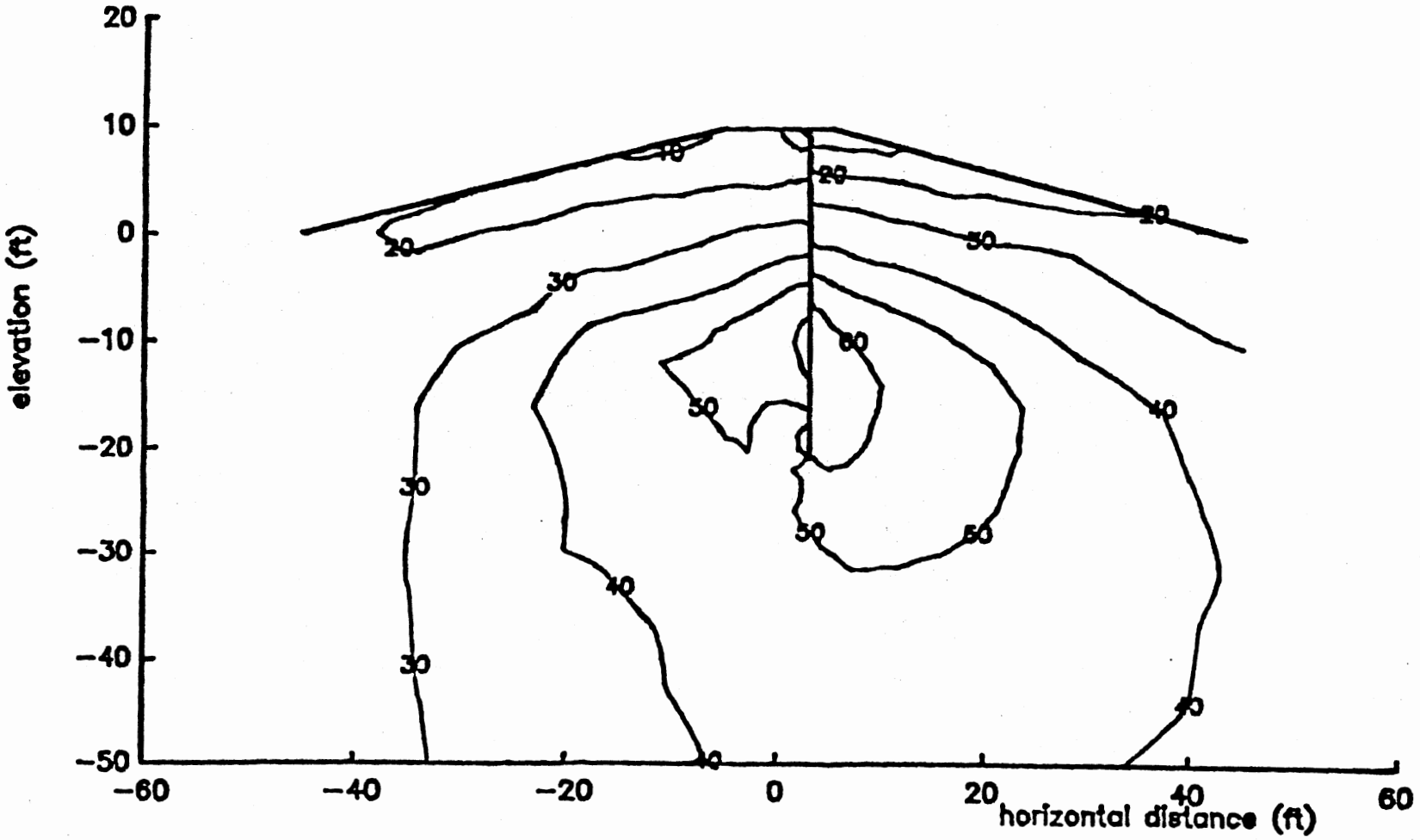

Figure 33(g). f contours at 14 ft head, high strength profile, 30 ft pile penetration.

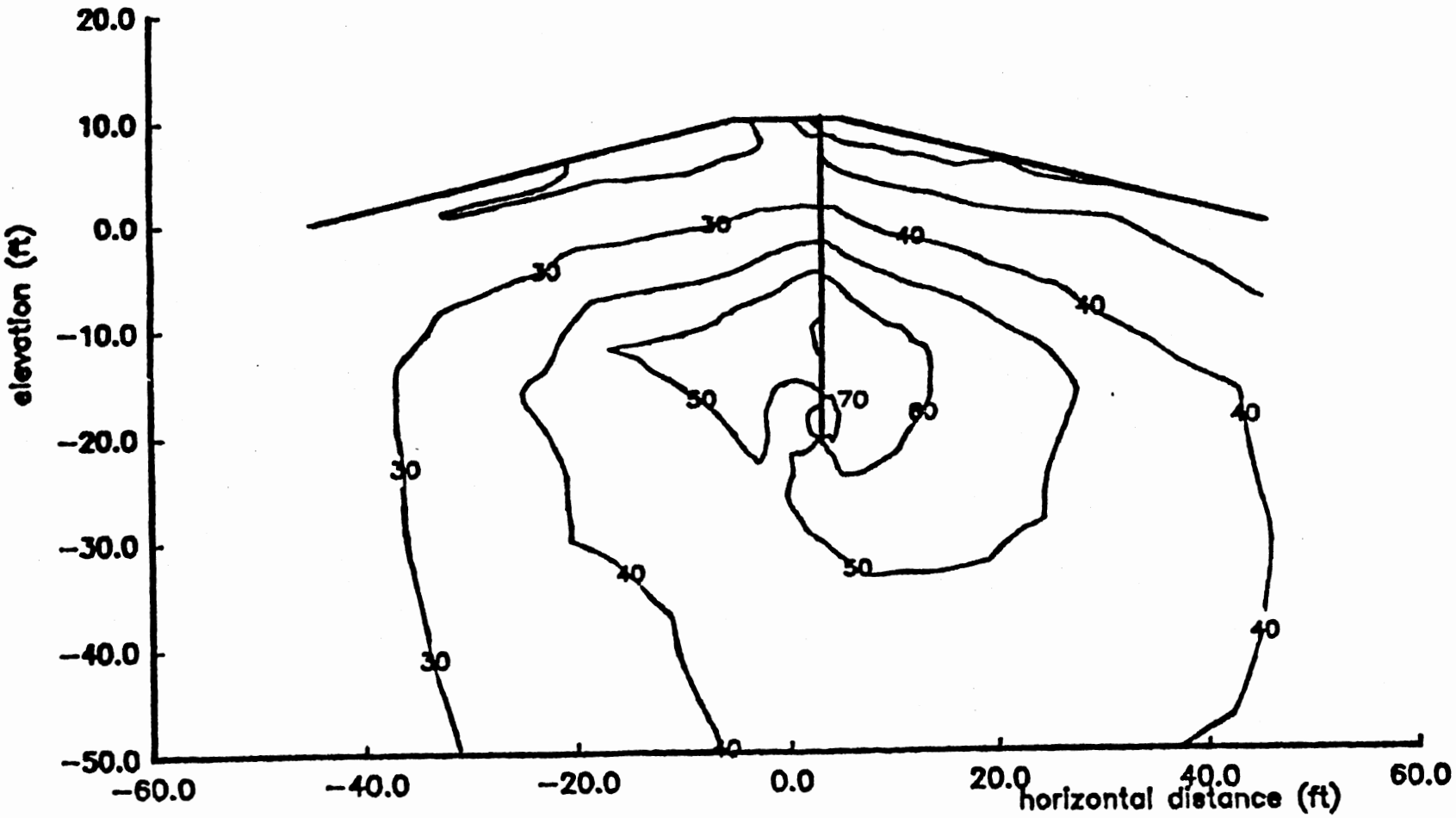

Figure 33(h). f contours at 16 ft head, high strength profile, 30 ft pile penetration.

Moment Diagrams

The moment diagrams at 14, 15, and 16 ft water heads for the 10, 20, and 30 ft pile penetrations are shown in figures 34a, 34b, and 34c, respectively. For the 10-ft case, only negative moments develop in the pile with the maximum at 9-ft elevation as shown in figure 34a. For the 20-ft and 30-ft cases the maximum negative moment magnitude and location remain the same. However, there is a positive moment distribution in the pile because the pile penetrated the soft layer that was excessively sheared. Also the upper portion of the pile, above the weak layer, rotated with the levee in a clockwise direction. The shearing of the soft layer and the tilting of the soil and the pile above this layer are due to the water load imposed on the levee slopes.

For the 20-ft case, the maximum positive moment for 14-ft water head is almost three times larger than the negative moment and it is located at -2 ft elevation. As the water head increases, the point of inflection (point of transition between positive and negative moments) shifts downward. Also, the magnitude of the maximum positive moment decreases slightly, and its location shifts down. At 16-ft water head, the location of the maximum positive moment is at -4 ft elevation and the magnitudes of maximum positive and negative moments are almost equal. The moment distribution near the tip of the pile shows a change in curvature; an indication for the development of the passive region in front of the pile at that level.

The 30-ft case shows similar effects to the 20-ft case. However, at 14-ft water head the magnitude of the maximum positive moment is almost seven times larger than the maximum negative moment and it is located at -5 ft elevation. In contrast to the 20-ft case, the

magnitude of the maximum positive moment increases slightly as the water head increases. The change in moment curvature is spread over a larger area near the pile tip as compared to the 20-ft case, hence, a larger passive region develops in front of the pile at that level.

The moment distribution along the pile reveals two effects: (1) the positive moments in the pile are introduced by the levee loads; since these loads are responsible for the rotation of the medium and the shearing of the soft layer, and (2) the negative moments in the pile are introduced by the lateral loads on the pile (cantilever action). However, as seen from the moment diagrams at the early stages of loading the levee loads dominate the behavior of the structure. As the pile started to be loaded (not to forget that the levee is still being loaded), the effect of this loading starts to become apparent over a major portion of the pile as shown in the downward shifting of the point of inflection (Figs. 34(b) and (c)).

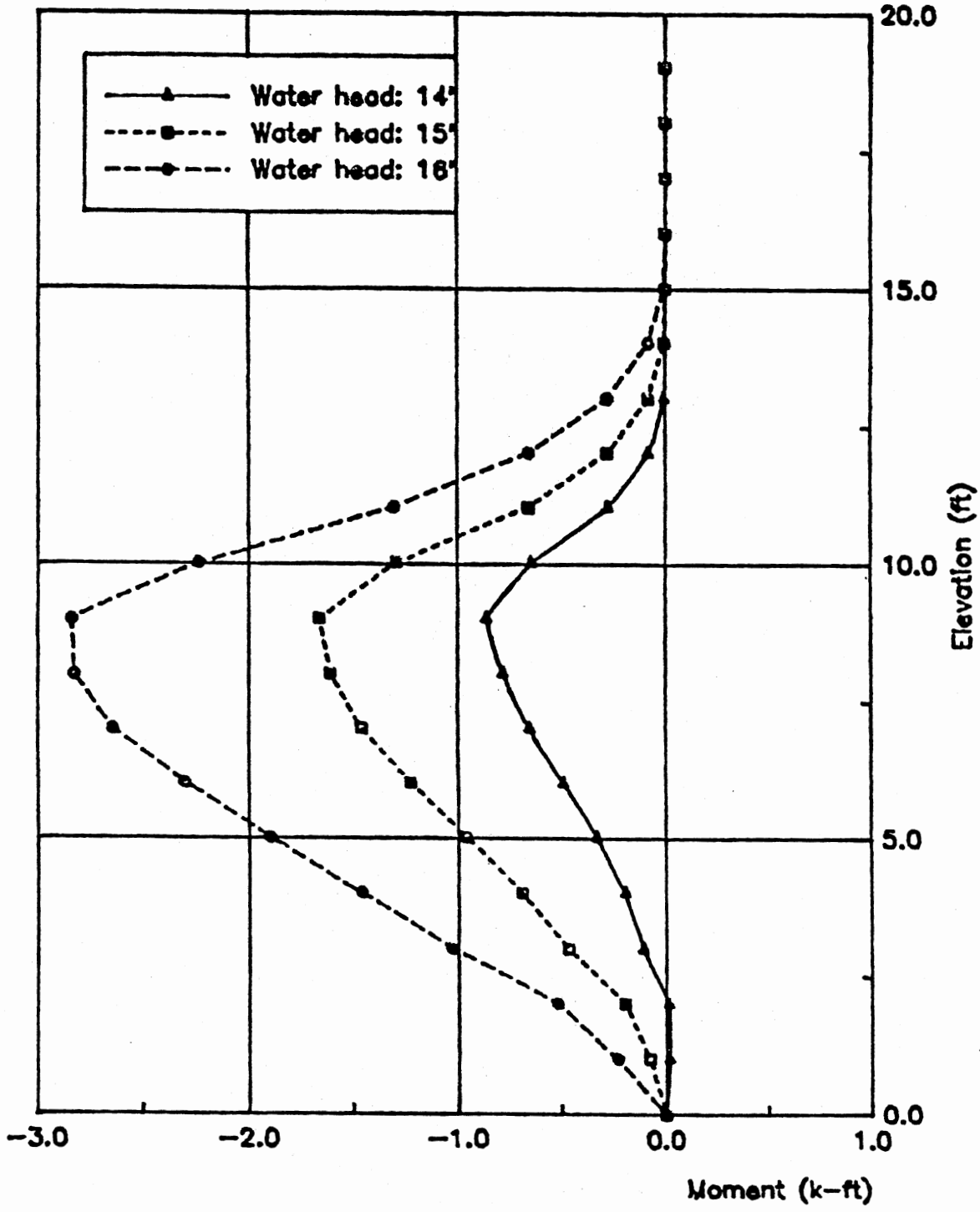

Figure 34(a). Bending moments, high strength profile, 10 ft pile penetration.

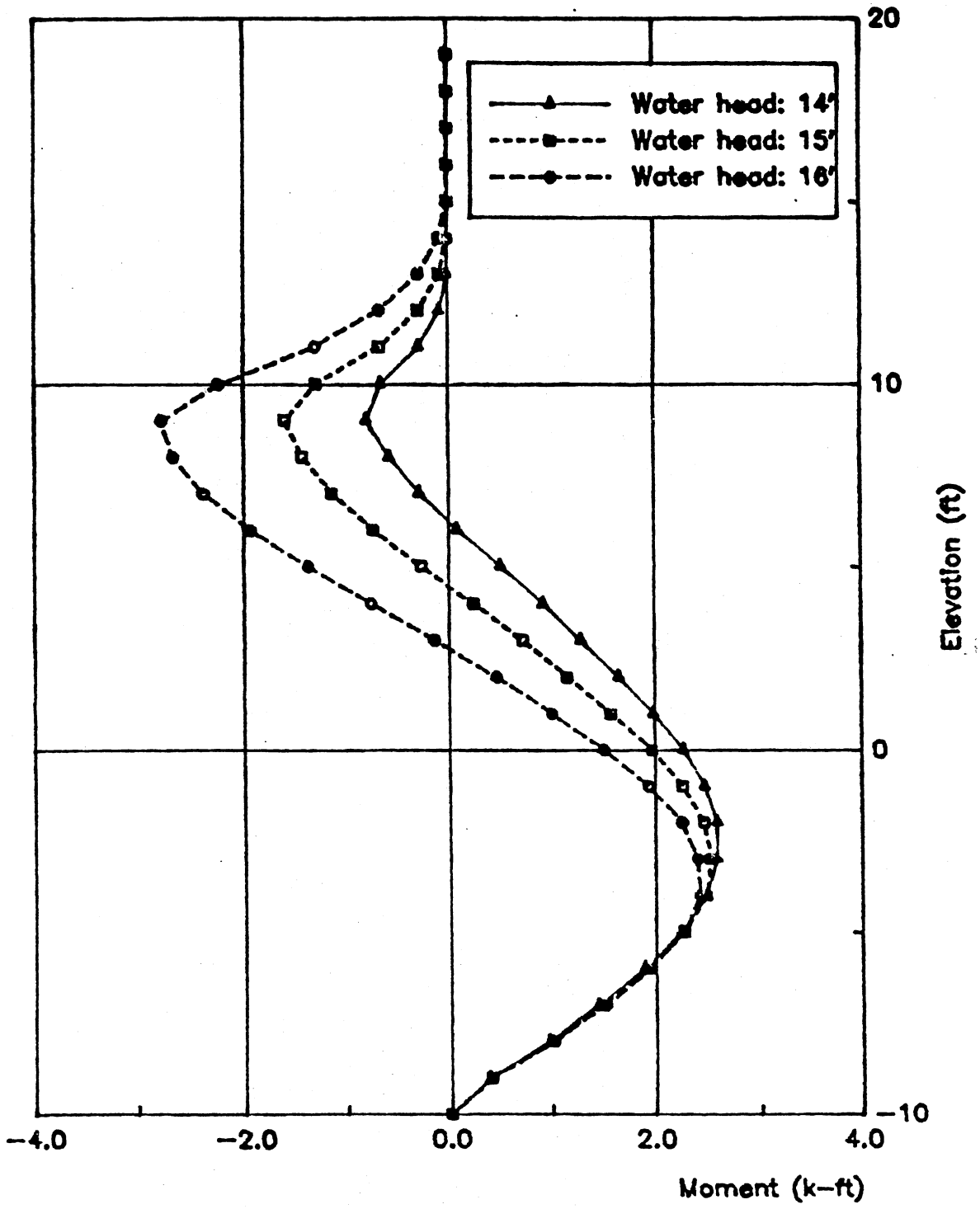

Figure 34(b). Bending moments, high strength profile, 20 ft pile penetration.

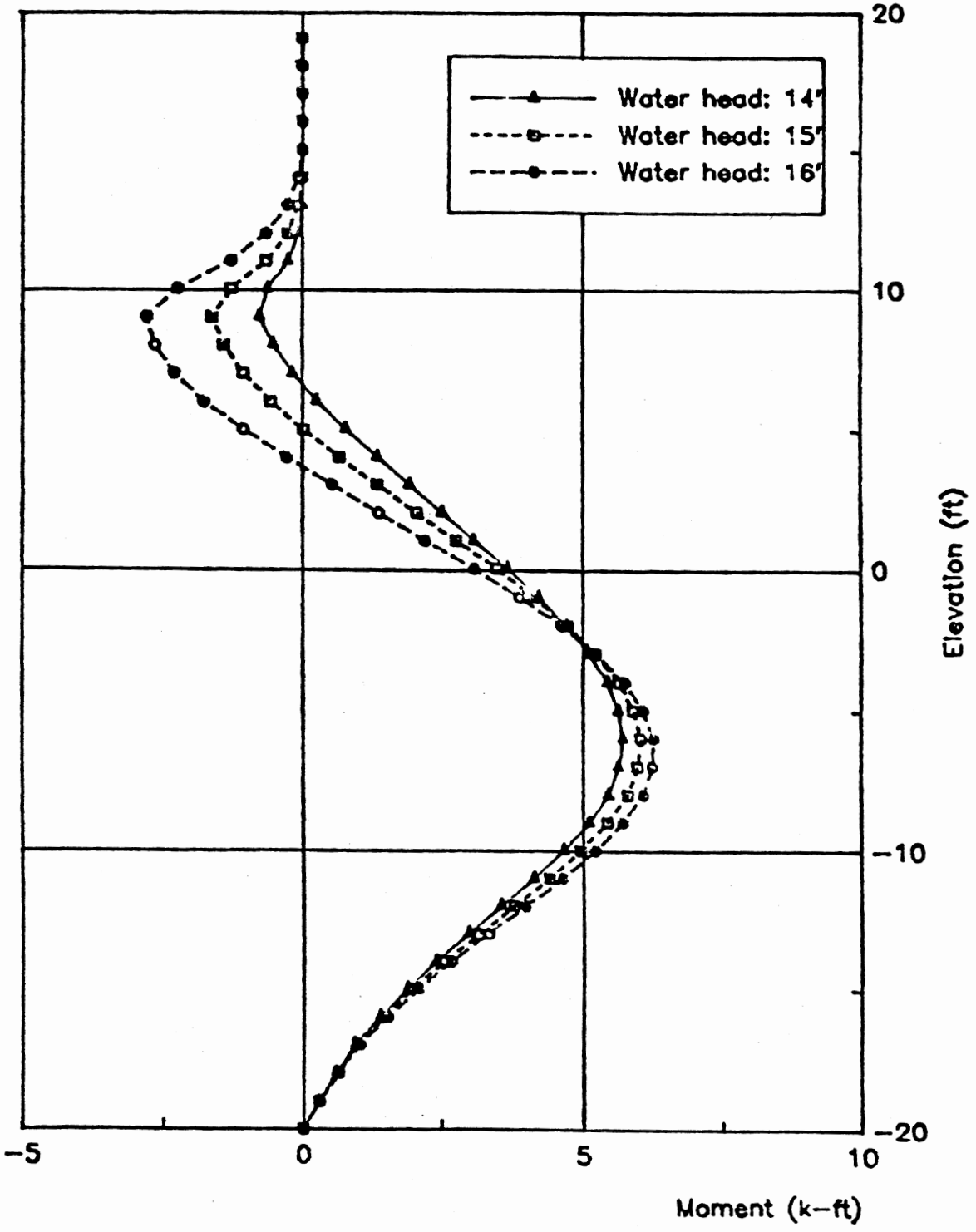

Figure 34(c). Bending moments, high strength profile, 30 ft pile penetration.

Pile Displacements

The pile displacement histories for the three penetrations (10, 20,and 30-ft) are shown in Figs 35a, 35b and 35c, respectively. These histories show similar effects; that is, at early stages of the load the pile first undergoes almost a rigid body translation and as the water head increases the rotation of the wall (clockwise) becomes more prominent. In the 10-ft case when the loads are exclusively on the levee, the pile displaces and rotates rigidly. Hence, the levee loads have no influence on the pile behavior for this penetration since the development of positive moments in the pile are due to these loads. Consequently, the pile loads dictate the behavior of the wall whereas the levee loads alter the magnitudes of the absolute displacements. In the 20-ft and 30-ft penetration cases, the pile penetrates the sheared soft soil layer and offers some resistance against the lateral movement and rotation of the soil medium above the soft layer. This is illustrated in Figs 35b and 35c by the curved lower portion of the pile. This curved region is greater in the 30-ft case since a larger portion of the pile is exposed to the soil lateral movement and rotation of the medium.

Another important observation can be obtained from the diagrams; namely that the depth of penetration has almost no influence on the absolute displacements of the system. This indicates that the pile is idle in that respect and only floats in the soil medium.

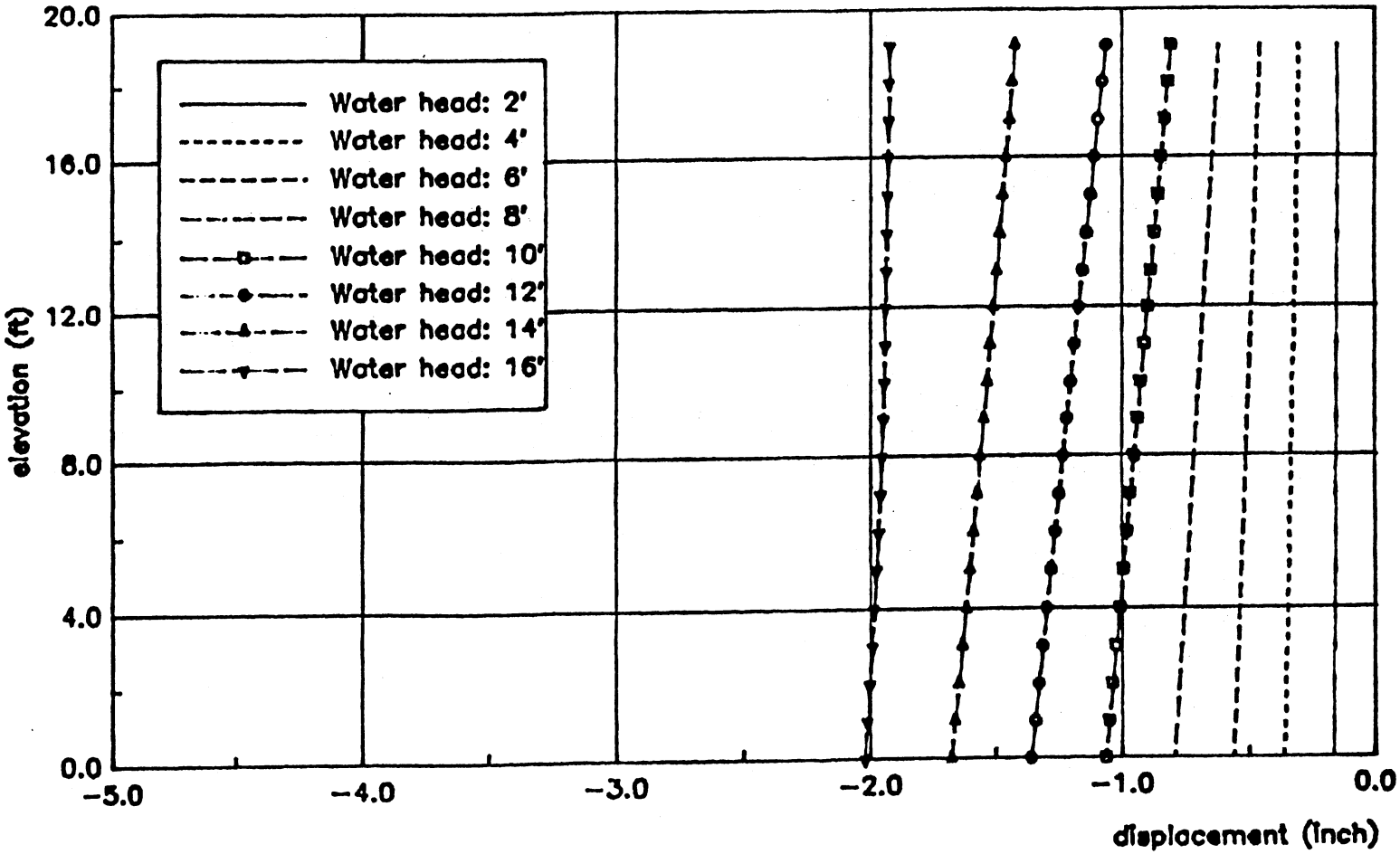

Figure 35(a). Pile deflections, high strength profile, 10 ft pile penetration.

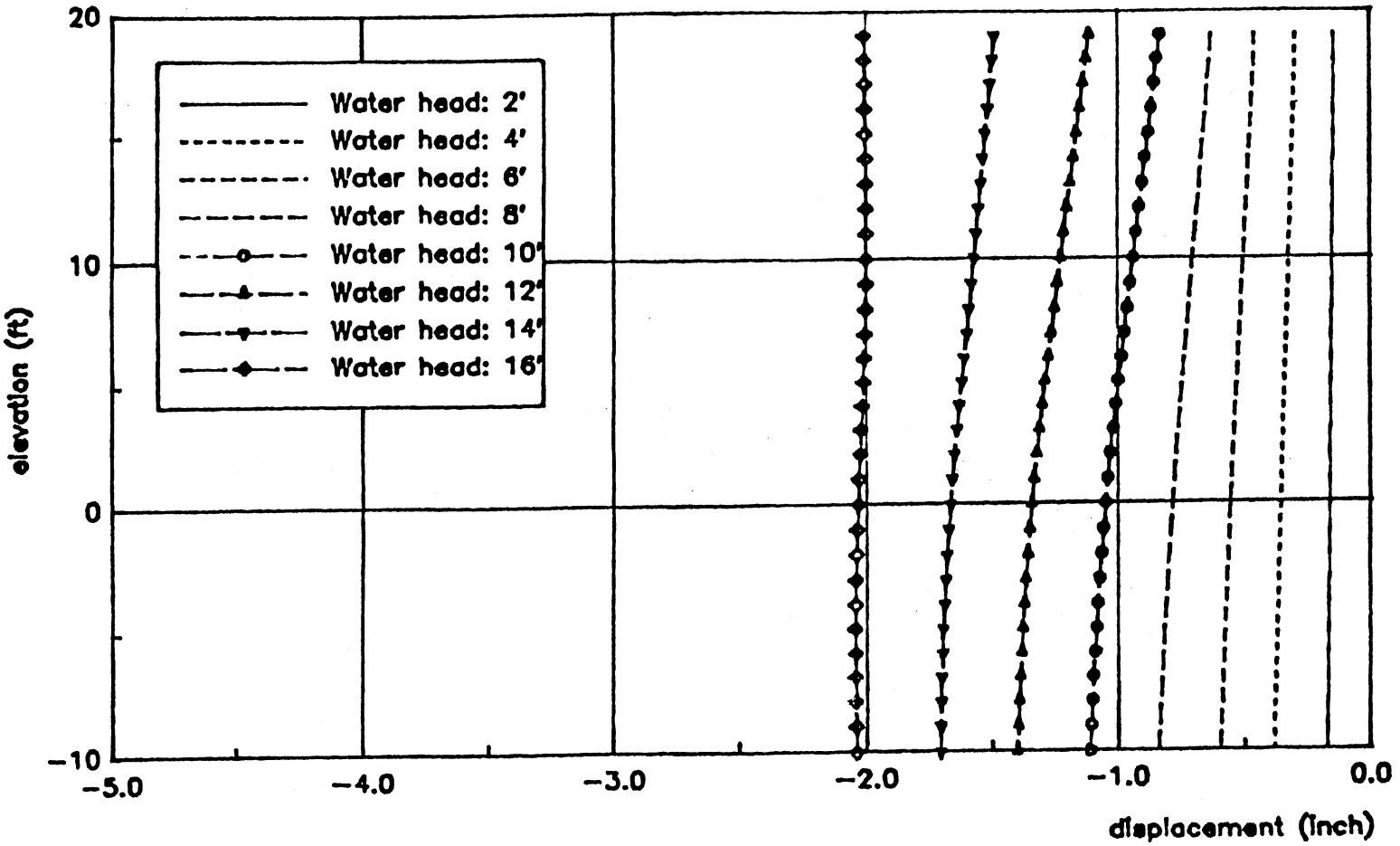

Figure 35(b). Pile deflections, high strength profile, 20 ft pile penetration.

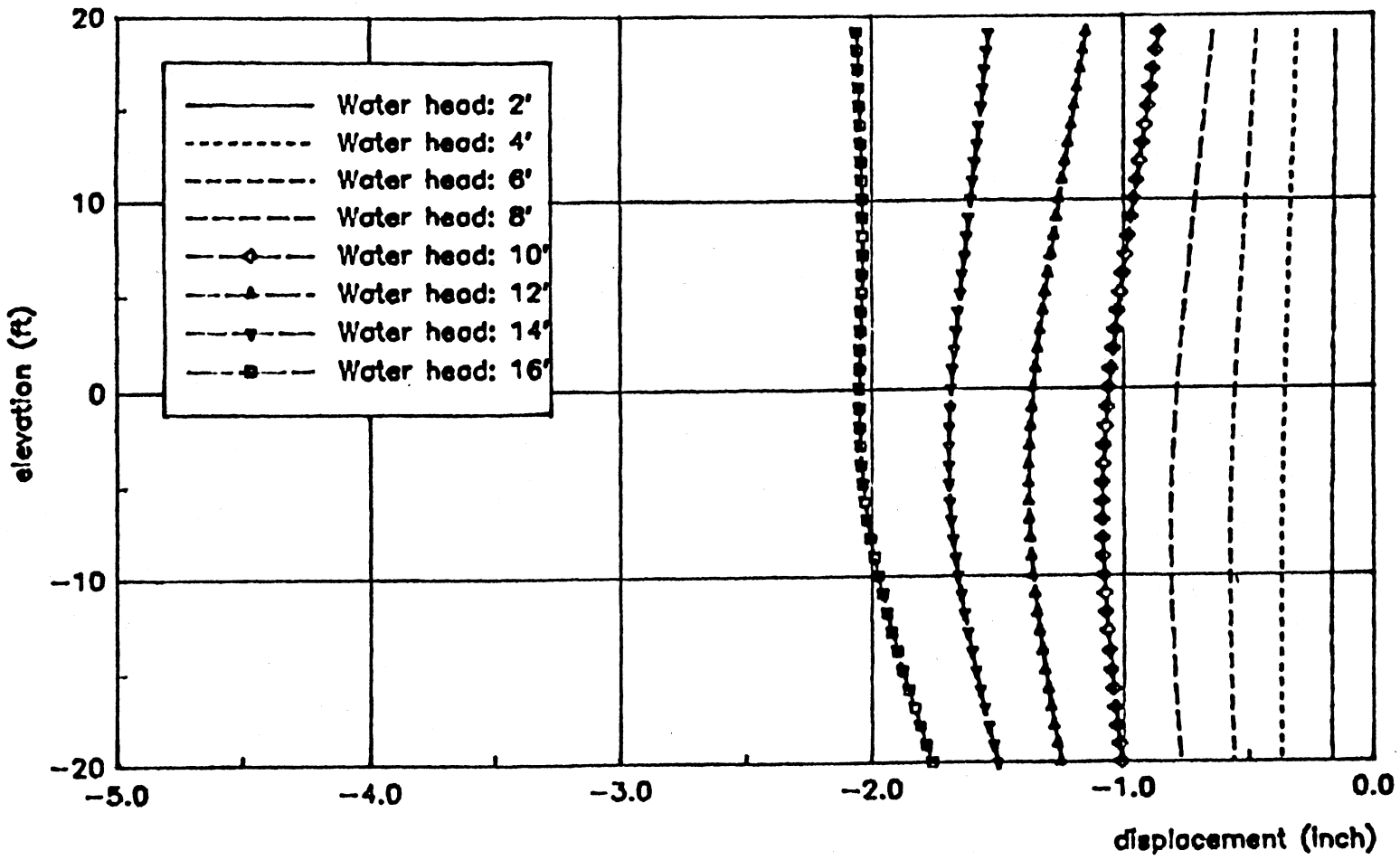

Figure 35(c). Pile deflections, high strength profile, 30 ft pile penetration.

Wall Pressure Distribution

The lateral stress distribution at 14, 15, and 16-ft water heads for the 10, 20, and 30-ft depth of penetration cases are shown in figures 36(a-c) and 37(a-c) on the front and the back side of the wall, respectively. Changes in stresses as the water head increases are more pronounced in the top levee soils. In general, there is a trend in the stress distribution profile along the depth irrespective of pile penetration.

The net pressure profiles (Figs. 38a-c) reveal some interesting points. While the 10-ft penetration case (Fig. 38a) resembles in shape and agrees in principle with the net pressure distribution assumed in classical methods, the 20-ft and 30-ft cases (Figs. 38b and c) tell a different story. The difference is not only in the pressure profile, but also in the philosophy embedded in the classical assumptions in that the soil in no way can develop a passive zone in front of the pile at greater depths. This passive zone arises because the bottom portion of the pile (near the tip) is dragging behind while the pile is attempting to resist the lateral movement of the soil above the soft layer.

The depth of penetration has an effect on the passive zone in the top levee soils in front of the pile. The greater the pile depth of penetration the larger this zone is. This is true because when longer piles deform they tend to displace more soil.

The increase in water head helps increase the passive zone in the top levee soils in front of the wall. This is more pronounced in shorter pile (Fig. 38a) where the transition from passive to active shifts down as the water head increases. However, it becomes less sensitive to the loads as the pile length increases (Figs 38b and c).

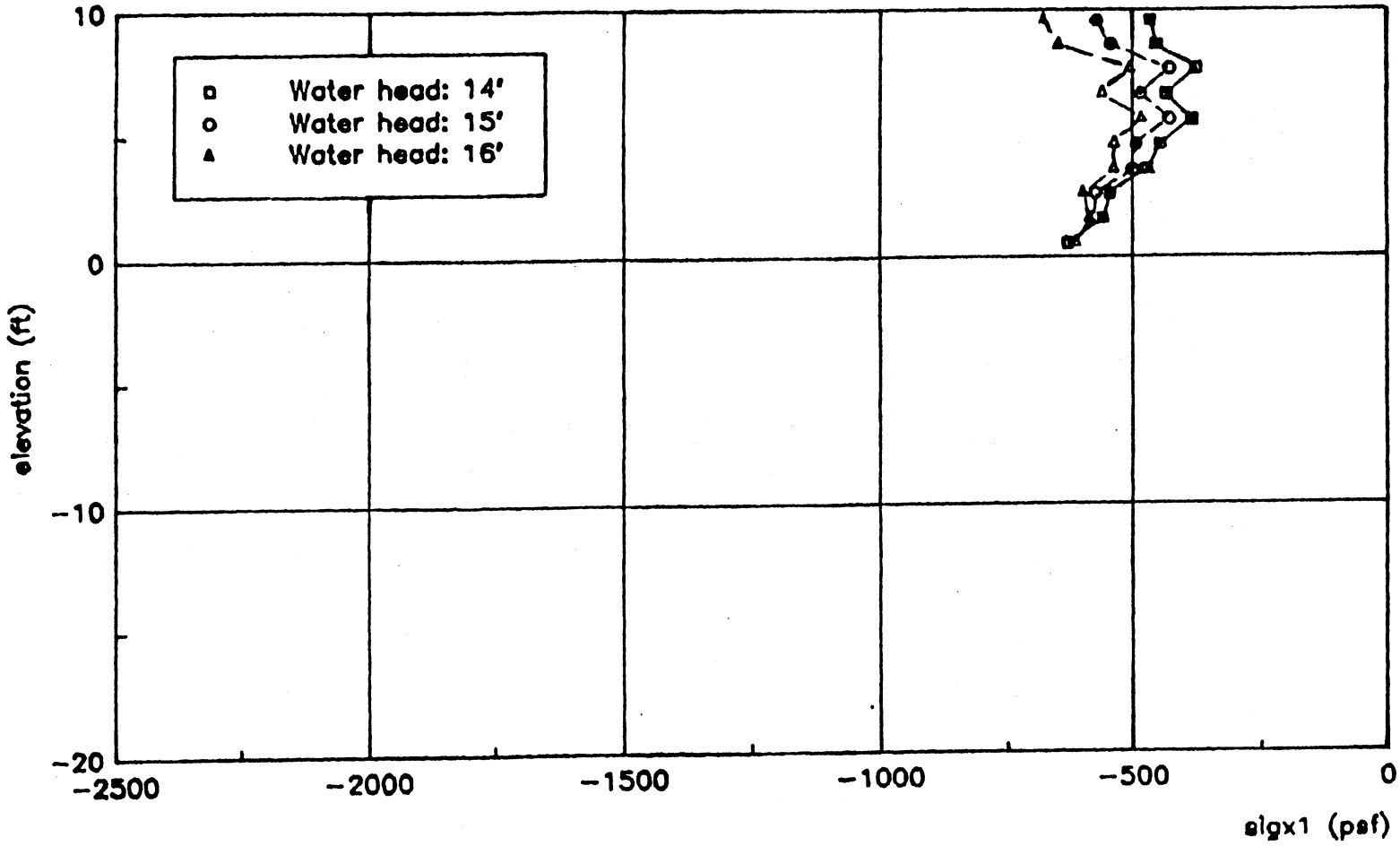

Figure 38(a). Stress profile in front of the pile, high strength profile, 10 ft pile penetration.

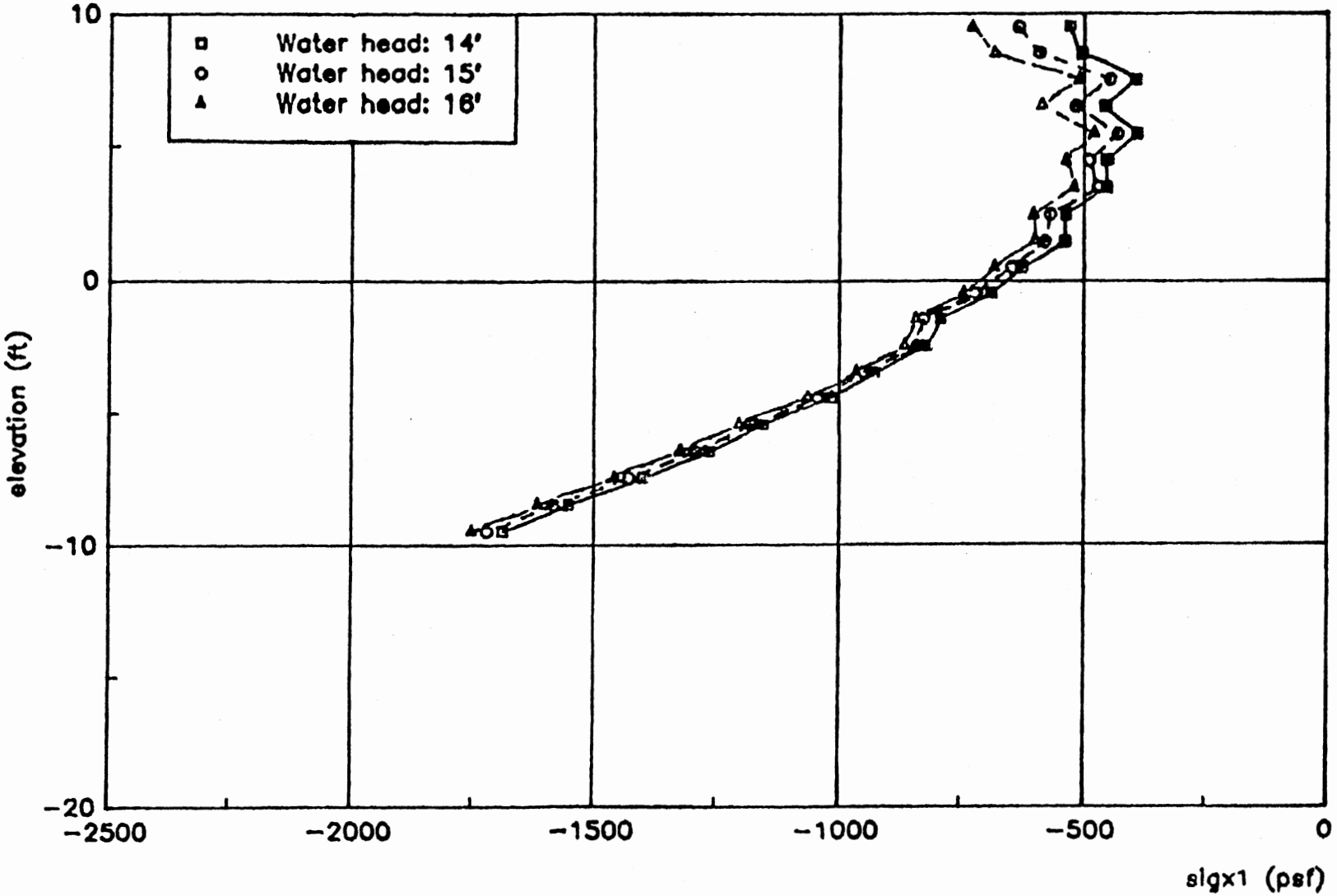

Figure 36(b). Stress profile in front of the pile, high strength profile, 20 ft pile penetration.

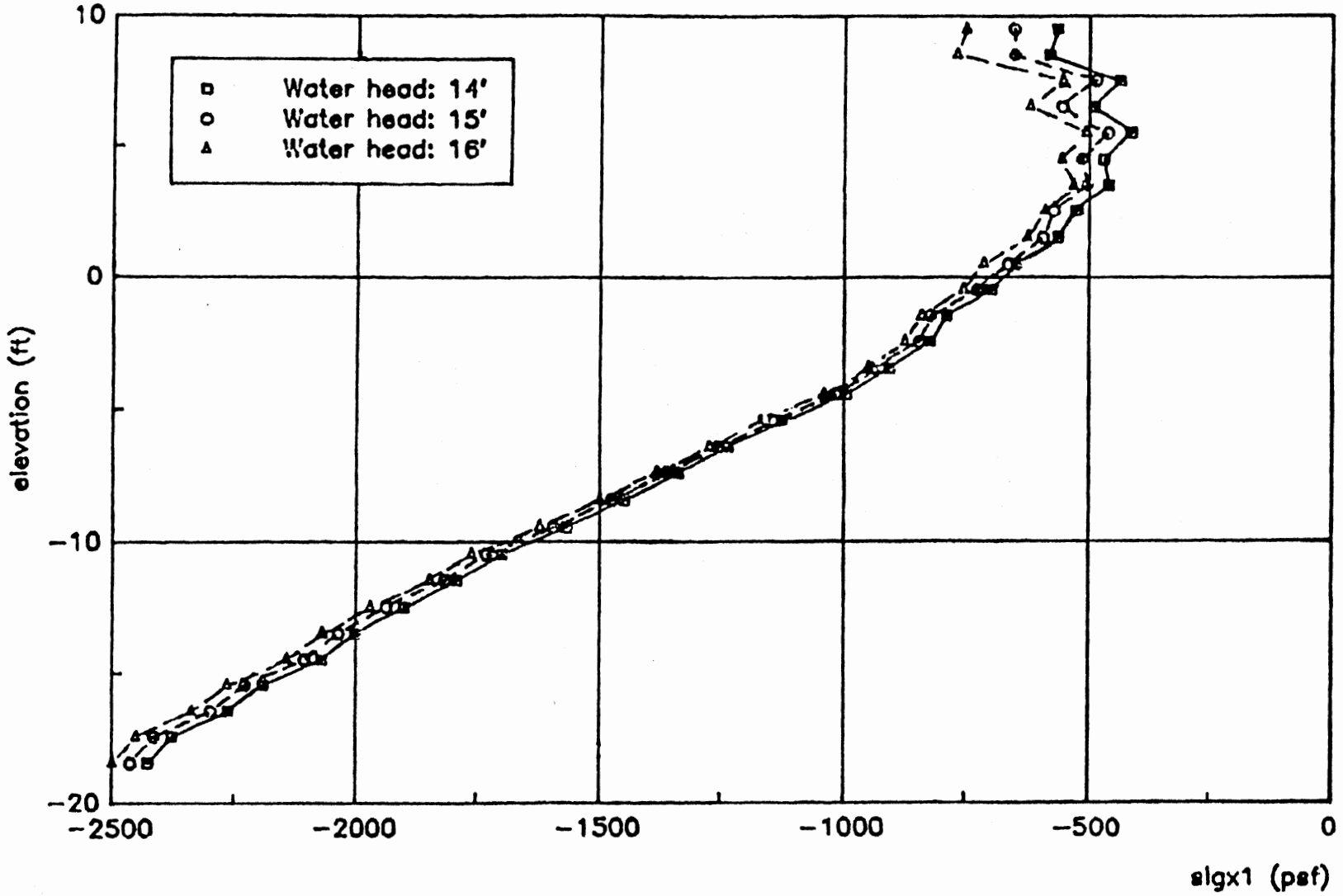

Figure 36(c). Stress profile in front of the pile, high strength profile, 30 ft pile penetration.

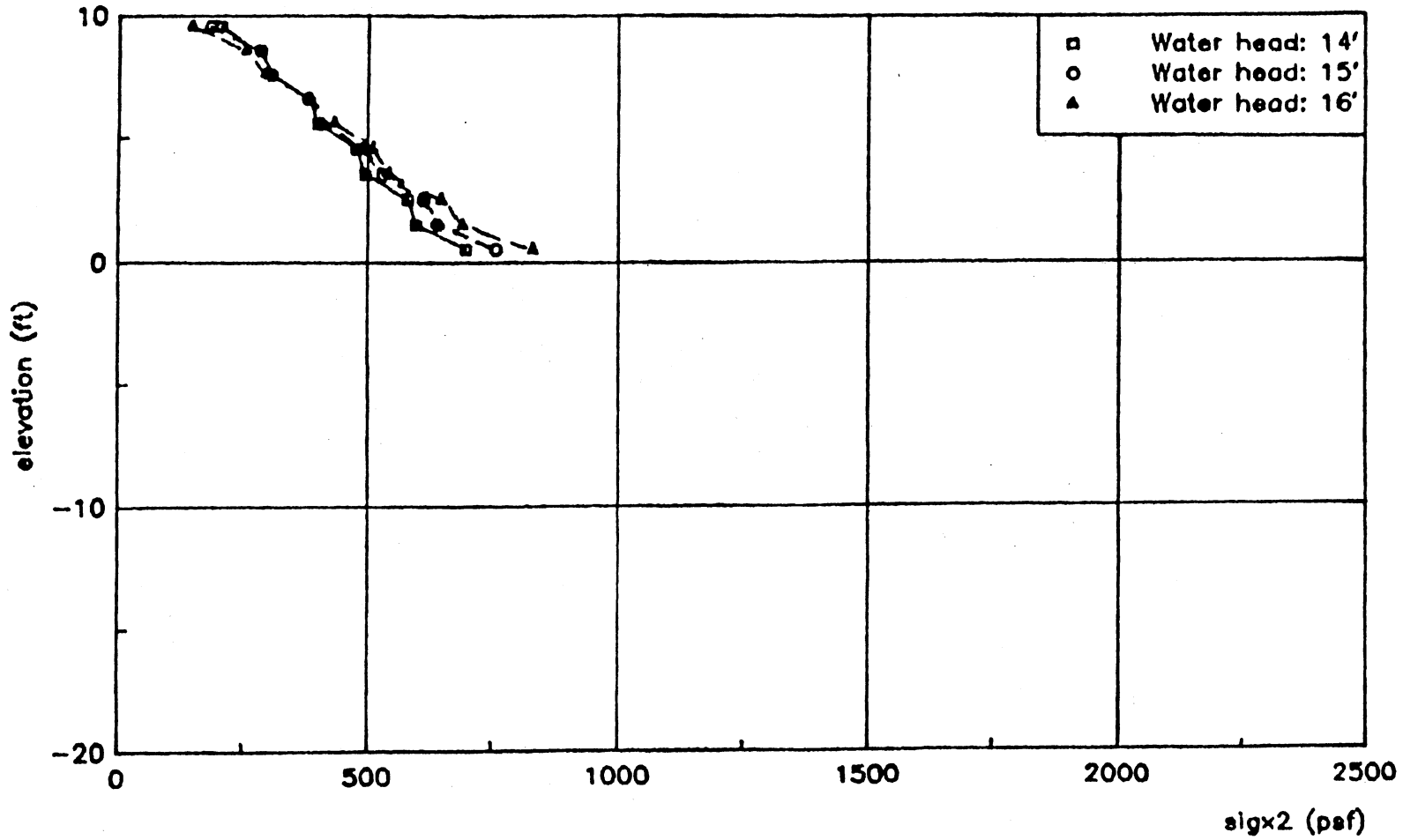

Figure 37(a). Stress profile in back of the pile, high strength profile, 10 ft pile penetration.

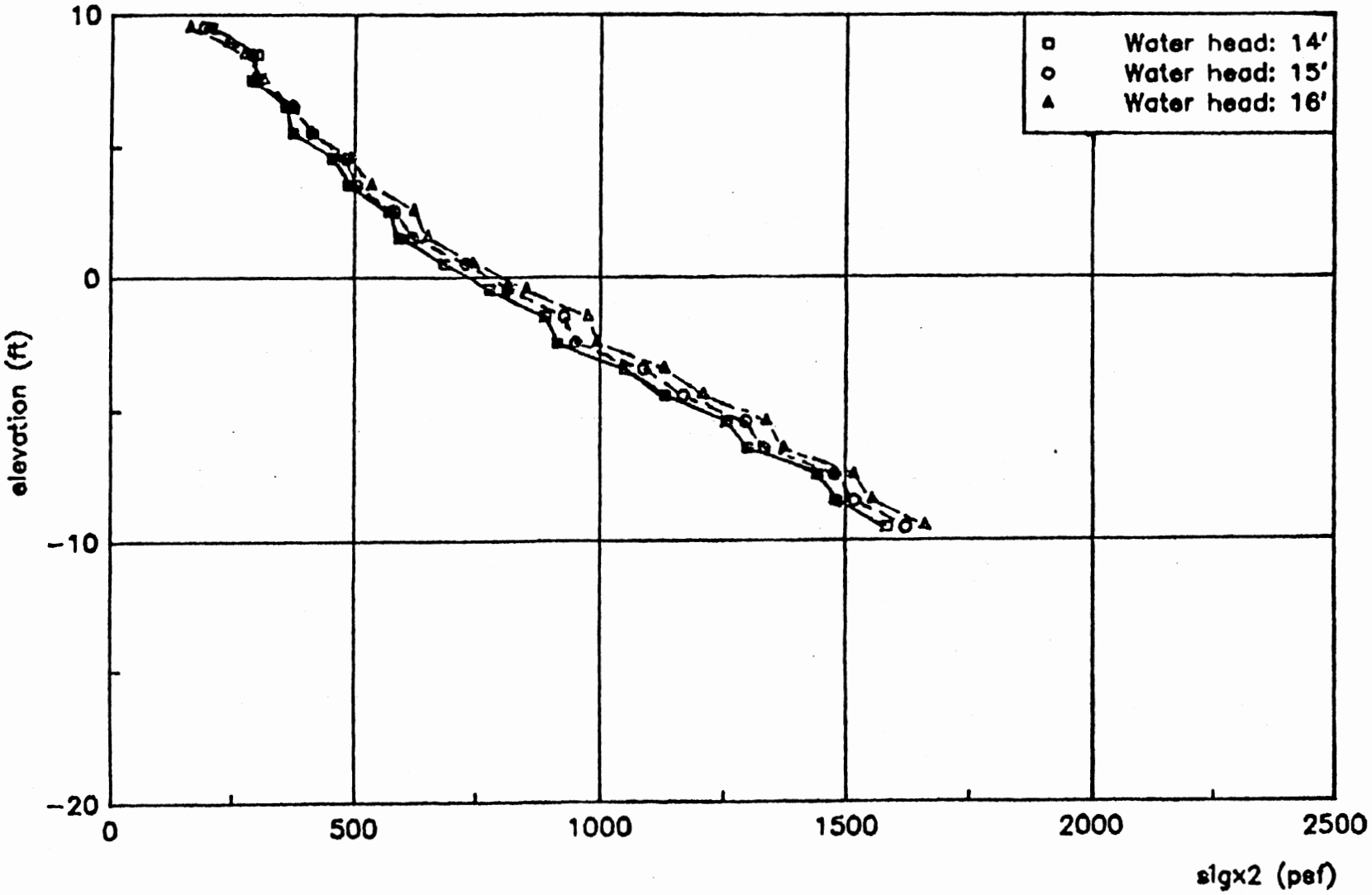

Figure 37(b). Stress profile in back of the pile, high strength profile, 20 ft pile penetration.

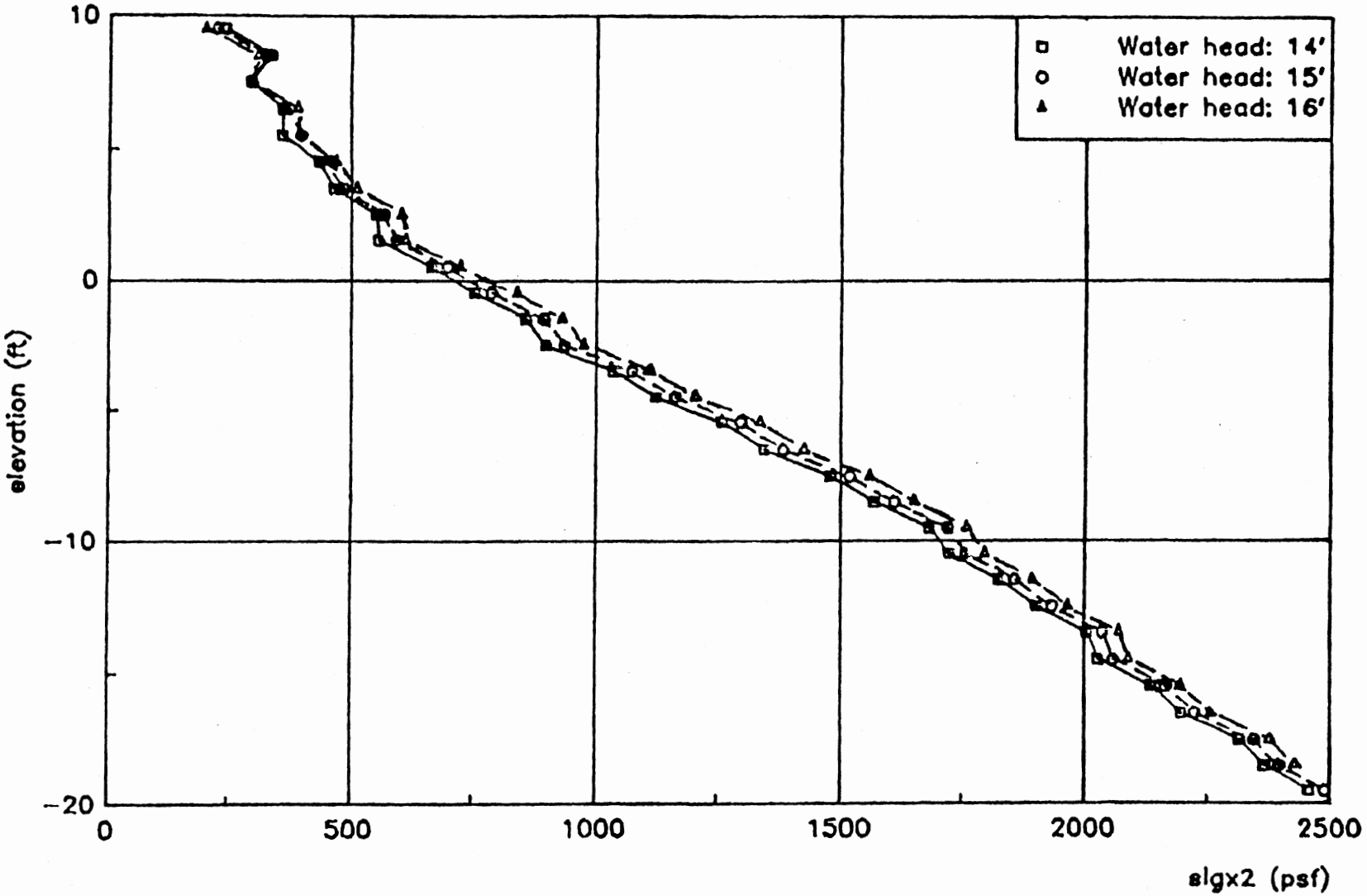

Figure 37(c). Stress profile in back of the pile, high strength profile, 30 ft pile penetration.

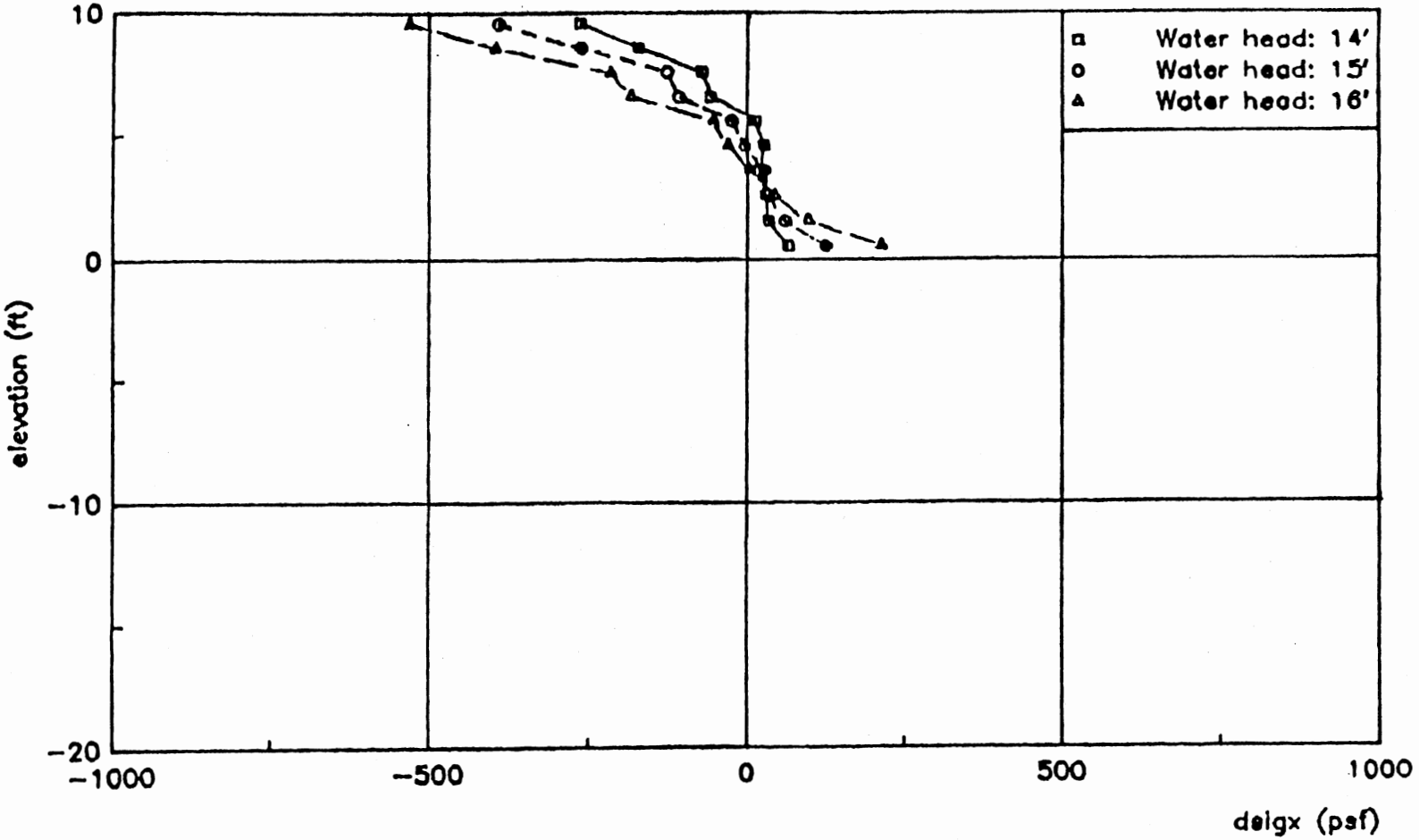

Figure 38(a). Net stress profile on the pile, high strength profile, 10 ft pile penetration.

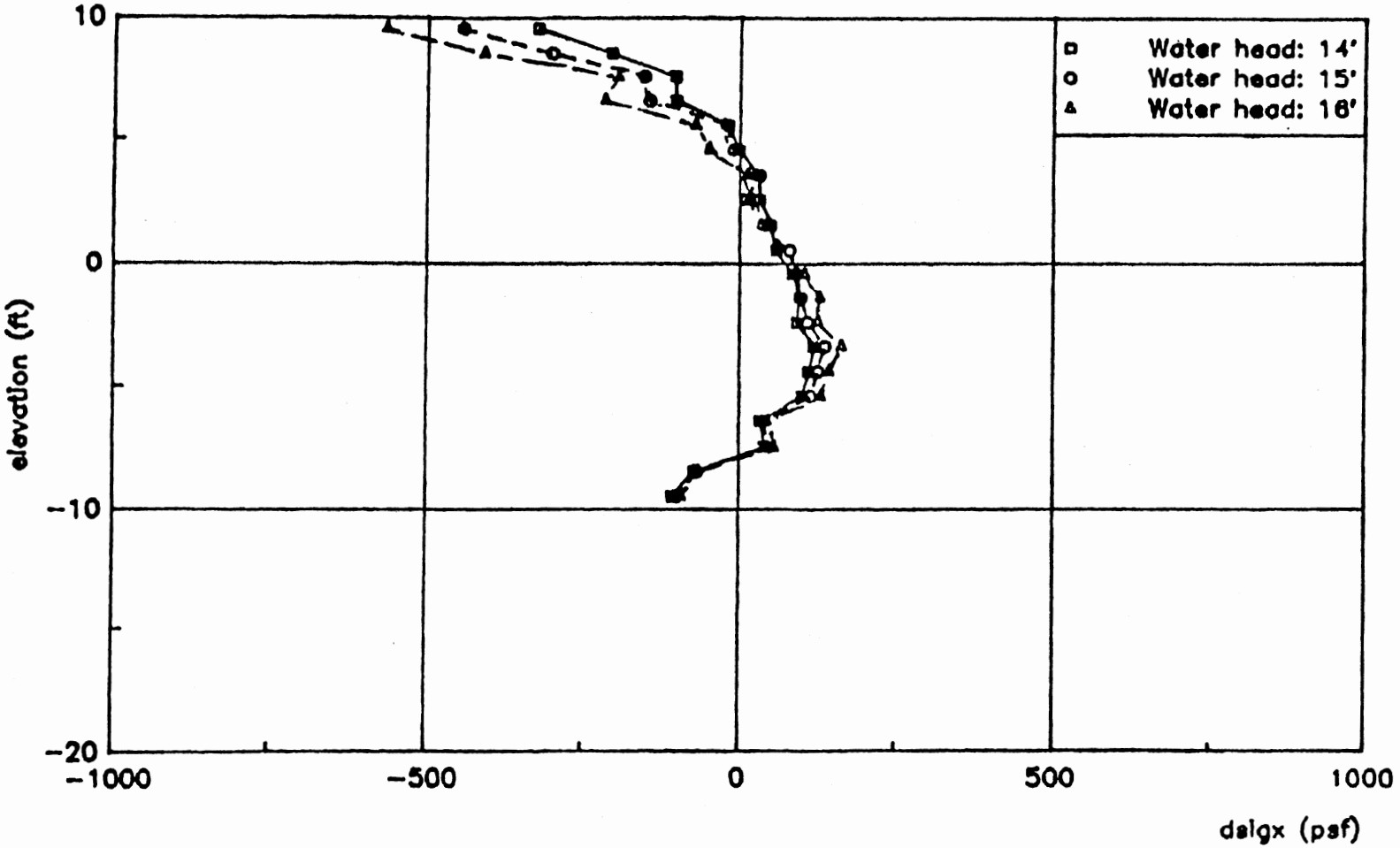

Figure 38(b). Net stress profile on the pile, high strength profile, 20 ft pile penetration.

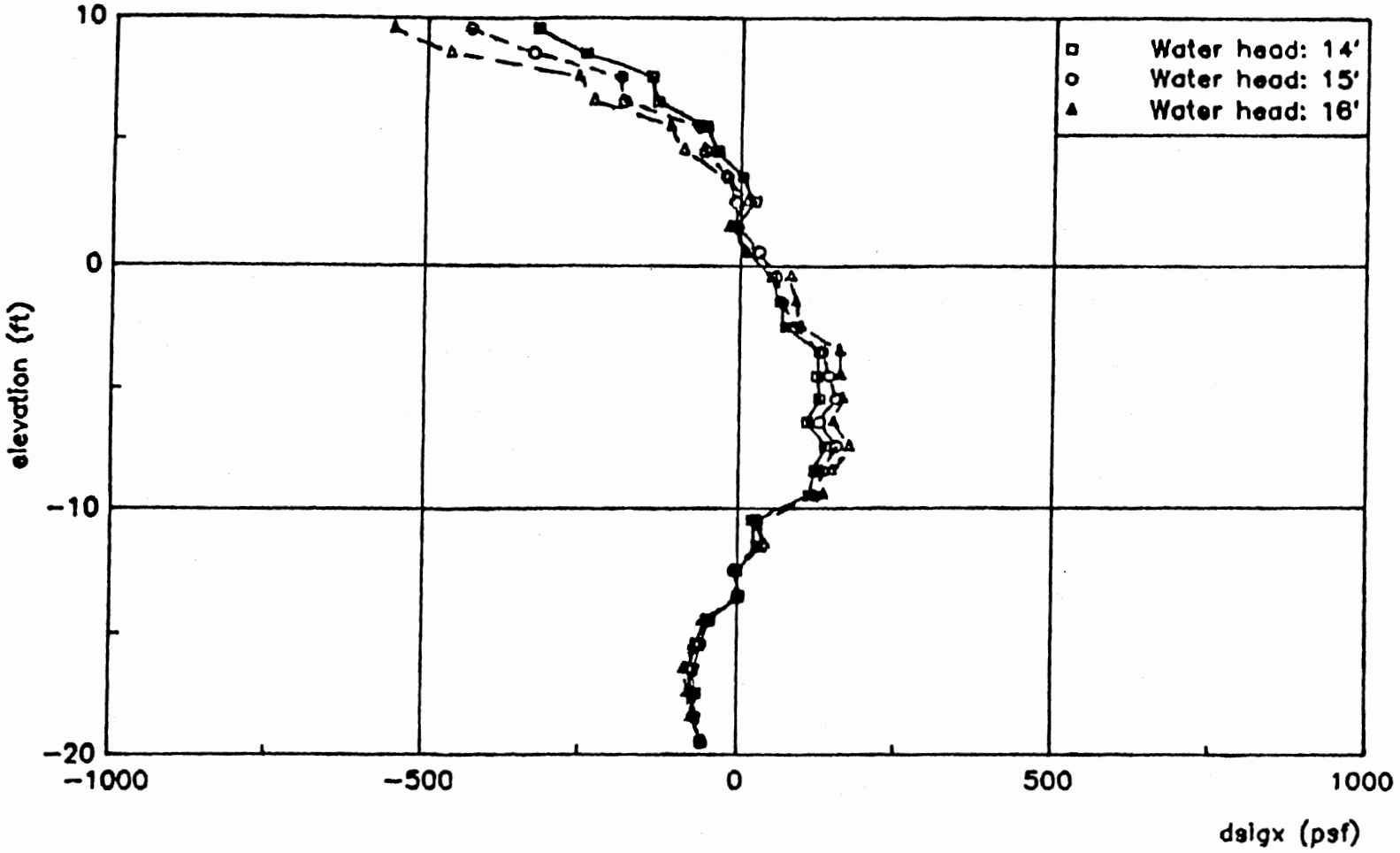

Figure 38(c). Net stress profile on the pile, high strength profile, 30 ft pile penetration.

Soil-Response Curves

Soil-response curves have been extracted for the locations shown in figure 39. The response curves for the upper 10 ft of soil (in the levee) are discussed in the following paragraph. This will make the comparison available for all depth of penetrations (10, 20, and 30 ft). However, soil-response curves at other locations are documented in Appendix C.

Figures 40a, b, and c show the soil response curves for the soils in front of the pile at 9-ft elevation for 10, 20, and 30-ft pile penetrations, respectively. At later stages of the loading, that is when the pile is directly loaded, all the diagrams show the state of stress is heading toward the passive envelope. It should be noted that at higher penetrations, the state of stress increases slightly. This action occurs because the displacements in the upper portion of the pile increase slightly as the depth of penetration increases (Figs. 35a-c). Figures 40d, e, and f show the soil-response curves at the back of the pile at the same elevation (9-ft). Similar behavior is obtained for the three penetrations. There is a slight increase in stress as the pile is being loaded at the early stages. This increase can be explained by the presence of horizontal forces on the levee slopes, but this effect later diminishes when the pile loading becomes dominant. The soil-response curves for the front soils at 5-ft elevation show that the soils are in passive state (Figs 41a, b, and c). These curves indicate a similar behavior for the three penetrations. They also show that the load on the levee and on the wall act together in loading the soil in passive direction. This is marked by the increase in slope as the load reaches the pile. For the soils at the same elevation (5 ft) but located at the

back of the wall, the soil response curves show again a similar effect for the three penetrations (Figs. 41d, e, and f). These soils are loaded toward the passive envelope due to the levee loads. When the pile is loaded in the early stages, the slope increases. However, at later heads, this slope decreases and the soils are susceptible to fail in active. This is due the increase of the passive zone in the top levee soils in front of the pile as the load on the pile increases.

At 1-ft elevation, the response curves for the 10-ft penetration differ from the 20-ft and 30-ft cases (Figs 42a, b, c, d, e, and f). This difference was explained when discussing the net soil profile development earlier. For the 10-ft case (Fig. 42a), the soils in front of the wall are loaded in passive. However, at higher water heads the curve is smoothed giving an indication that the soils are reverting toward an active state. This also indicates that the levee loads dictate the behavior in the early stages. When the pile loads become more dominant the transition to active prevails. The response curves for the soils in front of the wall for the 20-ft and 30-ft cases are similar (Figs 42b and c) and show a loading toward the passive envelope. The response curves for the soils on the back side of the wall at the same elevation (1-ft) are shown in Figs 42d, e, and f. In the 10-ft case, these soils are loaded in passive all the way. The 20-ft and 30-ft response curves are similar. When the pile is loaded, the slope of the curve decreases; an indication that the passive zone in front of the pile, or alternatively the active zone in the back, is growing as the displacing pile tends to mobilize more soils.

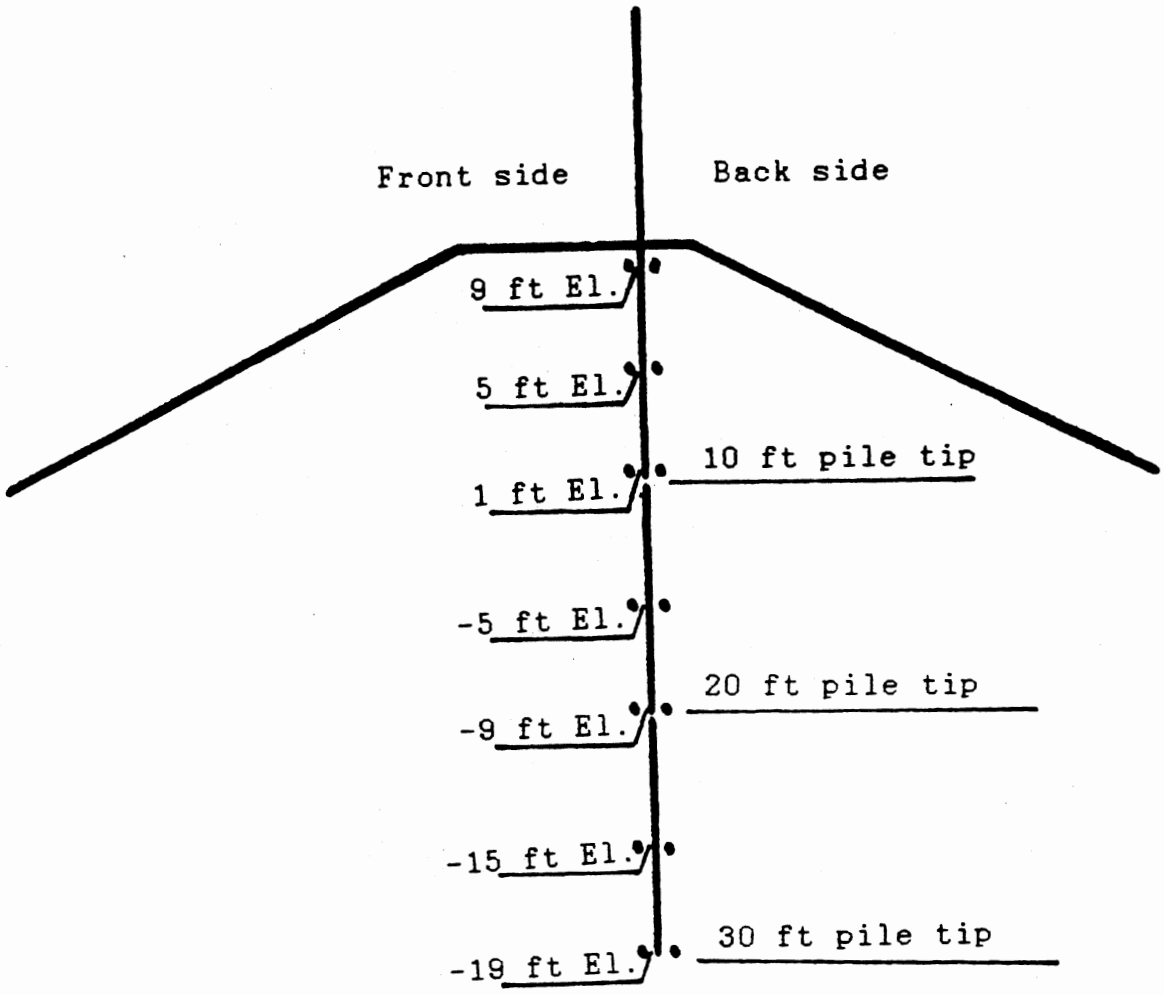

Figure 39. Locations of the extracted wall force-displacements.

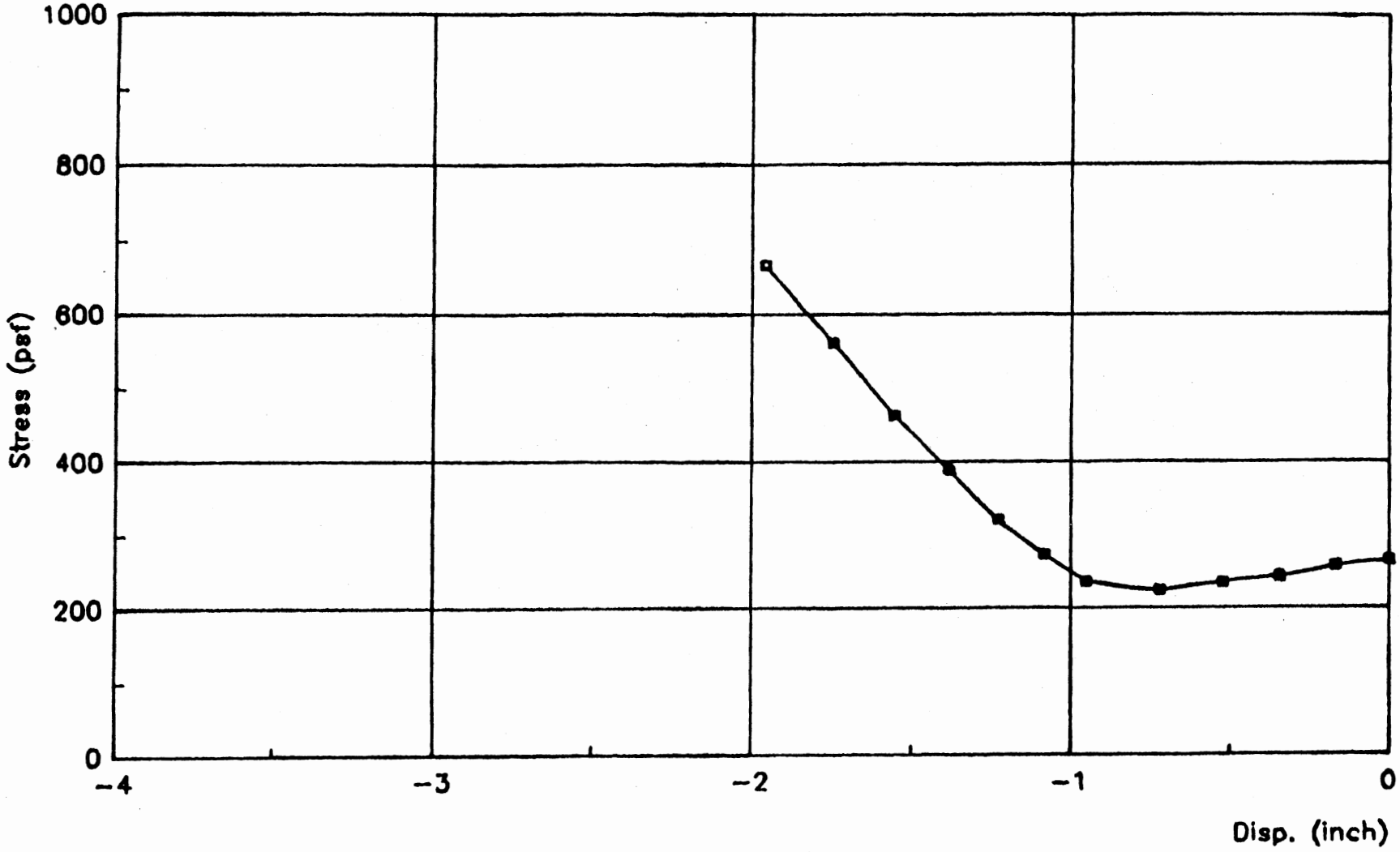

Figure 40(a). Soil-Response curve at 9 ft elevation, front side, high strength profile, 10 ft pile penetration.

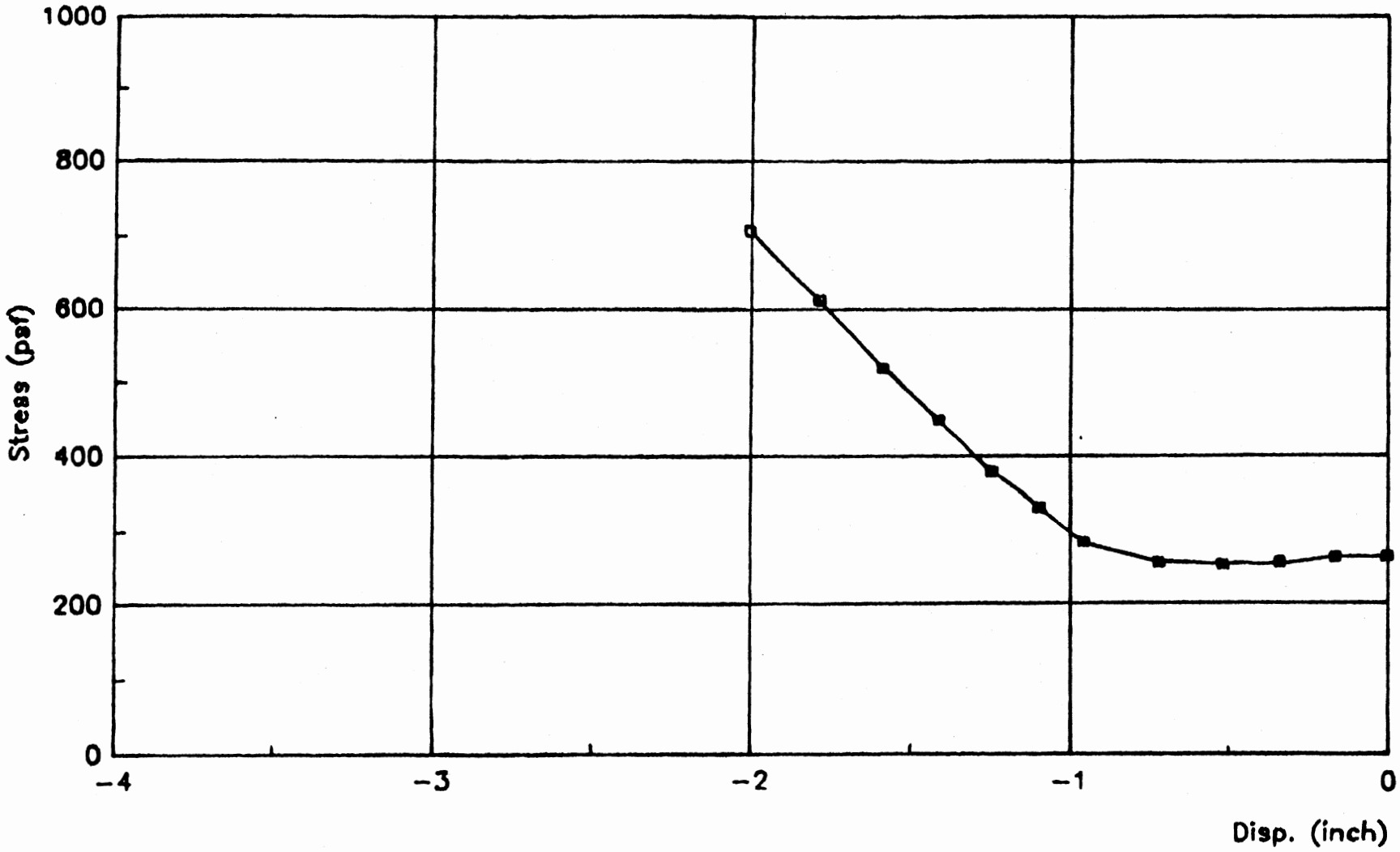

Figure 40(b). Soil-Response curve at 9 ft elevation, front side, high strength profile, 20 ft pile penetration.

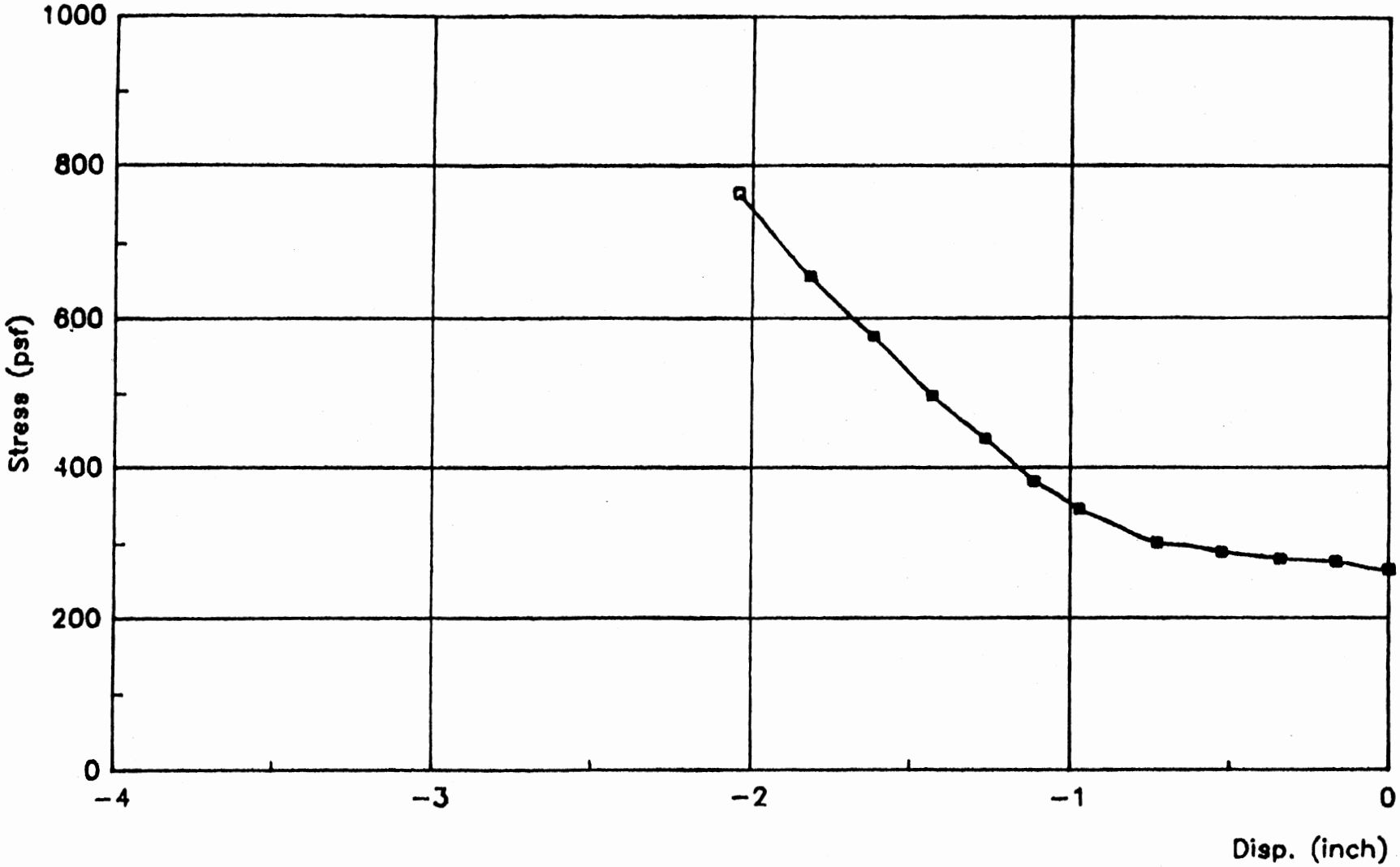

Figure 40(c). Soil-Response curve at 9 ft elevation, front side, high strength profile, 30 ft pile penetration.

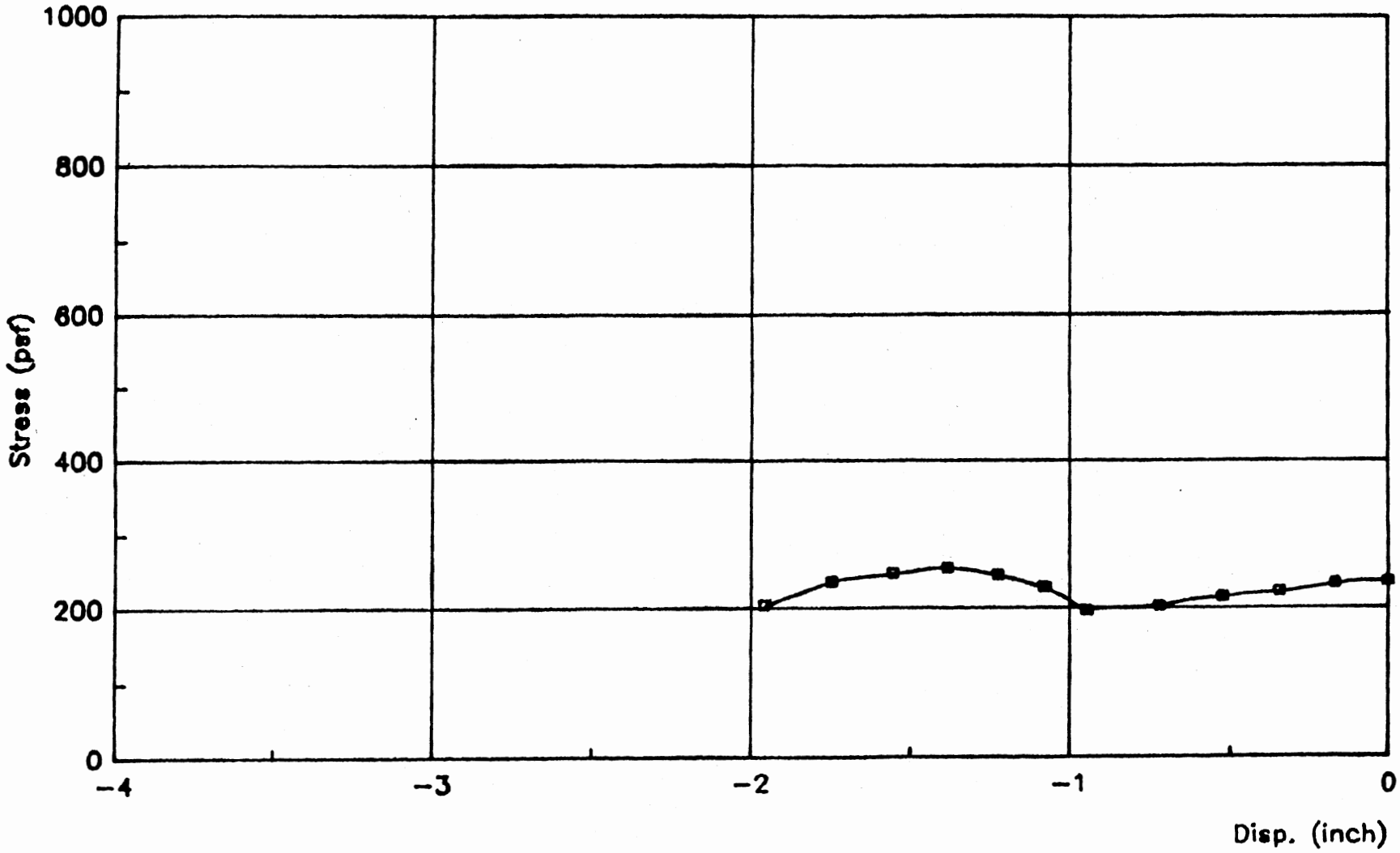

Figure 40(d). Soil-Response curve at 9 ft elevation, back side, high strength profile, 10 ft pile penetration.

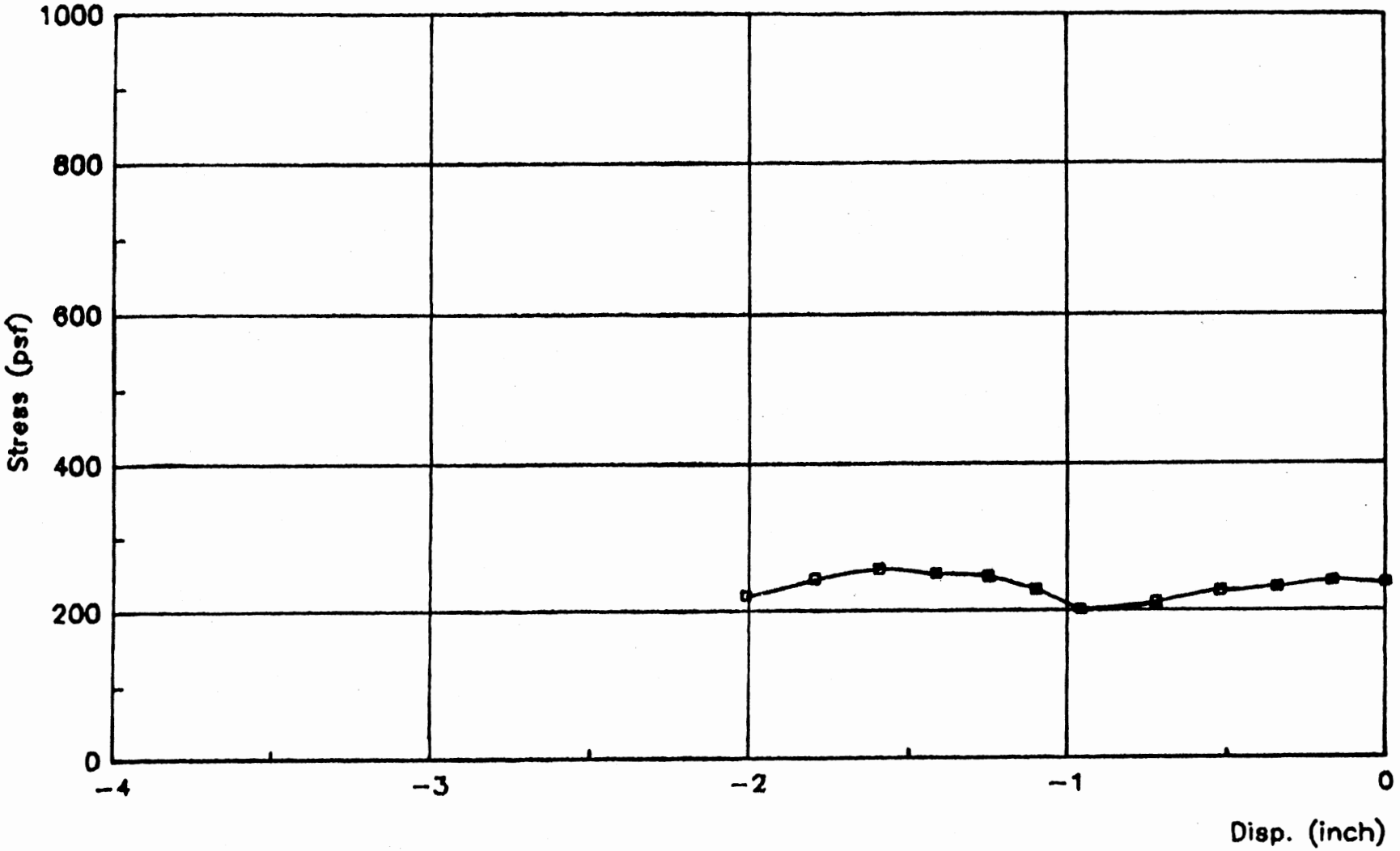

Figure 40(e). Soil-Response curve at 9 ft elevation, back side, high strength profile, 20 ft pile penetration.

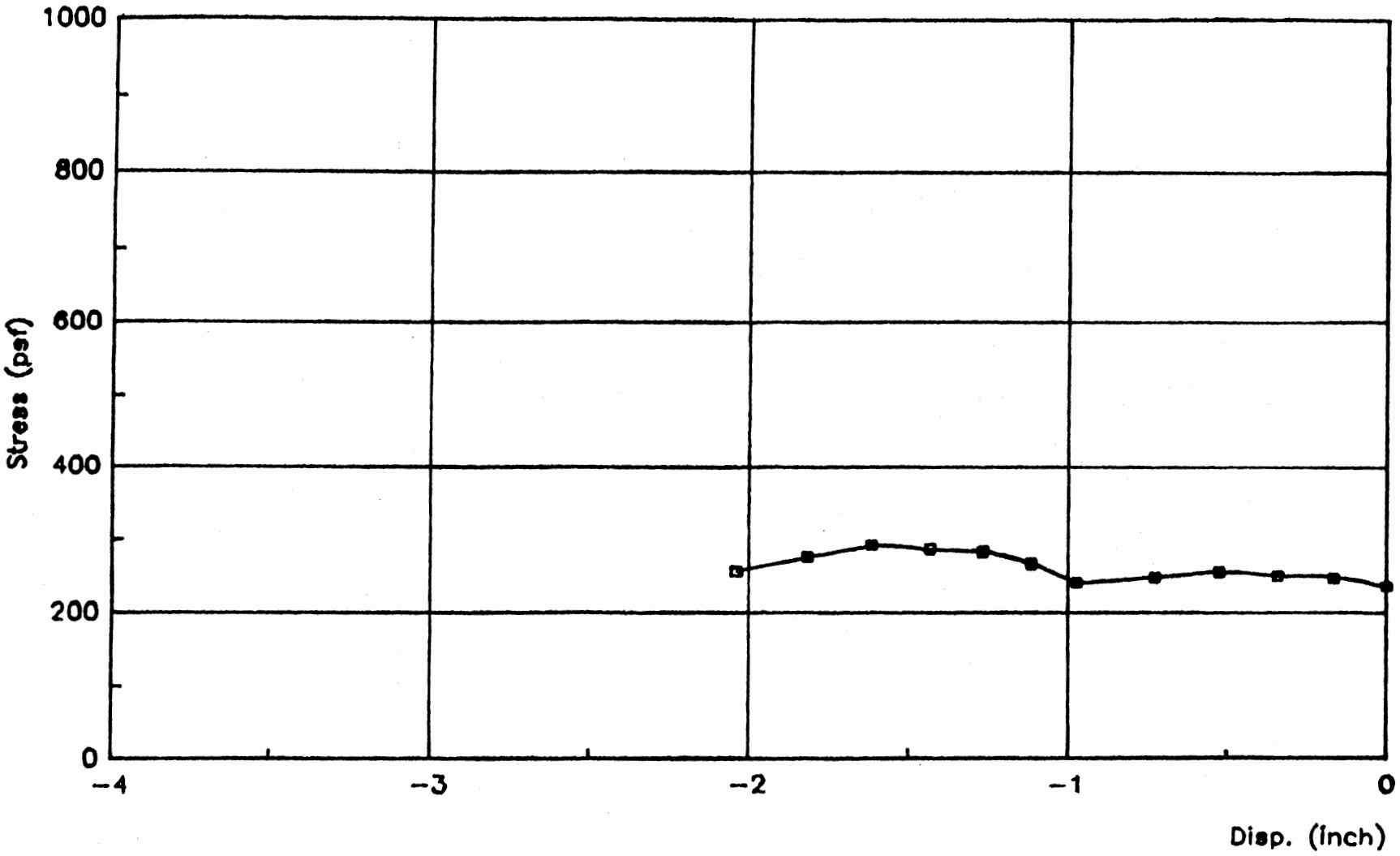

Figure 40(f). Soil-Response curve at 9 ft elevation, back side, high strength profile, 30 ft pile penetration.

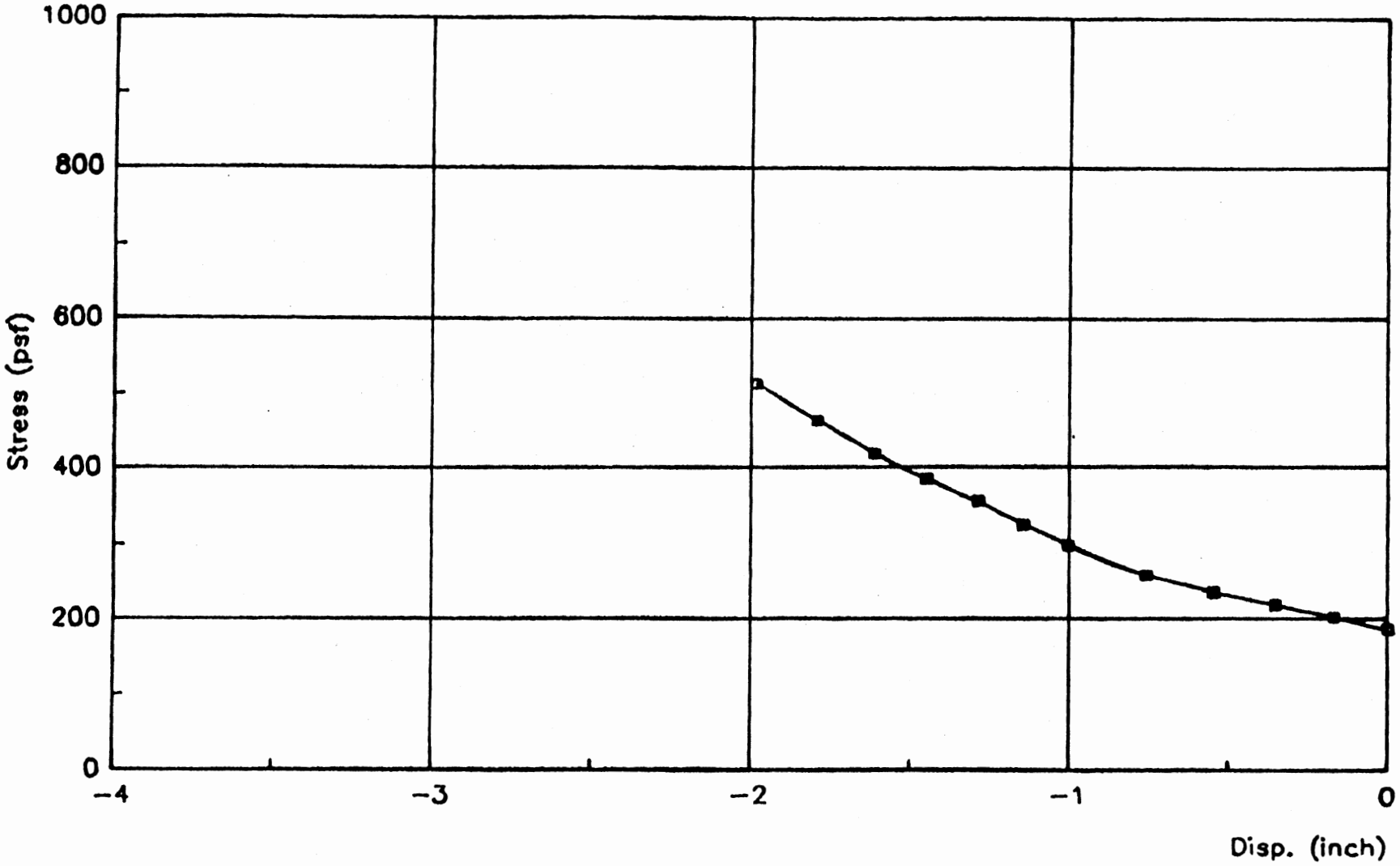

Figure 41(a). Soil-Response curve at 5 ft elevation, front side, high strength profile, 10 ft pile penetration.

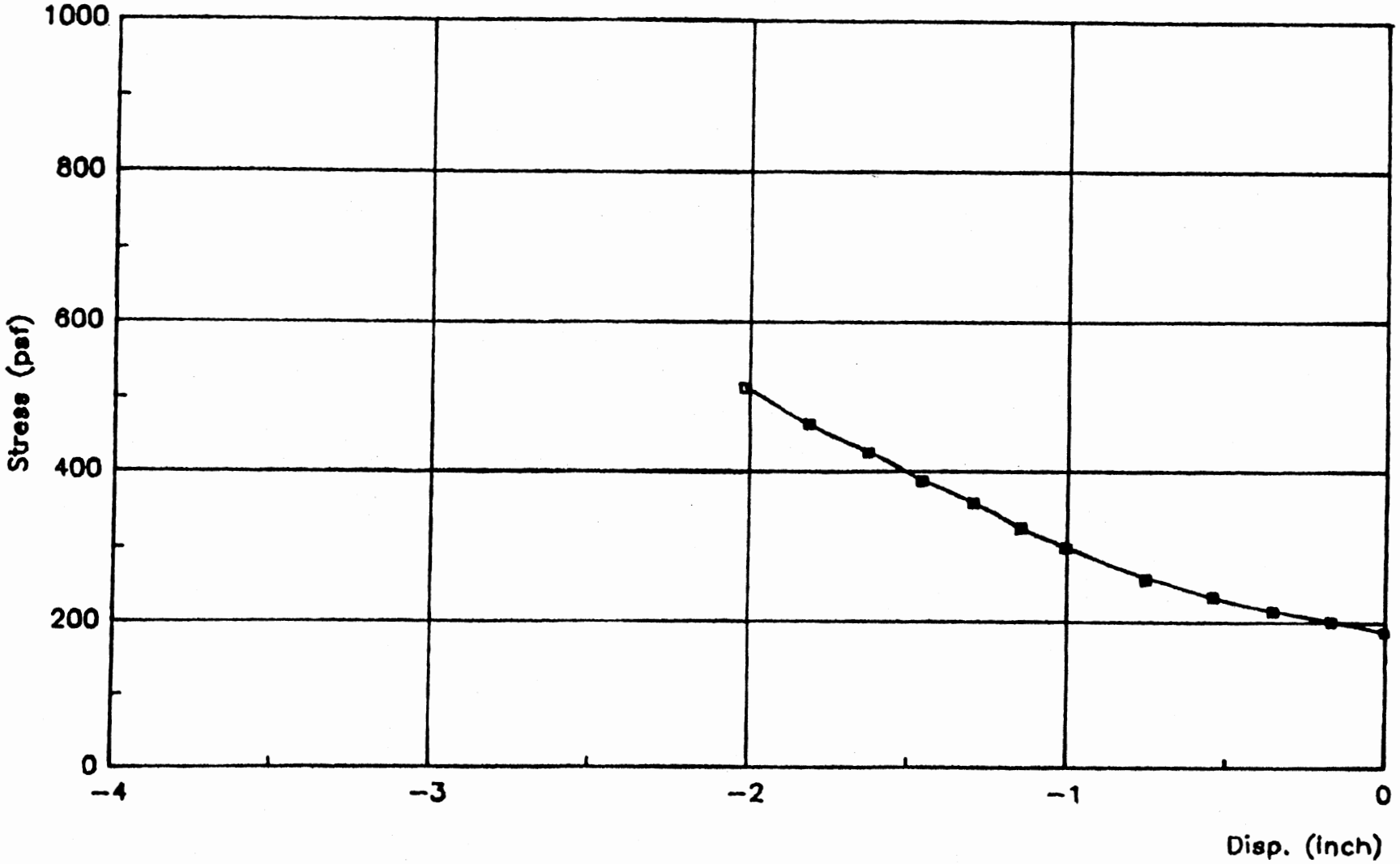

Figure 41(b). Soil-Response curve at 5 ft elevation, front side, high strength profile, 20 ft pile penetration.

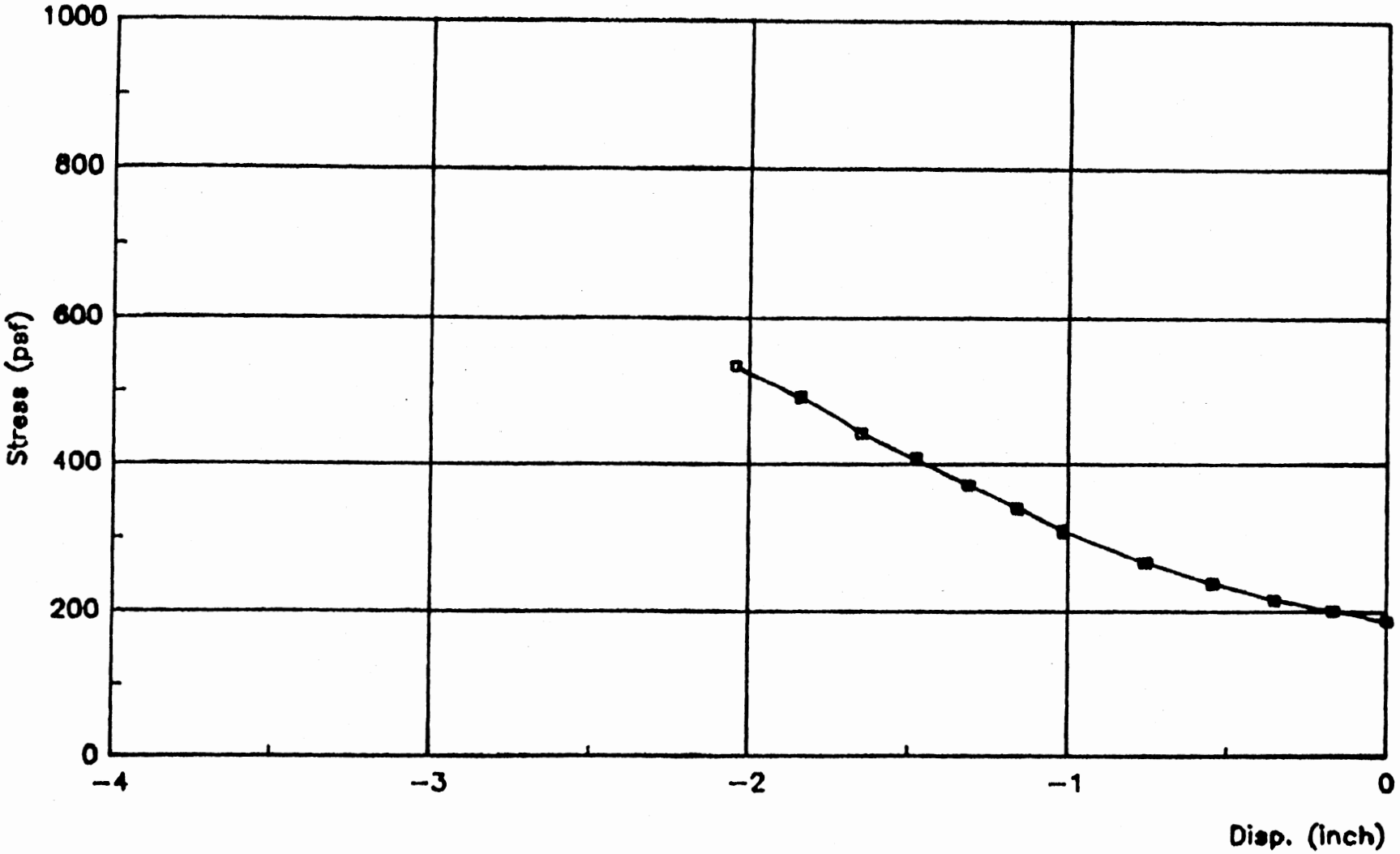

Figure 41(c). Soil-Response curve at 5 ft elevation, front side, high strength profile, 30 ft pile penetration.

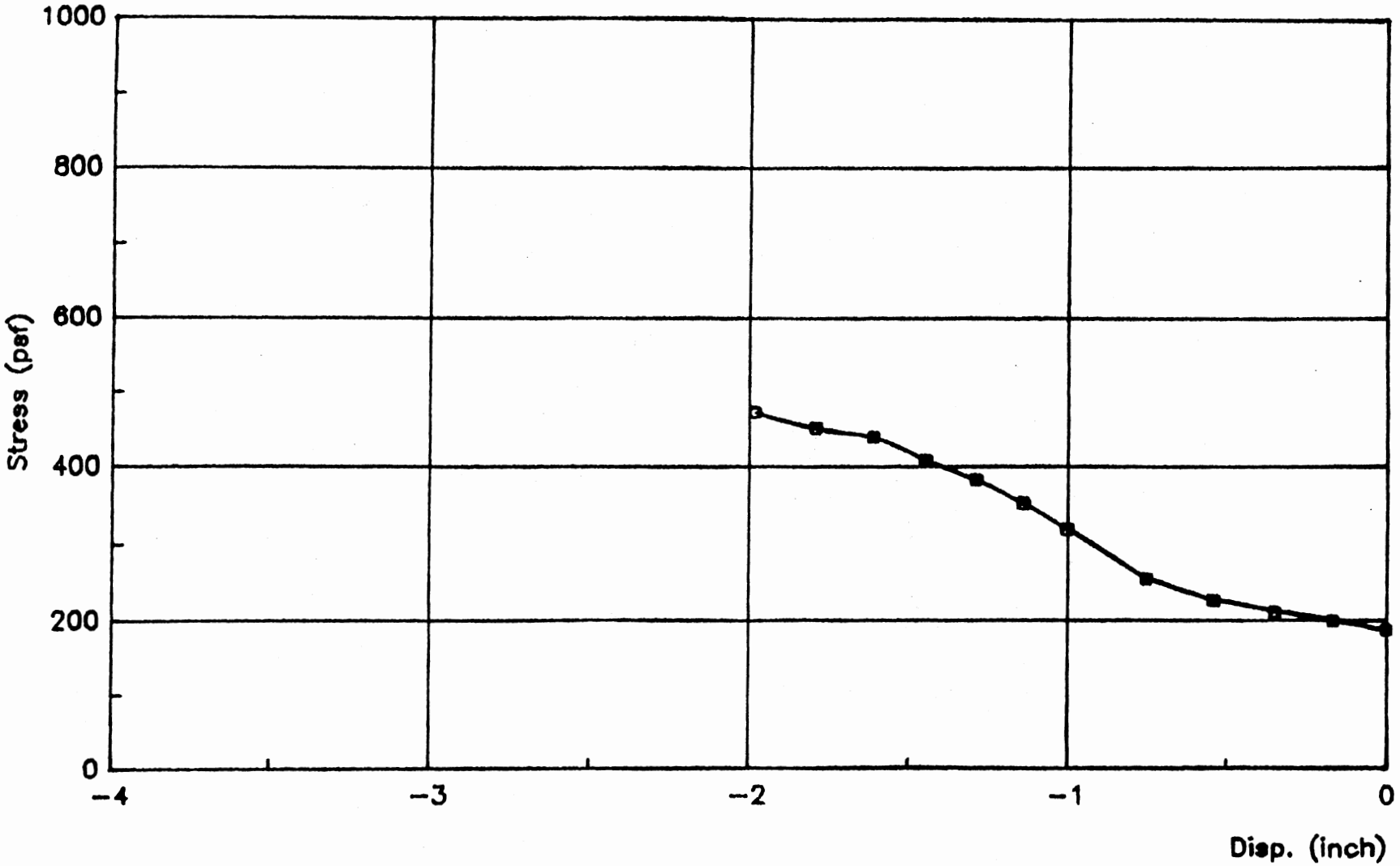

Figure 41(d). Soil-Response curve at 5 ft elevation, back side, high strength profile, 10 ft pile penetration.

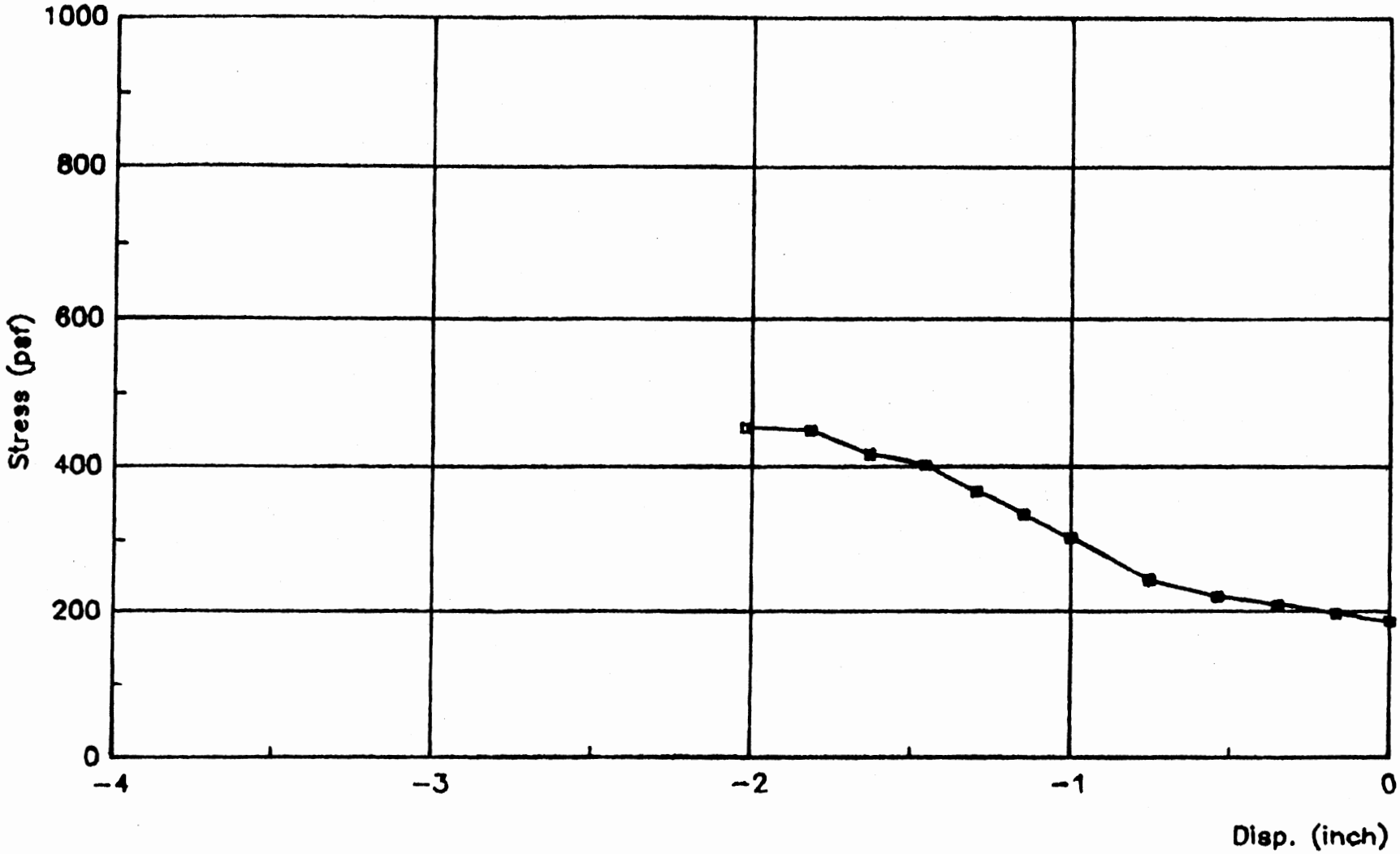

Figure 41(e). Soil-Response curve at 5 ft elevation, back side, high strength profile, 20 ft pile penetration.

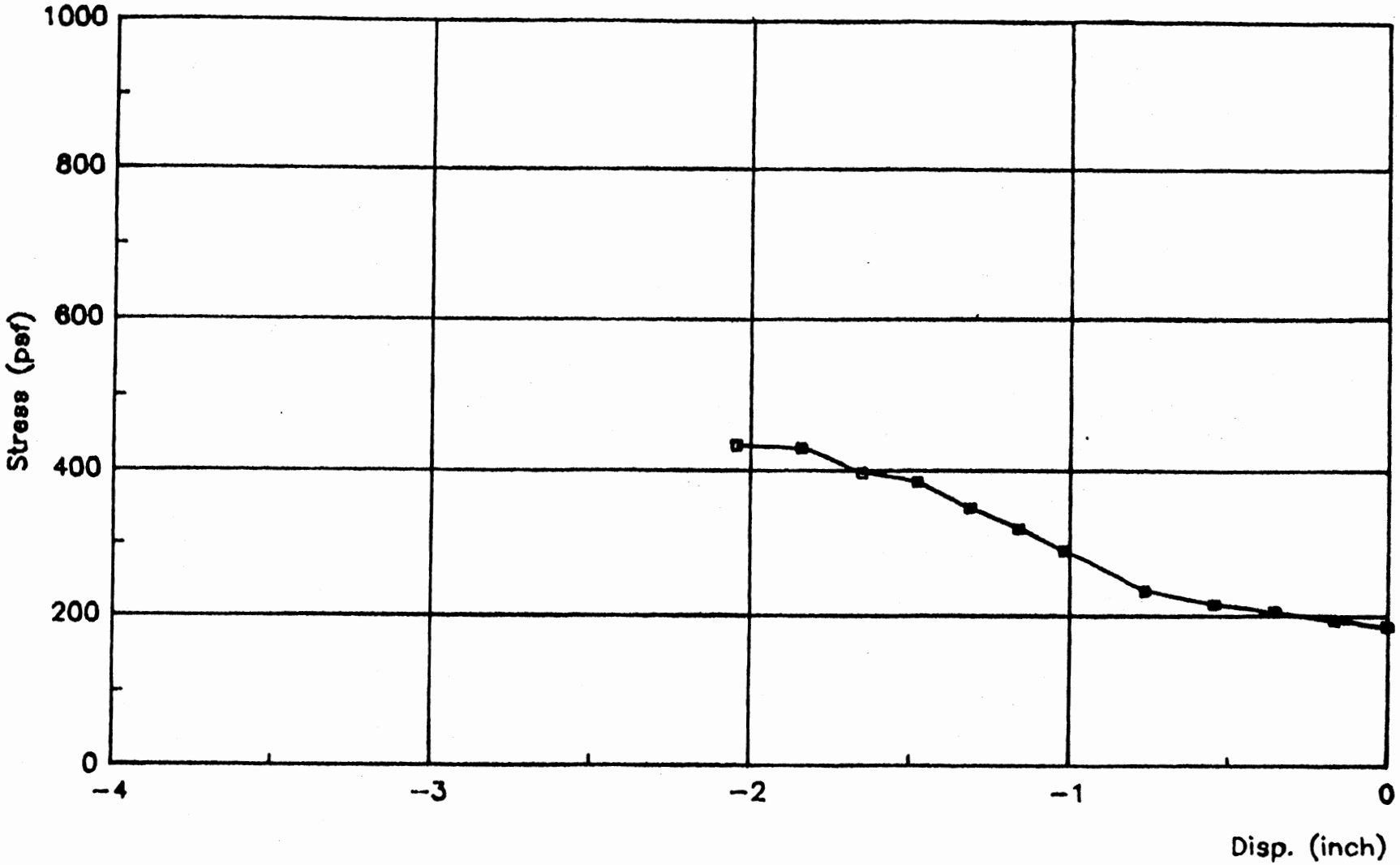

Figure 41(f). Soil-Response curve at 5 ft elevation, back side, high strength profile, 30 ft pile penetration.

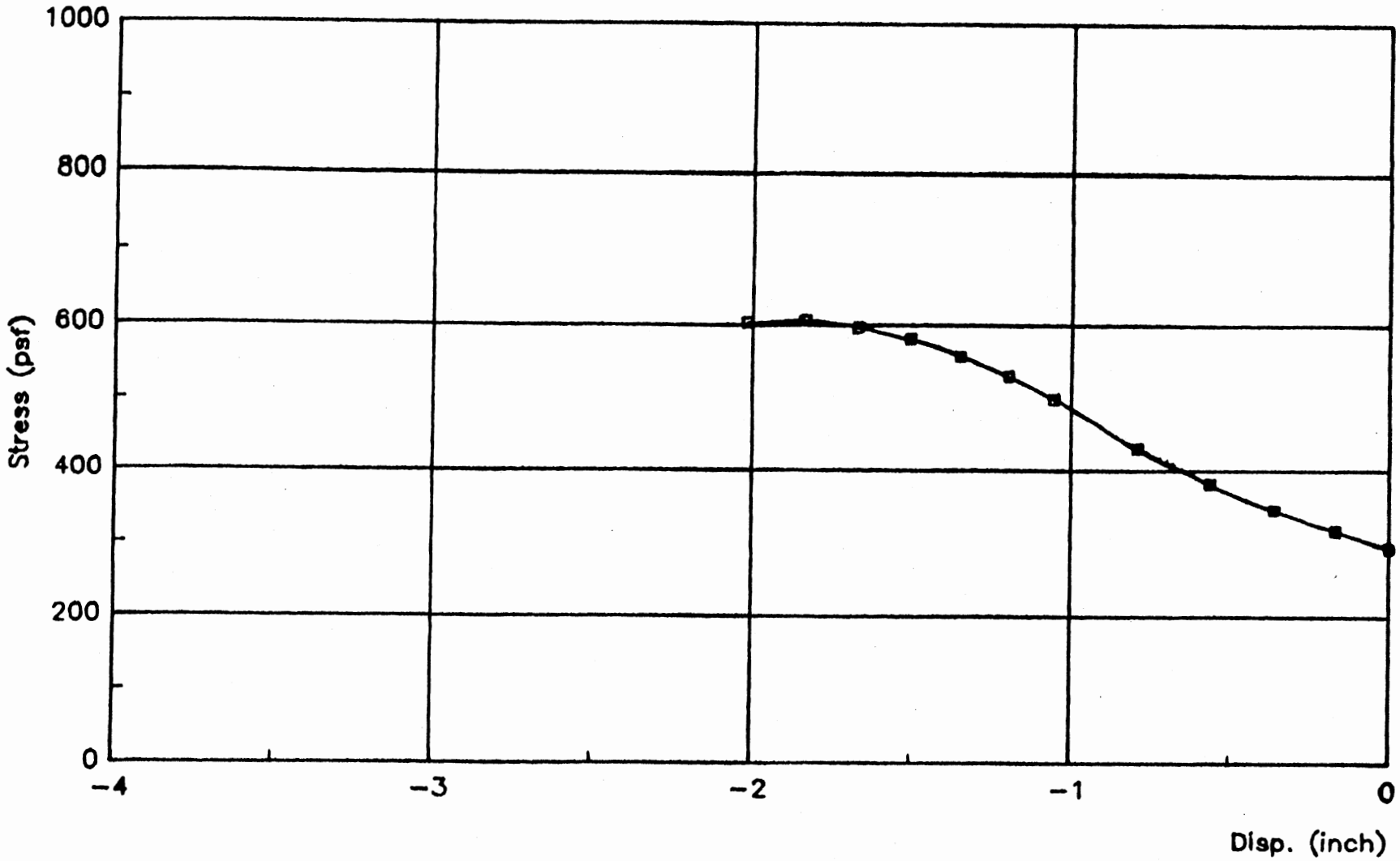

Figure 42(a). Soil-Response curve at 1 ft elevation, front side, high strength profile, 10 ft pile penetration.

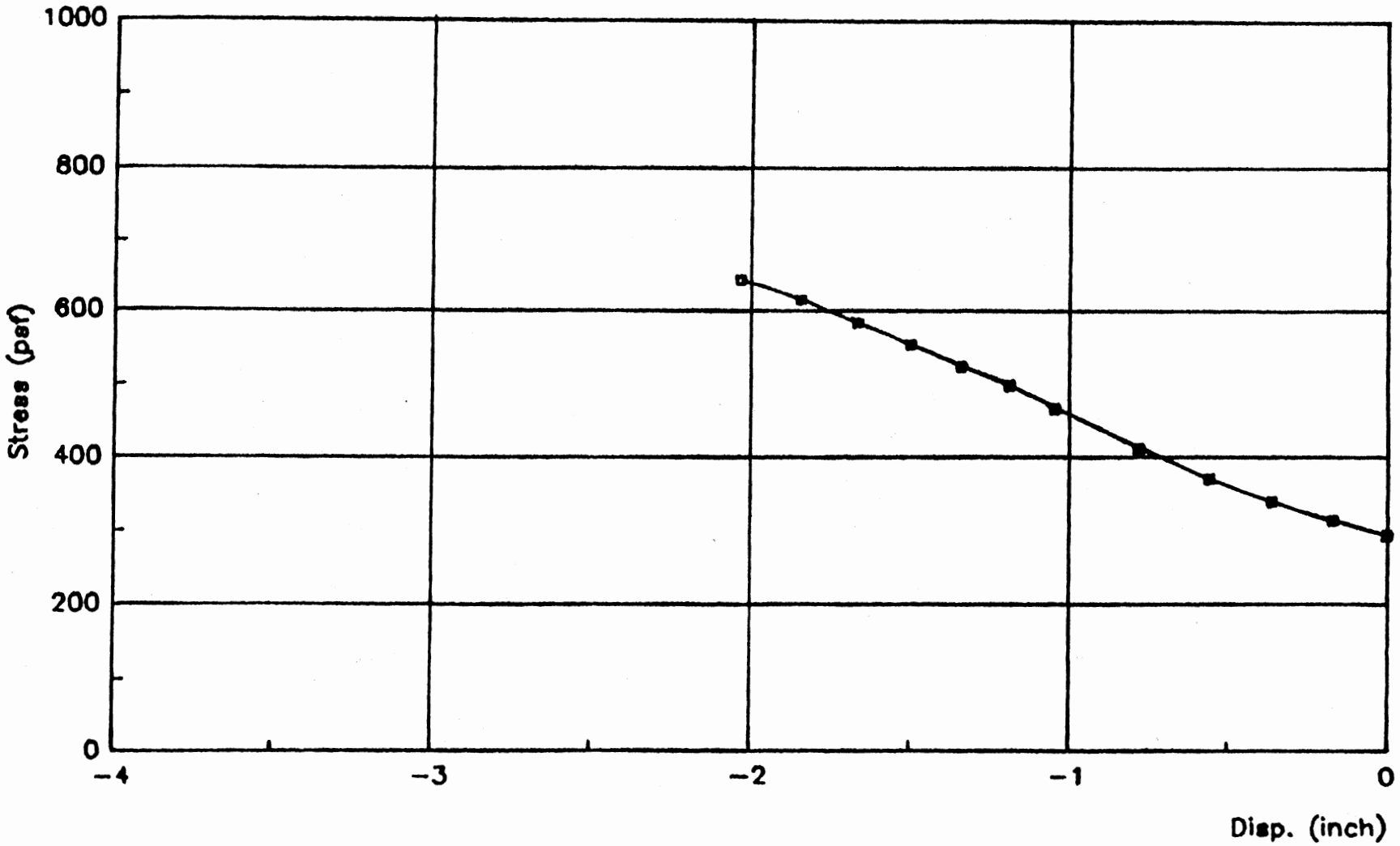

Figure 42(b). Soil-Response curve at 1 ft elevation, front side, high strength profile, 20 ft pile penetration.

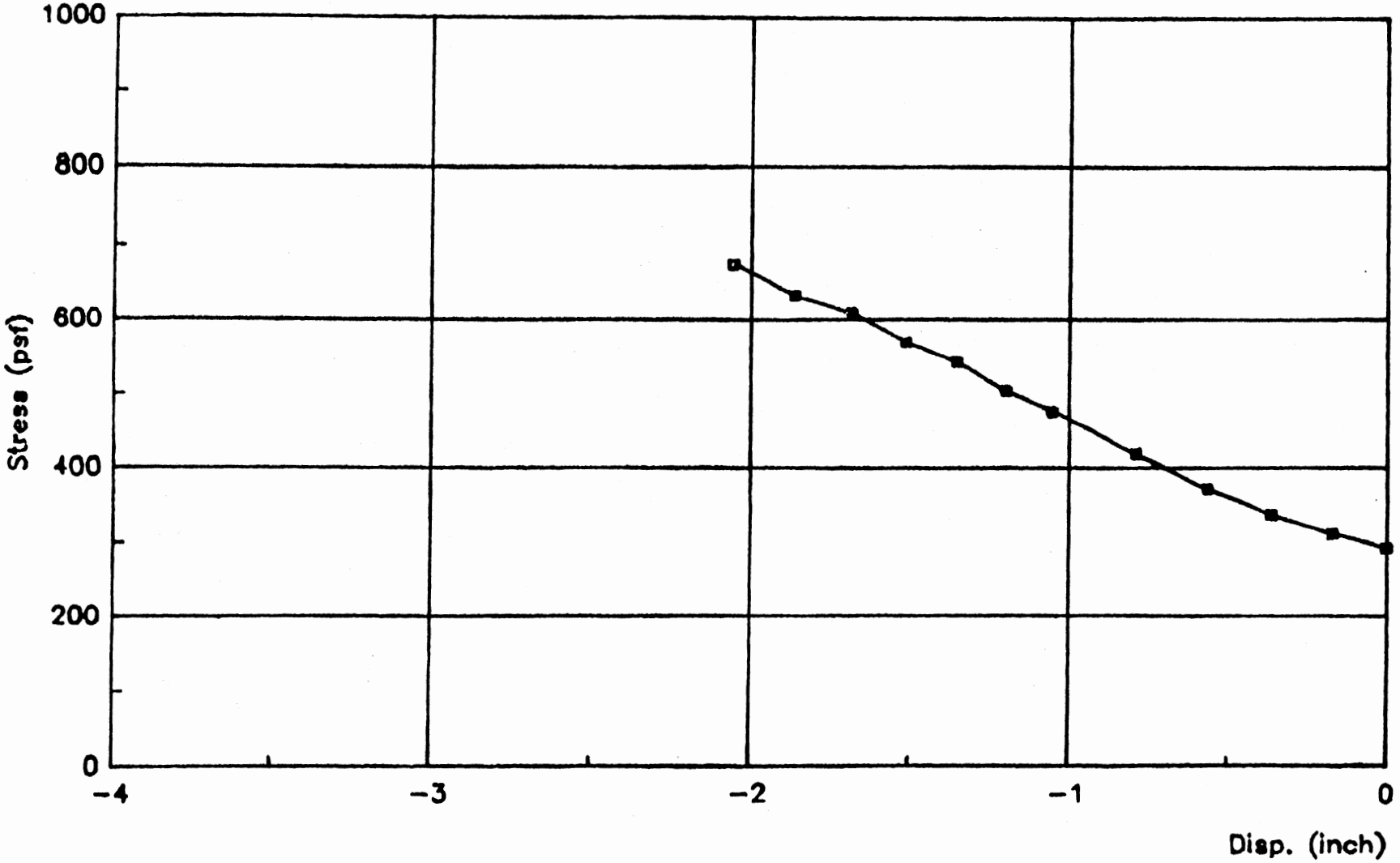

Figure 42(c). Soil-Response curve at 1 ft elevation, front side, high strength profile, 30 ft pile penetration.

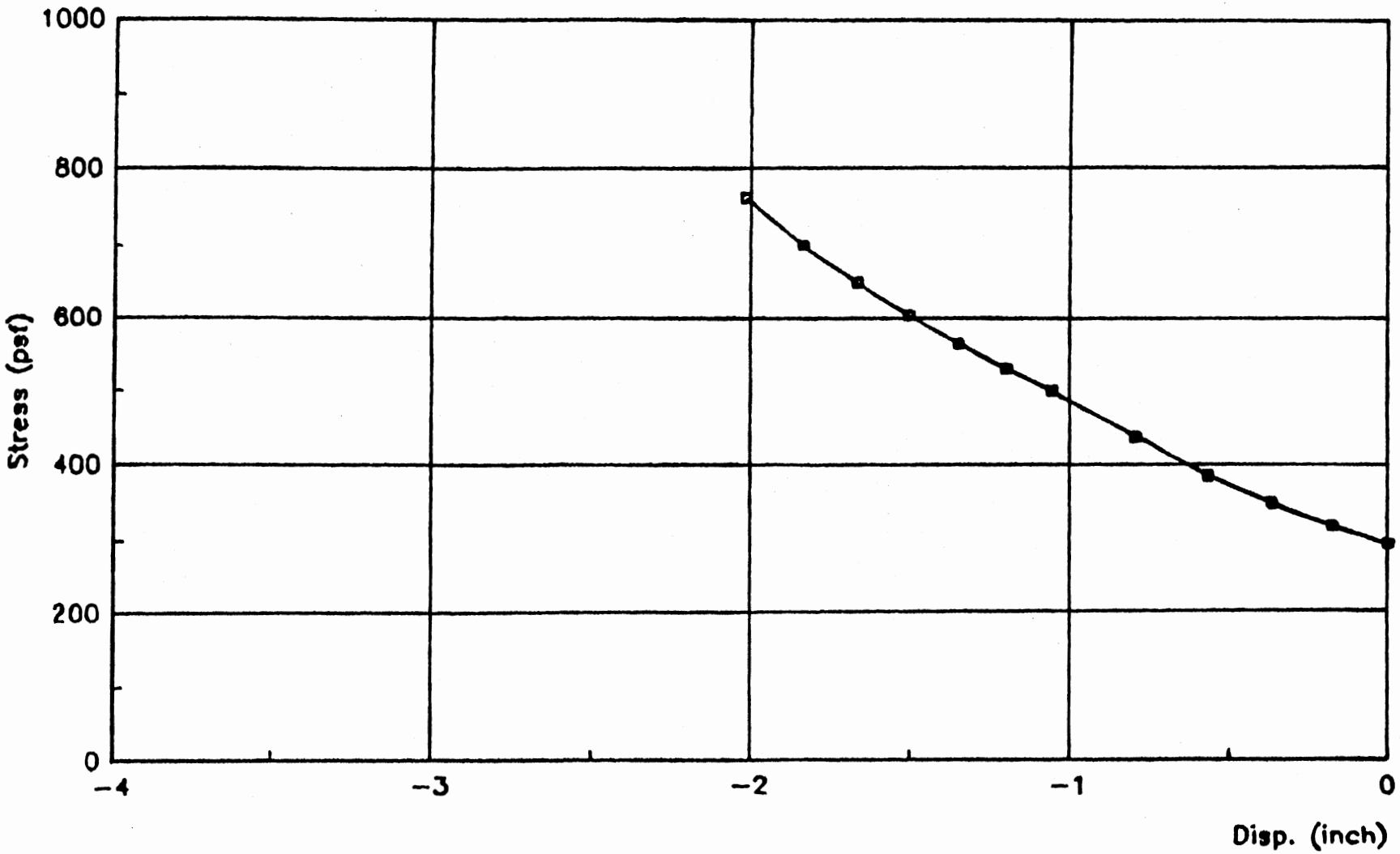

Figure 42(d). Soil-Response curve at 1 ft elevation, back side, high strength profile, 10 ft pile penetration.

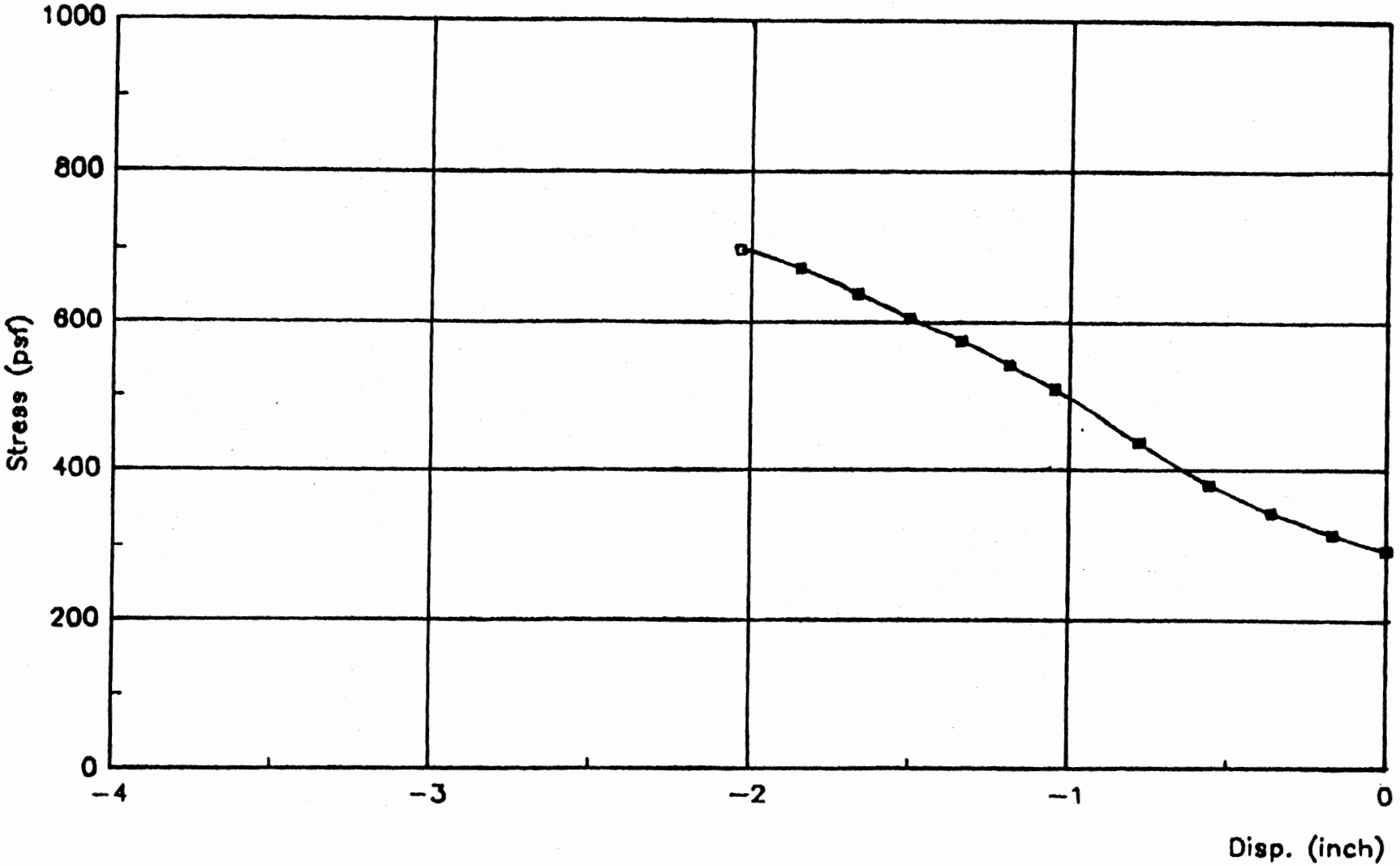

Figure 42(e). Soil-Response curve at 1 ft elevation, back side, high strength profile, 20 ft pile penetration.

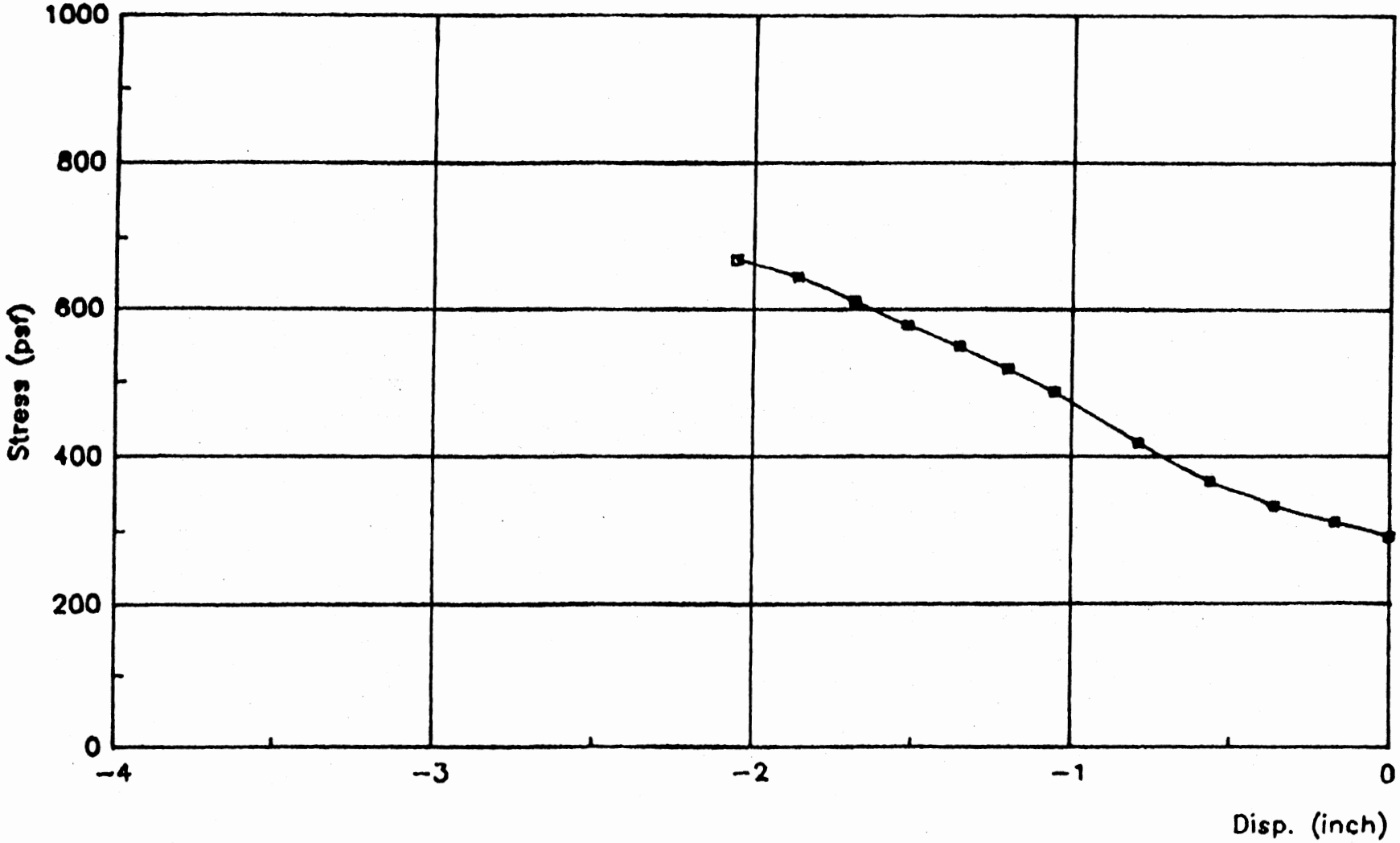

Figure 42(f). Soil-Response curve at 1 ft elevation, back side, high strength profile, 30 ft pile penetration.

Results of Analyses for the Medium Strength Profile

The results of the medium strength profile are similar in behavior to those of the high strength profile. The only difference is in the magnitudes of the obtained results such as f-distribution, moments, pile and soil displacements, net pressures on the pile, etc...

The figures and plots extracted from the medium case and for the three depth of penetrations are documented in Appendix D. However, a comparison between the high and the medium strength cases are discussed briefly below.

Degree of Mobilization

The "f" distribution for the medium case is similar to that of the high case. However, in the medium case, the f magnitude in the weak layer is equal to 80 % of the active strength (Fig. 43(a)) whereas in the high strength case this was about 60 % of the active capacity (Fig. 31(a)). At 16 ft head, f reaches 90 % of the active capacity for the medium case (Fig. 43(b)) as compared to 60 % for the high case (Fig. 31(h)).

Moment Diagrams

For the 10 ft case, the moments for the medium and the high strength cases are almost equal (Figs. 34(a) and 44(a)). This indicates that the moment distribution is solely due to the cantilever action of the hydrostatic water load on the portion of the pile above the levee crest.

In the 20 ft case, the difference between high and medium strength cases becomes apparent at greater depth. For water head of 16 ft, the

maximum positive moment is about 3.5 k-ft for the medium case (Fig. 44(b)) as compared to 2.5 k-ft for the high case (Fig. 34(b)).

In the 30 ft case and 16 ft head, the maximum positive moment is about 11 k-ft for the medium case (Fig. 44(c)) as compared to 6.25 k-ft for the high strength case (Fig. 34(c)).

In all cases, the negative moments and the location of the maximum positive moment remain the same irrespective of the soil strength.

Pile Displacements

The pile displacements and displacement history for the medium case portray the same behavior as that of the high strength case. However, the magnitudes of these displacements (Figs. 45(a), 45(b), and 45(c)) are 50 % higher than those of the high strength case (Figs. 35(a), 35(b), and 35(c)).

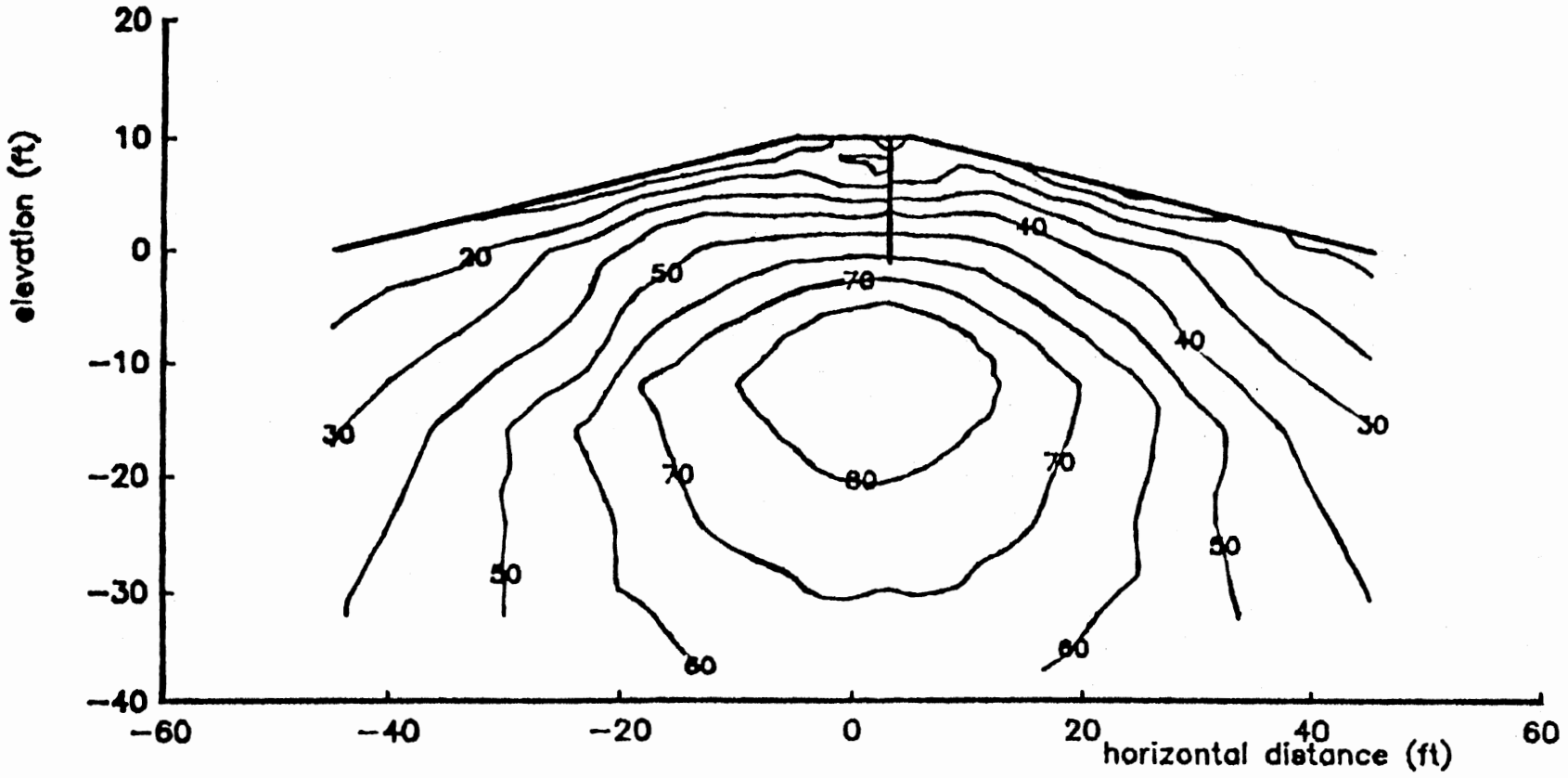

Figure 43(a). f contours at 2 ft head, medium strength profile, 10 ft pile penetration.

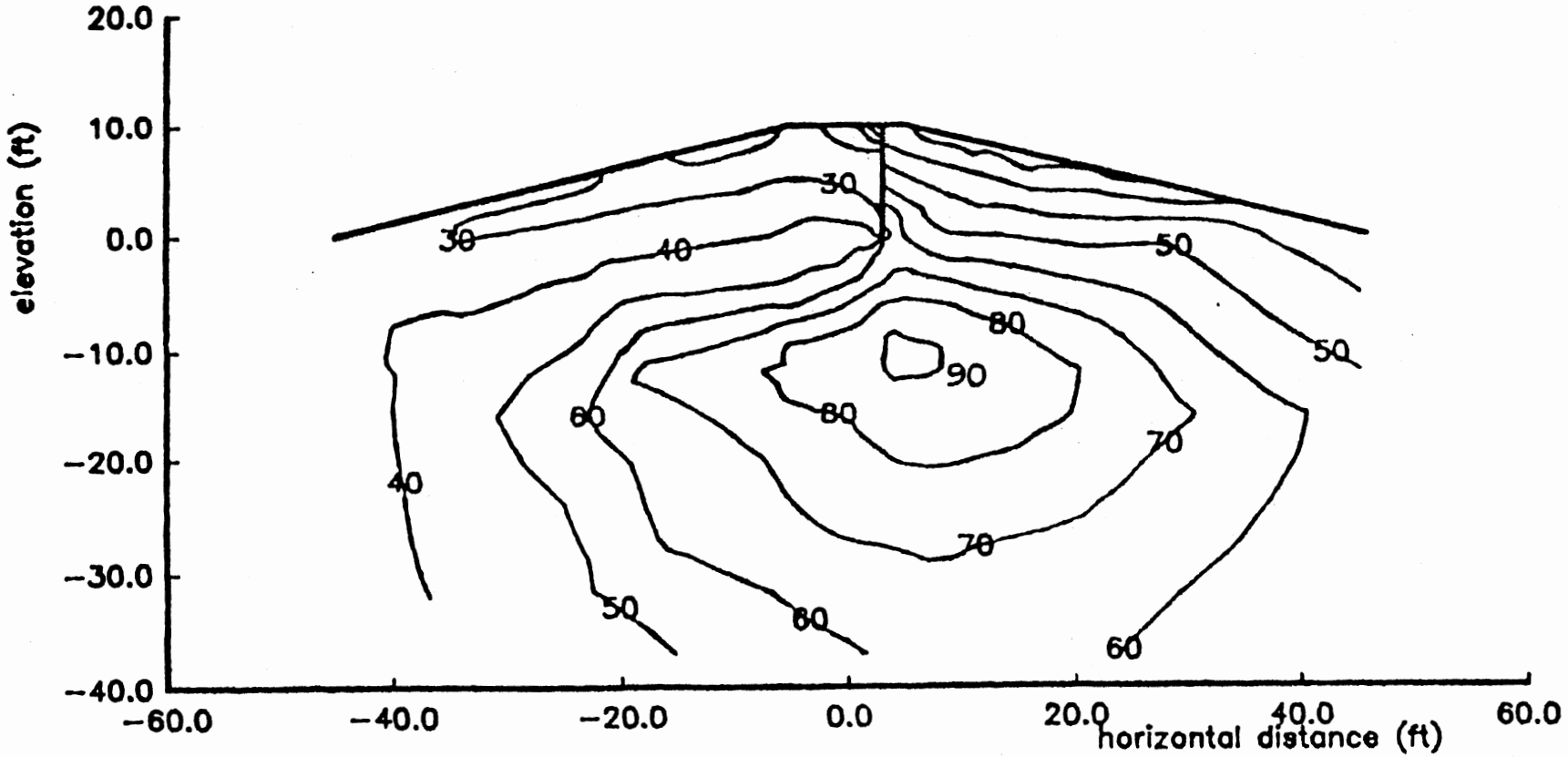

Figure 43(b). f contours at 16 ft head, medium strength profile, 10 ft pile penetration.

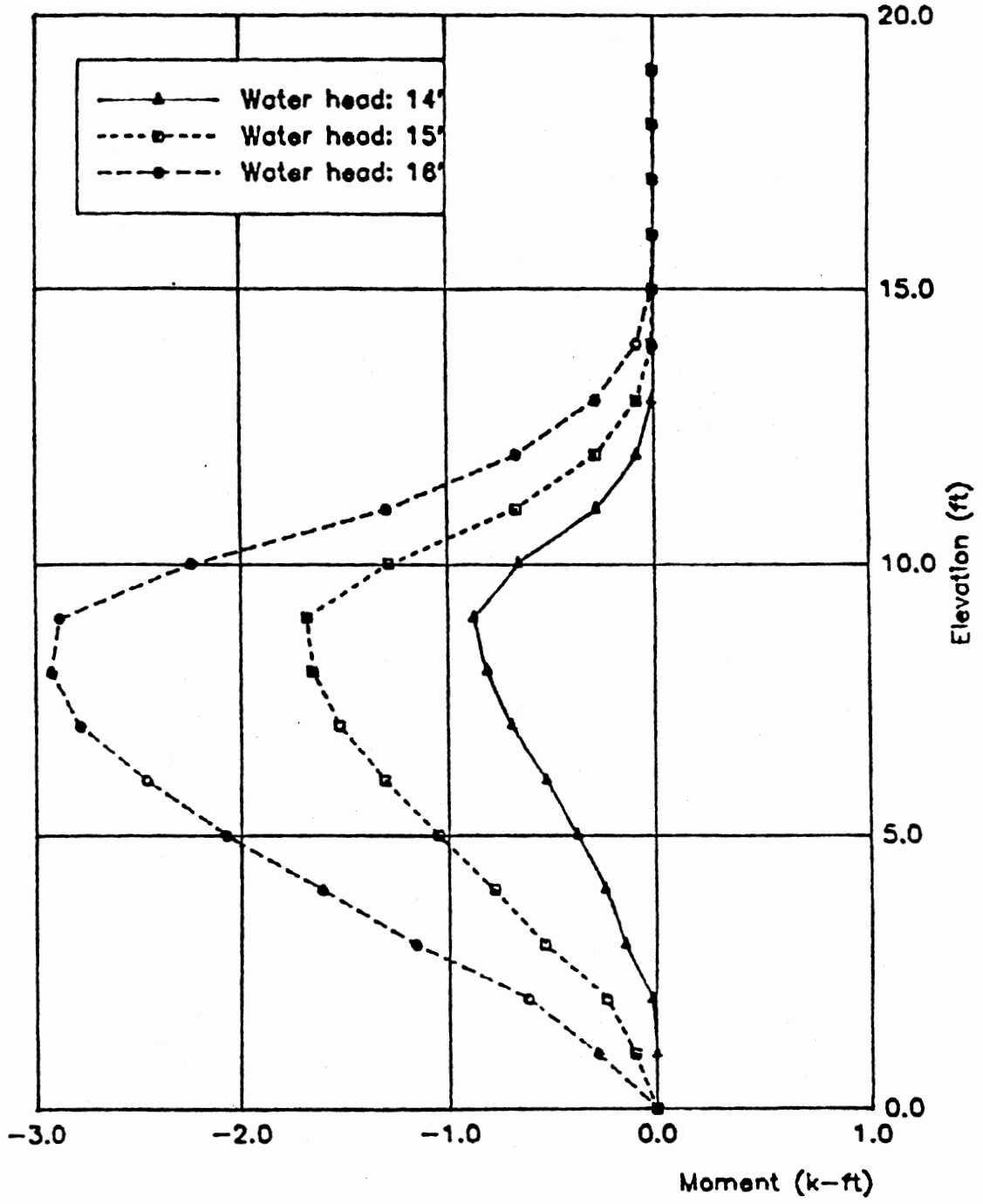

Figure 44(a). Bending moments, medium strength profile, 10′ pile penetration.

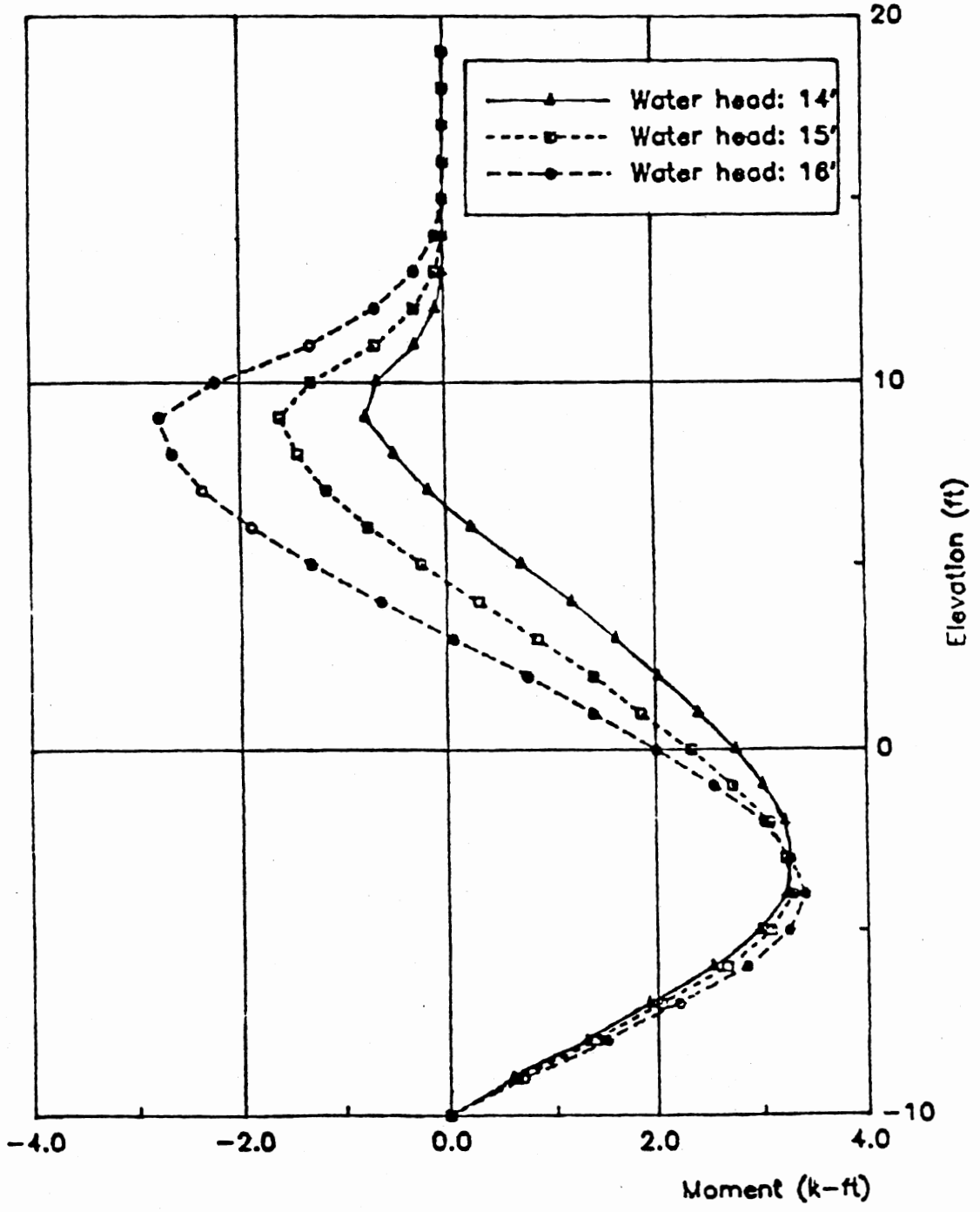

Figure 44(b). Bending moments, medium strength profile, 20′ pile penetration.

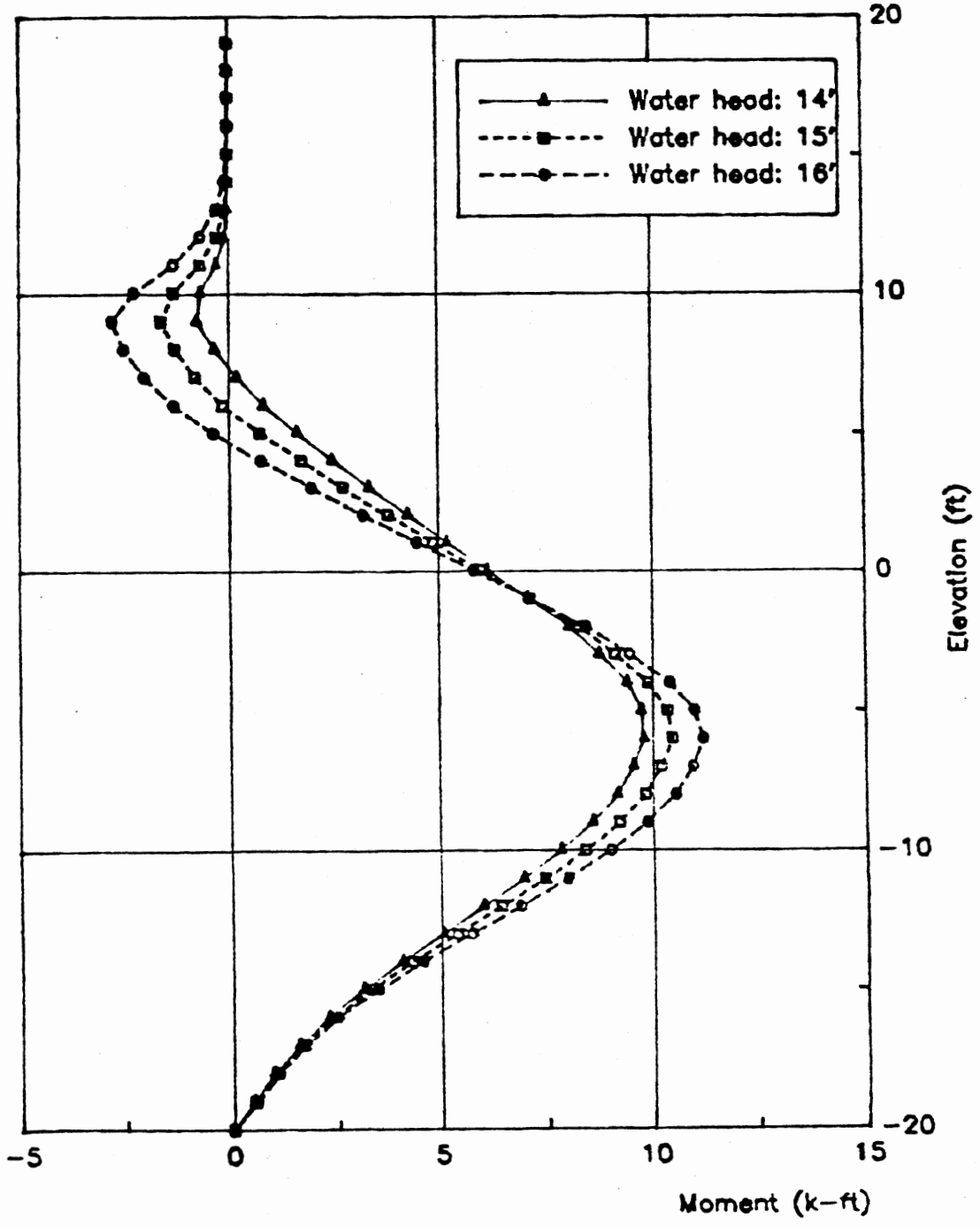

Figure 44(c). Bending moments, medium strength profile, 30′ pile penetration.

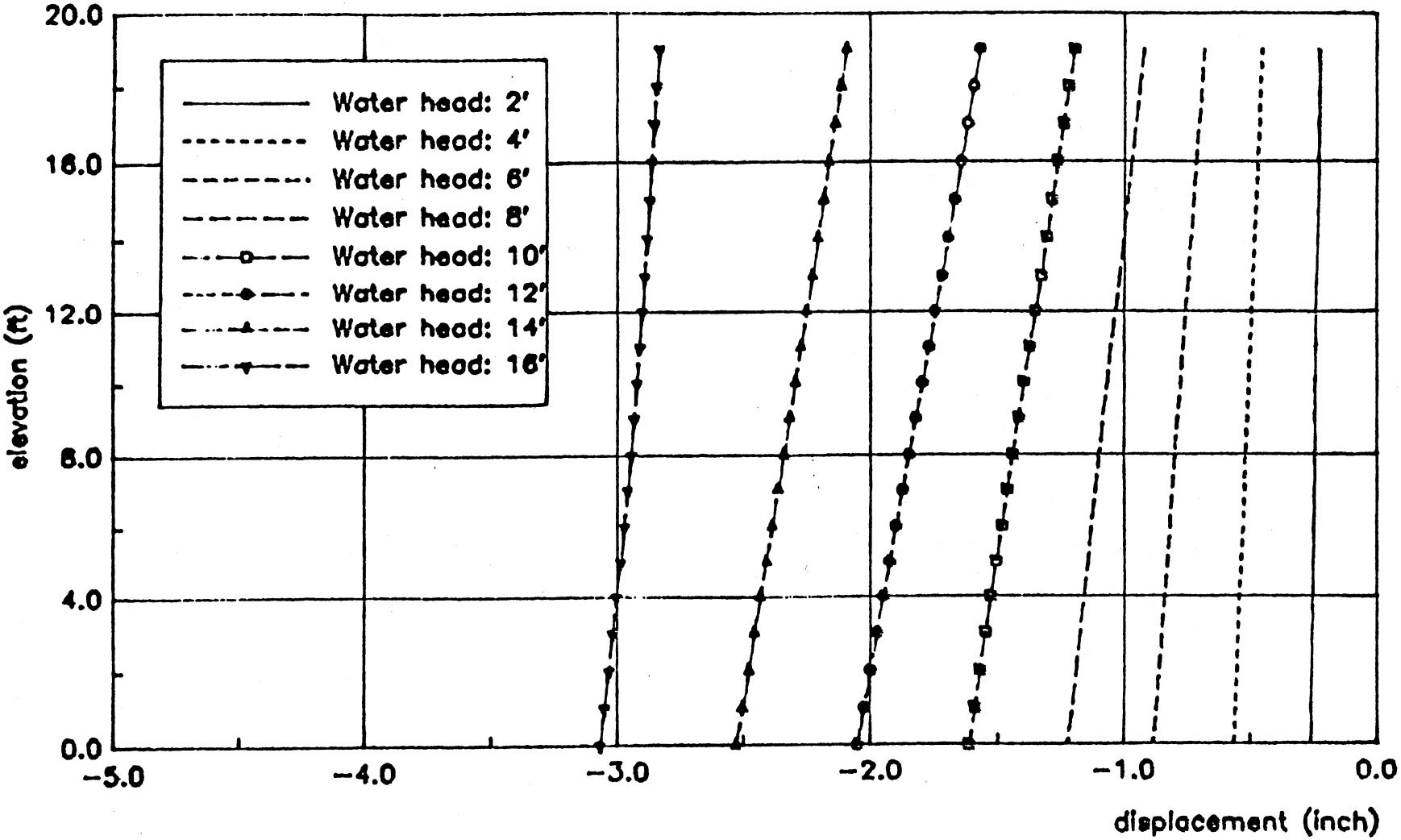

Figure 45(a). Pile deflections, medium strength profile, 10 ft pile penetration.

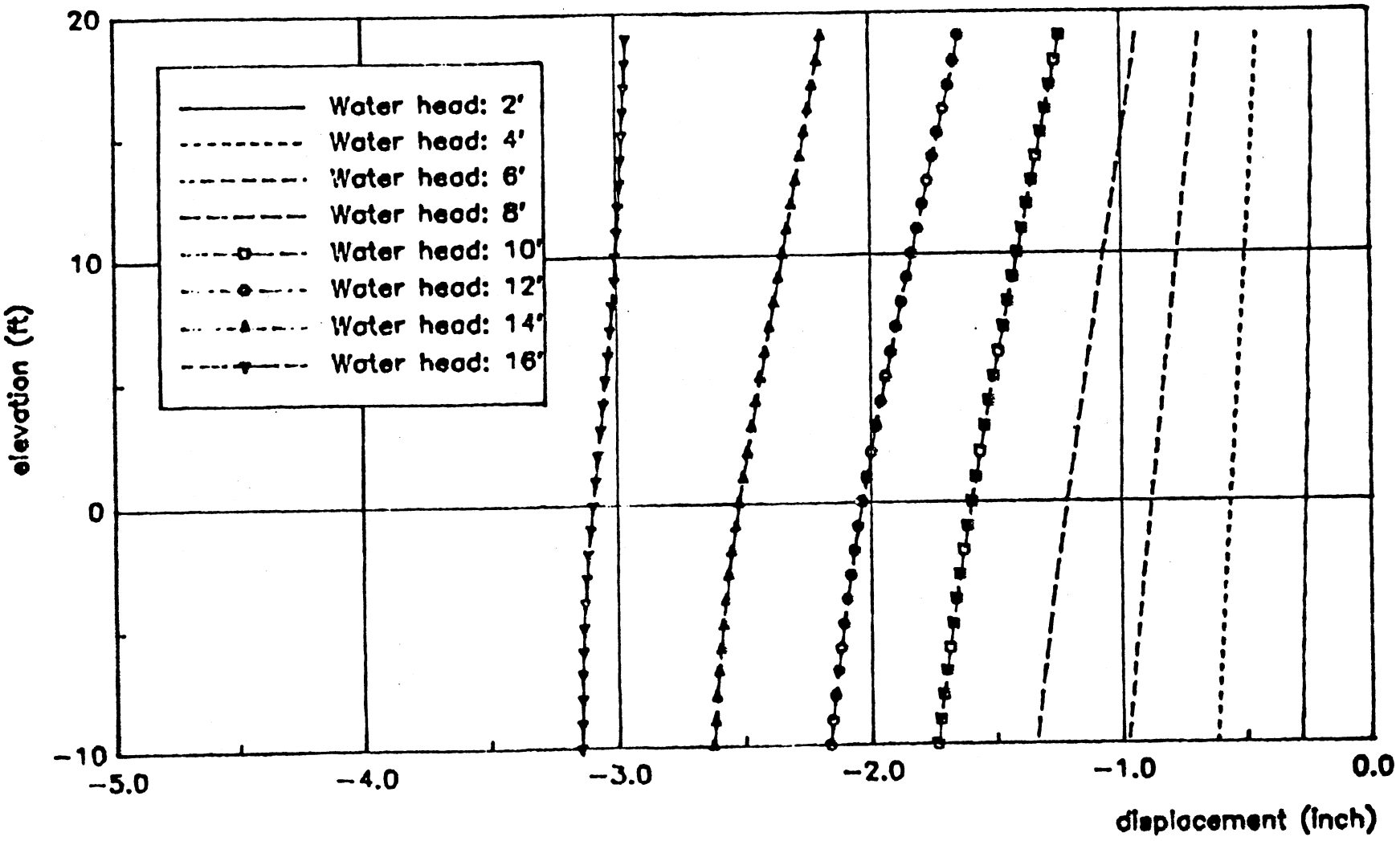

Figure 45(b). Pile deflections, medium strength profile, 20 ft pile penetration.

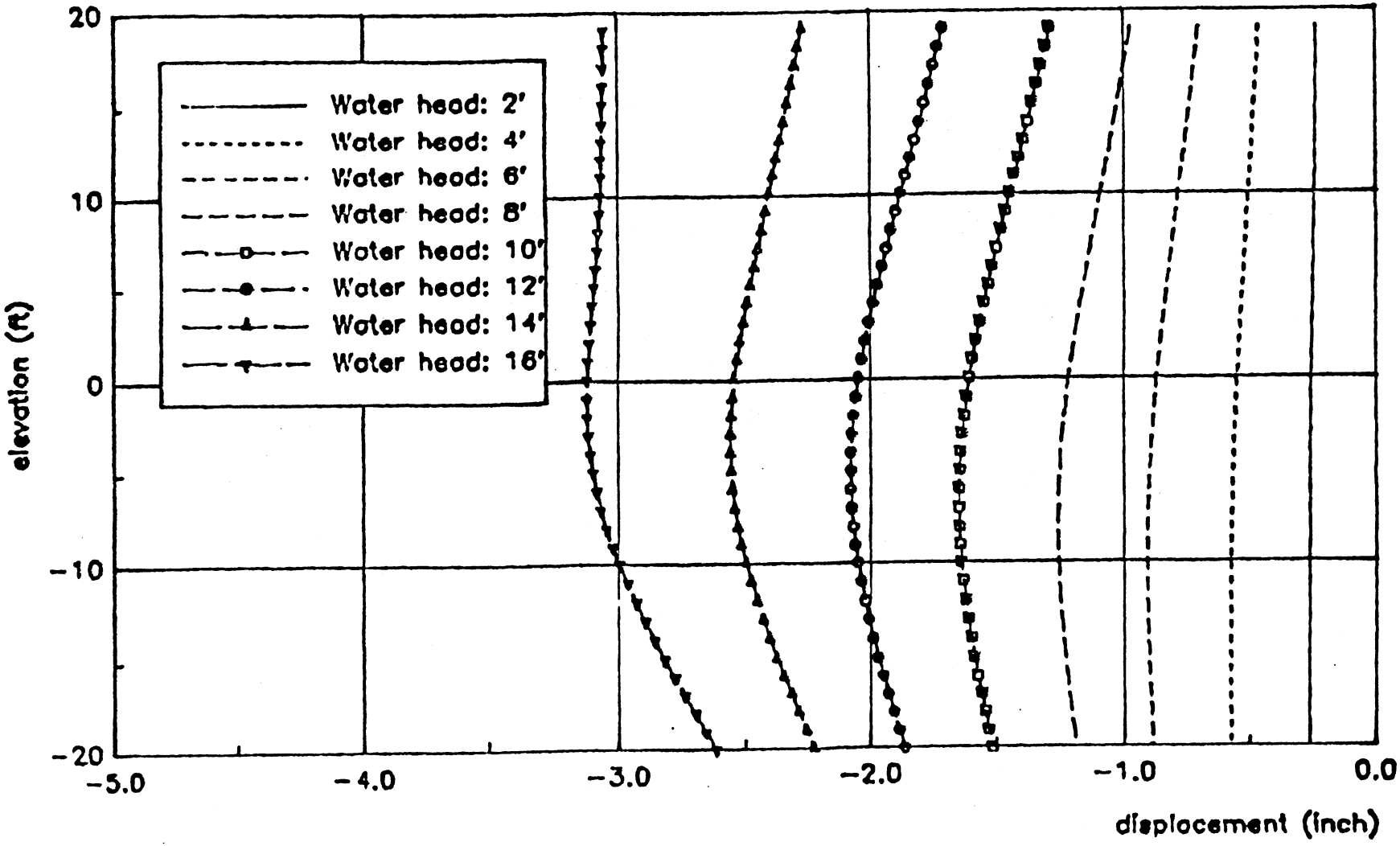

Figure 45(c). Pile deflections, medium strength profile, 30 ft pile penetration.

CHAPTER V

CONCLUSIONS AND RECOMMENDATIONS

Summary of Observations

A study on the behavior of floodwalls has been accomplished. The first part of this research was directed towards developing the analytical tool based on the finite element approach and incorporating adequate soil and interface models (Ref. 10). The second part of this study involved the testing of the analytical tool against test results obtained from the E99 wall test section. From the comparisons of the measured behavior of E99 wall and its response that has been calculated using the developed tool, it is clear that the methodology employed is capable of reproducing the test results within acceptable limits. The detail of the calculation results naturally surpass what can be measured in the field, and much needed information can easily be extracted from these analytical results. Finally, the whole behavior mechanism has been analyzed for typical levee systems especially in the vicinity of the pile. Each of the moments, displacements, soil responses, soil strength profiles, and depths of penetration help put the pieces of the puzzle together in a unique way.

Judging from the observed results, it is worthy to stress some of the important findings of this work:

(1) The pile floats in the soil mass and reacts to the soil deformation. This was demonstrated by the insensitivity of the pile

deflections to the pile penetration.

(2) The top of the pile tilted backwards with respect to its tip. This is a consequence of the clockwise rotation of the system. However, the absolute displacements of the pile continue to increase in the same direction (to the left) as the water head increases.

(3) The moment and pressure distributions for the 10 ft penetration case resemble those obtained from conventional or SSI analyses. However, for the 20 ft and 30 ft penetration cases; that is when the pile penetrated the weak layer, positive moments developed in the pile. Also, a passive zone developed in front of the pile tip; this is due the shearing of the weak layer which forces the pile to deflect to the left at the same time the pile tip is dragging behind in the stronger soil.

(4) It was discussed earlier that the depth of penetration does not resolve the problem of failure in flood walls in general. It was found that deeper driven piles sometimes aggravate the situation. This finding contradicts the results of the current classical and SSI design methods. In these methods, higher depths of penetration yield to safer structures and to smaller displacements. Hence, the validity of these methods for the floodwall problem is questionable. Consequently, the understanding of the behavior of the floodwall is very important in order to study the effect of the depth of penetration of the sheetpile on its performance.

Two failure criteria are acknowledged in this study (1) soil failure, and (2) loss of support or wall instability. To guard against the first type of failure, stronger soils are recommended whereas deeper pile penetration is recommended for the second type of failure.

However, there is an interaction between these two types and brought together with the development of a tension crack. The development of a tension crack introduces extra hydrostatic forces that are applied normal to the crack sides; that is the wall on one side and the soil on the other. These forces help push some of the soils closer to failure if not to failure. Also, the tearing of the interface as the crack propagates destroys some of the wall supports. Although the typical cases were not loaded to failure or to the initiation of a tension crack, the above observations should still be valid.

The different conditions that might occur when a tension crack develops are:

(1) A tension crack occurs while the soils are far from failure. That is the extra water loads will not bring some soils to failure. Hence, only a reliable depth of penetration is needed to guard against a total loss of support.

(2) A tension crack occurs while some of the soils are close to failure. Then a chain reaction type of failure can occur and probably an extremely high depth of penetration is required.

Future Recommendations

Due to the complexity of the finite element method and the volume of the input and output, it fails to qualify as a routine design procedure. A soil-structure interaction (SSI) analysis technique, capable of treating nonlinear supports, such as the CBEAMC program presented in Ref. 4, is a reasonably fast engineering tool that may be utilized in the design of floodwalls. However, the soil-structure interaction approach yields correct results only if the soil response

curves used are representative of the problem being analyzed. No such curves are presently available for the floodwall problem. The long term objective of the this research is the development of techniques that can be used for the derivation of this critical information for typical conditions of floodwalls, and inject this information into an SSI procedure. However, the SSI mechanical model in its present form cannot produce the following:

(1) A backward deflection of the pile top with respect to its tip.

(2) Pile displacements induced by the levee loads.

(3) Development of positive moments in the pile.

It is recommended that other soil profiles should also be analyzed to examine the effect of soil profiles on the behavior of floodwalls. It was shown in this study that the existence of the weak layer in the soil altered the behavior of the system a great deal. Also, the soil properties should be varied since only undrained soils were used in this study. Finally, the results of this research would hopefully help pave the road to achieving an SSI modeling, once the above mentioned complexities are resolved, or tailoring a new design method that considers the main aspects of the behavior of floodwalls.

BIBLIOGRAPHY

(1) Clough, G.W. and J.M. Duncan. Finite Element Analyses of Retaining Wall Behavior. Journal of the Soil Mechanics and Foundations Division, ASCE, Vol. 97, No. SM12, Dec., 1971, pp. 1657-1673.

(2) D'Appolonia, Poulos, and Ladd. Initial Settlement of Structures on Clay. Journal of the Soil Mechanics and Foundations Division, ASCE, Vol. 97, No. SM10, Oct., 1971, pp. 1359-1377.

(3) Dawkins, W.P. User's Guide: Computer Program for Soil-Structure Interaction Analysis of Sheet Pile Retaining Walls (CSHTSSI). Report to ADP Center, U. S. Army Engineer Waterways Experiment Station, Vicksburg, Miss., 1982.

(4) Dawkins, W.P. User's Guide: Computer Program for Analysis of Beam-Column Structures for Nonlinear Supports (CBEAMC). Instruction Report K-82-6, U. S. Army Engineer Waterways Experiment Station, Vicksburg, Miss., 1982.

(5) Duncan, J.M. and C.Y. Chang. Nonlinear Analysis of Stress and Strain in Soils. Journal of the Soil Mechanics and Foundations Division, ASCE, Vol. 96, No. SM5, Sept., 1970, pp. 1629-1653.

(6) Foott and Ladd. Undrained Settlement of Plastic and Organic Clays. Journal of the Geotechnical Engineering Division, ASCE, Vol 107, No. GT8, August, 1981, pp. 1079-1094.

(7) Janbu, N. Soil Compressibility as Determined by Oedometer and Triaxial Tests. Proc. European Conference on Soil Mechanics and Foundation Engineering, Vol. 1, Wiesbaden, pp. 19-25, 1963.

(8) Holtz, R.D., and W.D. Kovacs. Geotechnical Engineering. Prentice Hall, Inc. N.J., 1981, 733 pp.

(9) Kulhawy, F.H., J.M. Duncan, and H.B. Seed. Finite Element Analyses of Stresses and Movements in Embankments During Construction. Contract Report S-69-8 to U. S. Army Engineer Waterways Experiment Station, Vicksburg, Miss., November 1969.

(10) Oner, M. and I. Hallal. Nonlinear Plane Strain Finite Element Program (SIMULATE). Oklahoma State University, 1987.

(11) Oner, M. and N. Janbu. Nonlinear Analysis of Foundation Vibrations. Proc. Second International Conference on Numerical Methods in Geomechanics. Blacksburg, Virginia, Vol 2, pp.1025-1037, 1976.

(12) Radhakrishnan, N. and H.W. Jones. Documentation for Modified UFRAME Program. Technical Report K-76-1, U. S. Army Engineer Waterways Experiment Station, Vicksburg, Miss., July 1976.

(13) Terzaghi, K. Evaluation of Coefficients of Subgrade Reaction. Geotechnique, Vol. 5, December, 1955, pp. 297-326.

(14) Waterways Experiment Station. E99 Sheet Pile Wall Field Load Test Report. Vicksburg, MI, 1986.

(15) Wilson, E.L. Finite Elements for Foundations, Joints and Fluids. Finite Elements in Geomechanics, G. Gudehus, Ed., John Wiley & Sons, 1977.

APPENDIXES

APPENDIX A

Nonlinear Soil Model

Examining and Improving Model Behavior

Numerical Tests on the Model

In order to examine the behavior of the "f model" used, a simulation program was written using a microcomputer. This program reads the stress history to be imposed and calculates the corresponding strains from the model. The algorithm used simulates a finite element program that uses the f model by calling a model subroutine. The initial slope method is used ("initial slope" refers to the calculation of moduli from the soil model using the stress conditions at the beginning of a loading step). Using this program the behavior of the model under various stress paths was investigated.

Fig. 46(a) shows a computed curve for loading toward failure starting at K_o condition, and Fig. 46(b) shows another computed stress-strain curve for loading up to some point, then reversing the load (unloading) and further loading in the same direction until failure. Although these curves seem similar to observed behavior in lab tests on soils, they do not prove the validity of the model. Actual test results should be predicted by the model for that purpose. However, it should be noted at this point that no model should be expected to predict soil behavior under any stress path, they simply work best under conditions

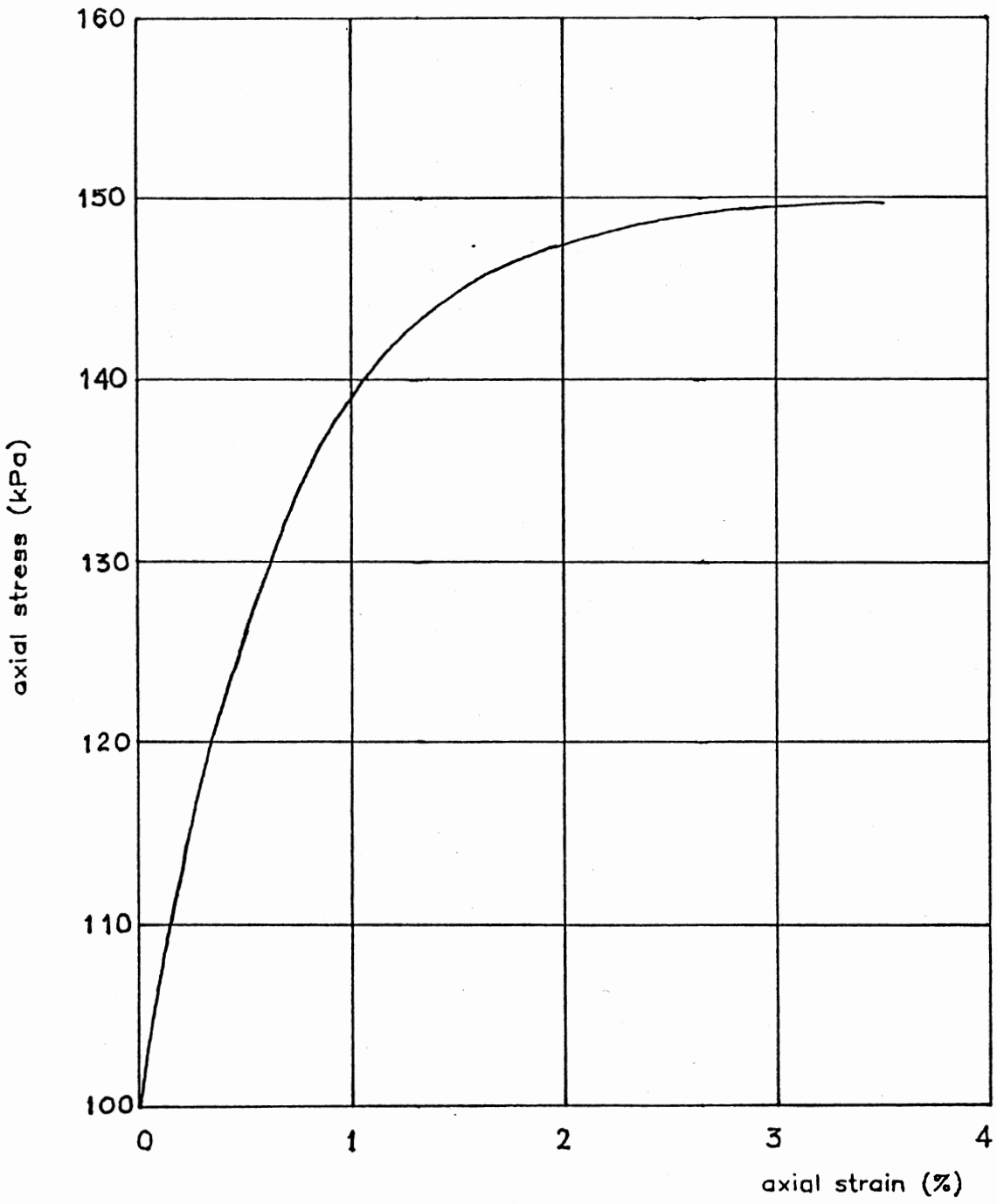

Figure 46(a). Loading to failure starting at k_o point m=100, n=0.5, phi=30, sig3=50 kpa.

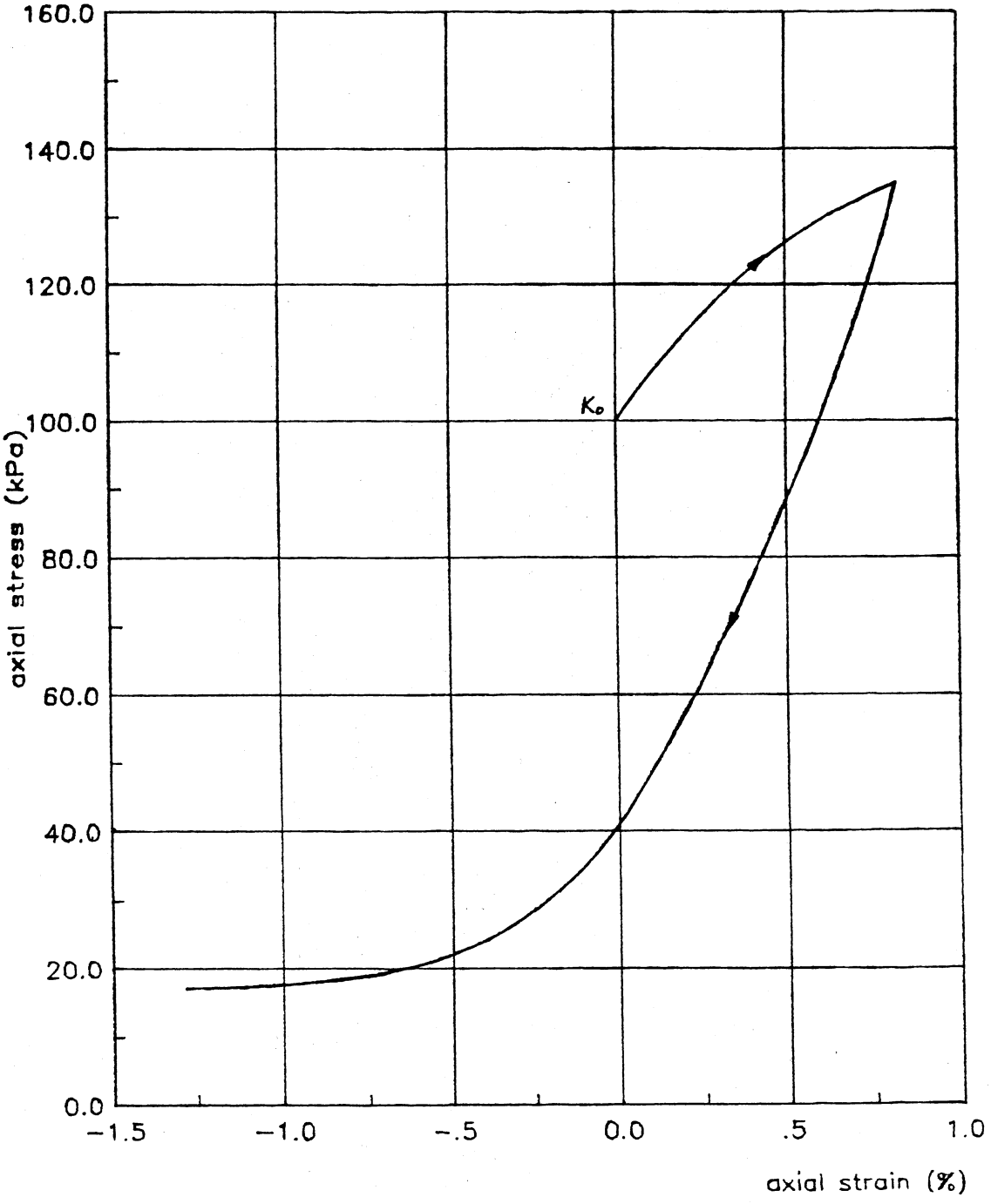

Figure 46(b). Unloading and reloading to failure, m=100, n=0.5, phi=30, sig3=50 kpa.

that have been emphasized during the model development. Therefore, the model should be tested for stress paths expected for the problem under consideration.

Model Behavior for Active/Passive Stress Paths

In the soil-structure interaction problem being analyzed, the elements of soil that govern the overall behavior of the system are those in the vicinity of the sheetpile. In a finite element model accurate representation of the stress-strain behavior of these elements is essential. Therefore, the soil model used should be capable of simulating the behavior of the soil mainly in active and passive stress paths.

An active stress path is defined here as one where the lateral stress decreases as the structure pulls away from the soil, and the passive stress path as one where lateral stresses increase, both starting at K_o condition. Perfect active and passive failure conditions may not exist in reality around a sheetpile in the conventional sense, i.e., vertical and horizontal planes may not be principal planes due to shear stresses that will exist on those planes.

Some triaxial (CU) test results simulating these stress paths are shown in Figure 47(a). Here, the path labeled LC (for Lateral Compression) is passive, and the path labeled LE (for Lateral Extension) is active. Stress-strain curves for these stress paths are shown in Figure 47(b).

Figure 48 presents the prediction of the model simulation program for the conditions of the tests shown in Figs. 47(a) and (b). The model parameters used were: m = 100, n = 1.0, phi = 32, c = 0, and initial

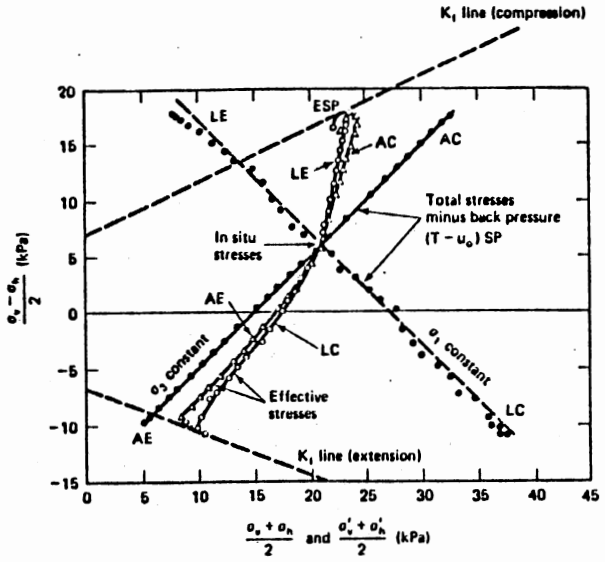

Figure 47(a). Total and effective stress paths.

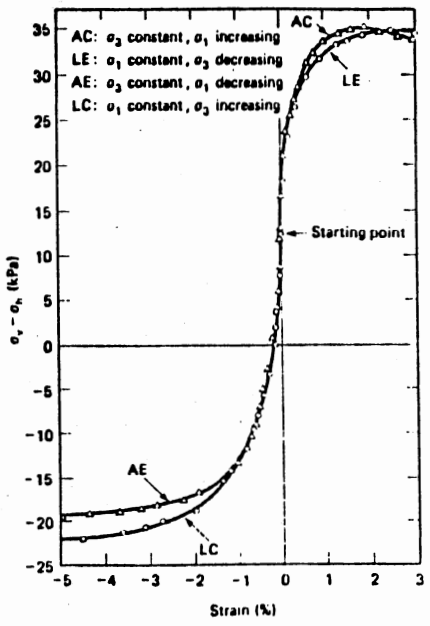

Figure 47(b). Stress-strain curves for k_o-consolidated undrained triaxial tests on a normally consolidated clay (after Bishop and Wesley, 1975).

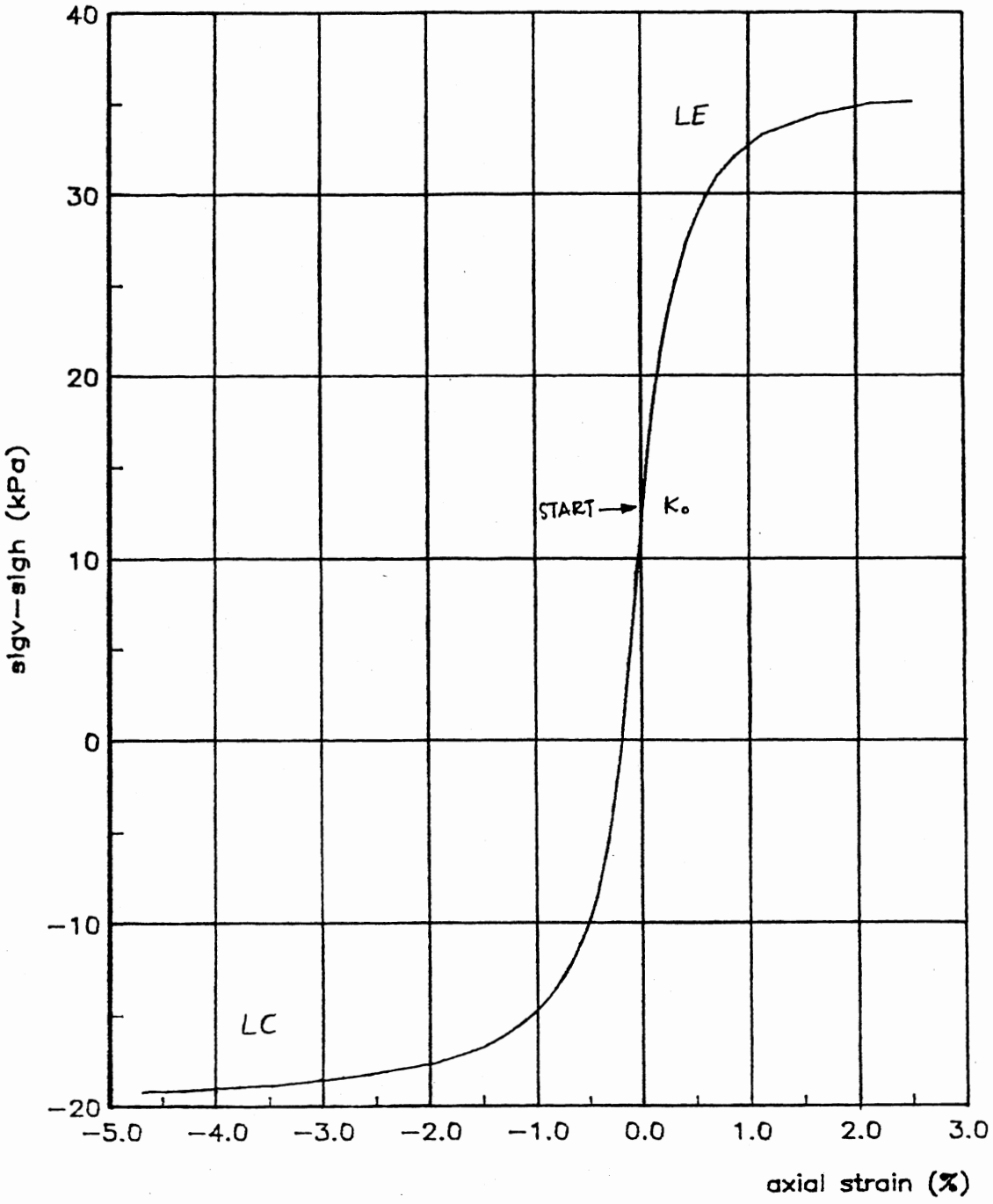

Figure 48. Bishop and Wesley data, LC and LE tests m=100, n=1.0, phi=32, sig3=4.8 kpa.

horizontal effective stress = 14.8 kPa. The phi angle and confining pressures are as given for the tests (Fig. 47), but m and n were chosen arbitrarily. A comparison of Figures 47(b) and 48 reveals the model is capable of representing soil stress-strain relationship accurately for these stress paths.

Behavior of the Model in a Finite Element Program

The initial slope method is used in the finite element analysis of the nonlinear SSI problem considered in this research. This model tends to be inaccurate if stress increments due to loading or geometry changes are large. Since relatively large loading steps are necessary in a finite element analysis to keep computing resource requirements within reasonable limits, some measures must be taken to minimize the errors due to the use of initial slope method.

To gain an understanding of the error involved, a numerical simulation was performed where loading started at Ko condition. Initially, vertical stress was 100 kPa, and horizontal stress was 50 kPa (Ko = 0.5).

Table V shows the results (vertical strain calculated) for 5, 10, 20, etc. steps of vertical stress increase, starting from 100 kPa to the failure value, 150 kPa. The last columns, 160 and 320 steps, are included for comparison with approximate cases. It is observed that the error in displacement can be as large as 20% if very few steps (such as 5) are used. If typically 10 to 20 steps are used, the calculated deformations will be about 3 to 5% smaller than "exact" values, and the error will increase as failure is approached.

TABLE V

CALCULATED VERTICAL STRAIN (%) USING VARIOUS STEP SIZES
INITIAL SLOPE METHOD

vertical stress	Total number of steps 5	10	20	40	80	160	320
110	.1333	.1393	.1425	.1441	.1449	.1454	.1456
120	.2938	.3097	.3183	.3228	.3251	.3262	.3268
130	.5012	.5362	.5555	.5656	.5708	.5734	.5747
140	.8043	.8874	.9364	.9629	.9767	.9838	.9873
145	-	1.1838	1.2812	1.3374	1.3677	1.3834	1.3914

Accelerating Model Convergence

To obtain good numerical accuracy while keeping relatively large loading step sizes, a simple and stable "acceleration" algorithm is devised. At the end of one loading step the degree of mobilization, f, is calculated for each element for use in computing the moduli for the next loading step. If an element is being loaded towards failure (the model subroutine keeps track of this), then shear modulus reduction is accelerated using a modified-f (say, f_1) rather than the computed-f (f_0) as:

$$f_1 = f_0 + (\text{change in f in last step}) * AF$$

In this equation AF is an acceleration factor that can be between 0 and 1. AF = 0 means no-acceleration (take the initial slope), and AF = 1 means to double the change in f as an estimate of the "mid-point" value for the next step. For example, if the change in f is 0.1 and f0 = 0.7, this means that the element is approaching failure (f increased from 0.6 to 0.7 in this step); the next load step will cause a further change in

f. If the loading is applied uniformly, then f will probably increase to 0.8 at the end of the next step. If no acceleration (AF = 0) is used, then the modulus will be based on f = 0.7; and if an AF value of 1.0 is used then the modulus calculation will be based on f = 0.7 + (0.1)*1.0 = 0.8.

After experimenting with different AF values in the simulation program it was found that AF should not be a constant number because when f is small (modulus close to initial slope), the curvature of the stress-strain curve is small and little acceleration is needed. On the other hand, as failure is approached (f approaches 1) the curvature changes rapidly, and a larger AF is needed. Therefore, the AF should depend on f; the simplest choice being AF = f_o.

The results in Table VI show the computed stress-strain curves with AF = f_o. It is observed that the acceleration algorithm works well for a reasonable number of steps such as 10 and 20. It is also seen that it is stable; it does not induce erratic behavior even for a very small (5) number of steps, and the correction applied is not excessive.

TABLE VI

CALCULATED VERTICAL STRAINS (%)
ACCELERATED METHOD

vertical stress	--Total number of steps-- 5	10	20
110	.1333	.1442	.1449
120	.3261	.3241	.3255
130	.5471	.5707	.5729
140	1.0127	.9819	.9851
145	(?)	1.3530	1.3883

It should be mentioned that the "f" terms in the acceleration algorithm above are replaced by the corresponding f′ values if an element is unloading and reloading. Since Masing's criterion is employed in generalizing the basic model for these cases, the shape of the stress-strain curve is the same; therefore, the behavior of the acceleration algorithm should be the same for unloading-reloading cases.

APPENDIX B

TYPICAL TEST RESULTS ON FlOODWALL FOUNDATION SOILS

Analysis of Test Results

In this section the field and laboratory test data obtained at typical floodwall sites of USAE Corps of Engineers New Orleans District are examined. Data were obtained from five sites and detailed undrained test data are available for four of these sites:

Site 1: Jeff. & St. Charles Parishes, PS#1 I-Wall

Site 2: New Orleans East Back Levee Enlargement

Site 3: Caernarvon Freshwater Diversion Structure

Site 4: Jeff. & St. Charles Parishes, PS#4 I-Wall

Tables VII and VIII give the data extracted from laboratory test sheets and other accompanying documents. Two parameters that are of main interest in this work are c_u and E_{50}; the former are given on the lab sheets, and the latter were determined for this study from the stress-strain curves. E_{50} is obtained from these curves by measuring the strain at the point where the deviator stress is one-half of the failure value. It can easily be shown that the inverse of this number is precisely the E_{50}/c_u ratio. From this ratio and the value of the undrained shear strength for that sample the E_{50} is calculated.

All calculated results are also given in the extensions of Tables VII and VIII. In order to examine the correlation of the modulus and

strength values with the index properties of these soils, other pertinent data are also shown in the same table. The column labeled "LI" contains the Liquidity Index values. LI is known to correlate with shear strength of a soil better than the more conventional parameters such as water content.

The average values of all parameters are given at the bottom of the table. The average values of interest are undrained shear strength = 566 psf, E_{50}/c_u = 130, water content = 60%, void ratio = 1.7, LL = 78. To examine the trends and correlations in this data set, various plots have been prepared as shown in Figures 49 through 55.

Depth Effect

Fig. 49 shows the variation of c_u with depth, and Fig. 50 shows the variation of E_{50} with depth. Although the scatter is considerable, there are some very clear trends. In both these figures it is seen that the soil is stiffer and stronger in the top 10 feet, and there is a weak zone around 20 ft depth. Strength and stiffness both start to increase beginning at about 20 ft. In all four sites, the borings were made on the levees and the heights of the levee fills are about 10 ft. Therefore, the top stiffer layer is the levee material. The increase with depth seems to start at about the original ground surface elevation (as is normally the case with NC clays). The stronger layer around 20 ft depth is either the desiccated natural top soil or the soil is somewhat consolidated under the weight of the levee fill. The four points (at depth 25′) that lie outside the main correlation in Fig. 49 belong to an exceptional type of soil (probably montmorillonite) where water contents are in the order of 300. However, the fact that LL about

400 makes LI approximately 0.3, explains the strength of this soil.

Void Ratio Effect

Fig. 51 shows the variation of E_{50} with void ratio. The high void ratio range is apparent in this figure: the typical range is from 1 to 2 and there are values as high as 8. The scatter clouds the expected correlation (stiffness should decrease with e). The trend becomes somewhat clearer in Fig. 52 where the void ratio scale is inverted. The points that are offset from the main stream belong to various sites at about 40 to 50 ft depth. The shear strength of these soils is proportionately larger; thus the modulus/strength ratio remains in the same general range.

Water Content/LI Effect

The effect of water content should be expressed in terms of its relative value with respect to the plasticity parameters of the soil. Indeed, when the shear strength or stiffness is plotted against water content, no correlation is observed. But when liquidity index is used, the correlation is obvious. The shear strength versus liquidity index correlation is shown in Fig. 53, and that for E_{50} is shown in Fig. 54. The nature and rate of change of these two key parameters with LI are the same.

Modulus/Strength Ratio

Finally, E_{50}/c_u ratios for all samples can be seen in Fig. 55. The straight lines superposed on this plot show that the modulus/strength ratio range for these soils is 50 to 350 with an average of about 150.

The average value may not be very significant as there are few points around this average; it appears the soils fall in two groups, one in the range 50-100, and the other in the range 200-350.

Choice of Parameters for Case Studies

There is a wide scatter in strength and stiffness parameters of the soft clay soils involved in typical floodwall sites of the New Orleans District, but there are also some clear trends. The first attempt made in examining the data available shows that the levee fill materials have strength values falling in the range generally classified as medium to very soft clays. The soil immediately underneath the levee fills (for about a thickness of 5 to 10 ft) seems to have consolidated somewhat and reached a strength only slightly less than that of the fills. Below a depth of about 20 ft the soil shows the typical normally-consolidated behavior; both strength and stiffness increase with depth. The modulus/strength ratio ranges between 50 and 350 for these soils. These observations may be used in selecting idealized sections and analysis basis parameters for future studies of the floodwall problem.

TABLE VII

USAE COE NEW ORLEANS DISTRICT
SOIL TEST DATA

	sheet		c_u (psf)	PL (%)	LL (%)	PI (%)	w (%)
Site 1	1	sample 1	1710	17.0	50.0	33.0	24.0
		sample 2	2030	17.0	50.0	33.0	23.2
	2	sample 1	560	19.0	58.0	39.0	36.0
		sample 2	500	19.0	58.0	39.0	34.0
		sample 3	500	19.0	58.0	39.0	34.2
	3	sample 1	113	21.0	83.0	62.0	64.6
		sample 2	113	21.0	83.0	62.0	66.8
		sample 3	113	21.0	83.0	62.0	61.9
	4	sample 1	125	17.0	57.0	40.0	47.6
		sample 2	125	17.0	57.0	40.0	49.1
		sample 3	125	17.0	57.0	40.0	42.3
	5	sample 1	370	18.0	53.0	35.0	47.3
		sample 2	400	18.0	53.0	35.0	45.9
		sample 3	610	18.0	53.0	35.0	40.0
		sample 4	570	18.0	53.0	35.0	42.9
	6	sample 1	530	22.0	88.0	66.0	61.6
		sample 2	510	22.0	88.0	66.0	62.9
		sample 3	590	22.0	88.0	66.0	61.9
	7	sample 1	690	18.0	53.0	35.0	50.5
		sample 2	500	18.0	53.0	35.0	51.5
		sample 3	510	18.0	53.0	35.0	53.1
Site 2	1	sample 1	420	13.0	41.0	28.0	24.6
		sample 2	680	13.0	41.0	28.0	35.6
		sample 3	600	13.0	41.0	28.0	27.4
		sample 4	510	13.0	41.0	28.0	27.1
	2	sample 1	500	19.0	58.0	39.0	47.8
		sample 2	210	19.0	58.0	39.0	40.1
		sample 3	210	19.0	58.0	39.0	73.3
		sample 4	320	19.0	58.0	39.0	59.2
	3	sample 1	630	18.0	55.0	37.0	42.6
		sample 2	630	18.0	55.0	37.0	43.0
		sample 3	500	18.0	55.0	37.0	44.8
Site 3	1	sample 1	130	30.0	150.0	120.0	39.0
		sample 2	130	30.0	150.0	120.0	37.3
		sample 3	140	30.0	150.0	120.0	37.7
	2	sample 1	90	22.0	68.0	46.0	74.7
		sample 2	100	22.0	68.0	46.0	75.3
		sample 3	110	22.0	68.0	46.0	75.9
	3	sample 1	110	21.0	73.0	52.0	66.9
		sample 2	130	21.0	73.0	52.0	72.7
		sample 3	180	21.0	73.0	52.0	72.5

TABLE VII (Continued)

	sheet		c_u (psf)	PL (%)	LL (%)	PI (%)	w (%)
Site 3	4	sample 1	370	21.0	59.0	38.0	76.3
		sample 2	420	21.0	59.0	38.0	75.3
		sample 3	340	21.0	59.0	38.0	76.1
	5	sample 1	420	18.0	49.0	31.0	63.1
		sample 2	510	18.0	49.0	31.0	64.2
		sample 3	430	18.0	49.0	31.0	63.4
	6	sample 1	650	24.0	83.0	59.0	66.3
		sample 2	560	24.0	83.0	59.0	66.3
		sample 3	680	24.0	83.0	59.0	65.7
Site 4	1	sample 1	540	13.0	51.0	38.0	28.3
		sample 2	870	13.0	51.0	38.0	29.0
		sample 3	890	13.0	51.0	38.0	31.4
	2	sample 1	280	15.0	51.0	36.0	35.2
		sample 2	390	15.0	51.0	36.0	34.5
		sample 3	390	15.0	51.0	36.0	33.9
		sample 4	390	15.0	51.0	36.0	33.9
	3	sample 1	600	15.0	39.0	24.0	33.5
		sample 2	540	15.0	39.0	24.0	34.4
		sample 3	410	15.0	39.0	24.0	56.9
		sample 4	410	15.0	39.0	24.0	41.2
	4	sample 1	1220	213.0	414.0	201.0	294.8
		sample 2	1860	213.0	414.0	201.0	326.9
		sample 3	1700	213.0	414.0	201.0	340.3
		sample 4	1310	213.0	414.0	201.0	314.5
	5	sample 1	820	25.0	88.0	63.0	62.8
		sample 2	640	25.0	88.0	63.0	62.6
		sample 3	620	25.0	88.0	63.0	62.3
		sample 4	740	25.0	88.0	63.0	61.9
	6	sample 1	990	23.0	74.0	51.0	61.4
		sample 2	1000	23.0	74.0	51.0	60.3
		sample 3	980	23.0	74.0	51.0	63.3
	7	sample 1	1420	20.0	72.0	52.0	27.0
		sample 2	1600	20.0	72.0	52.0	29.5
		sample 3	1910	20.0	72.0	52.0	22.7
		sample 4	1320	20.0	72.0	52.0	28.4
Averages:			559	27.4	77.6	50.2	59.1

TABLE VIII

USAE COE NEW ORLEANS DISTRICT
SOIL TEST DATA

	sheet	LI	e	S (%)	depth (ft)	E_{50}/c_u	E_{50} (ksf)
Site 1	1	0.21	0.780	82.2	2.2	58.8	100.6
		0.19	0.712	87.0	2.2	83.3	169.2
	2	0.44	0.971	99.0	2.2	250.0	140.0
		0.38	0.921	98.6	9.4	250.0	125.0
		0.39	0.945	96.6	9.4	250.0	125.0
	3	0.70	1.712	100.7	20.0	333.3	37.7
		0.74	1.767	100.9	20.0	333.3	37.7
		0.66	1.655	99.9	20.0	333.3	37.7
	4	0.77	1.293	98.3	21.4	100.0	12.5
		0.80	1.327	98.8	21.4	100.0	12.5
		0.63	1.171	96.4	21.4	100.0	12.5
	5	0.84	1.256	100.6	29.3	80.0	29.6
		0.80	1.252	97.9	29.3	80.0	32.0
		0.63	1.100	97.1	29.3	80.0	48.8
		0.71	1.181	97.0	29.3	80.0	45.6
	6	0.60	1.657	99.3	40.7	250.0	132.5
		0.62	1.683	99.8	40.7	250.0	127.5
		0.60	1.647	100.3	40.7	250.0	147.5
	7	0.93	1.453	92.8	51.8	111.1	76.7
		0.96	1.473	93.4	51.8	83.3	41.7
		1.00	1.474	96.2	51.8	100.0	51.0
Site 2	1	0.41	0.684	96.0	12.0	100.0	42.0
		0.81	0.998	95.2	12.0	100.0	68.0
		0.51	0.750	97.5	12.0	71.4	42.9
		0.50	0.772	93.7	12.0	71.4	36.4
	2	0.74	1.526	83.6	21.0	62.5	31.3
		0.54	1.332	80.4	21.0	62.5	13.1
		1.39	1.801	108.7	21.0	66.7	14.0
		1.03	1.706	92.7	21.0	100.0	32.0
	3	0.66	1.238	91.9	37.0	83.3	52.5
		0.68	1.209	95.0	37.0	83.3	52.5
		0.72	1.285	93.1	37.0	62.5	31.3
Site 3	1	0.08	3.323	31.3	2.2	52.6	6.8
		0.06	3.518	28.3	2.2	52.6	6.8
		0.06	3.472	29.0	2.2	62.5	8.8
	2	1.15	2.063	96.7	9.0	50.0	4.5
		1.16	2.082	96.6	9.0	55.6	5.6
		1.17	2.106	96.2	9.0	76.9	8.5
	3	0.88	1.830	97.6	21.0	250.0	27.5
		0.99	1.945	99.8	21.0	200.0	26.0
		0.99	1.915	101.1	21.0	200.0	36.0

Table VIII (Continued)

	sheet	LI	e	S (%)	depth (ft)	E_{50}/c_u	E_{50} (ksf)
Site 3	4	1.46	2.021	100.8	32.0	200.0	74.0
		1.43	2.012	99.9	32.0	200.0	84.0
		1.45	2.022	100.5	32.0	200.0	68.0
	5	1.45	1.696	99.3	45.0	181.8	76.4
		1.49	1.717	99.8	45.0	166.7	85.0
		1.46	1.701	99.5	45.0	181.8	78.2
	6	0.72	1.771	100.0	56.1	200.0	130.0
		0.72	1.777	99.6	56.1	250.0	140.0
		0.71	1.749	100.3	56.1	250.0	170.0
Site 4	1	0.40	0.875	86.4	4.5	200.0	108.0
		0.42	0.866	89.4	4.5	100.0	87.0
		0.48	0.924	90.7	4.5	200.0	178.0
	2	0.56	0.972	96.7	13.0	333.3	93.3
		0.54	0.997	92.4	13.0	181.8	70.9
		0.52	0.931	97.2	13.0	200.0	78.0
		0.52	0.969	93.4	13.0	200.0	78.0
	3	0.77	0.931	96.1	20.6	35.7	21.4
		0.81	0.969	94.8	20.6	100.0	54.0
		1.75	1.584	95.9	20.6	55.6	22.8
		1.09	1.154	95.3	20.6	55.6	22.8
	4	0.41	7.641	103.0	25.0	52.6	64.2
		0.57	8.509	102.6	25.0	55.6	103.3
		0.63	8.845	102.7	25.0	50.0	85.0
		0.50	8.192	102.5	25.0	50.0	65.5
	5	0.60	1.653	101.4	40.4	222.2	182.2
		0.60	1.659	100.7	40.4	153.8	98.5
		0.59	1.650	100.8	40.4	125.0	77.5
		0.59	1.640	100.8	40.4	125.0	92.5
	6	0.75	1.665	98.5	52.0	166.7	165.0
		0.73	1.644	97.9	52.0	166.7	166.7
		0.79	1.694	99.8	52.0	166.7	163.3
	7	0.13	0.730	98.8	60.7	62.5	88.8
		0.18	0.784	100.5	60.7	153.8	246.2
		0.05	0.680	89.1	60.7	105.3	201.1
		0.18	0.791	99.2	60.7	181.8	240.0
Averages:		0.63	1.709	87.4	25.5	132.7	71.3

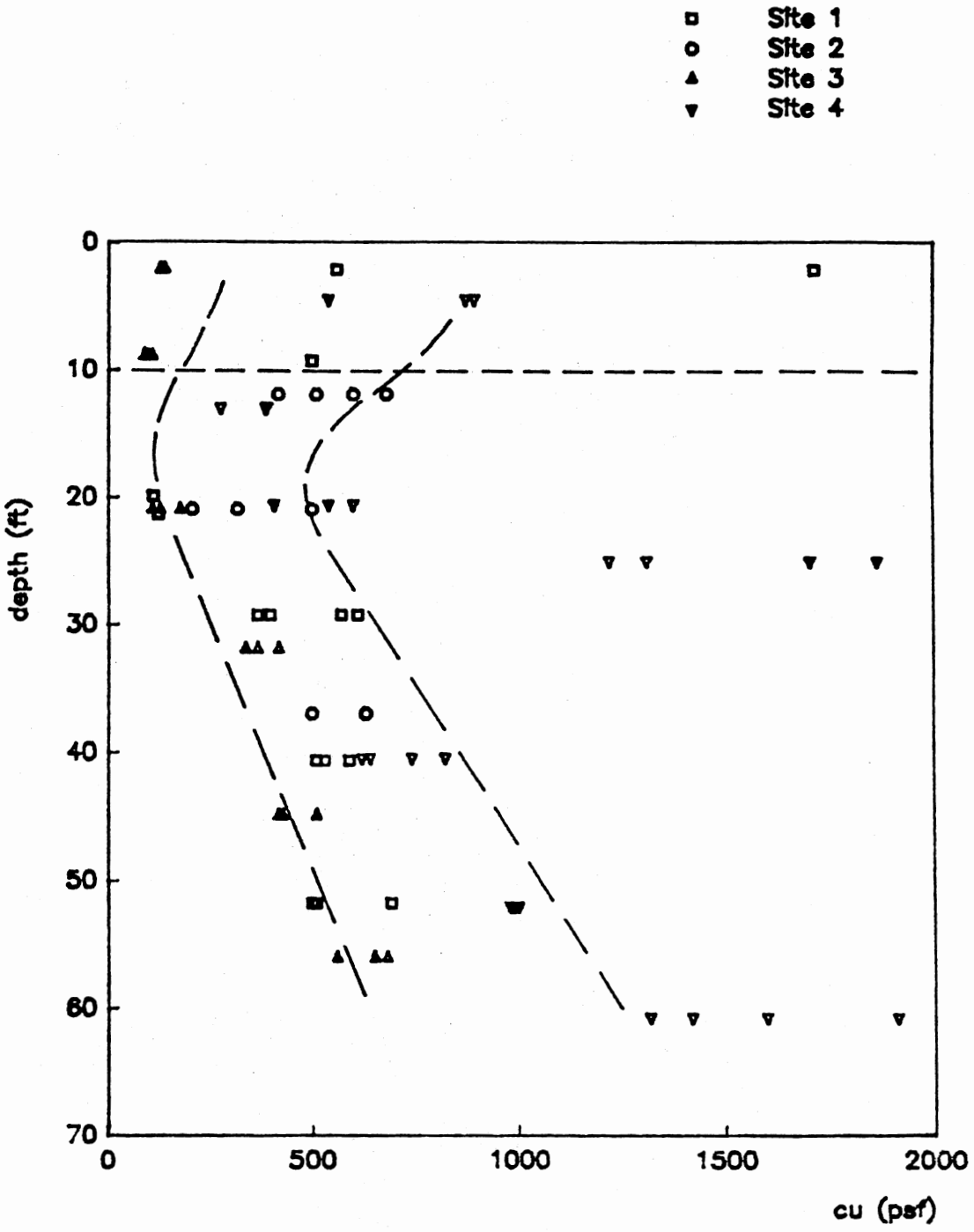

Figure 49. Strength variation with depth.

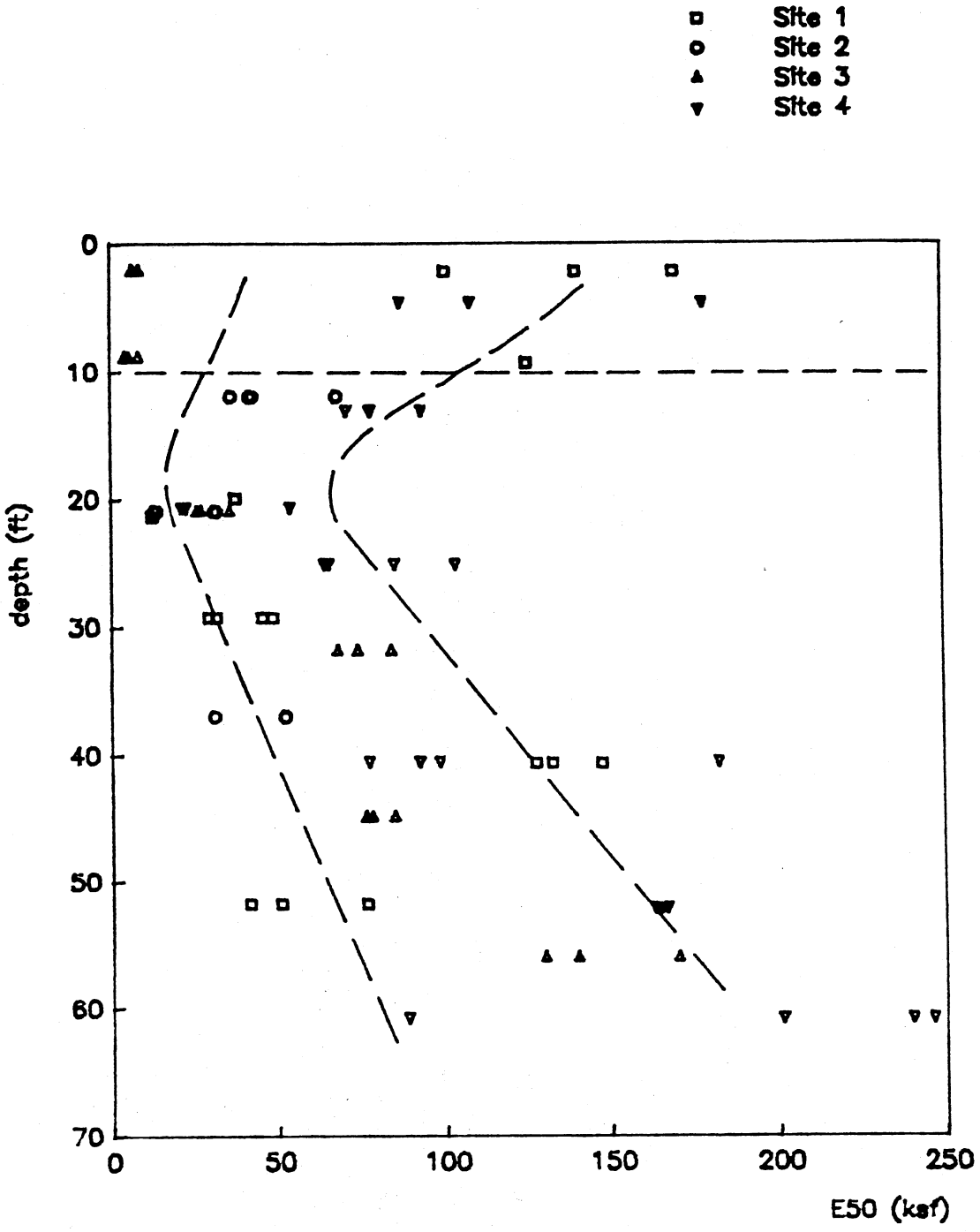

Figure 50. E50 variation with depth.

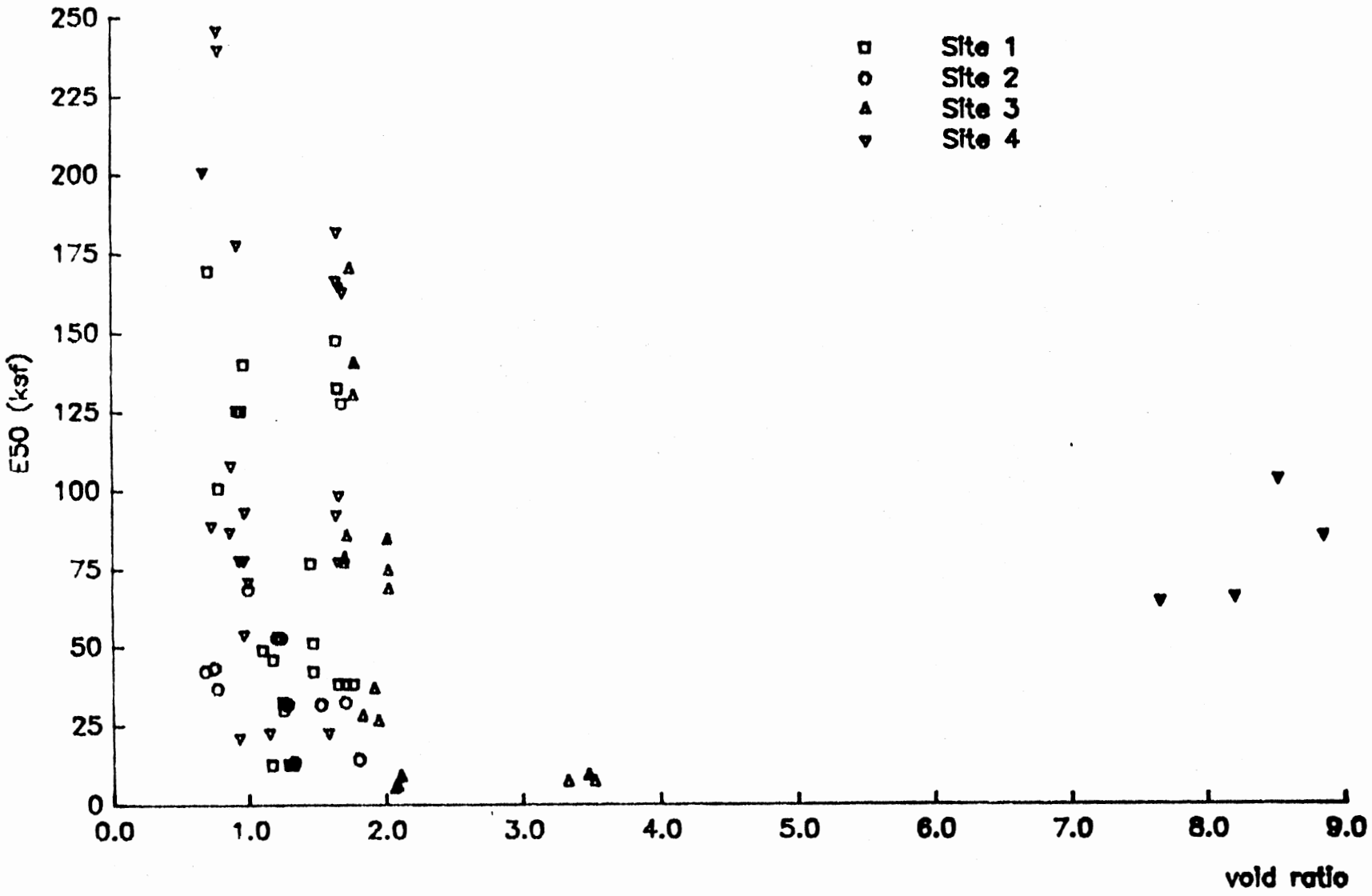

Figure 51. E50 versus void ratio.

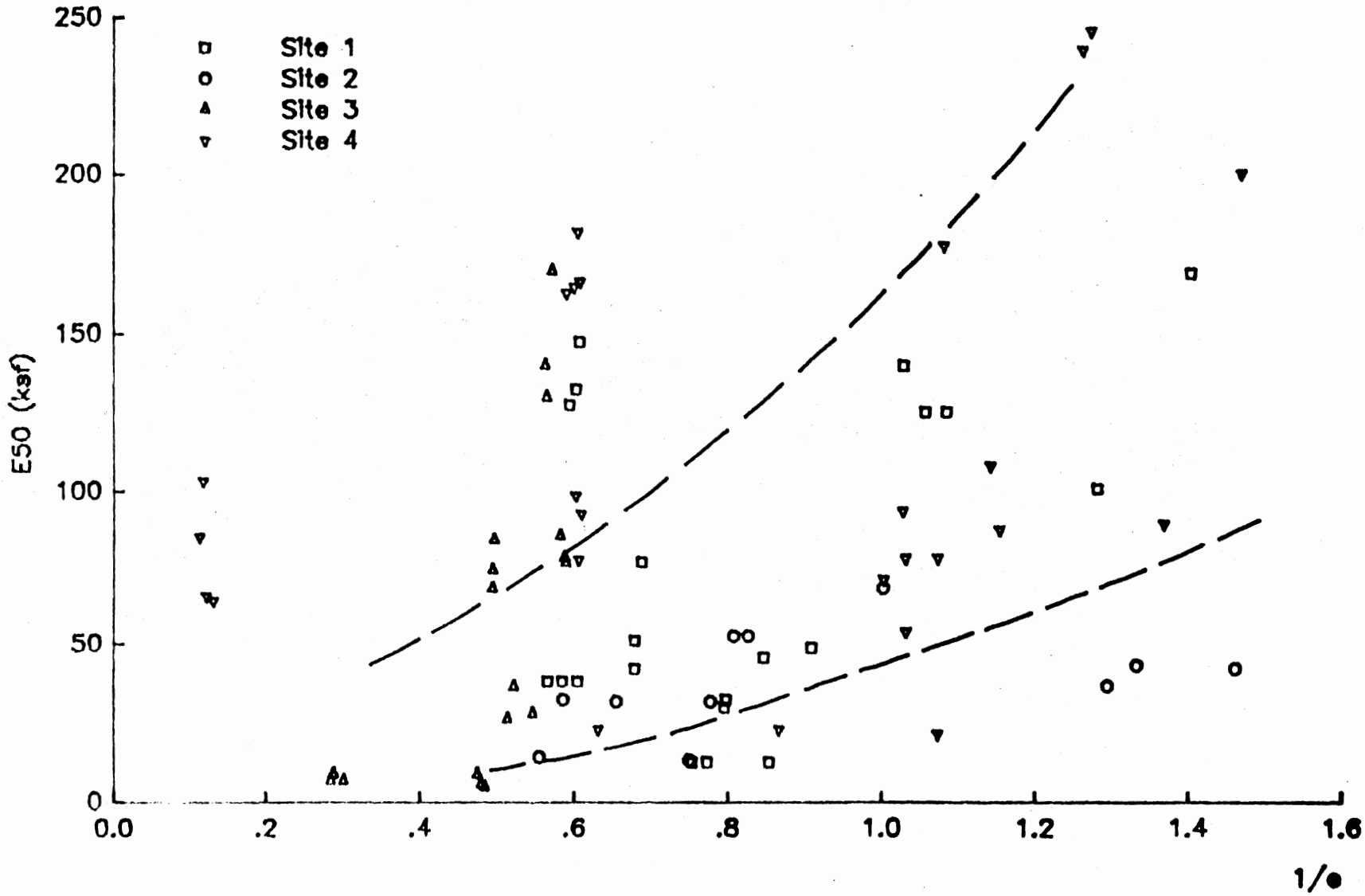

Figure 52. Variation of E50 with 1/e.

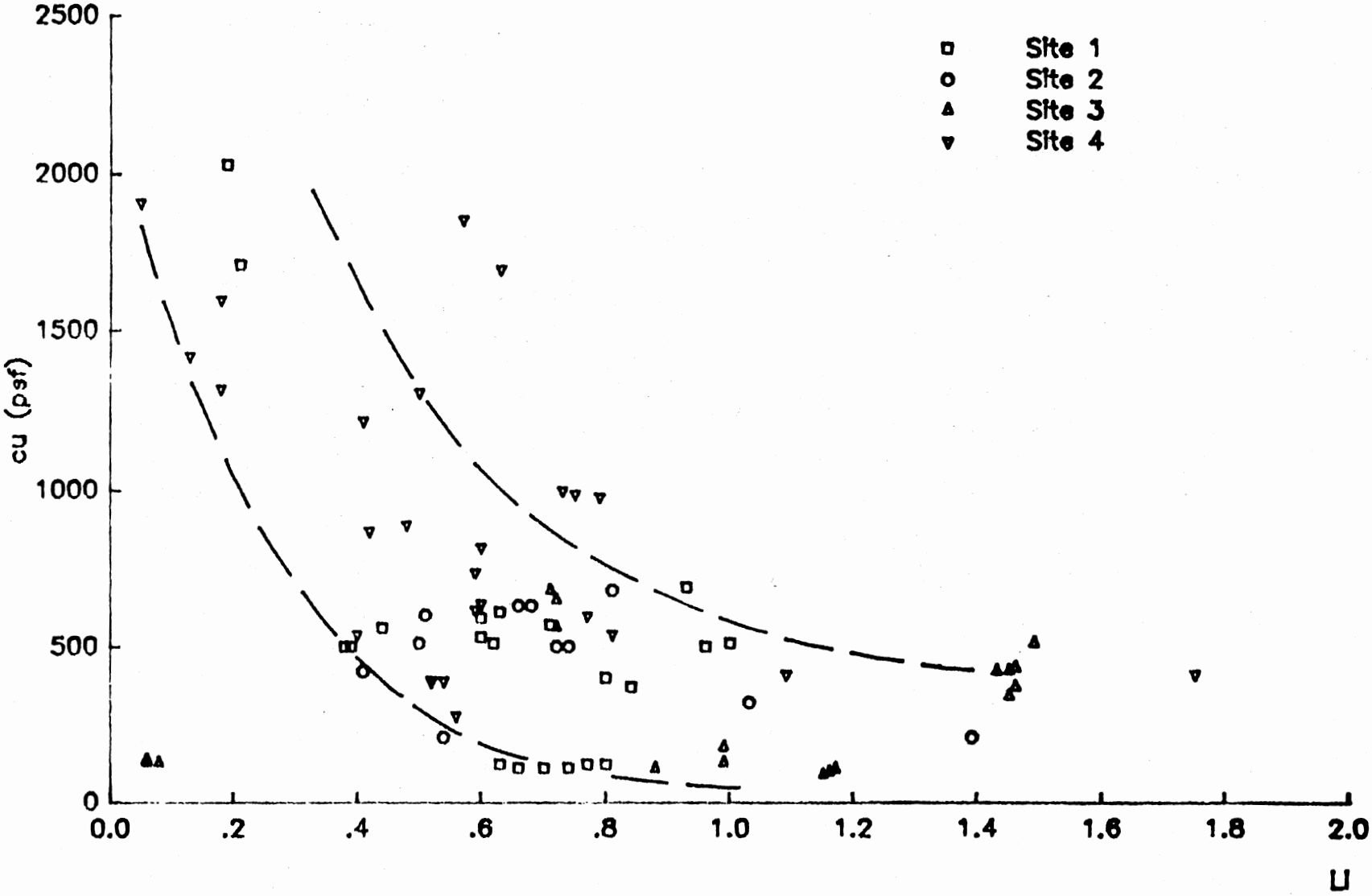

Figure 53. Liquidity index versus cu.

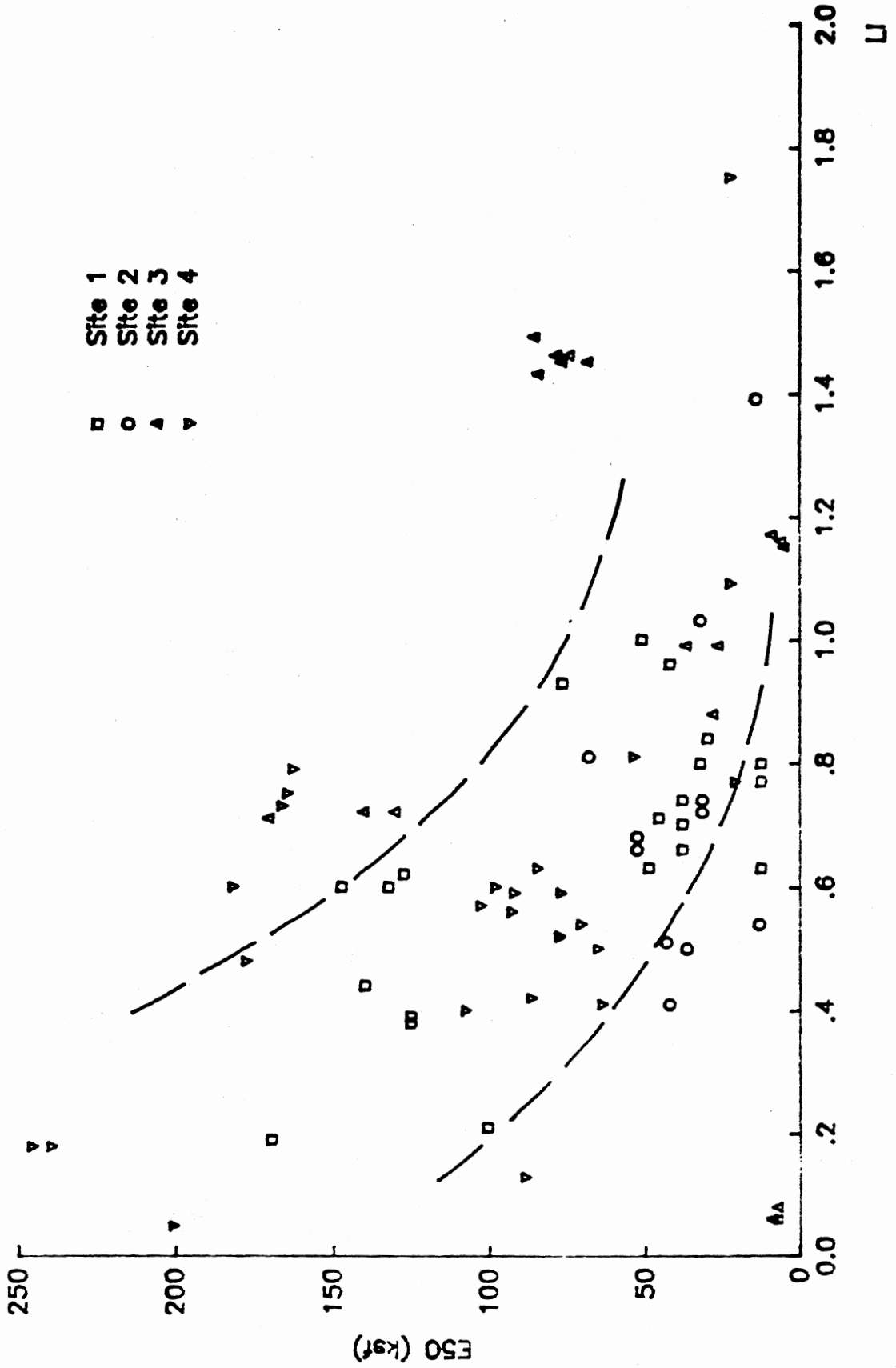

Figure 54. Liquidity index effect on E50.

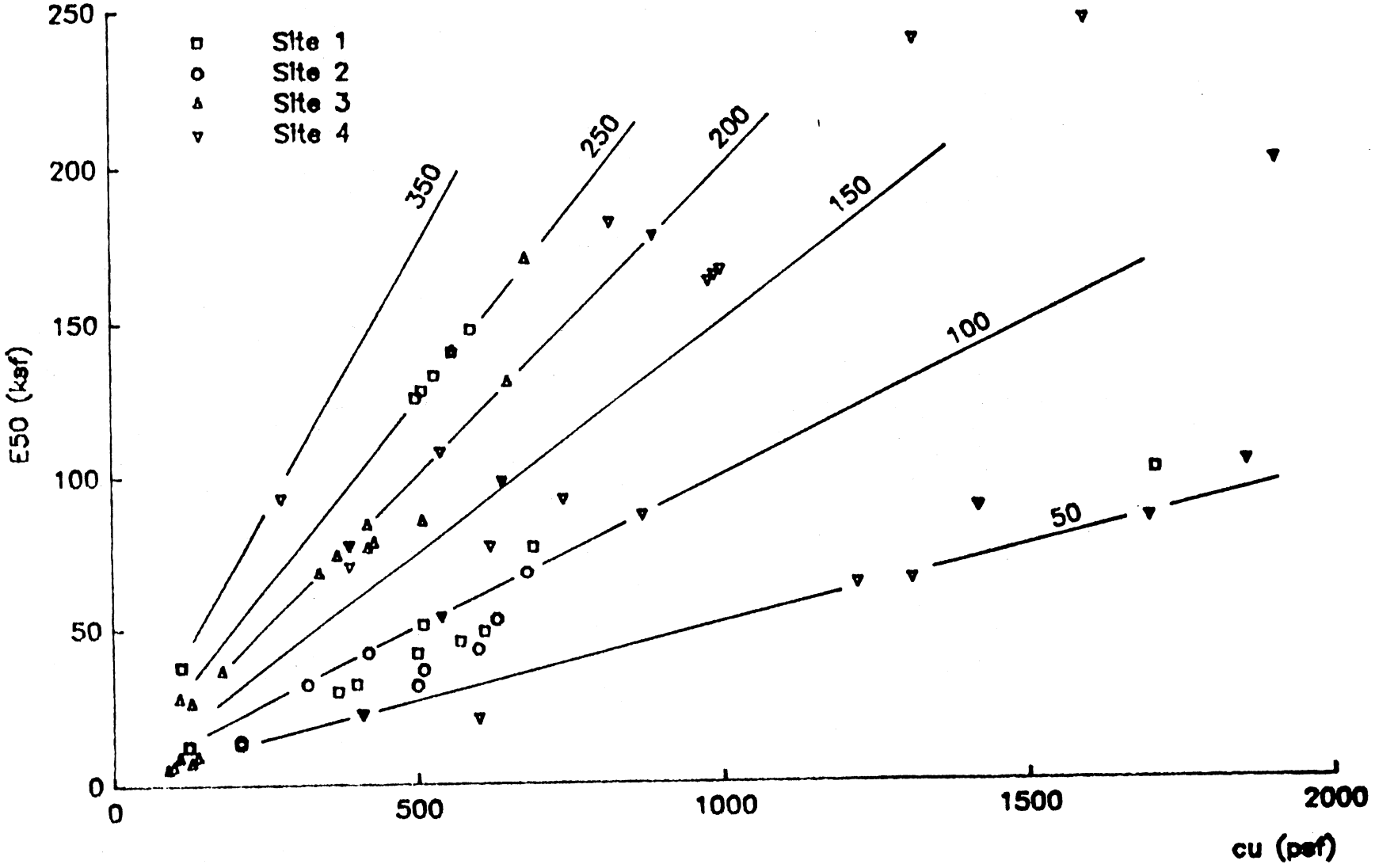

Figure 55. E50 versus strength.

APPENDIX C

HIGH STRENGTH CASE RESULTS

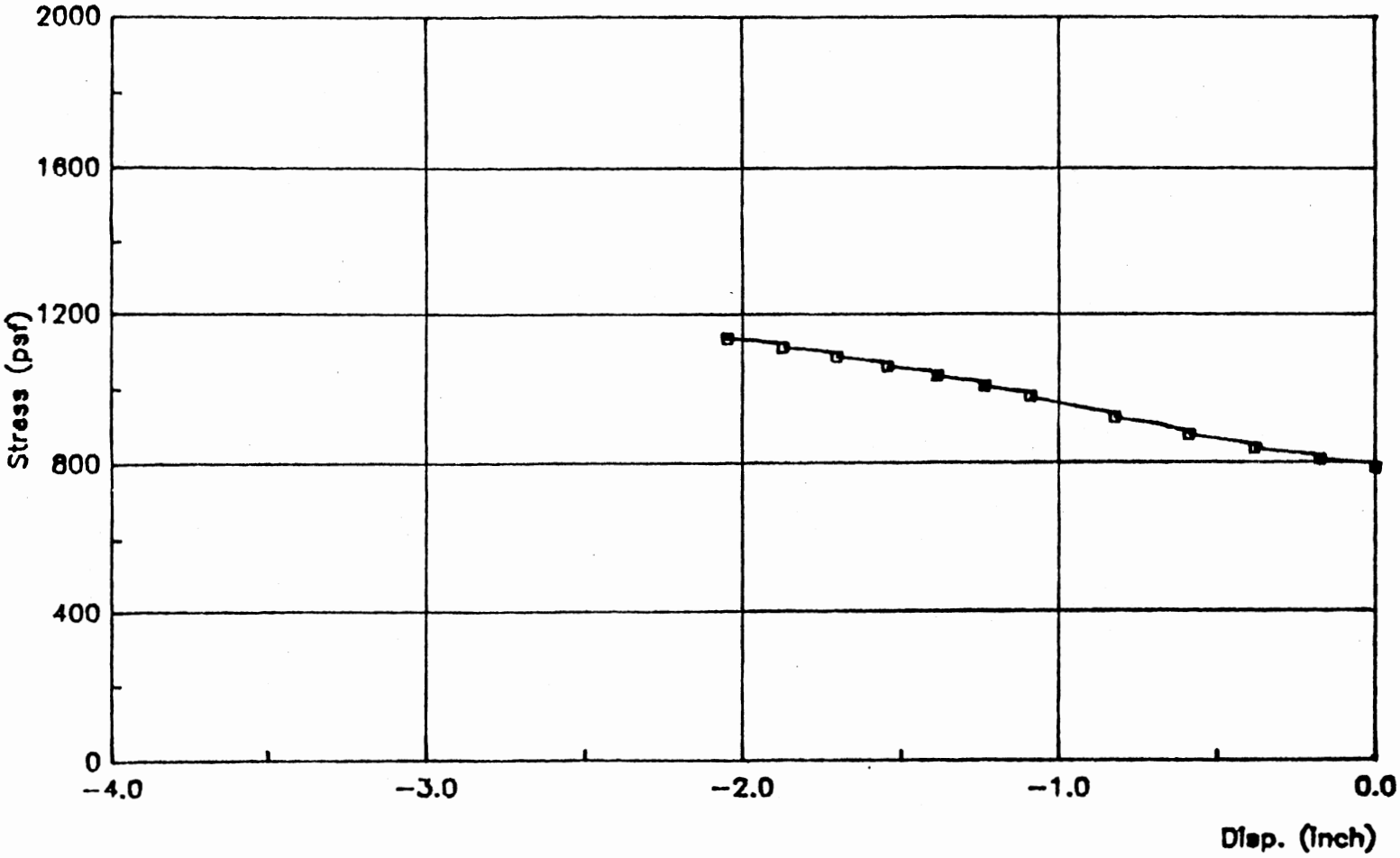

Figure 56(a). Soil-Response curve at -5 ft elevation, front side, high strength profile, 20 ft pile penetration.

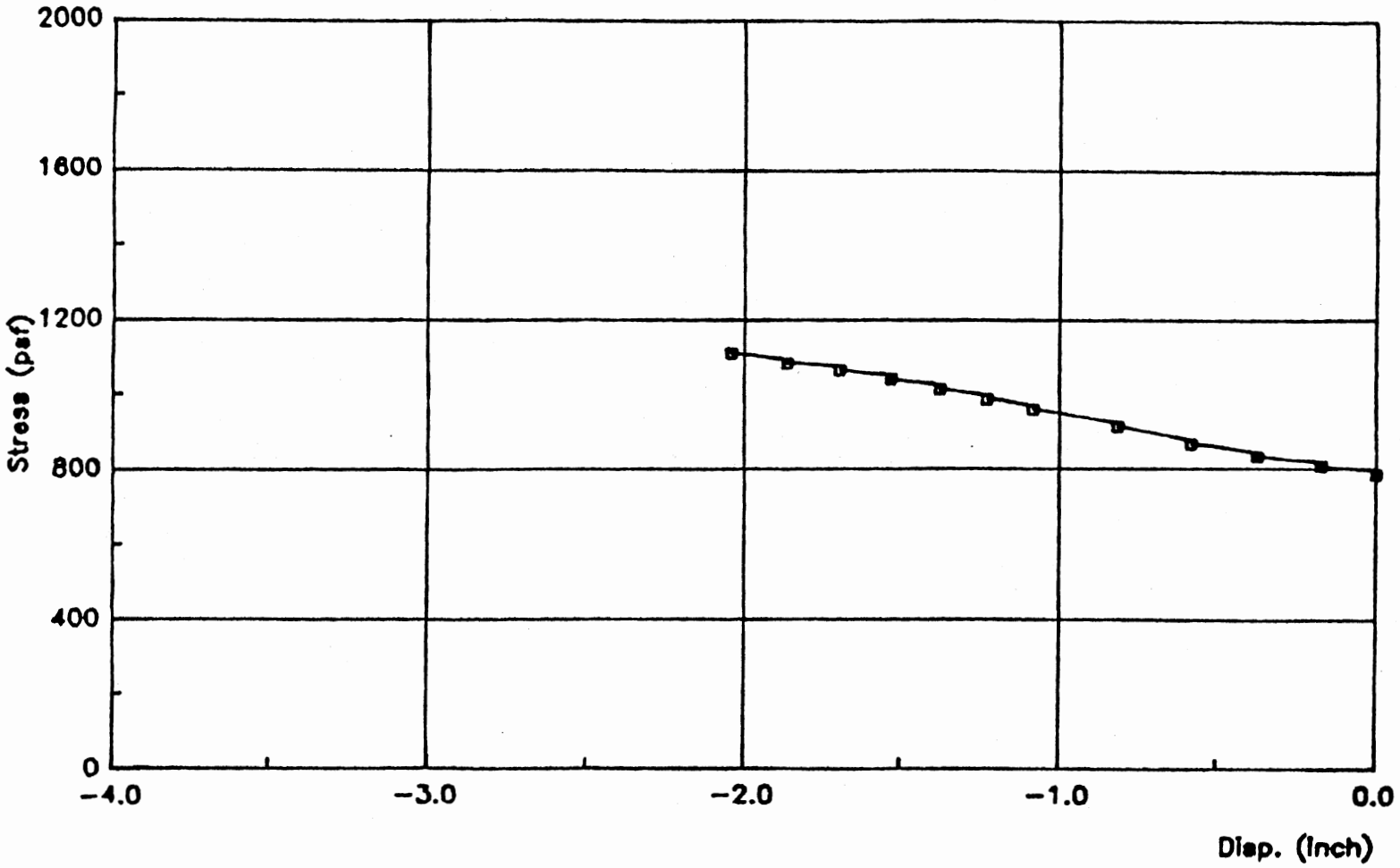

Figure 56(b). Soil-Response curve at -5 ft elevation, front side, high strength profile, 30 ft pile penetration.

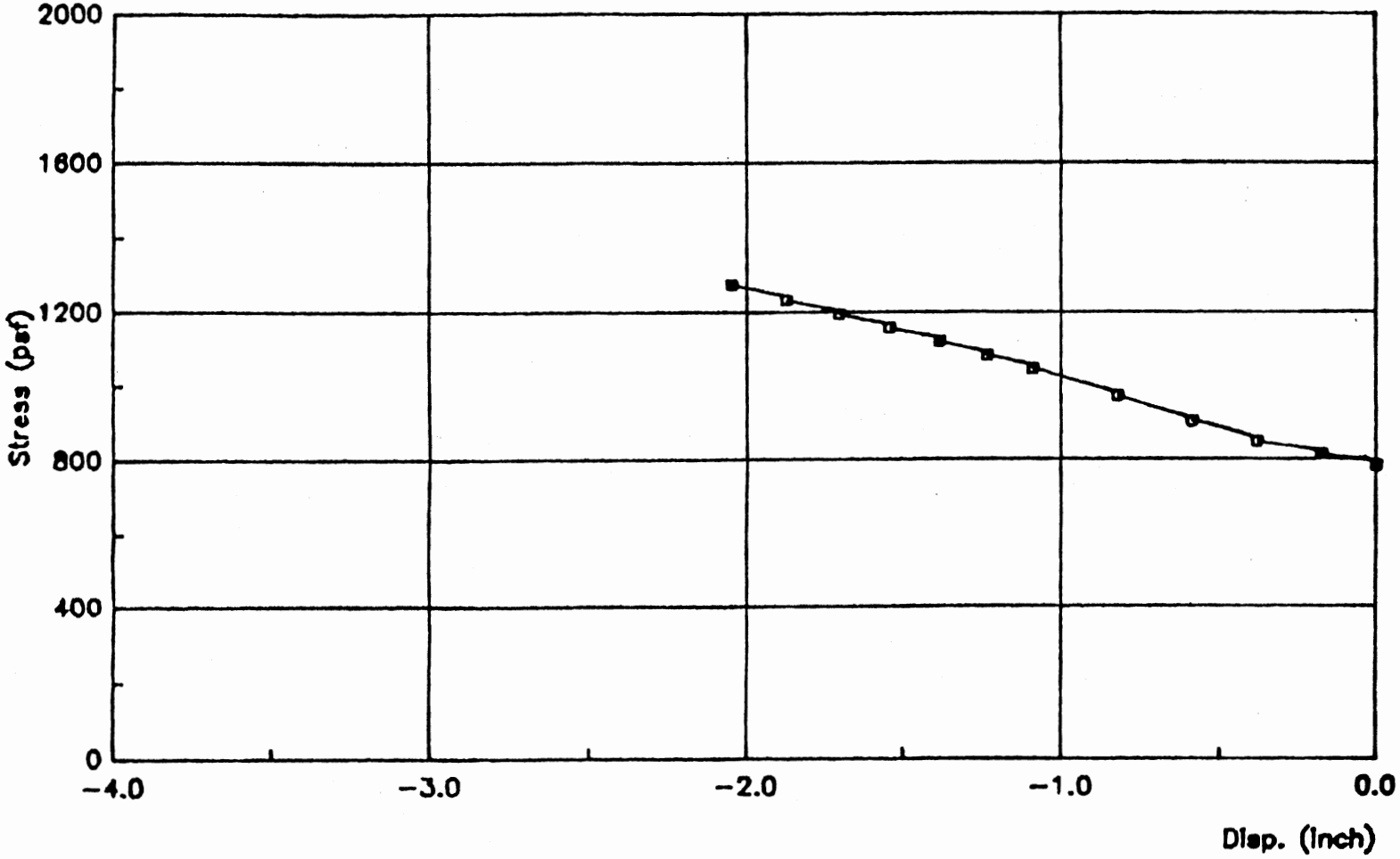

Figure 56(c). Soil-Response curve at -5 ft elevation, back side, high strength profile, 20 ft pile penetration.

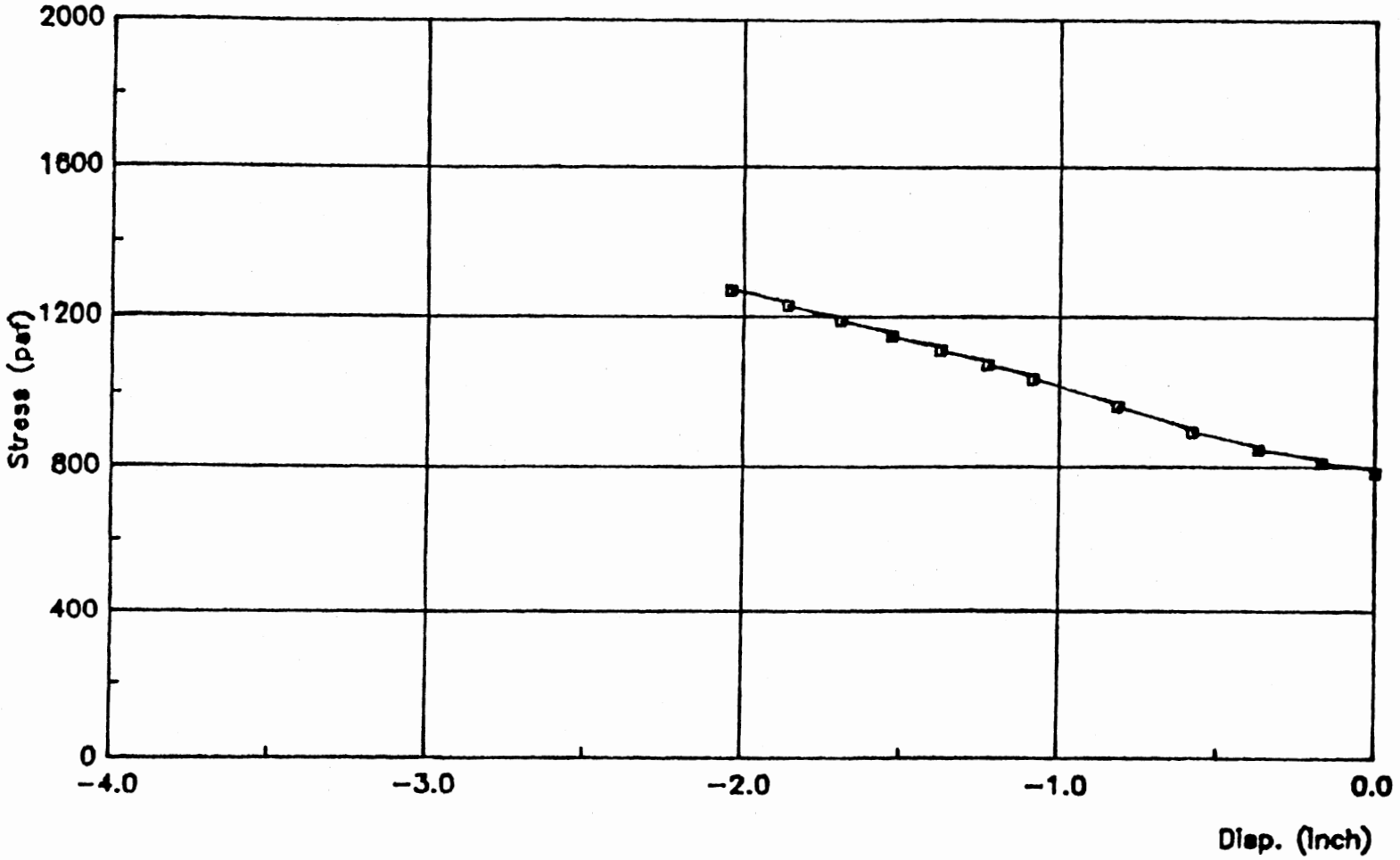

Figure 56(d). Soil-Response curve at -5 ft elevation, back side, high strength profile, 30 ft pile penetration.

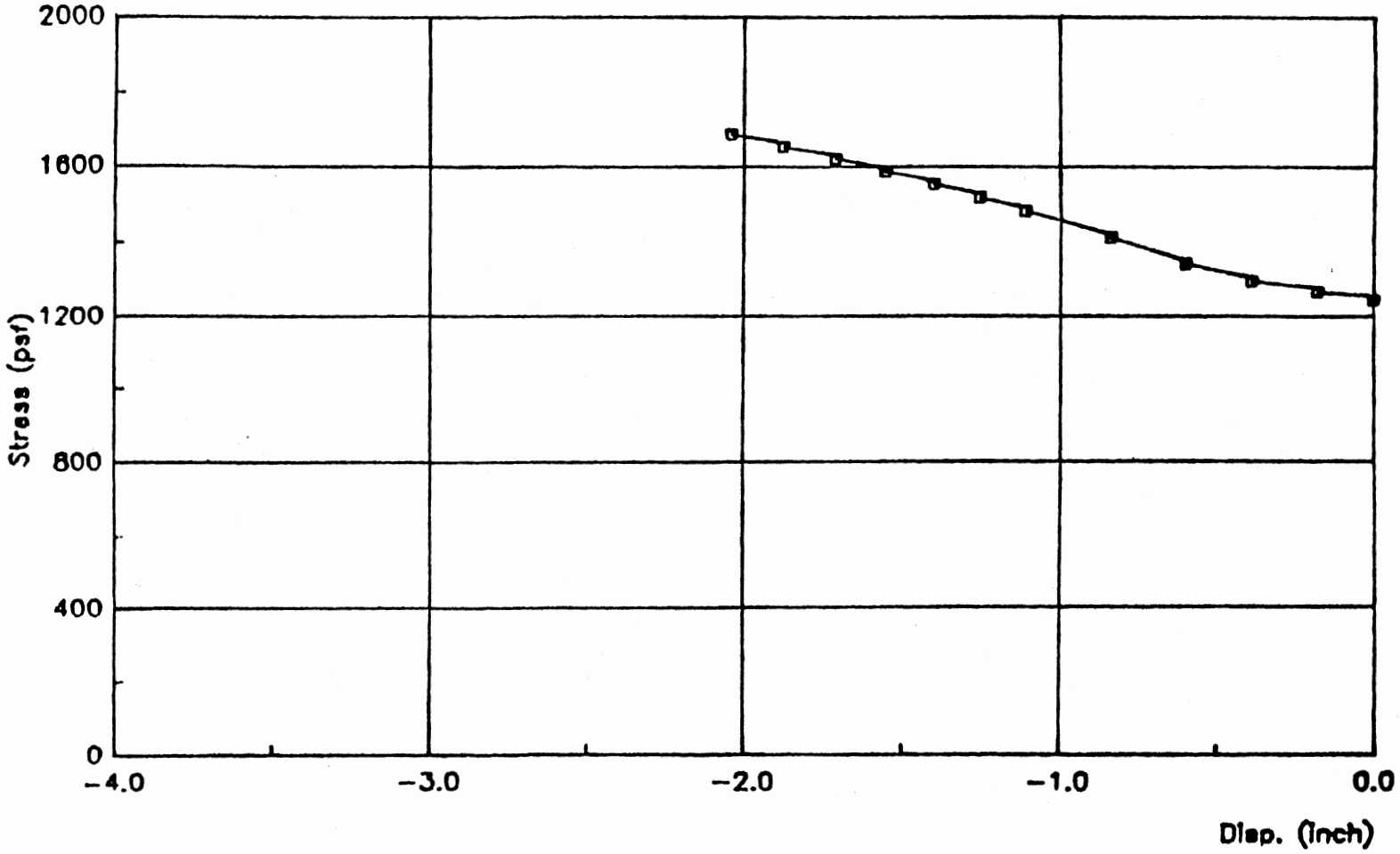

Figure 57(a). Soil-Response curve at -9 ft elevation, front side, high strength profile, 20 ft pile penetration.

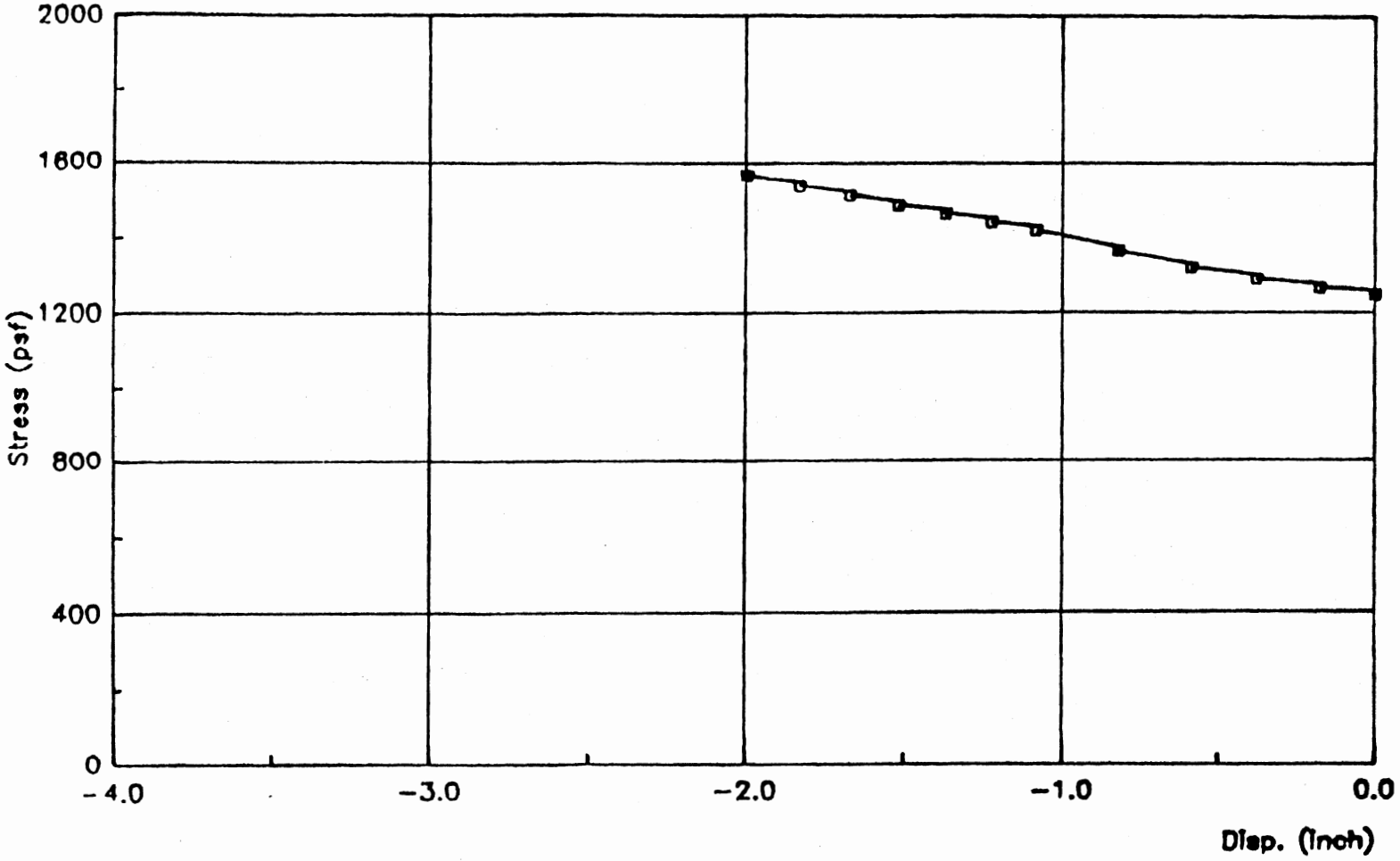

Figure 57(b). Soil-Response curve at -9 ft elevation, front side, high strength profile, 30 ft pile penetration.

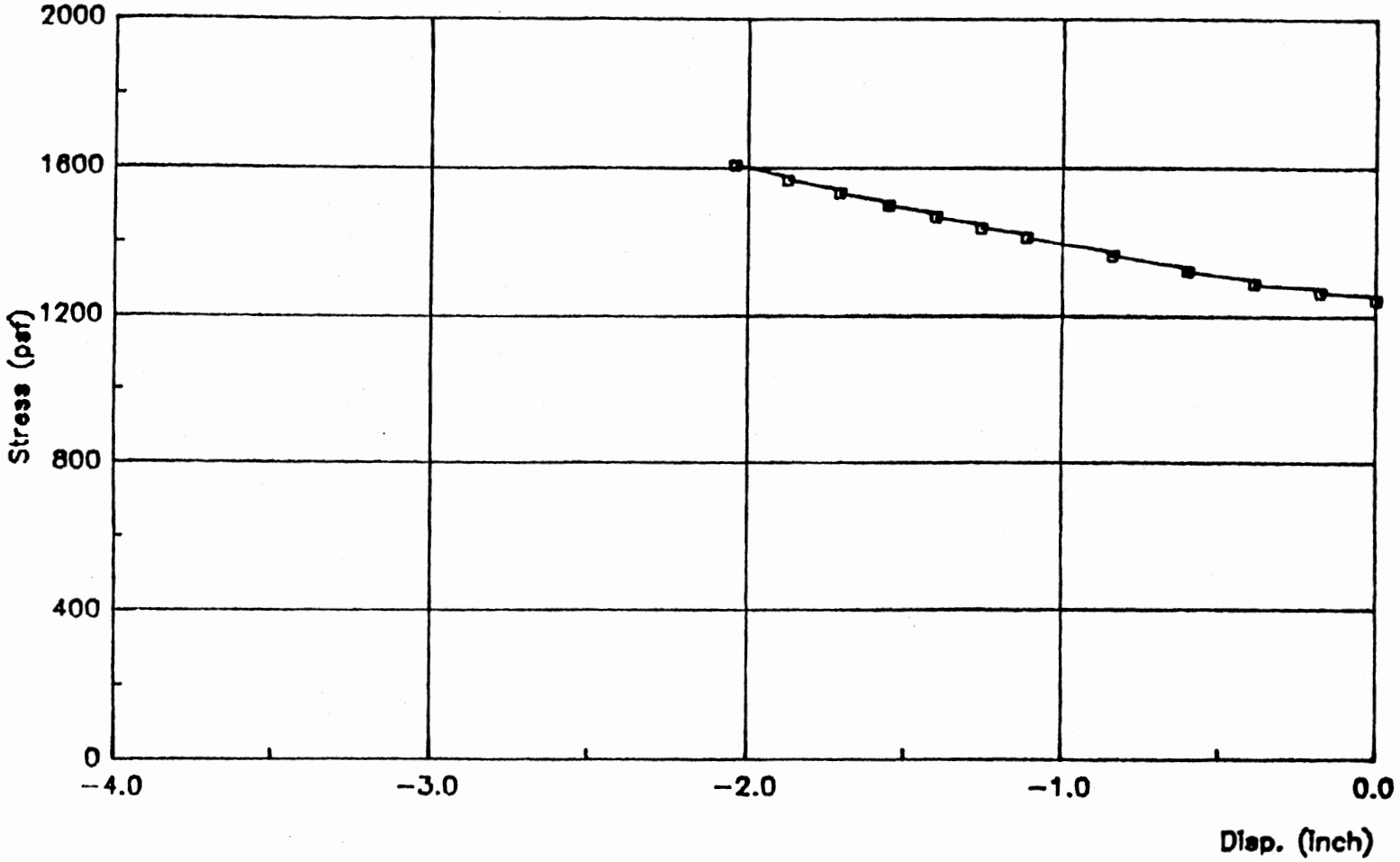

Figure 57(c). Soil-Response curve at -9 ft elevation, back side, high strength profile, 20 ft pile penetration.

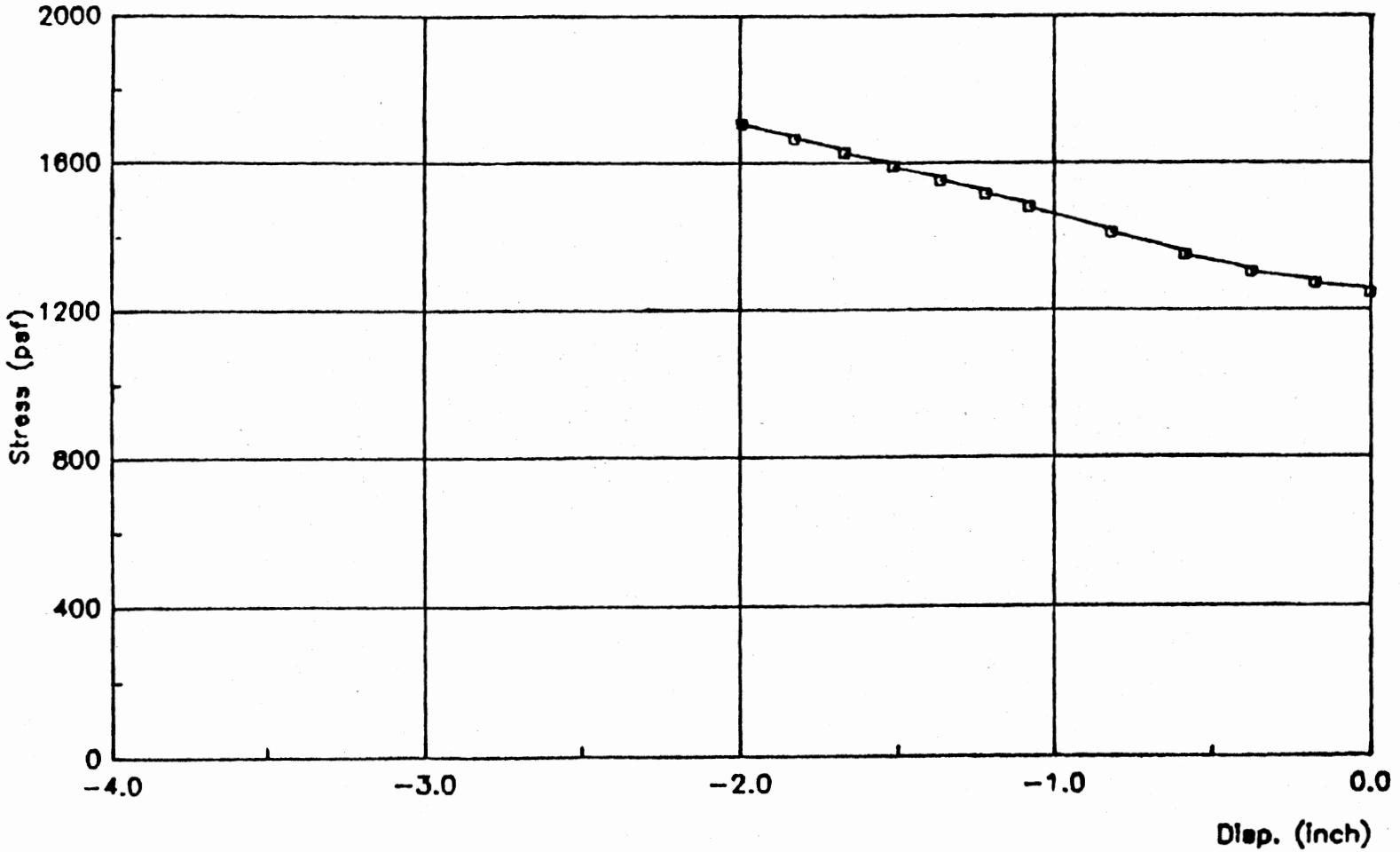

Figure 57(d). Soil-Response curve at -8 ft elevation, back side, high strength profile, 30 ft pile penetration.

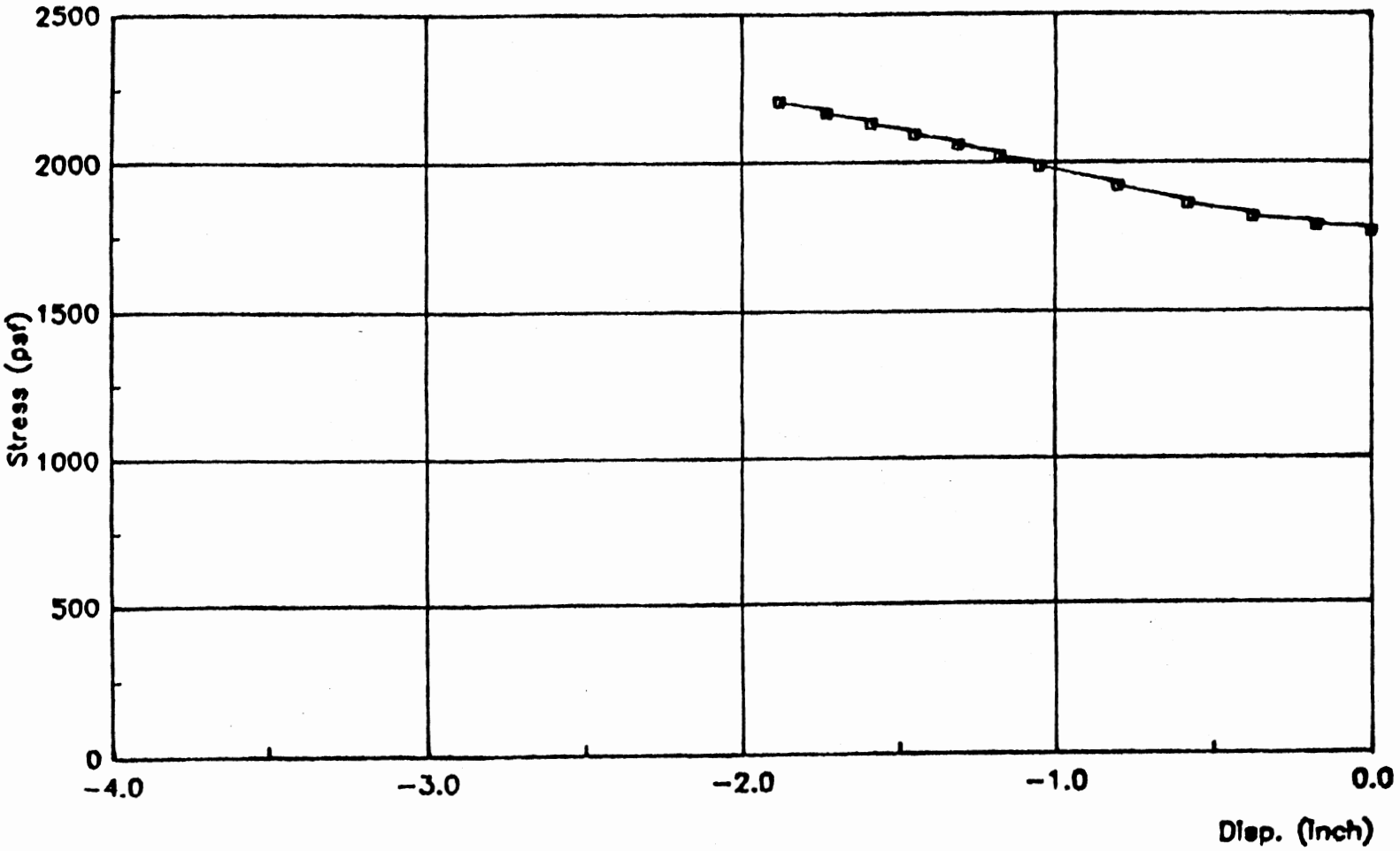

Figure 58(a). Soil-Response curve at -15 ft elevation, front side, high strength profile, 30 ft pile penetration.

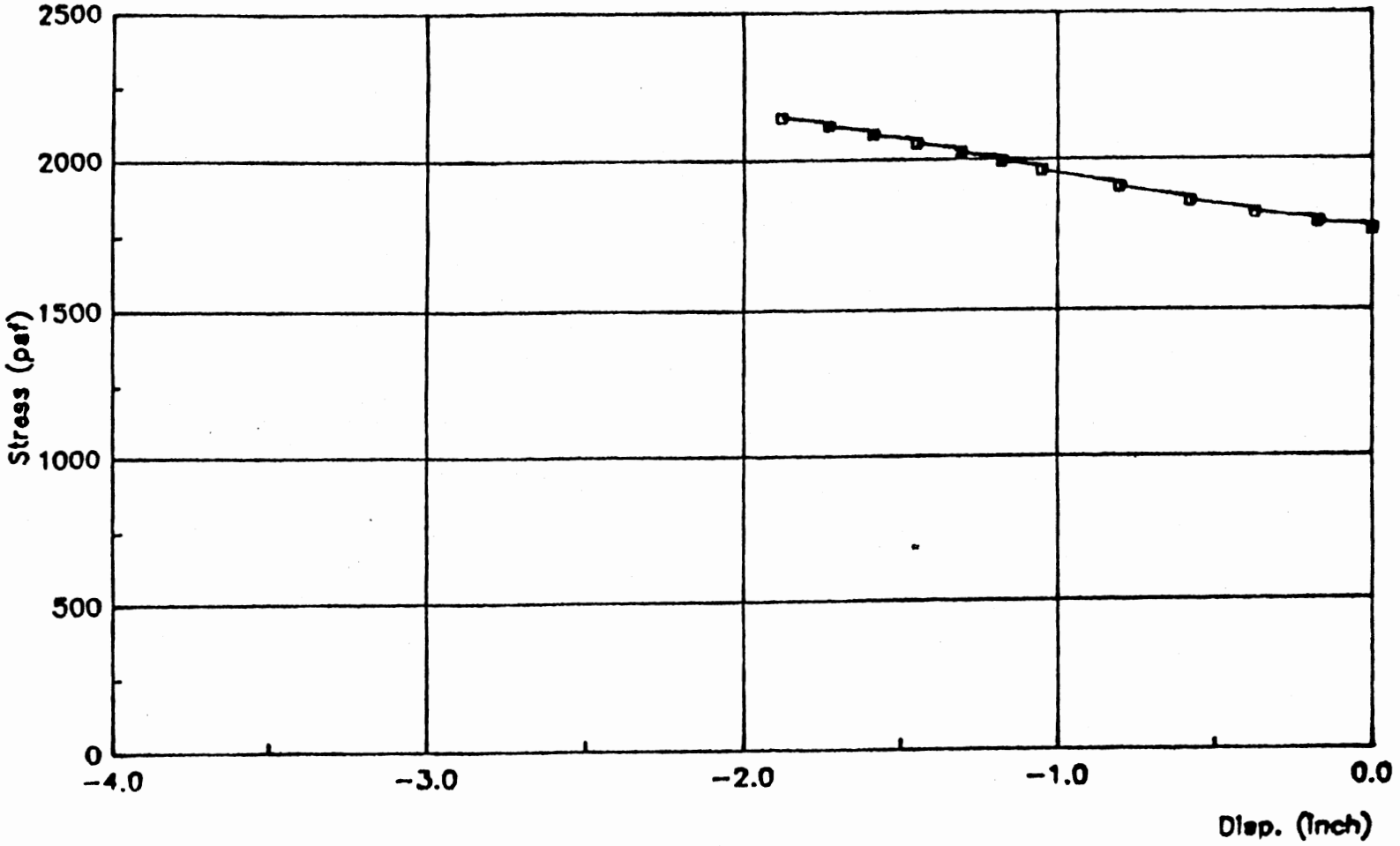

Figure 58(b). Soil-Response curve at -15 ft elevation, back side, high strength profile, 30 ft pile penetration.

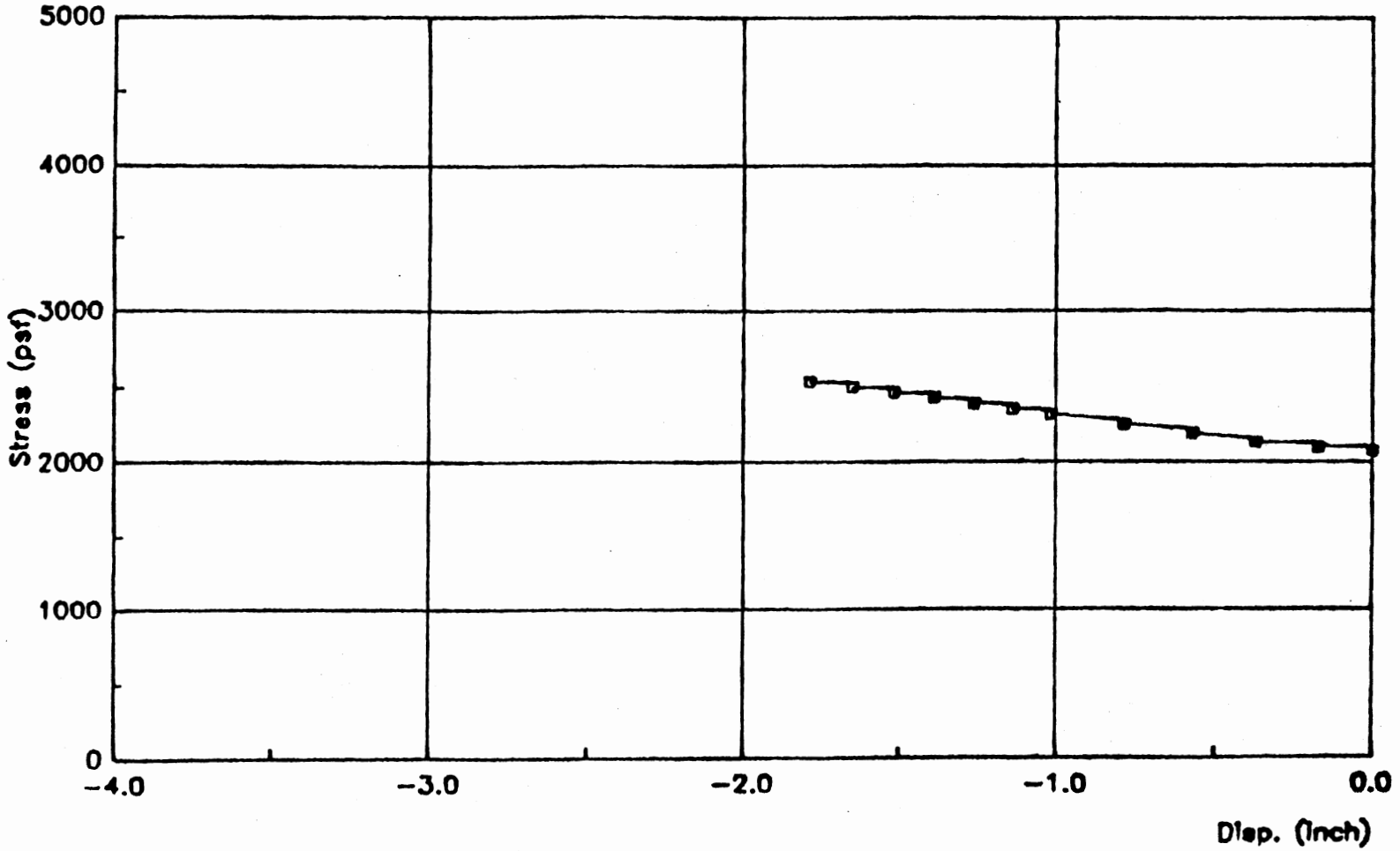

Figure 59(a). Soil-Response curve at -19 ft elevation, front side, high strength profile, 30 ft pile penetration.

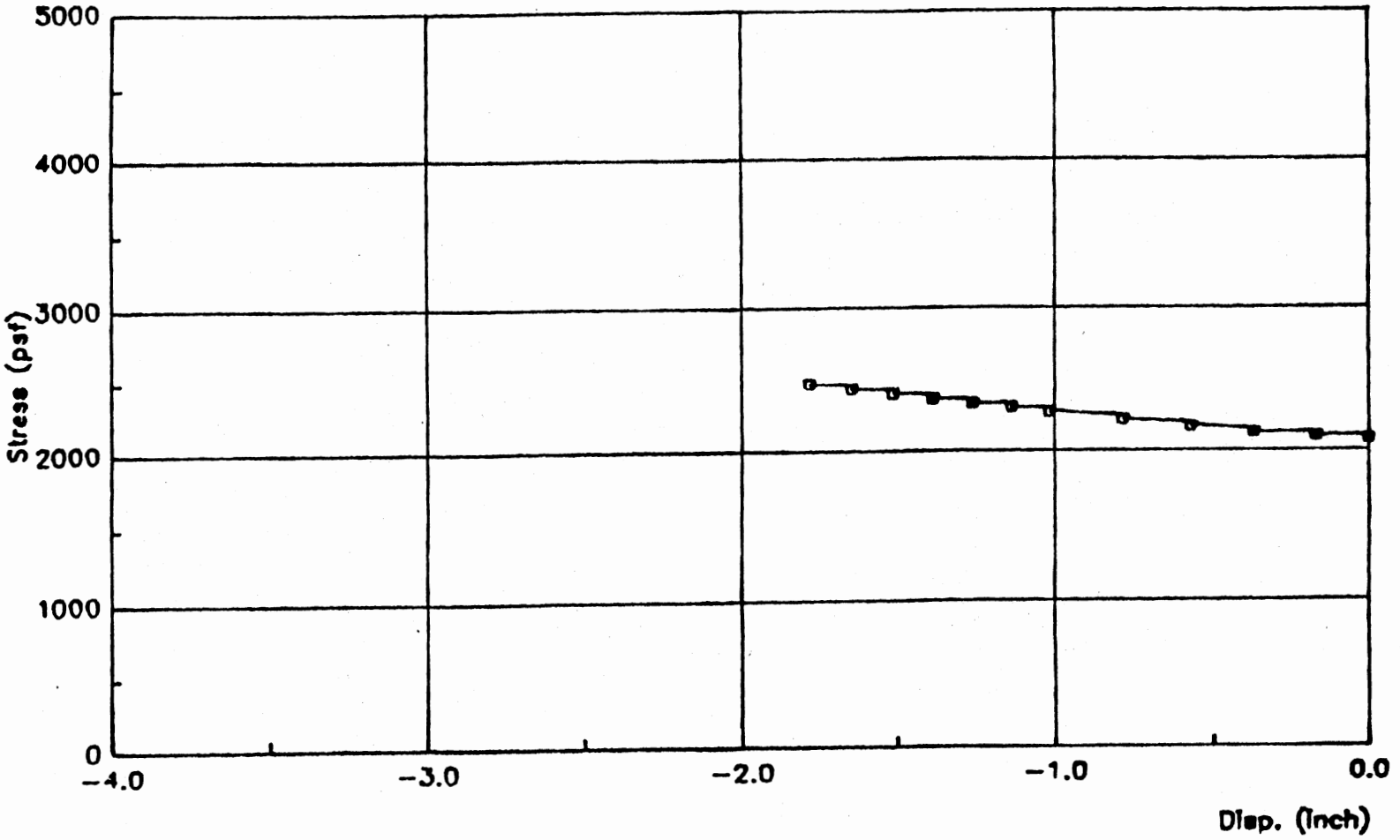

Figure 59(b). Soil-Response curve at -18 ft elevation, back side, high strength profile, 30 ft pile penetration.

APPENDIX D

MEDIUM STRENGTH CASE RESULTS

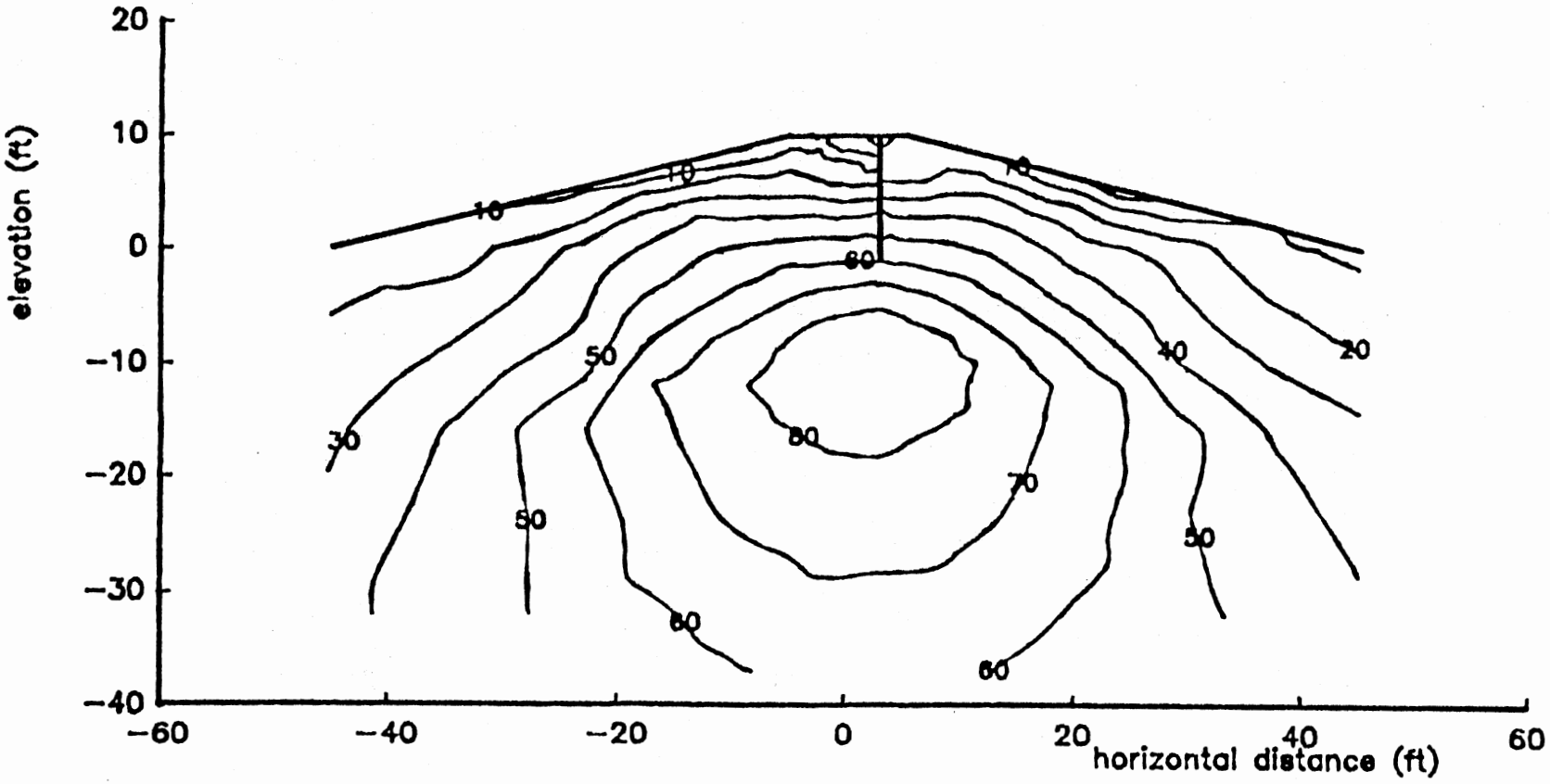

Figure 60(a). f contours at 4 ft head, medium strength profile, 10 ft pile penetration.

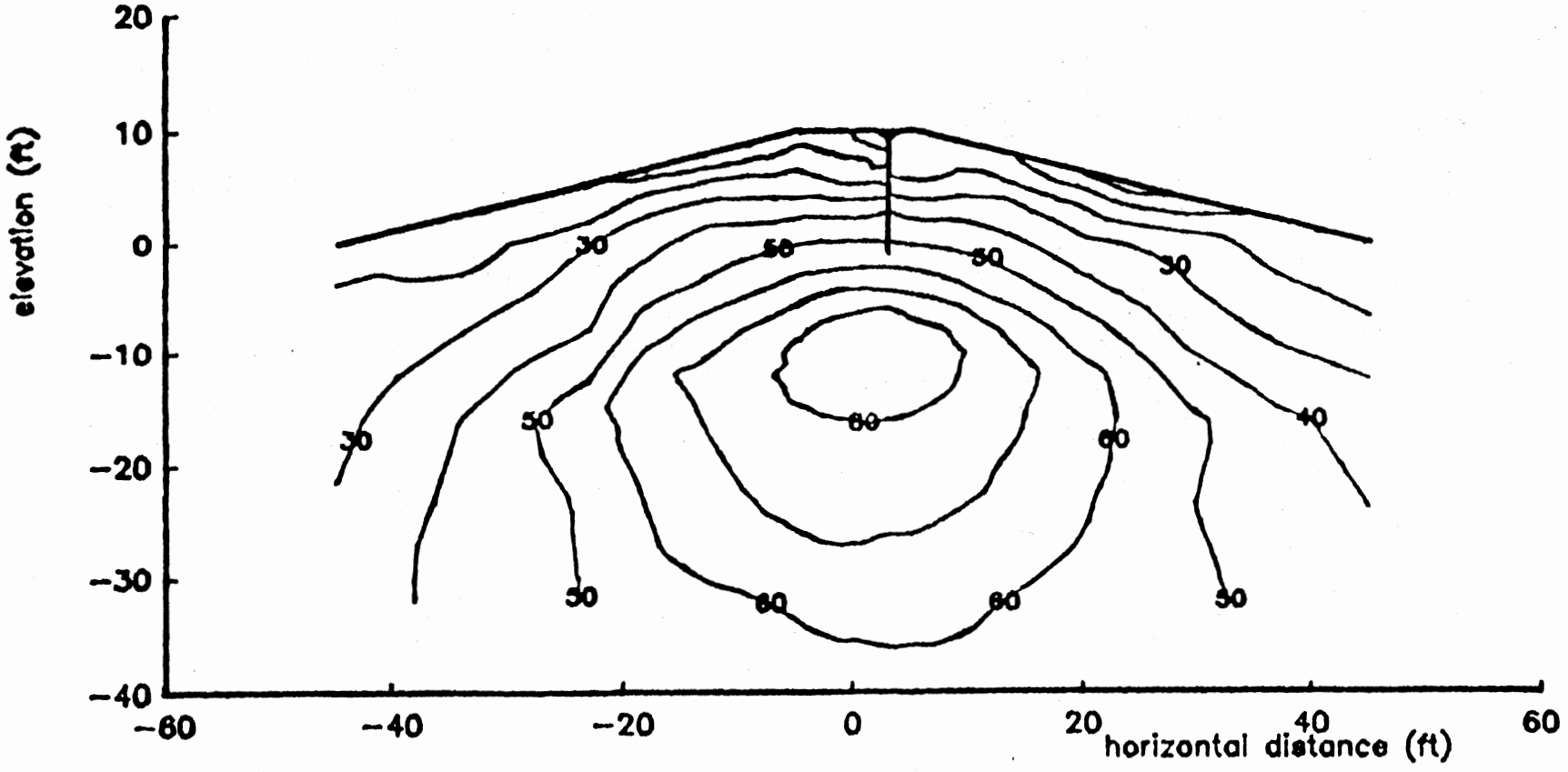

Figure 60(b). f contours at 6 ft head, medium strength profile, 10 ft pile penetration.

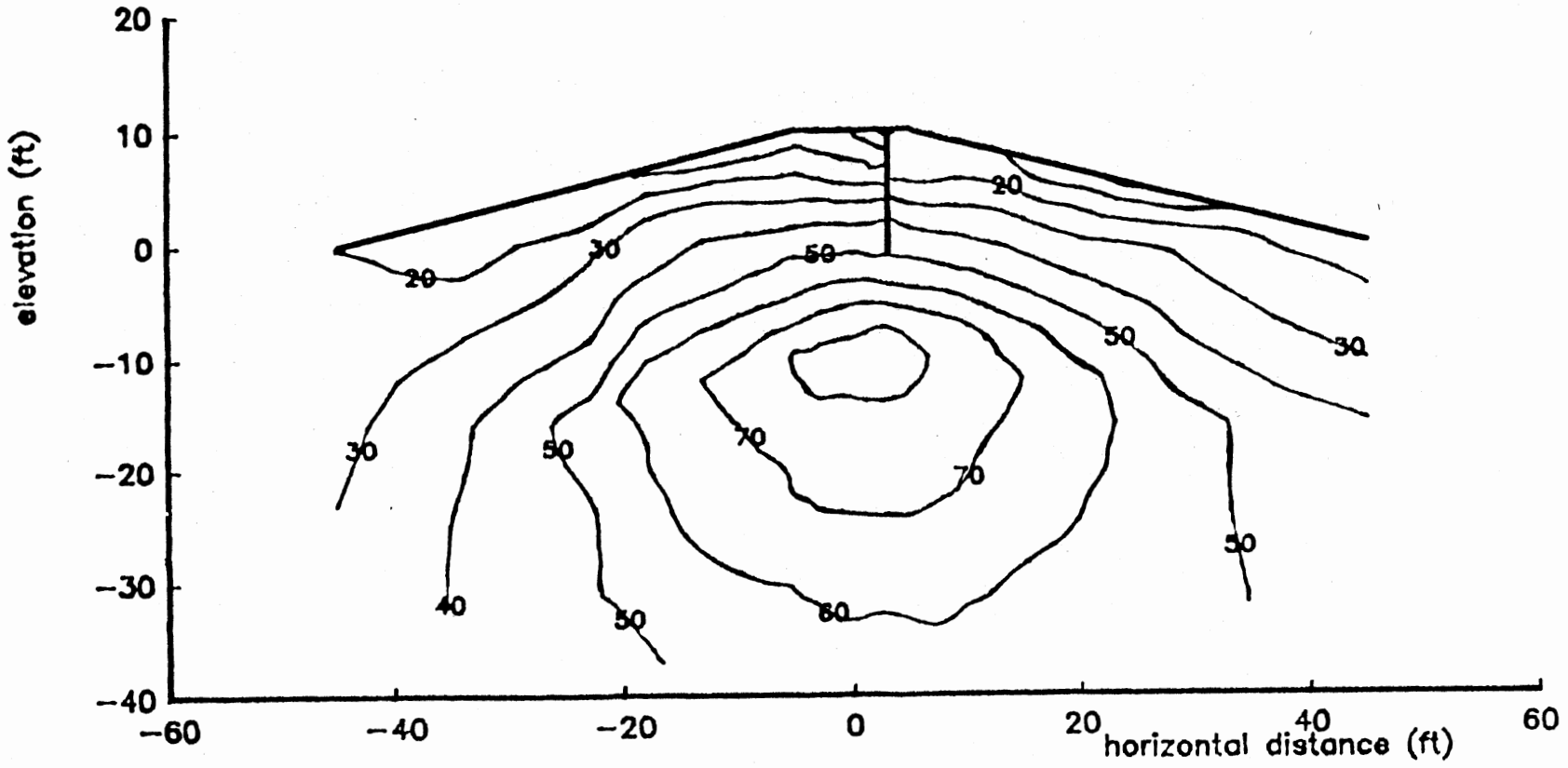

Figure 60(c). f contours at 8 ft head, medium strength profile, 10 ft pile penetration.

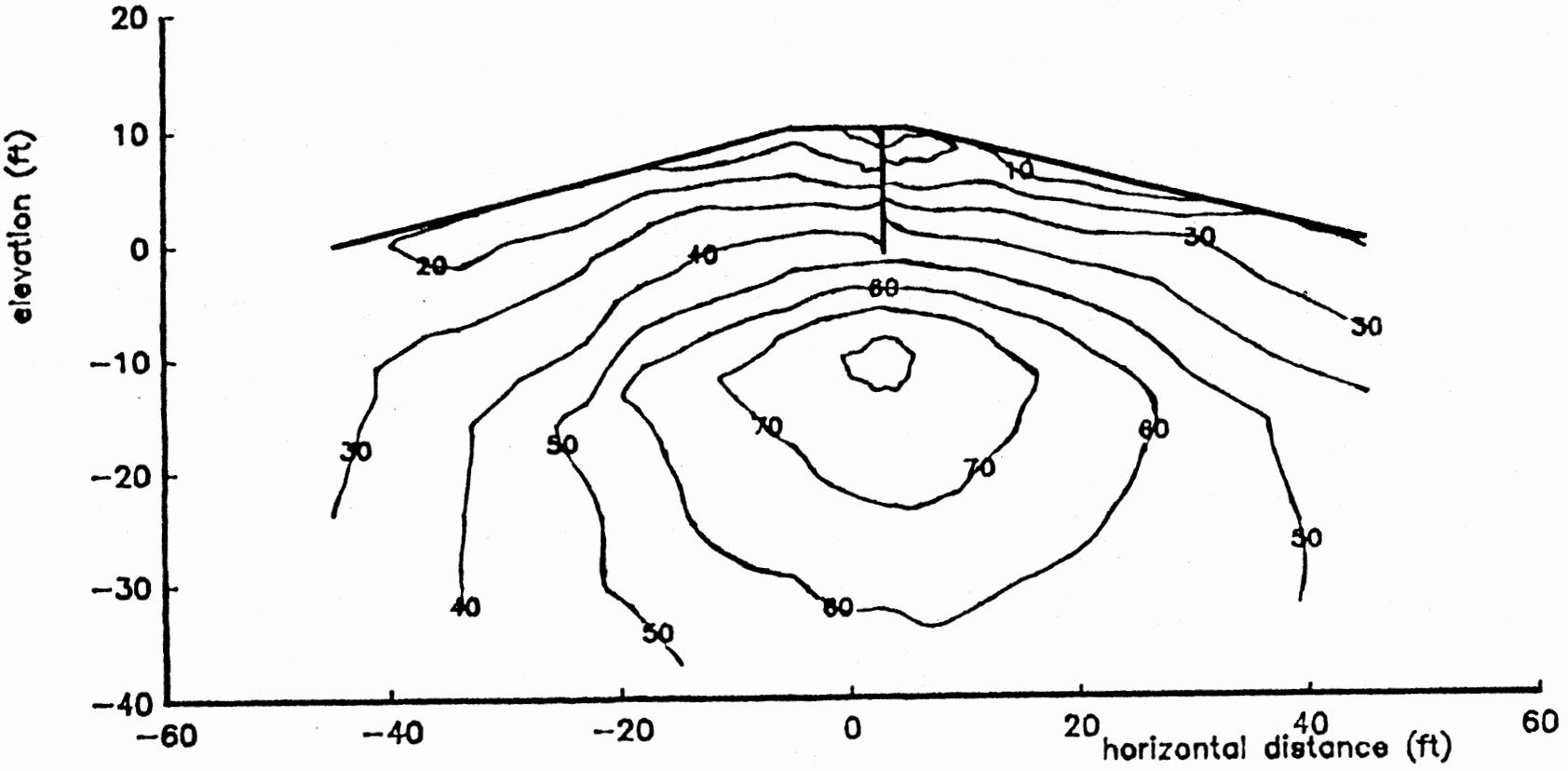

Figure 80(d). f contours at 10 ft head, medium strength profile, 10 ft pile penetration.

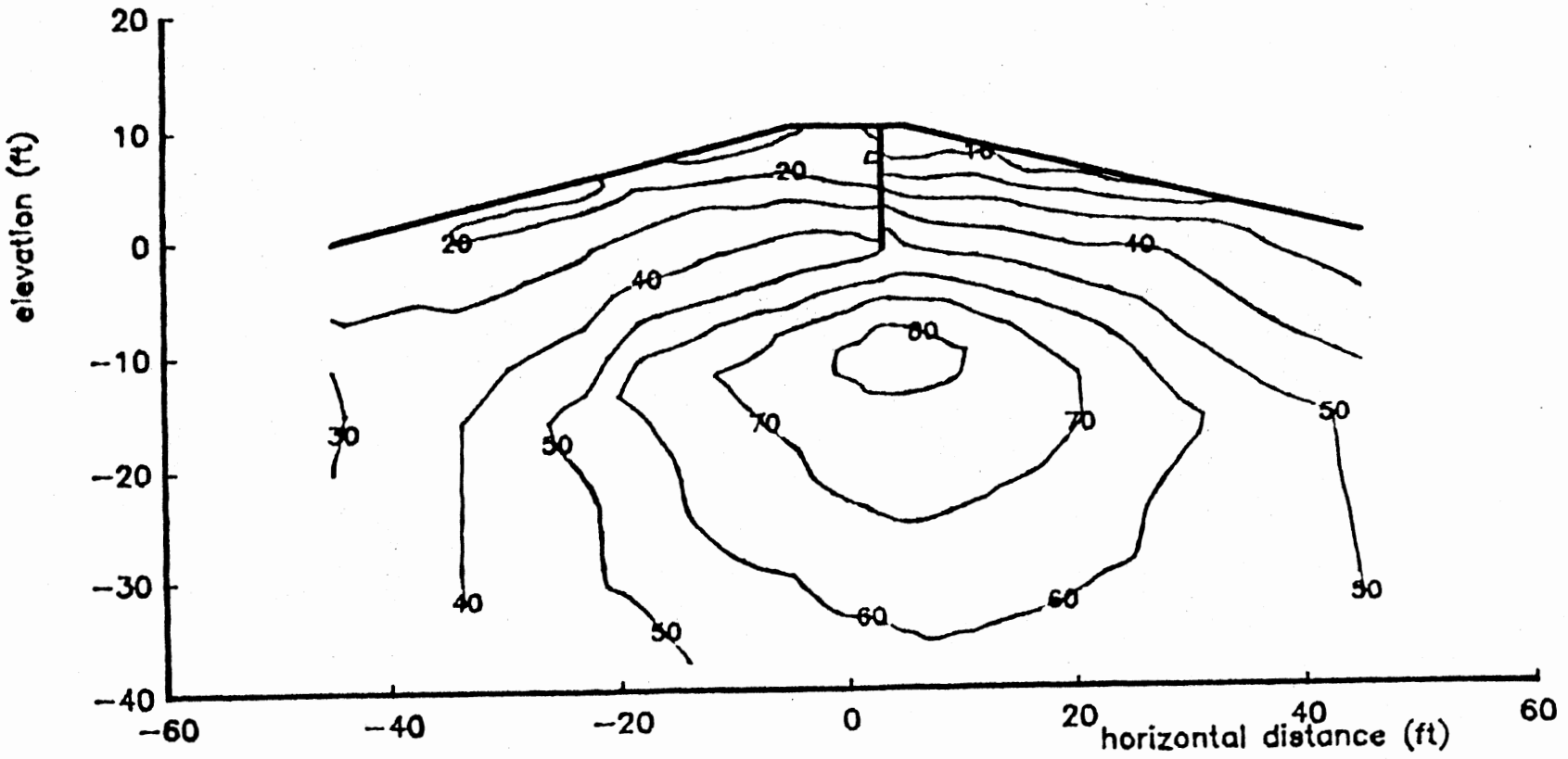

Figure 60(e). f contours at 12 ft head, medium strength profile, 10 ft pile penetration.

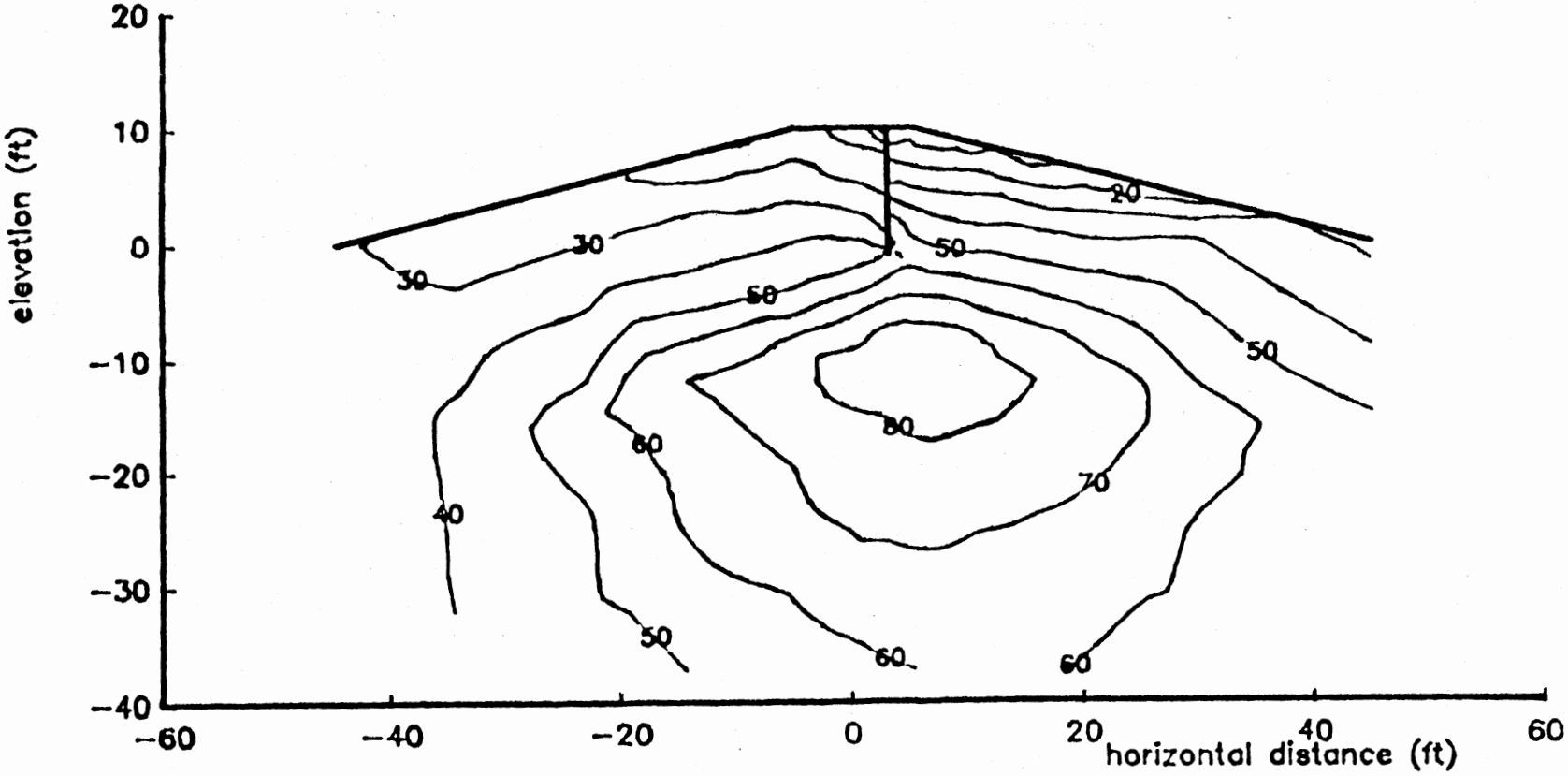

Figure 60(f). f contours at 14 ft head, medium strength profile, 10 ft pile penetration.

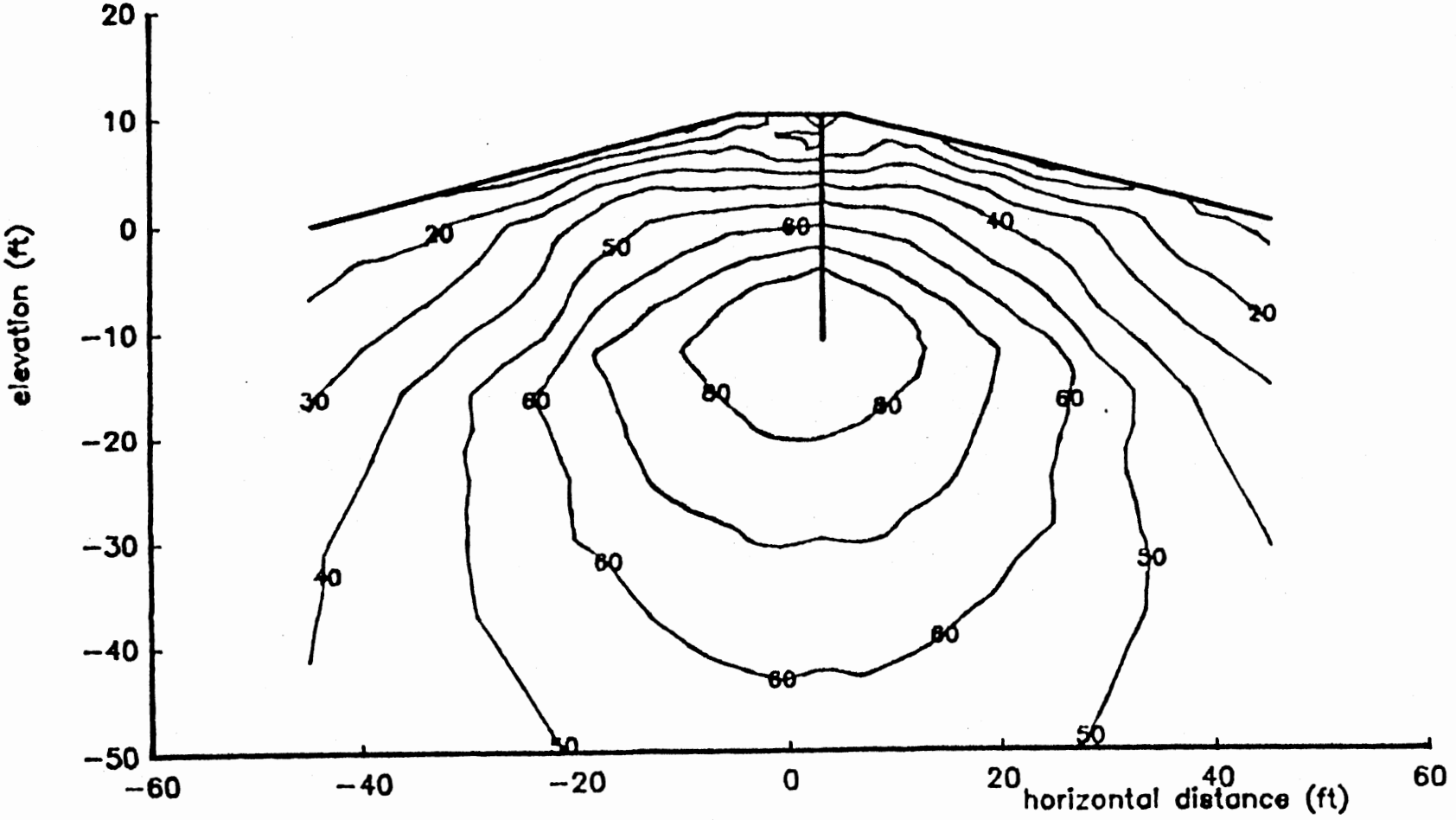

Figure 61(a). f contours at 2 ft head, medium strength profile, 20 ft pile penetration.

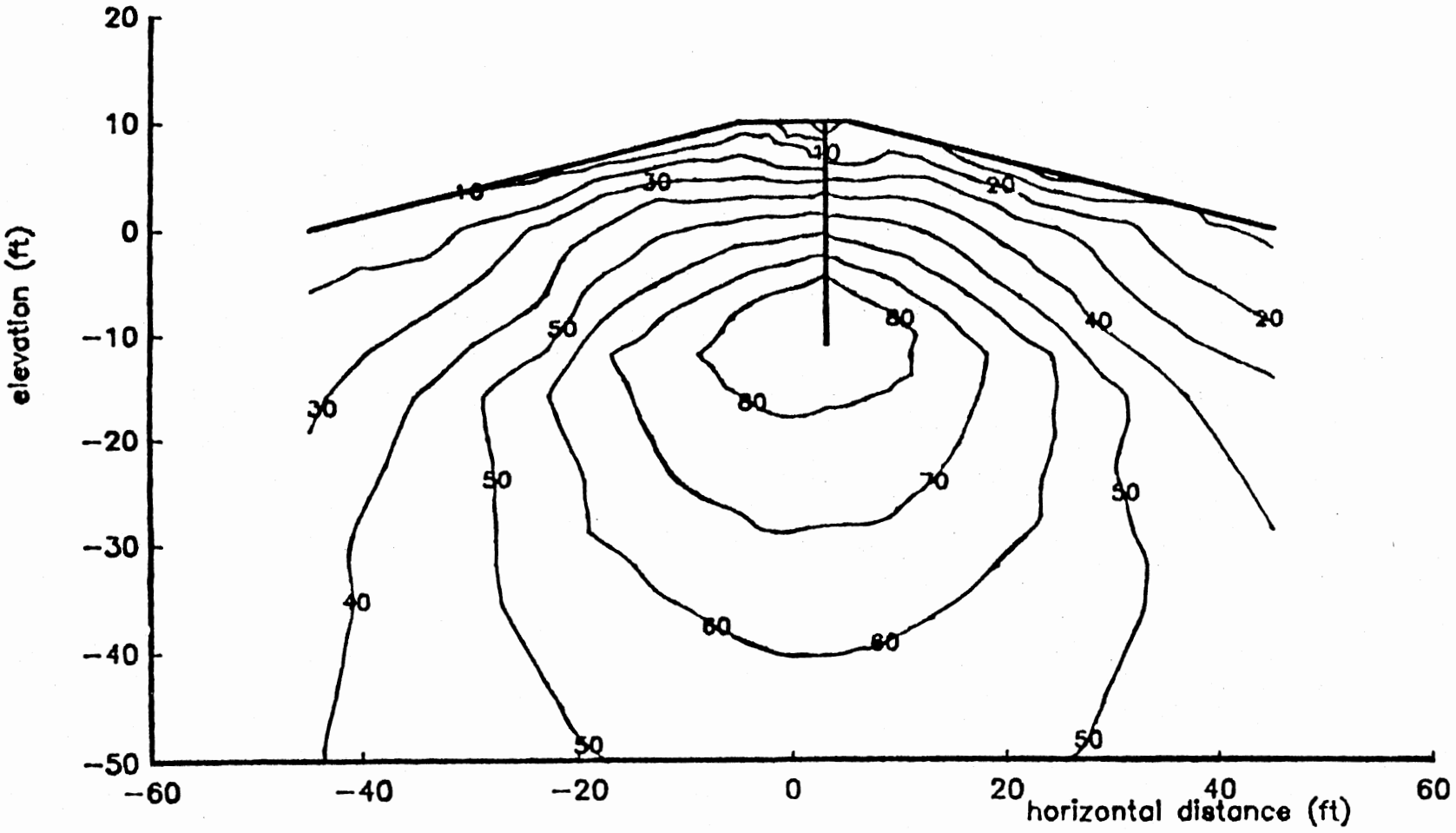

Figure 61(b). f contours at 4 ft head, medium strength profile, 20 ft pile penetration.

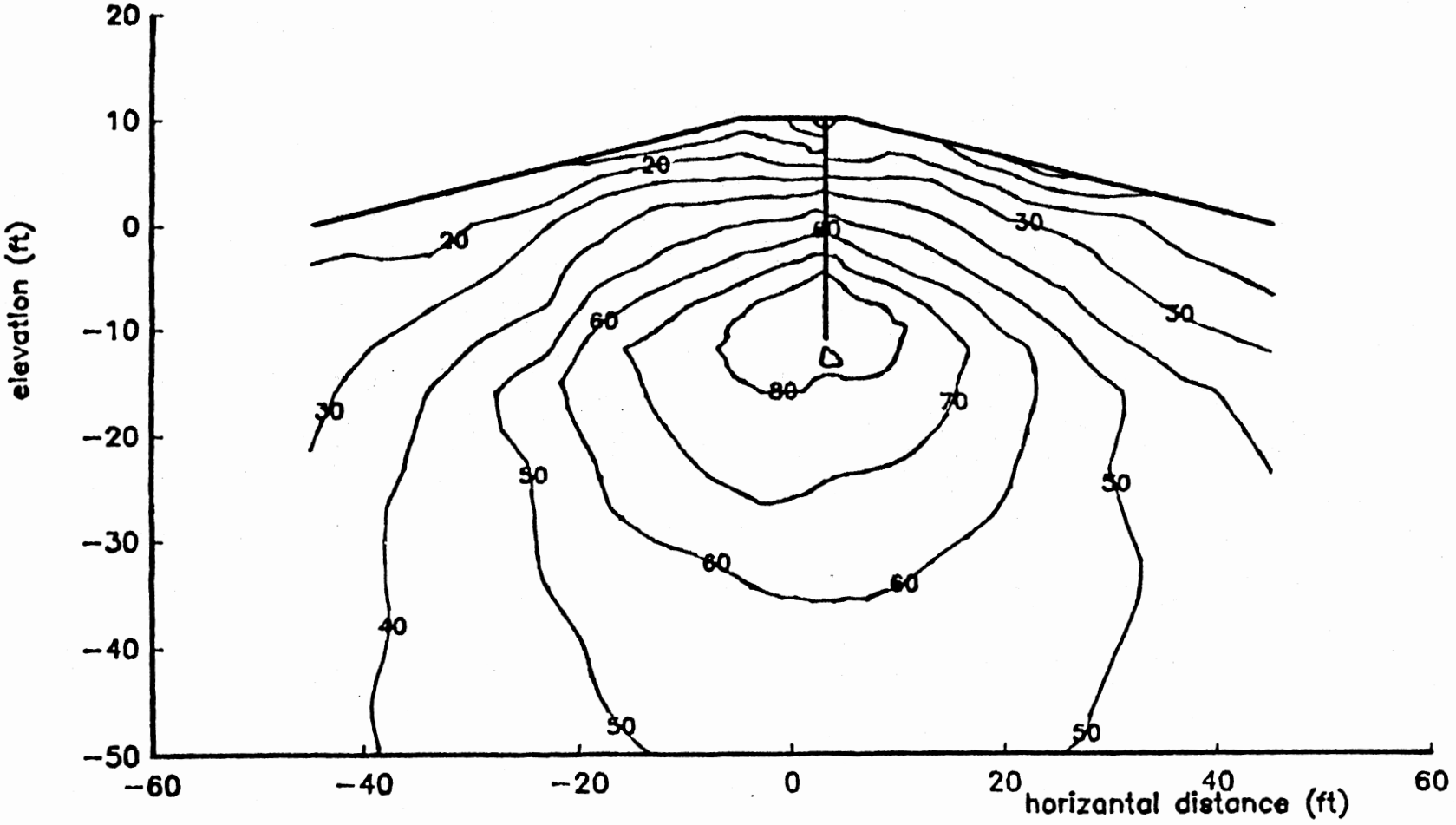

Figure 61(c). f contours at 6 ft head, medium strength profile, 20 ft pile penetration.

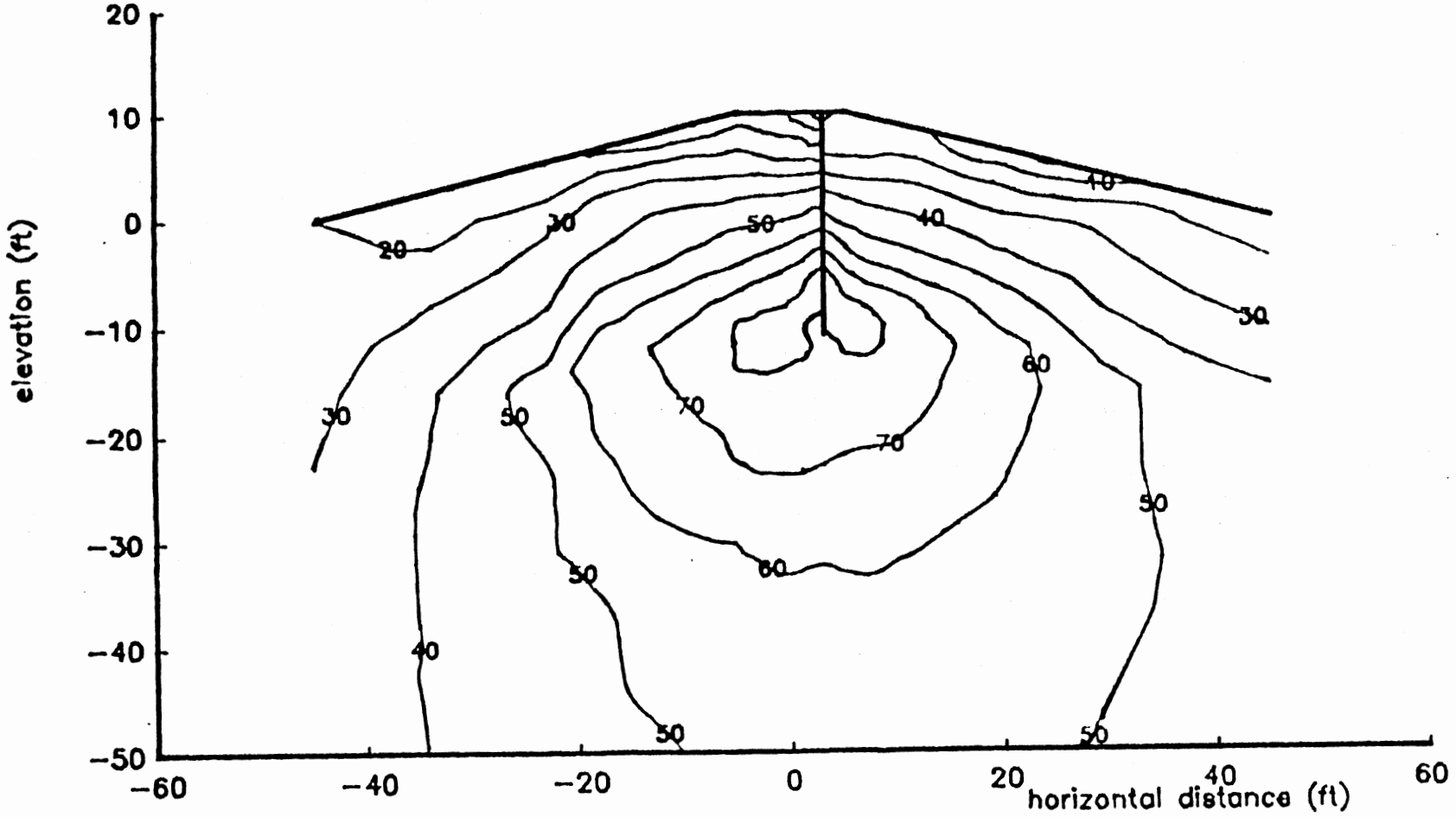

Figure 61(d). f contours at 8 ft head, medium strength profile, 20 ft pile penetration.

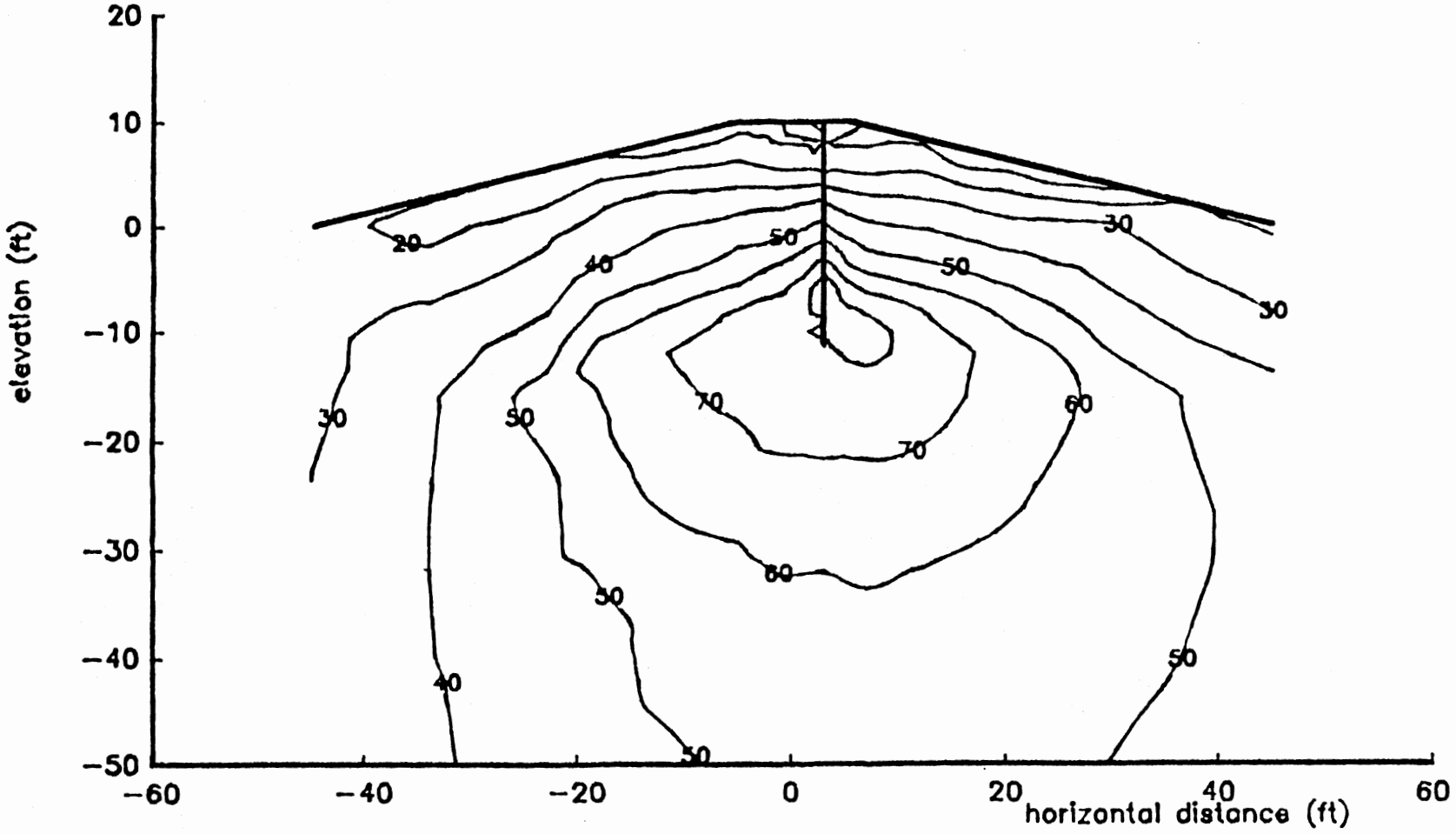

Figure 61(e). f contours at 10 ft head, medium strength profile, 20 ft pile penetration.

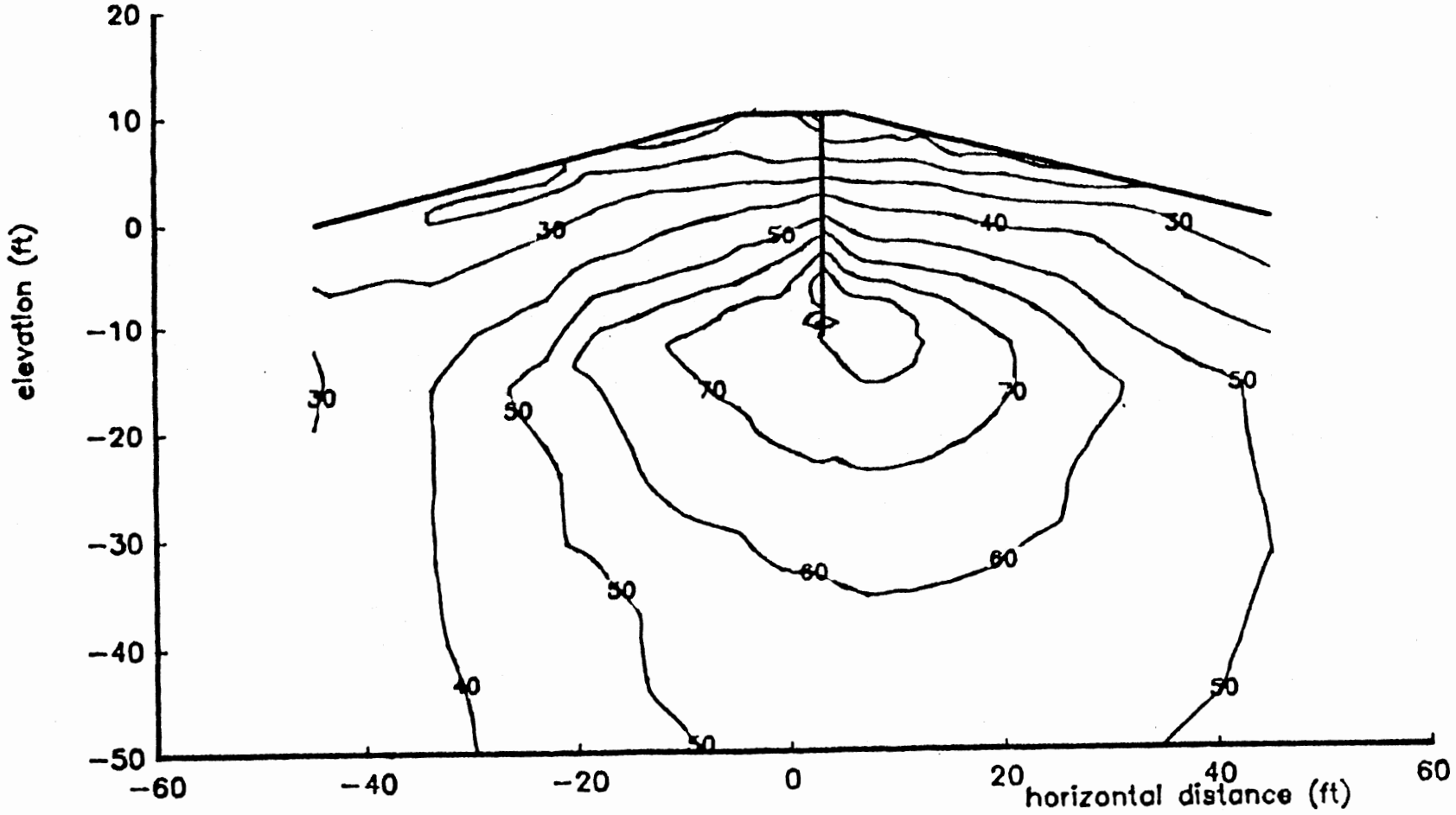

Figure 61(f). f contours at 12 ft head, medium strength profile, 20 ft pile penetration.

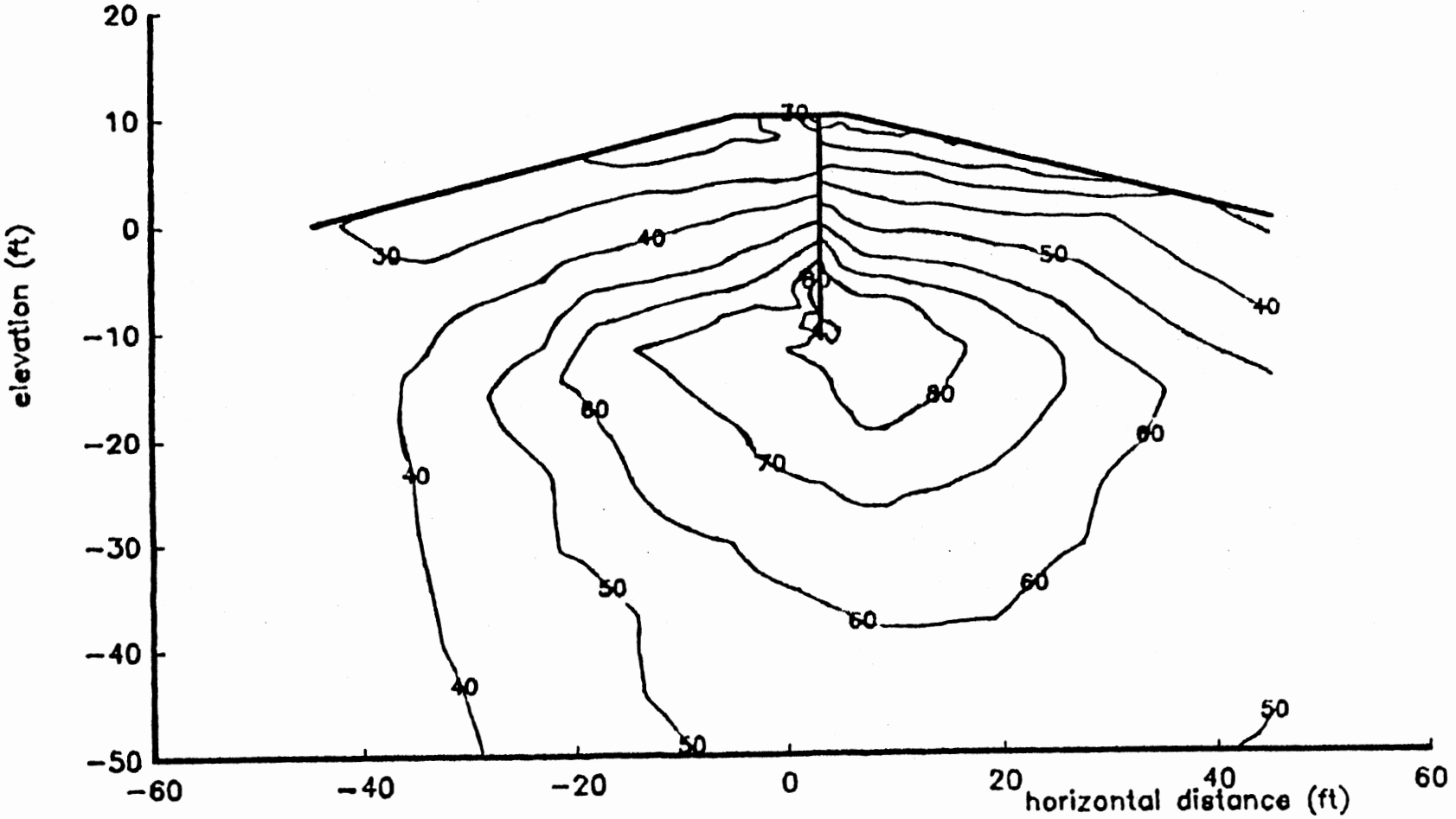

Figure 61(g). f contours at 14 ft head, medium strength profile, 20 ft pile penetration.

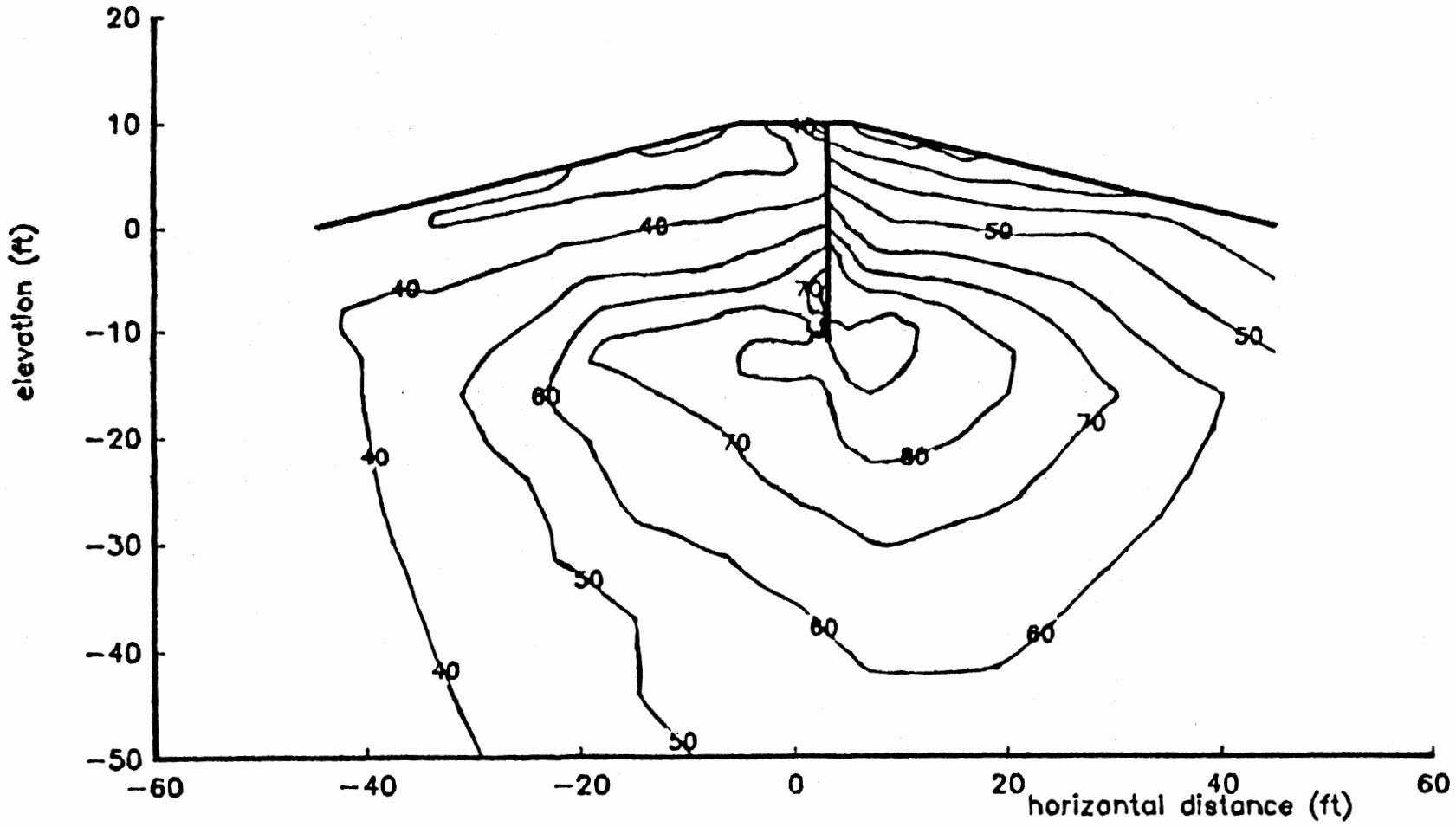

Figure 61(h). f contours at 16 ft head, medium strength profile, 20 ft pile penetration.

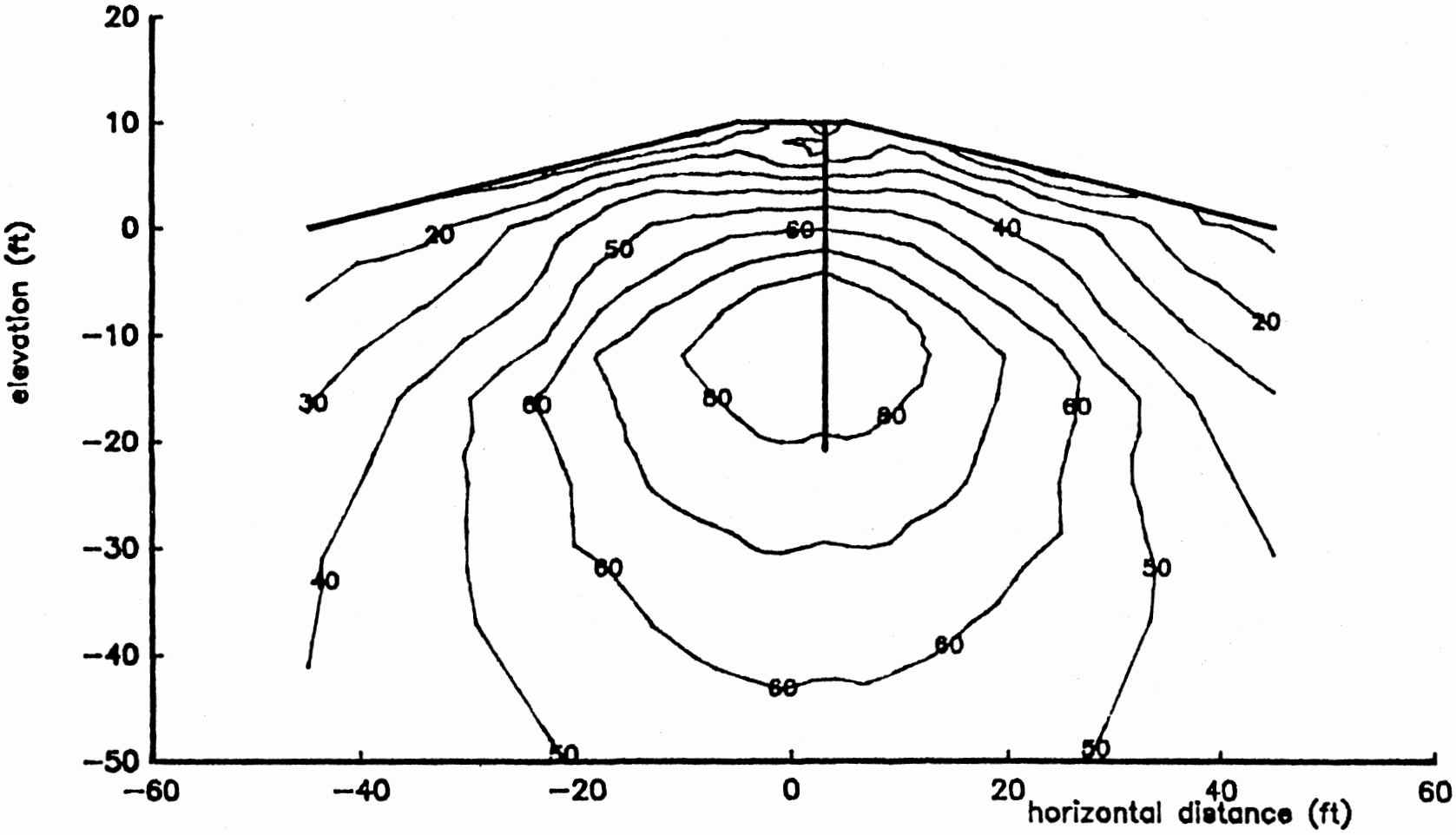

Figure 62(a). f contours at 2 ft head, medium strength profile, 30 ft pile penetration.

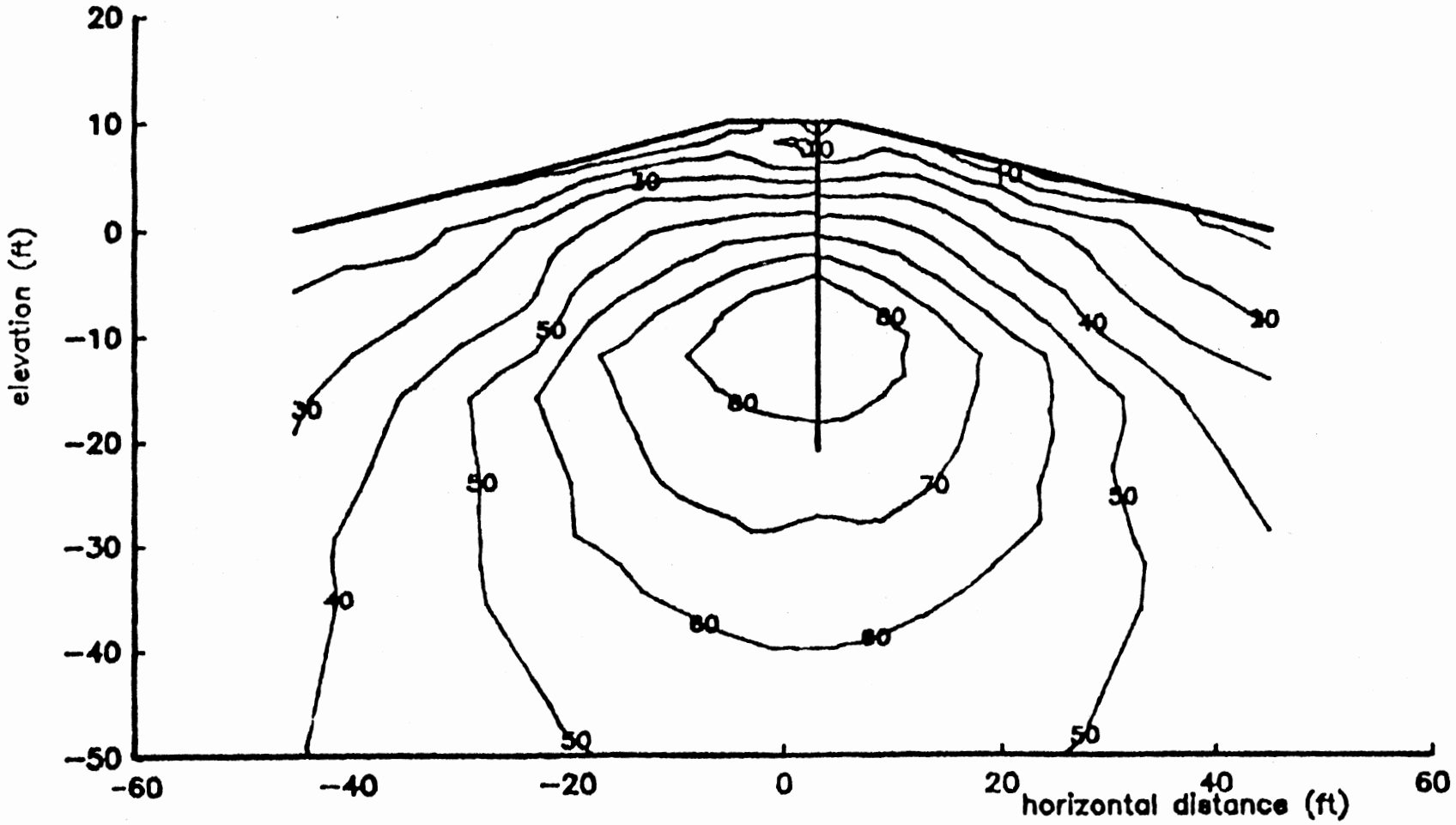

Figure 62(b). f contours at 4 ft head, medium strength profile, 30 ft pile penetration.

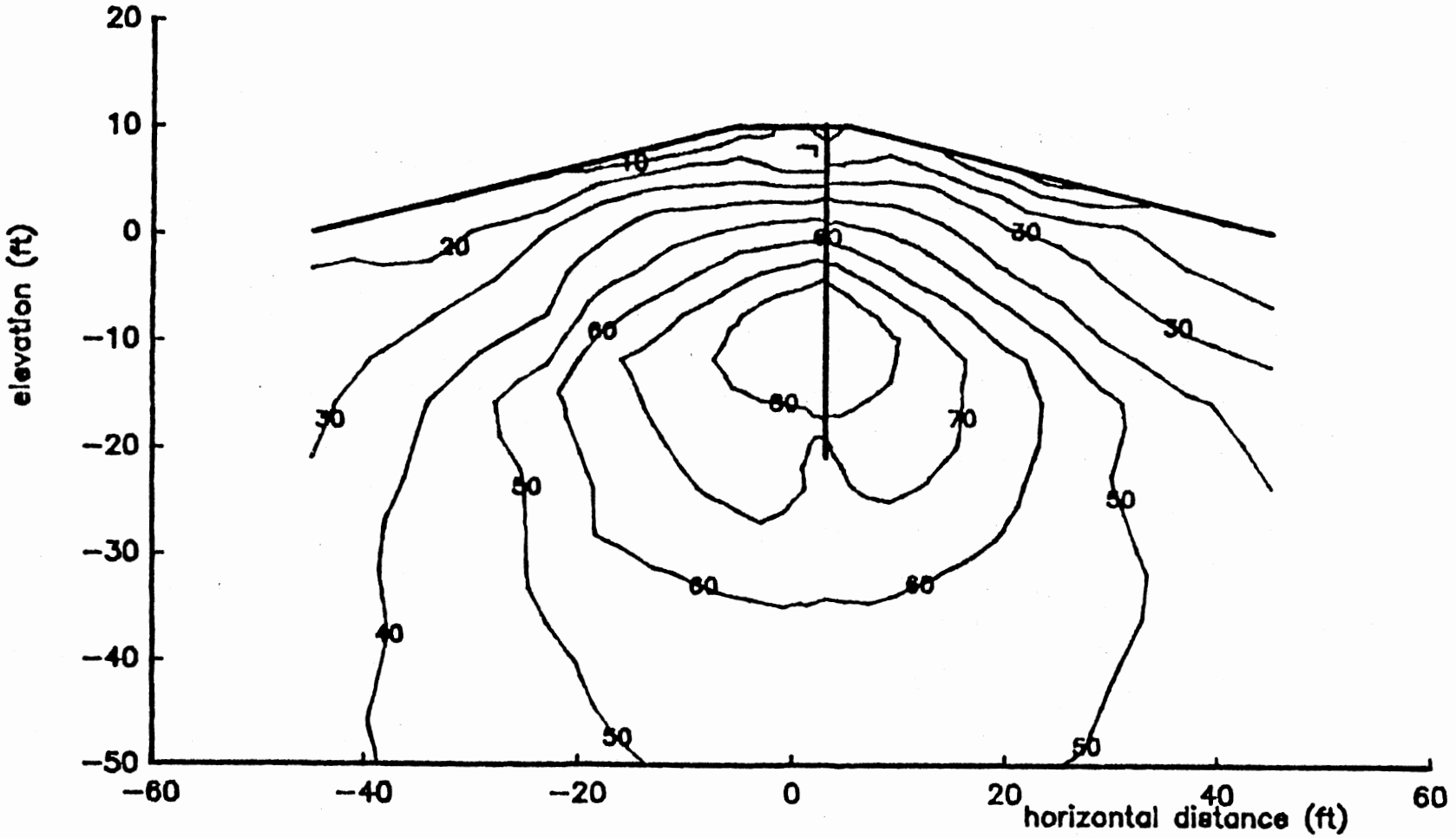

Figure 62(c). f contours at 6 ft head, medium strength profile, 30 ft pile penetration.

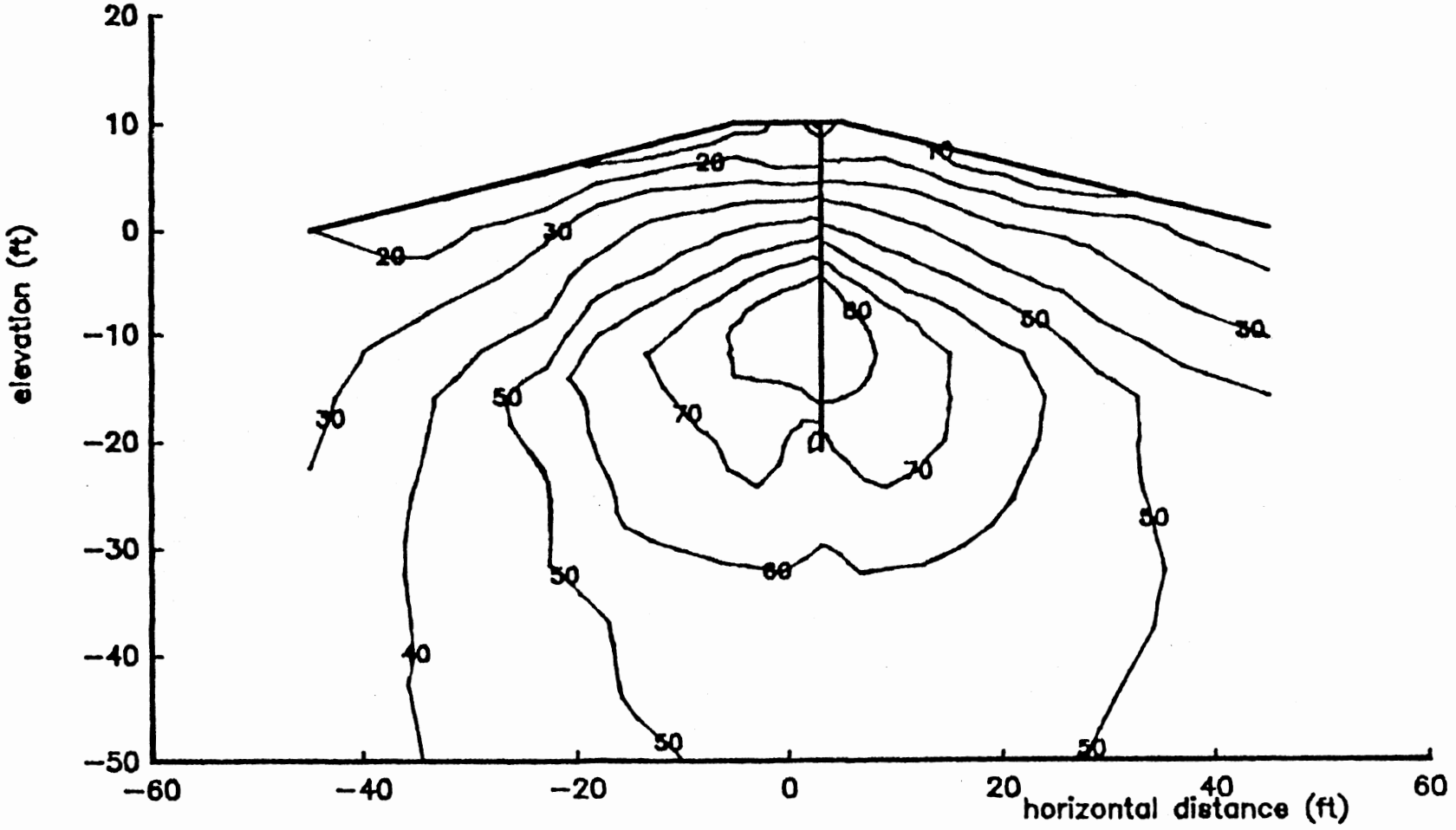

Figure 62(d). f contours at 8 ft head, medium strength profile, 30 ft pile penetration.

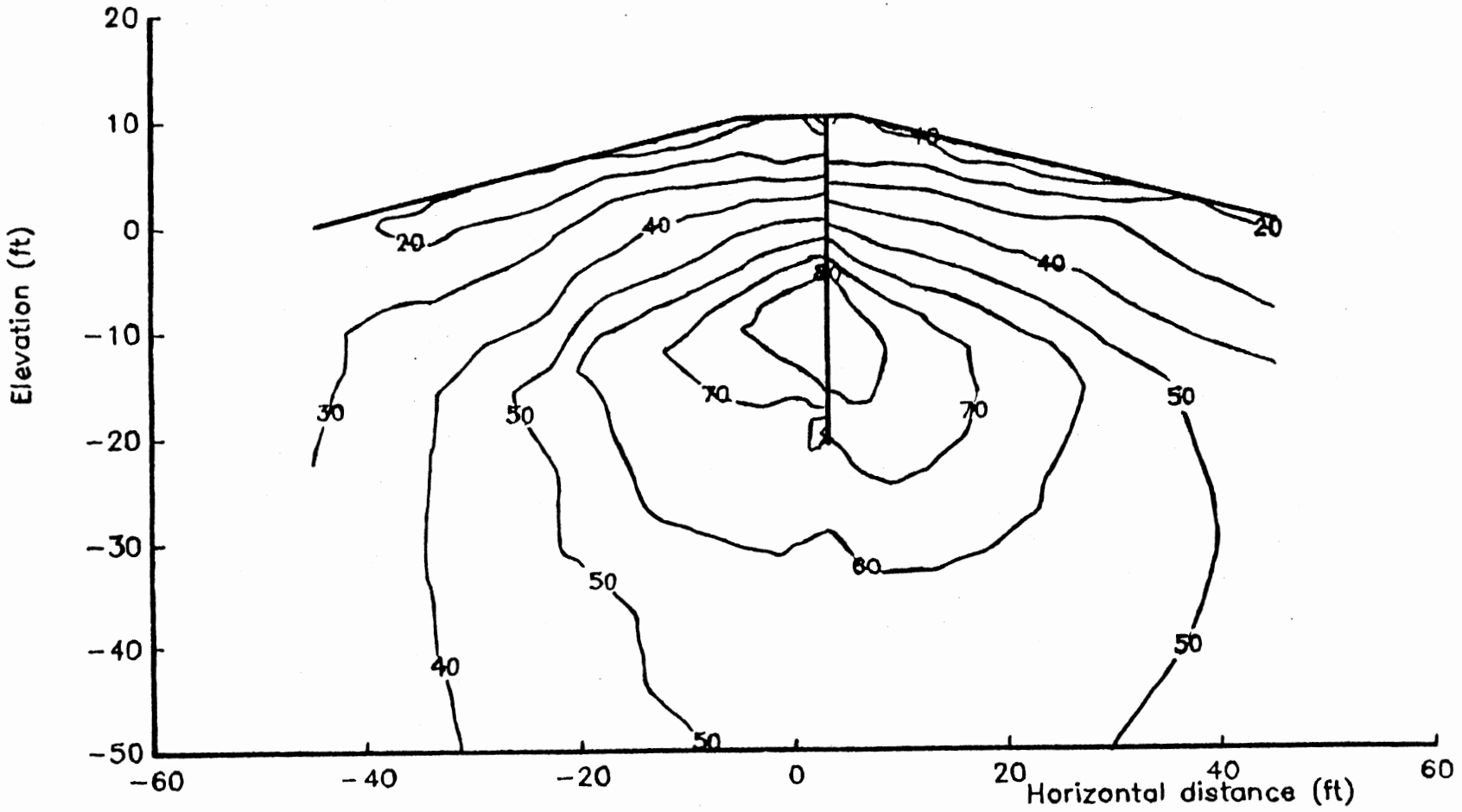

Figure 62(e). f contours at 10 ft head, medium strength profile, 30 ft pile penetration.

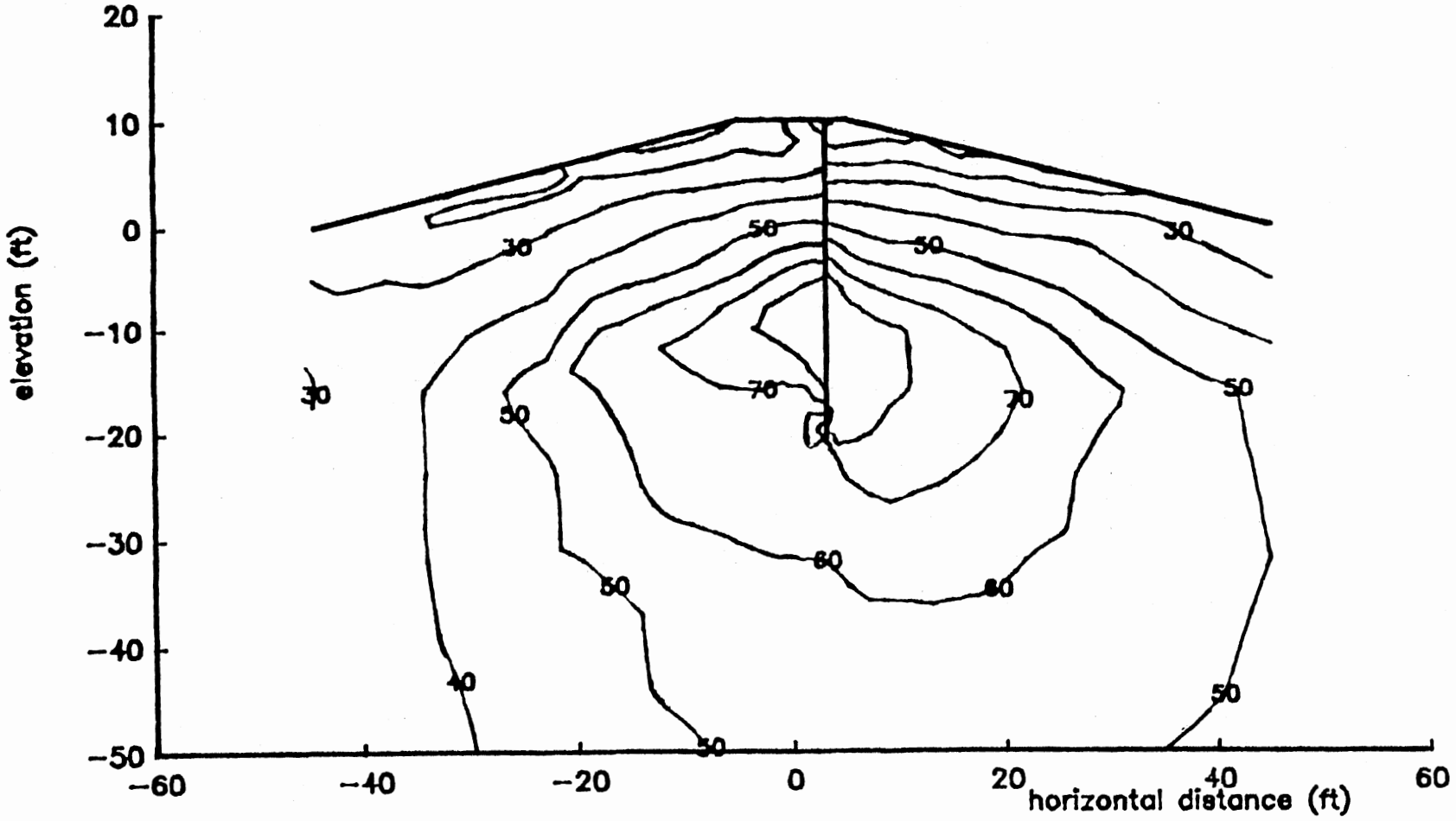

Figure 62(f). f contours at 12 ft head, medium strength profile, 30 ft pile penetration.

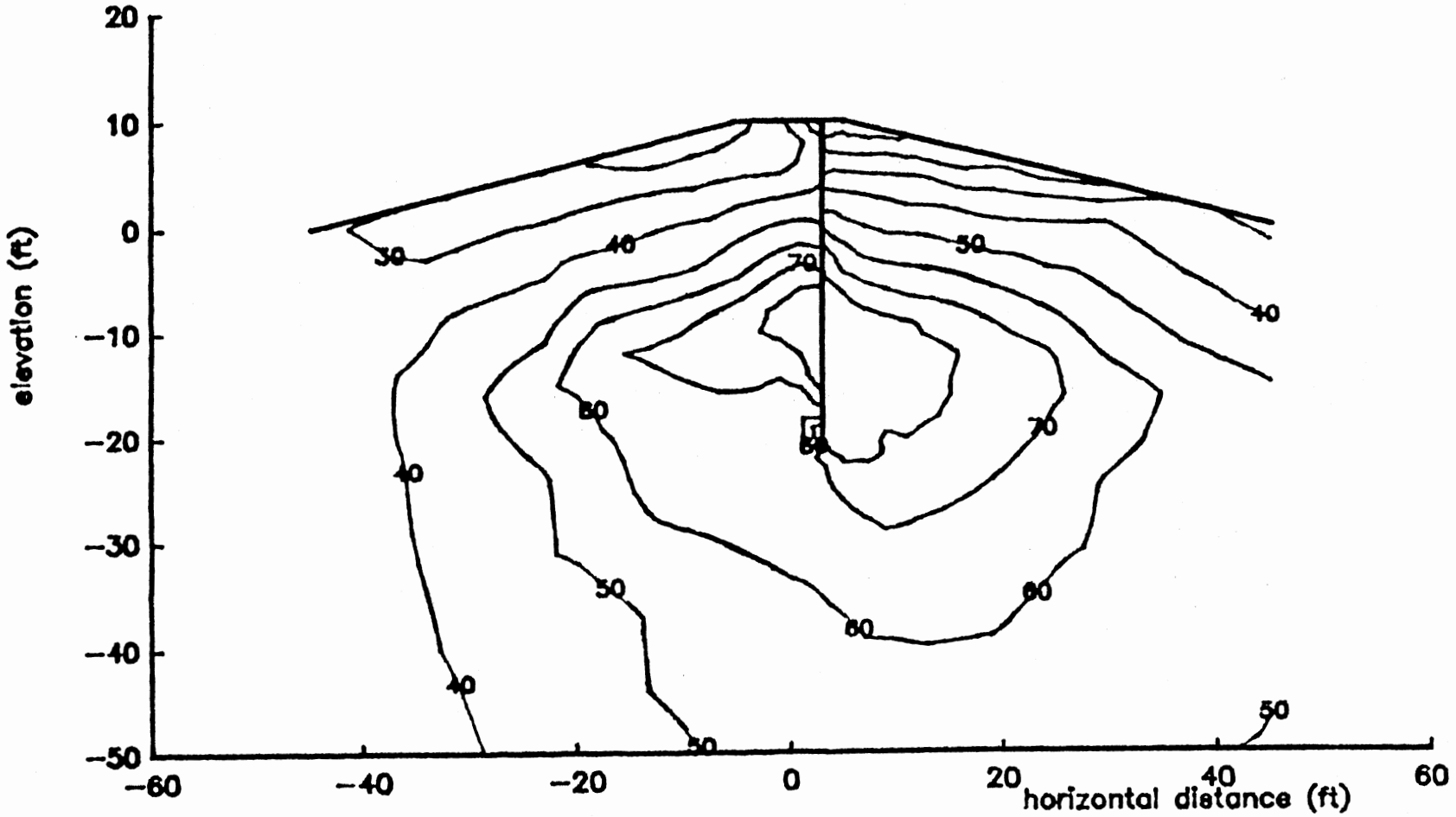

Figure 62(g). f contours at 14 ft head, medium strength profile, 30 ft pile penetration.

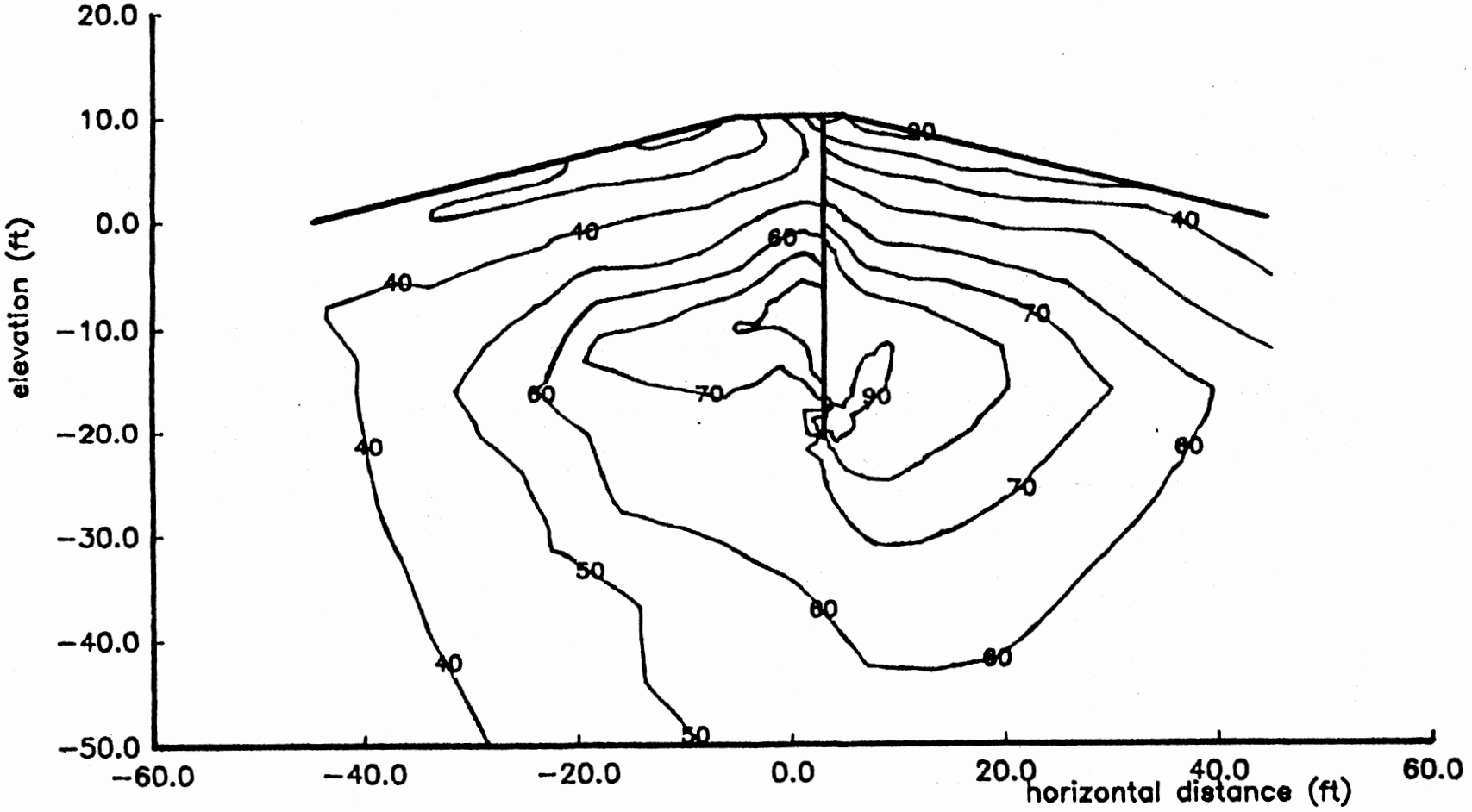

Figure 62(h). f contours at 16 ft head, medium strength profile, 30 ft pile penetration.

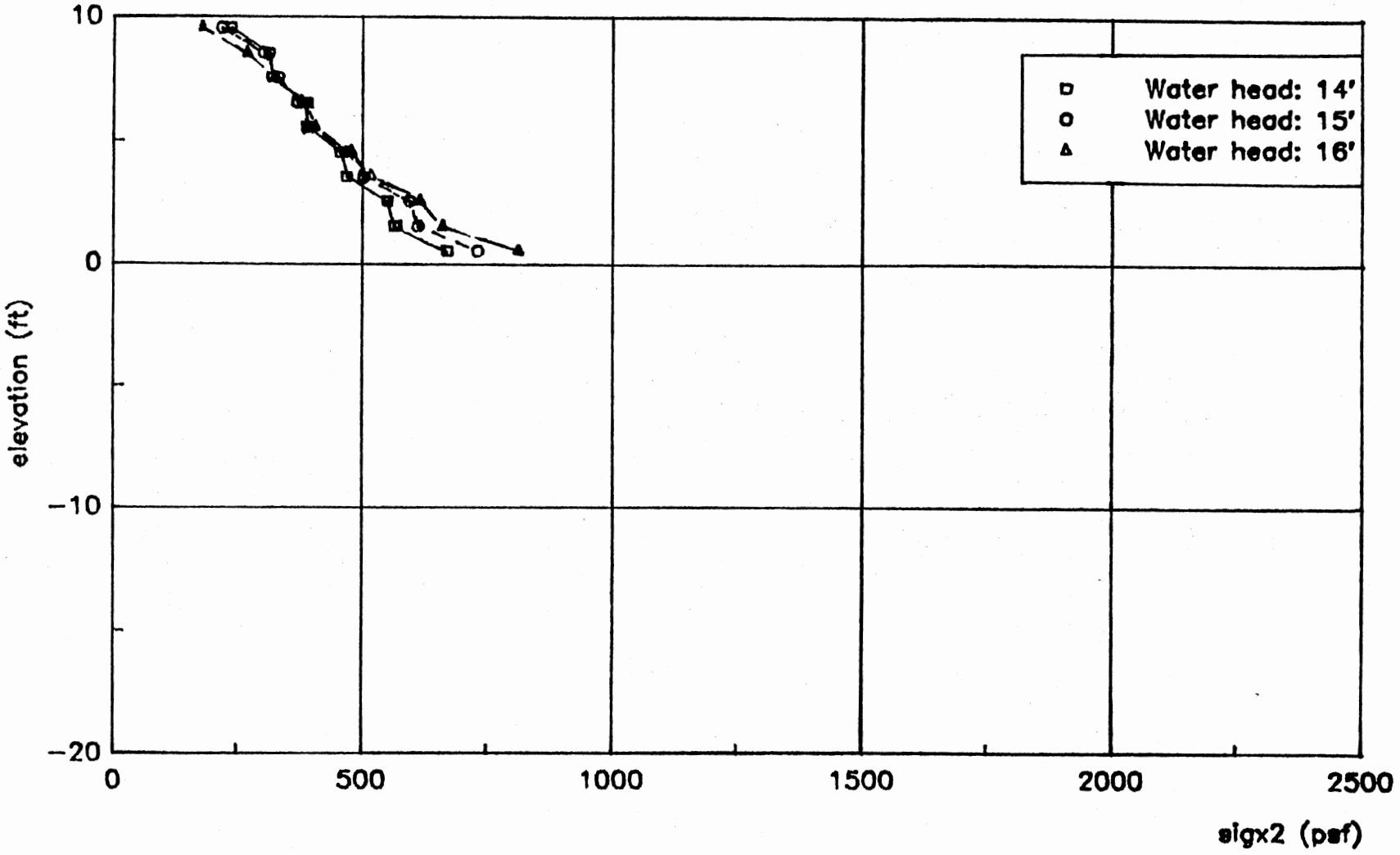

Figure 63(a). Stress profile in back of the pile, medium strength profile, 10 ft pile penetration.

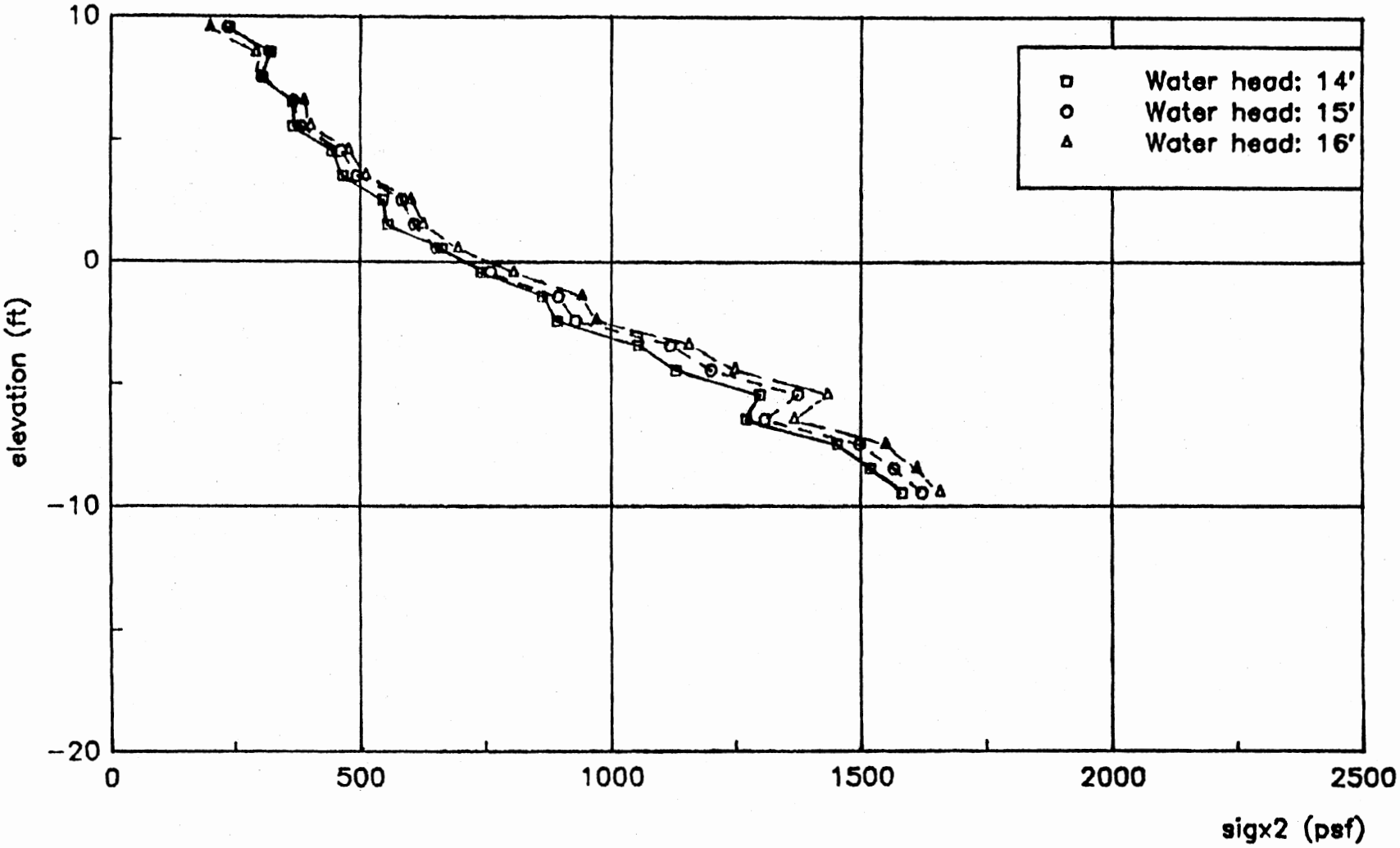

Figure 83(b). Stress profile in back of the pile, medium strength profile, 20 ft pile penetration.

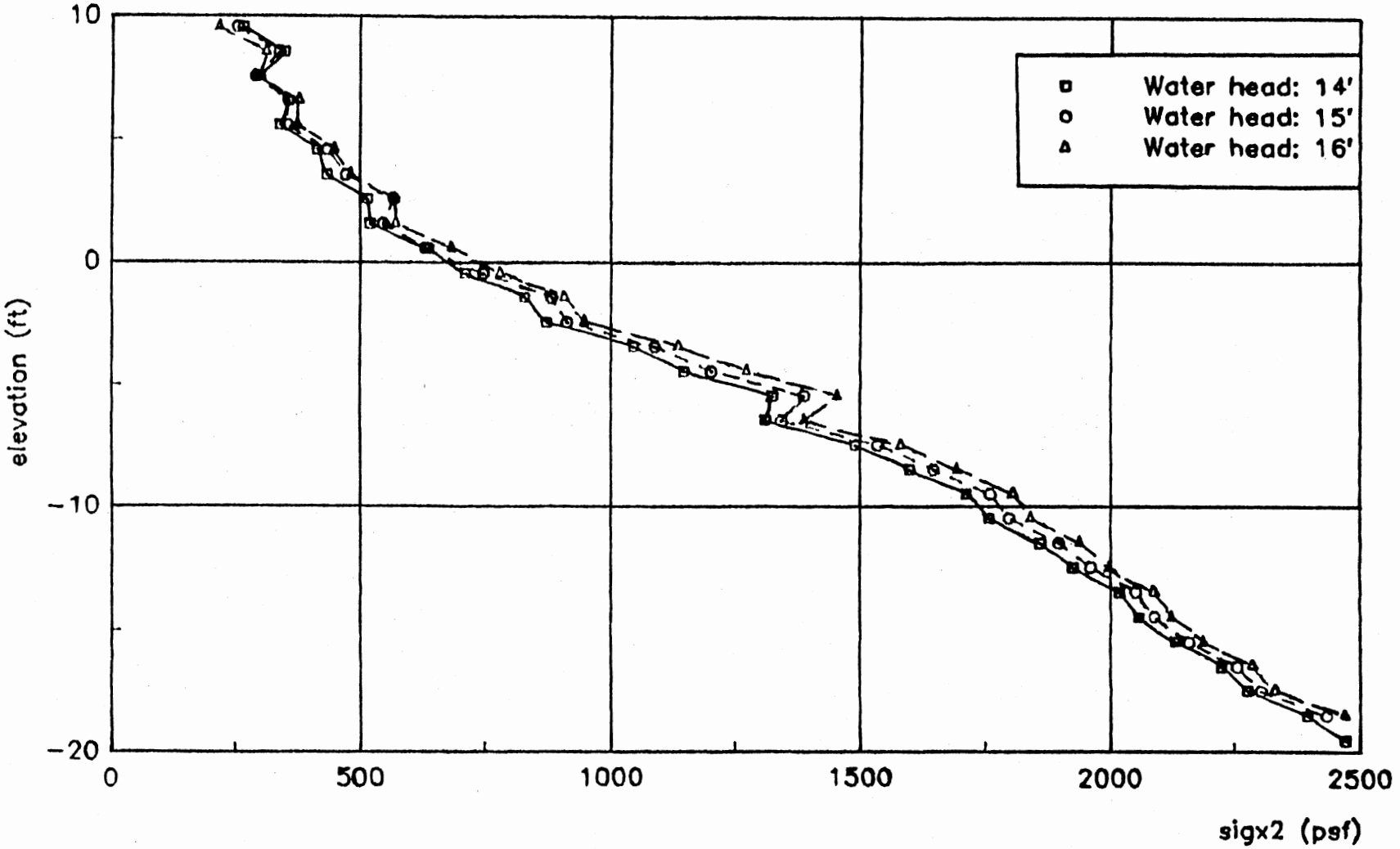

Figure 63(c). Stress profile in back of the pile, medium strength profile, 30 ft pile penetration.

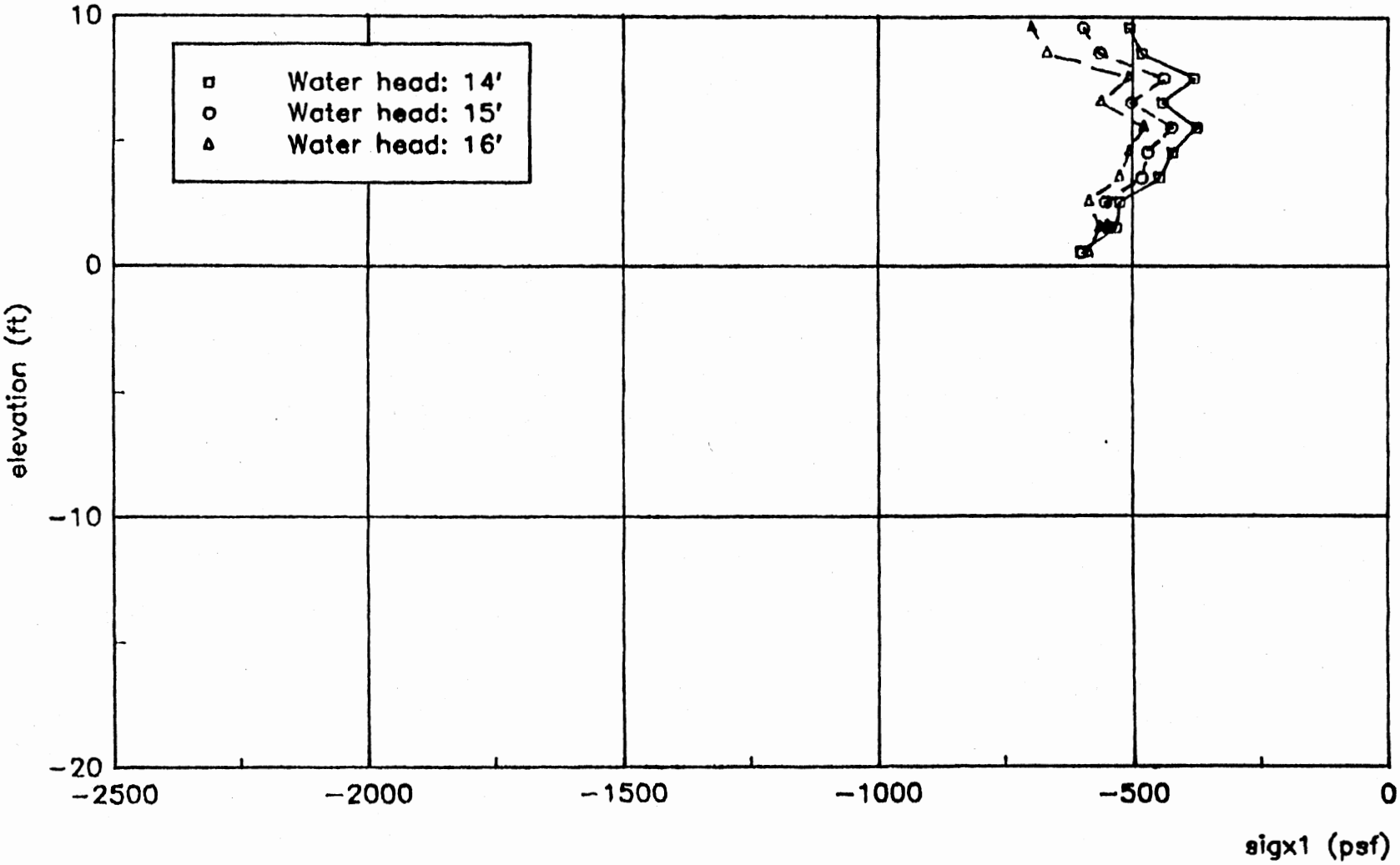

Figure 64(a). Stress profile in front of the pile, medium strength profile, 10 ft pile penetration.

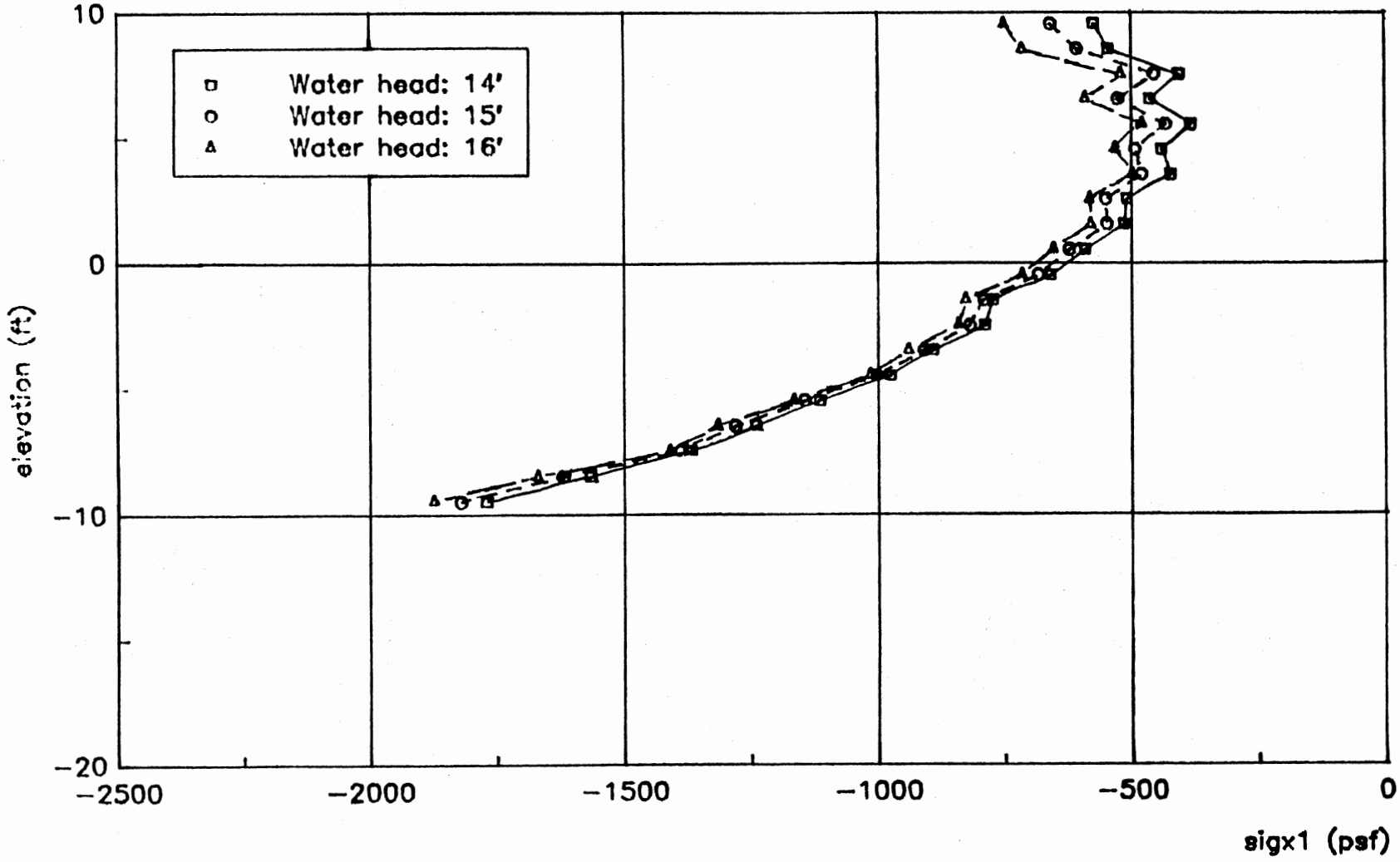

Figure 64(b). Stress profile in front of the pile, medium strength profile, 20 ft pile penetration.

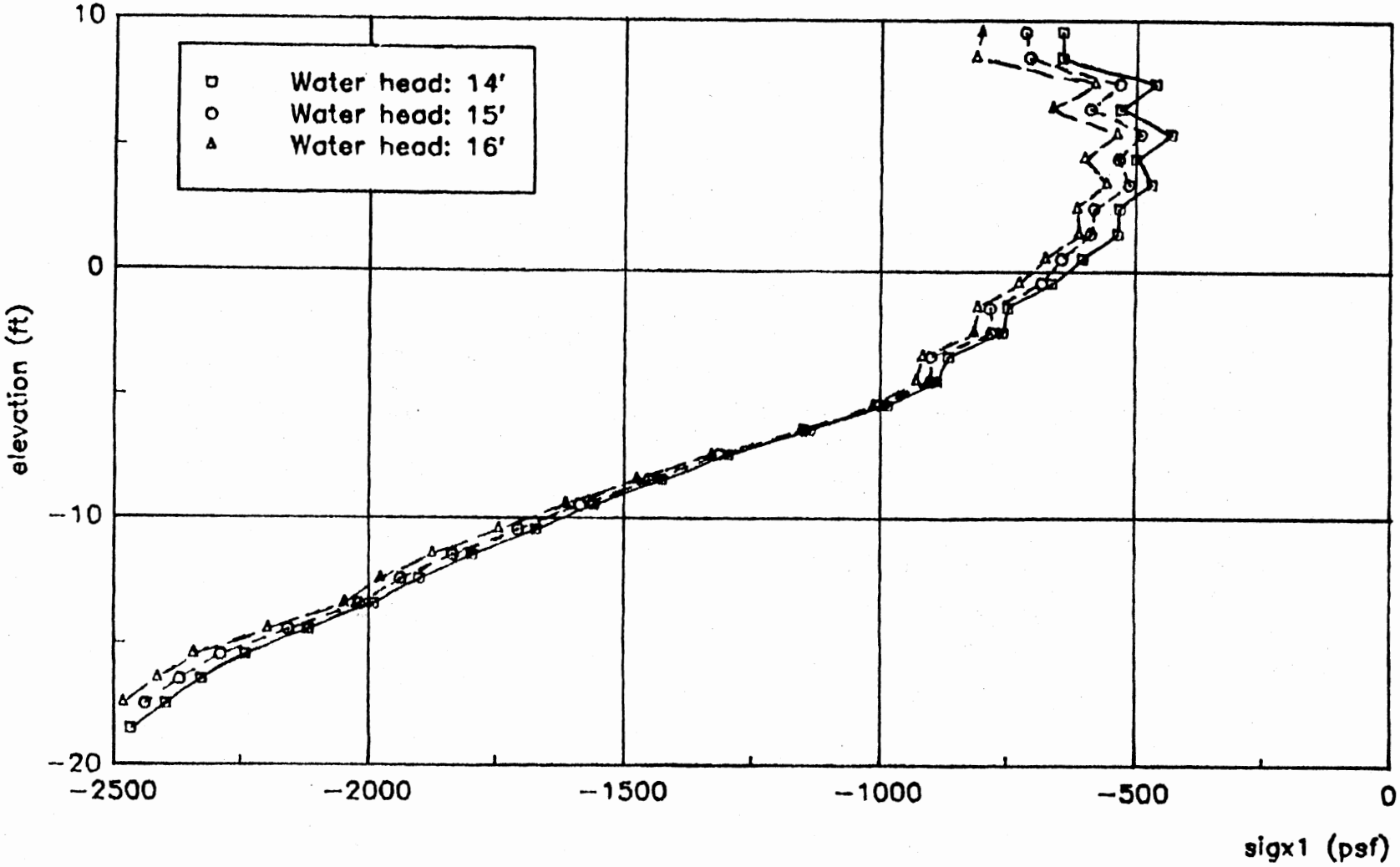

Figure 64(c). Stress profile in front of the pile, medium strength profile, 30 ft pile penetration.

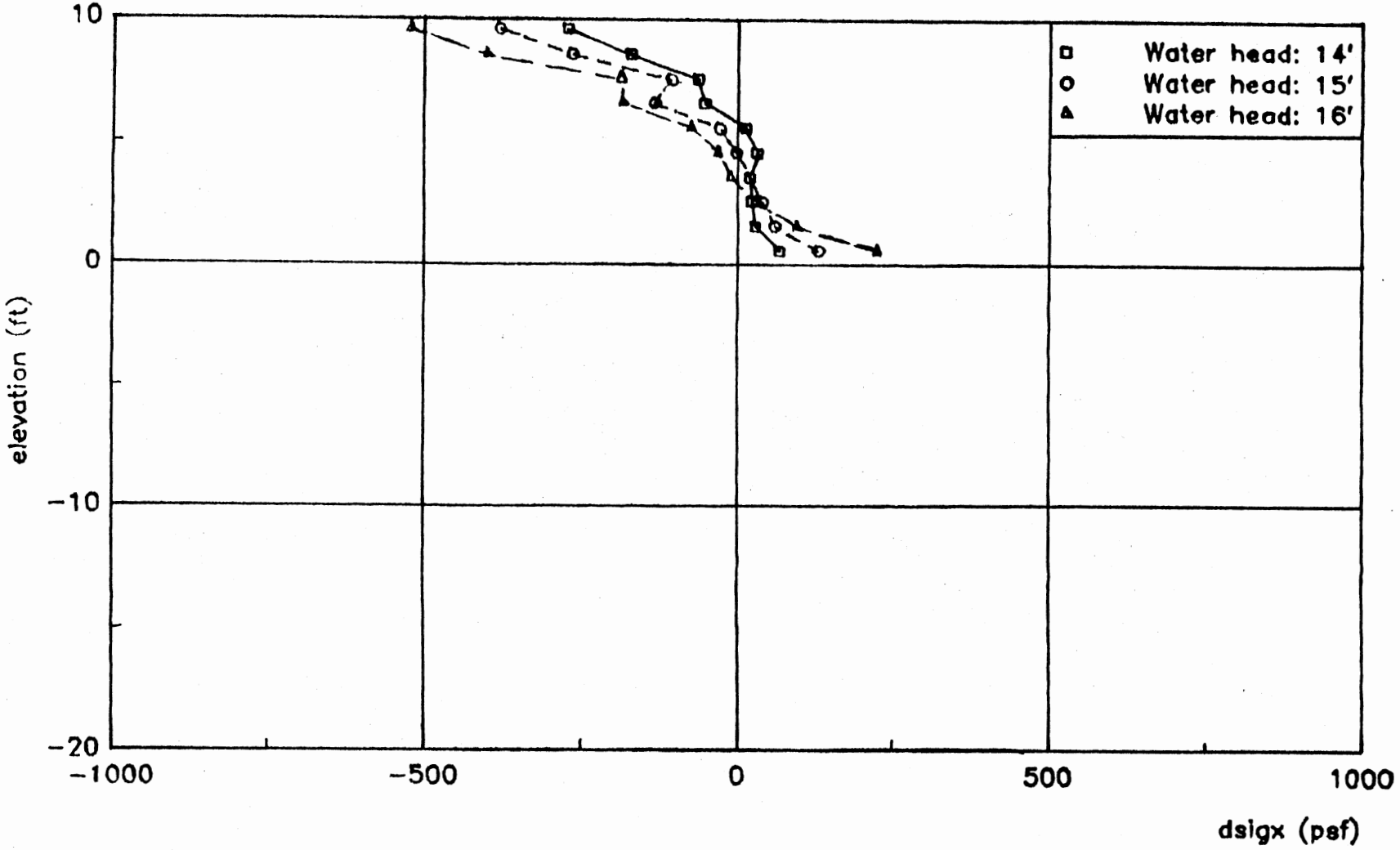

Figure 65(a). Net stress profile on the pile, medium strength profile, 10 ft pile penetration.

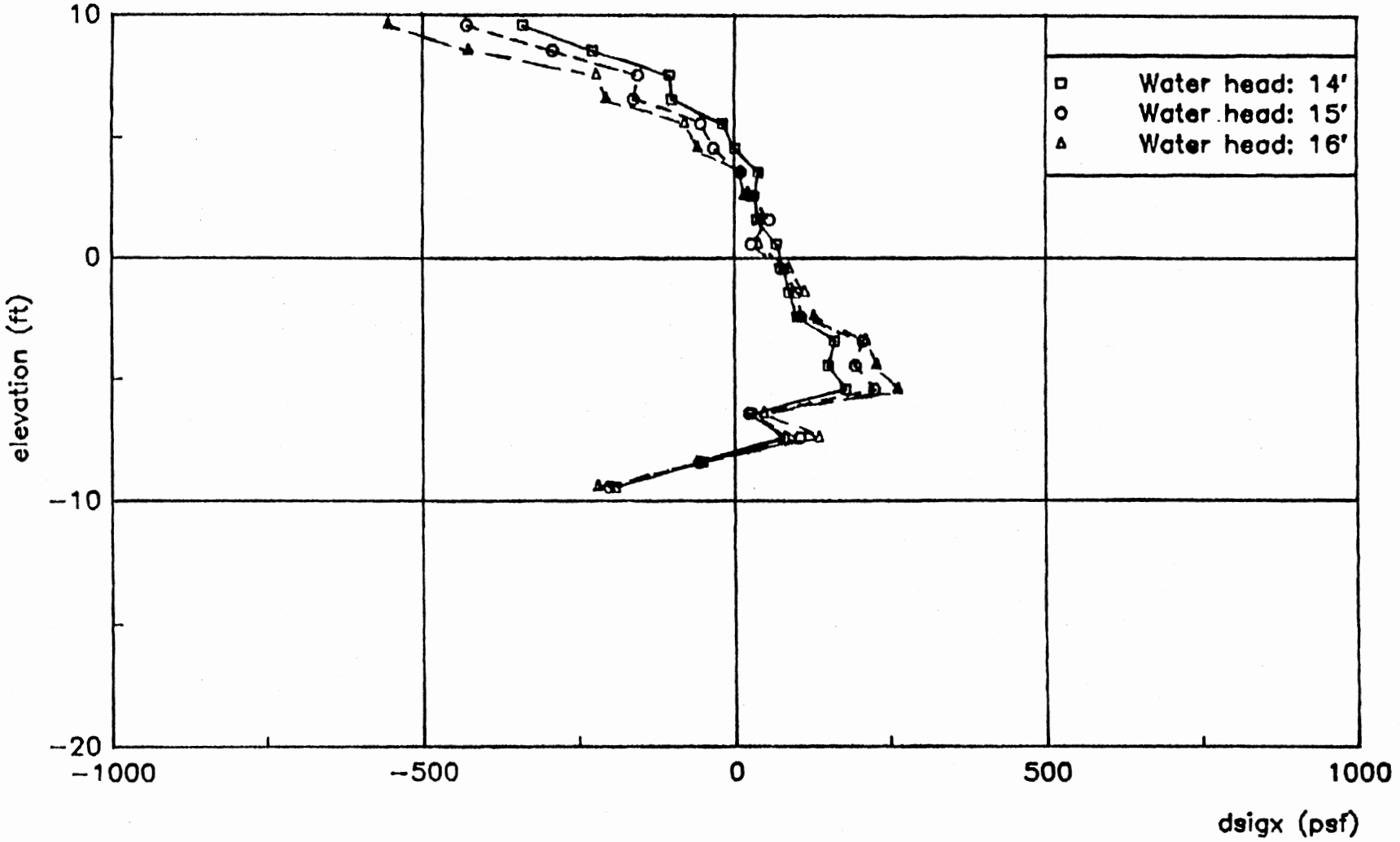

Figure 65(b). Net stress profile on the pile, medium strength profile, 20 ft pile penetration.

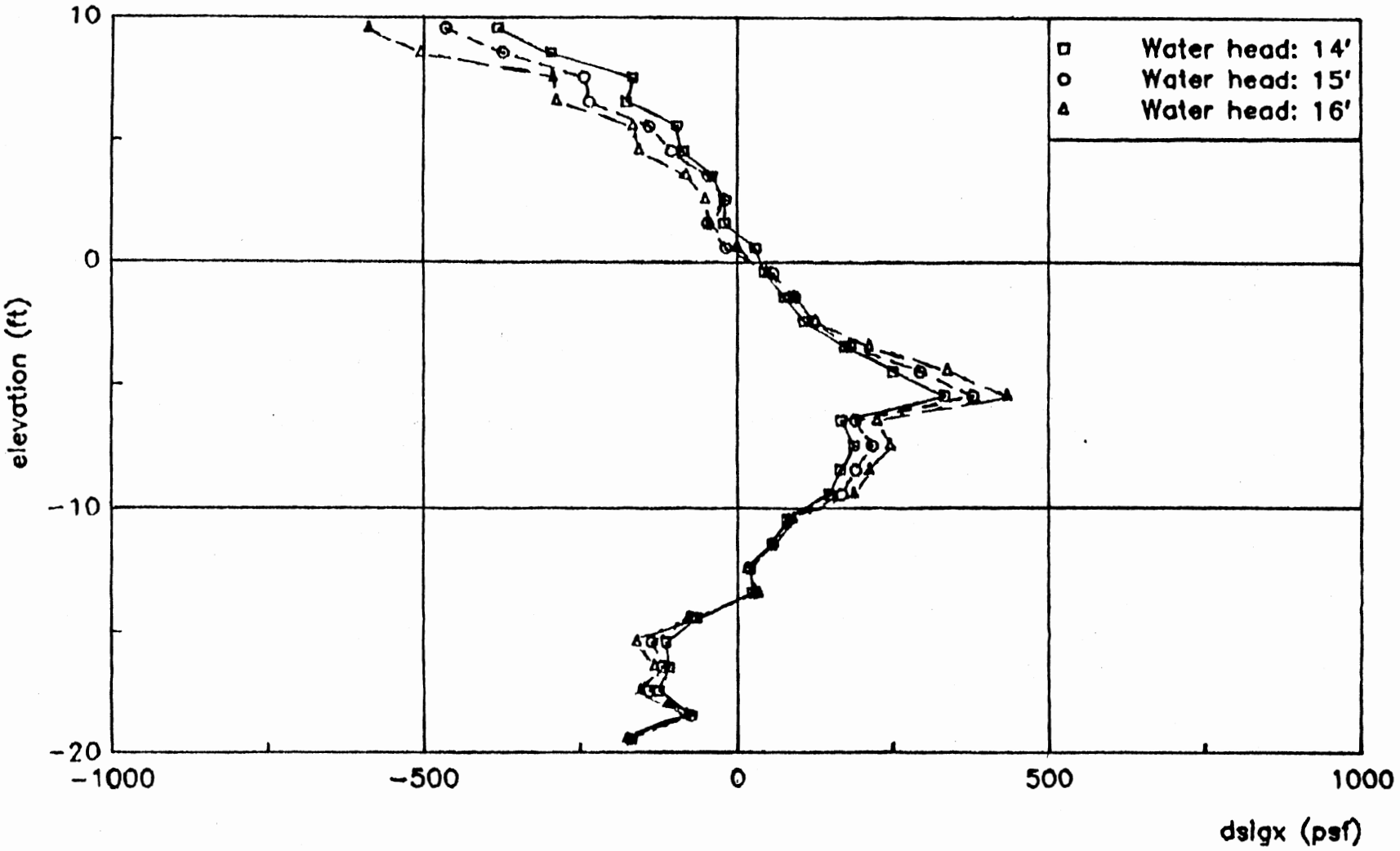

Figure 65(c). Net stress profile on the pile, medium strength profile, 30 ft pile penetration.

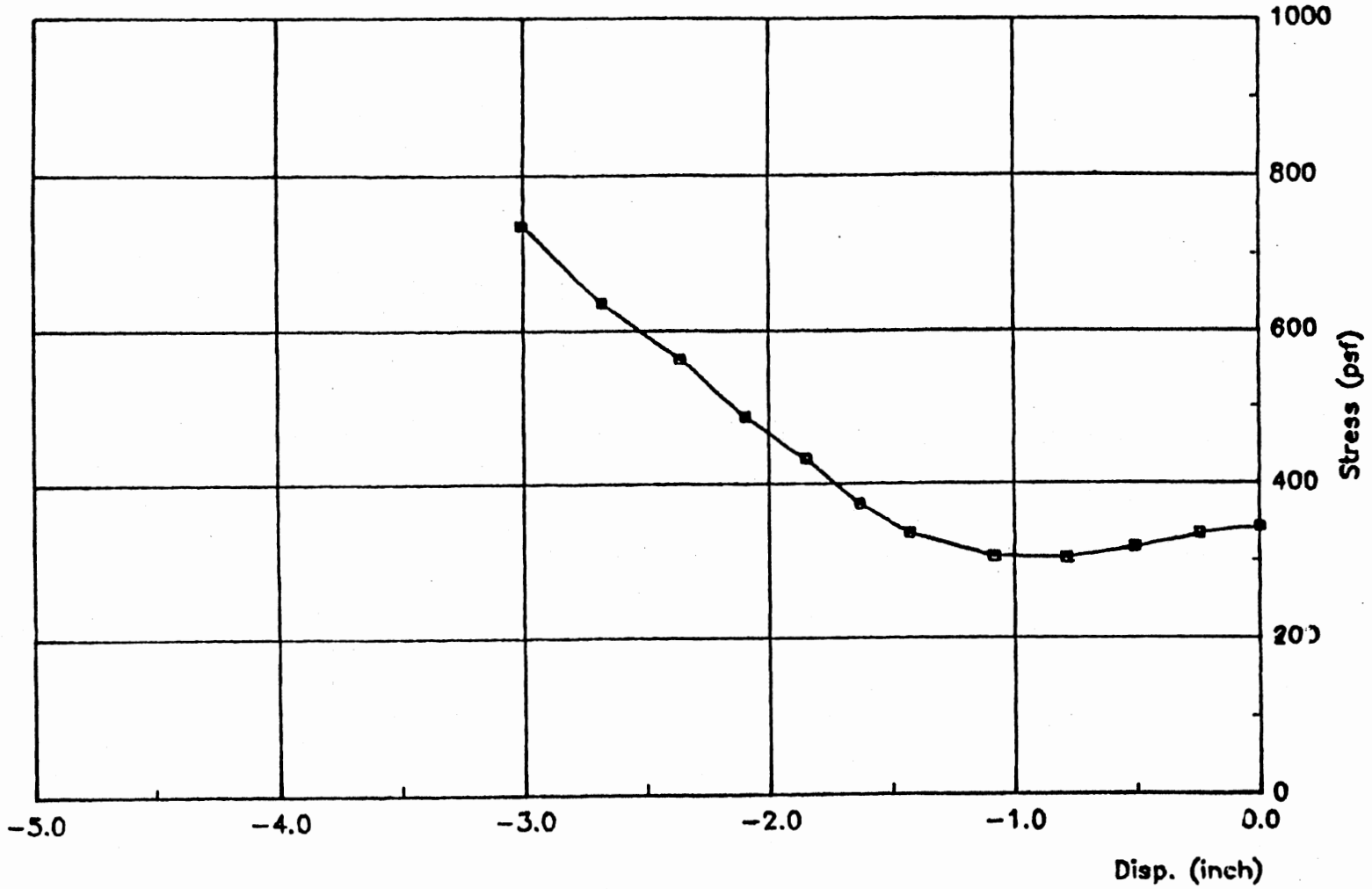

Figure 66(a). Soil-Response curve at 9 ft elevation, front side, medium strength profile, 10 ft pile penetration.

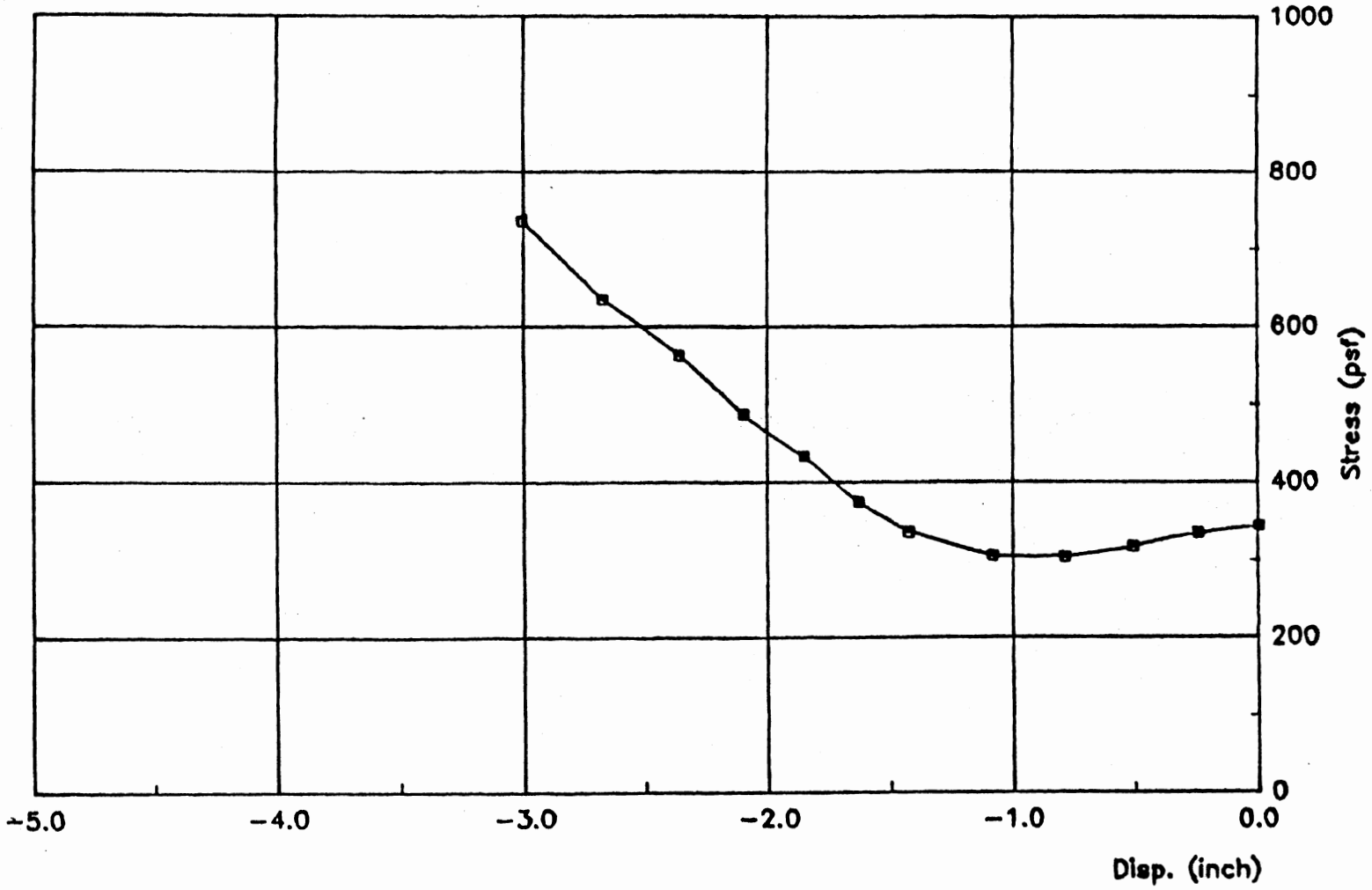

Figure 66(b). Soil-Response curve at 9 ft elevation, front side, medium strength profile, 20 ft pile penetration.

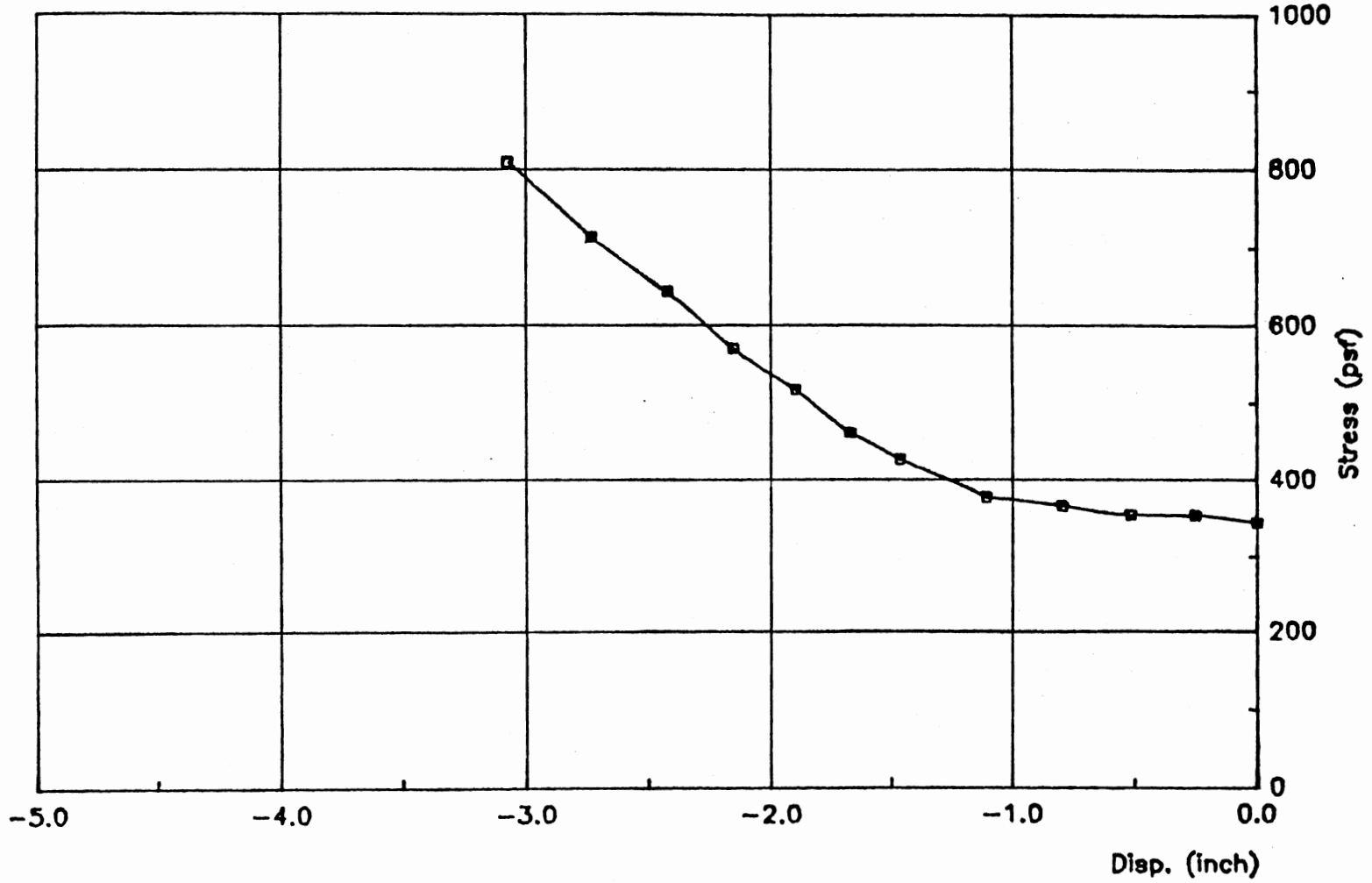

Figure 66(c). Soil-Response curve at 9 ft elevation, front side, medium strength profile, 30 ft pile penetration.

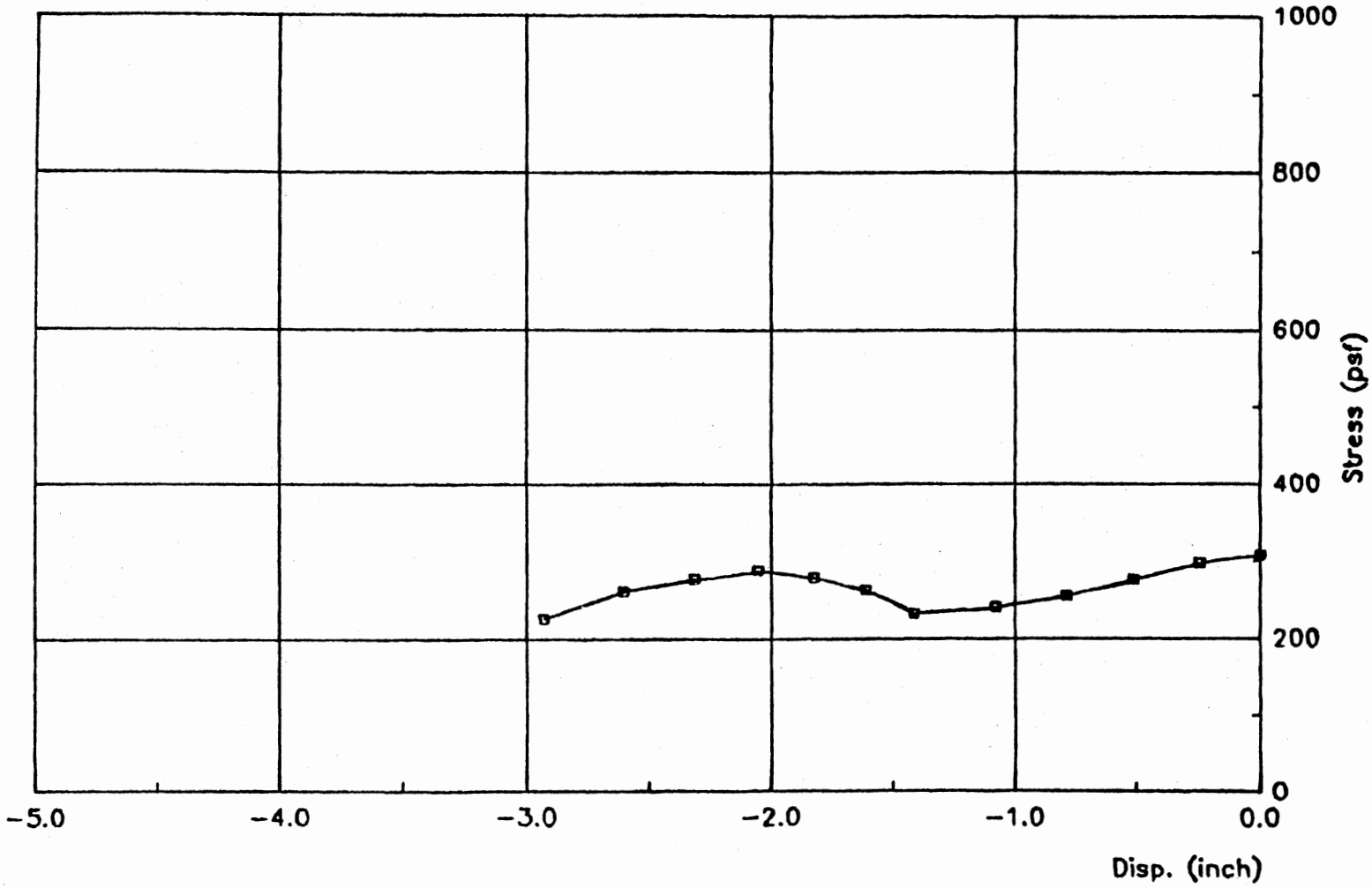

Figure 66(d). Soil-Response curve at 9 ft elevation, back side, medium strength profile, 10 ft pile penetration.

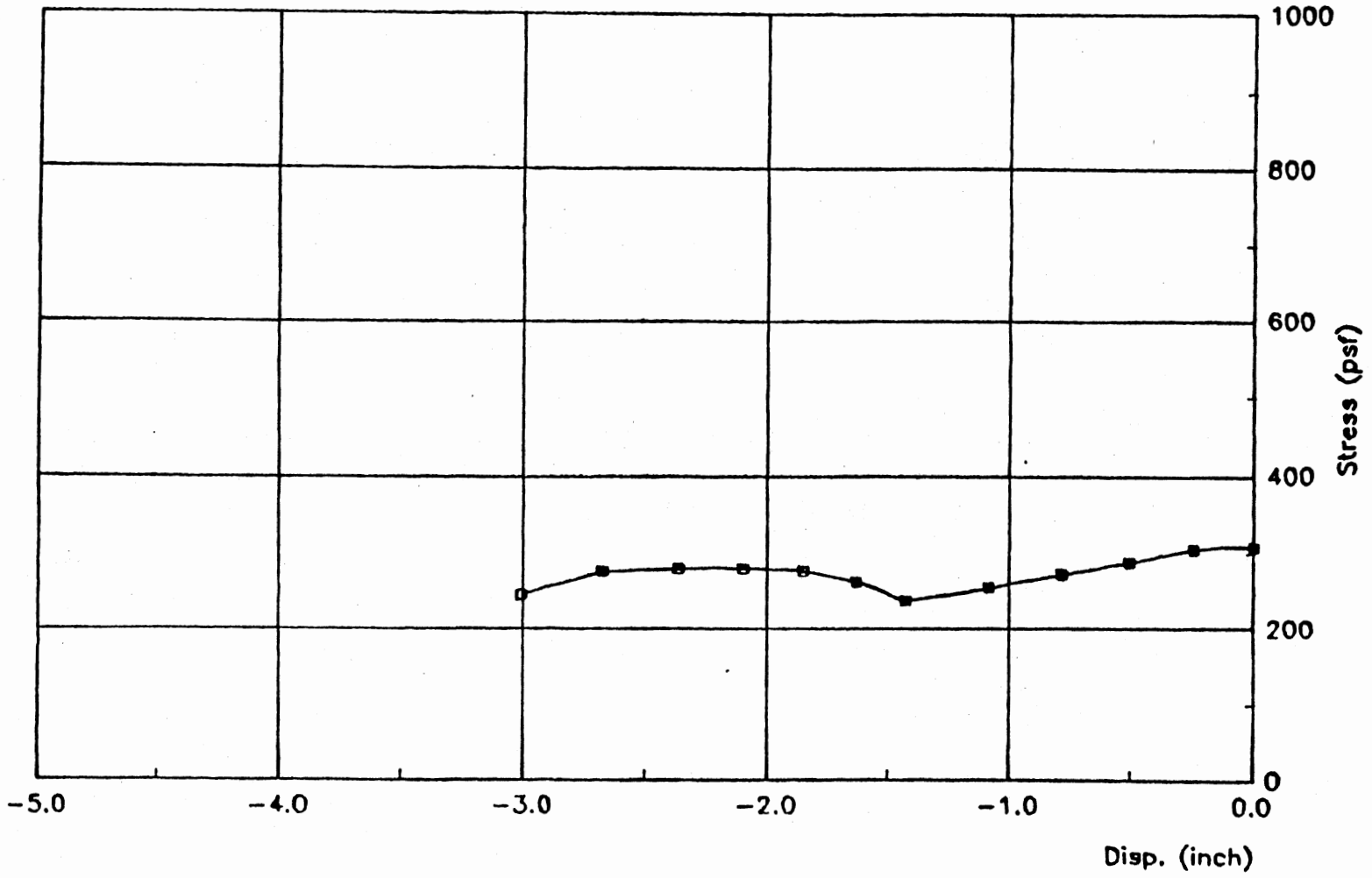

Figure 66(e). Soil-Response curve at 9 ft elevation, back side, medium strength profile, 20 ft pile penetration.

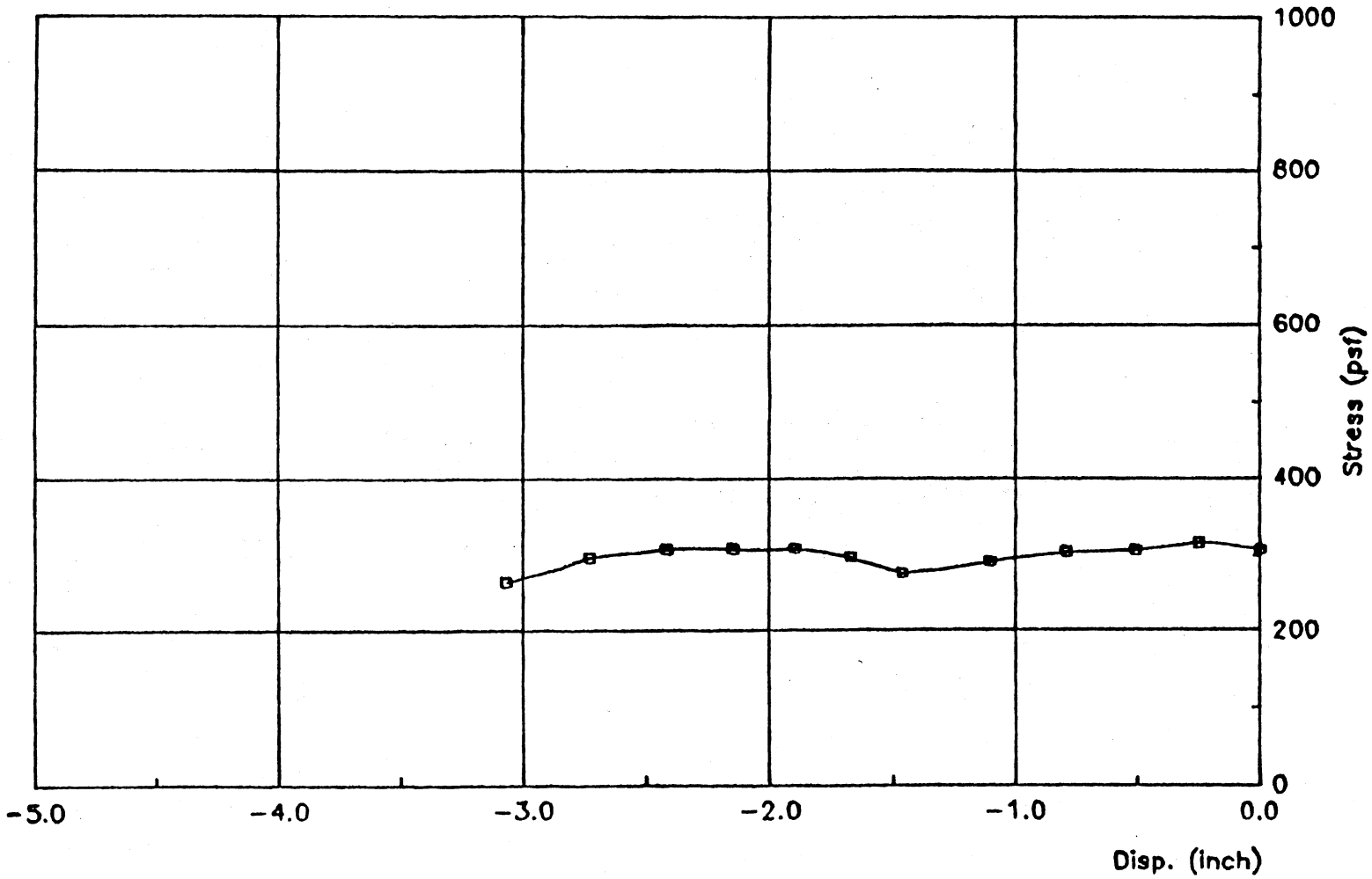

Figure 66(f). Soil-Response curve at 9 ft elevation, back side, medium strength profile, 30 ft pile penetration.

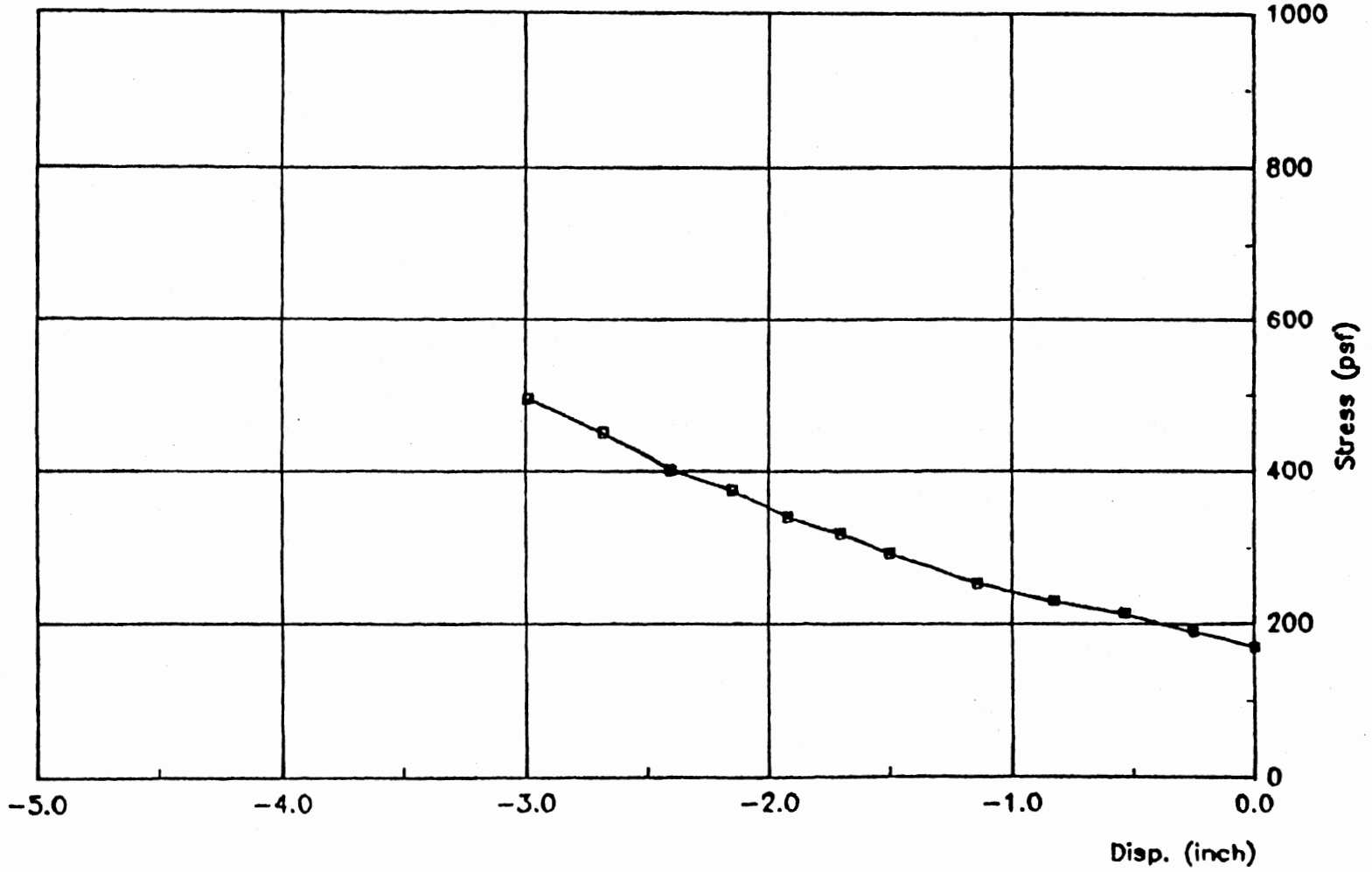

Figure 87(a). Soil-Response curve at 5 ft elevation, front side, medium strength profile, 10 ft pile penetration.

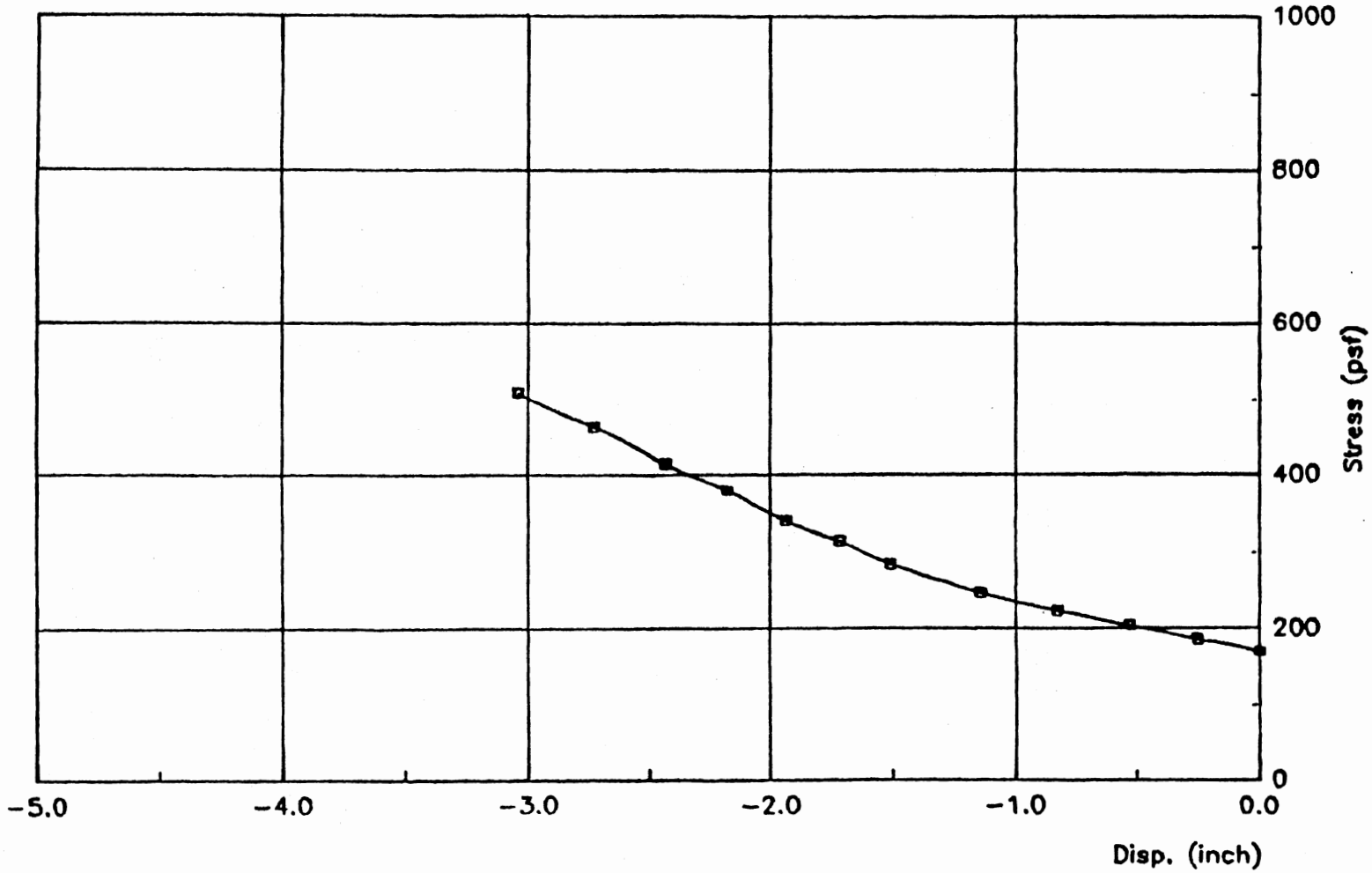

Figure 67(b). Soil-Response curve at 5 ft elevation, front side, medium strength profile, 20 ft pile penetration.

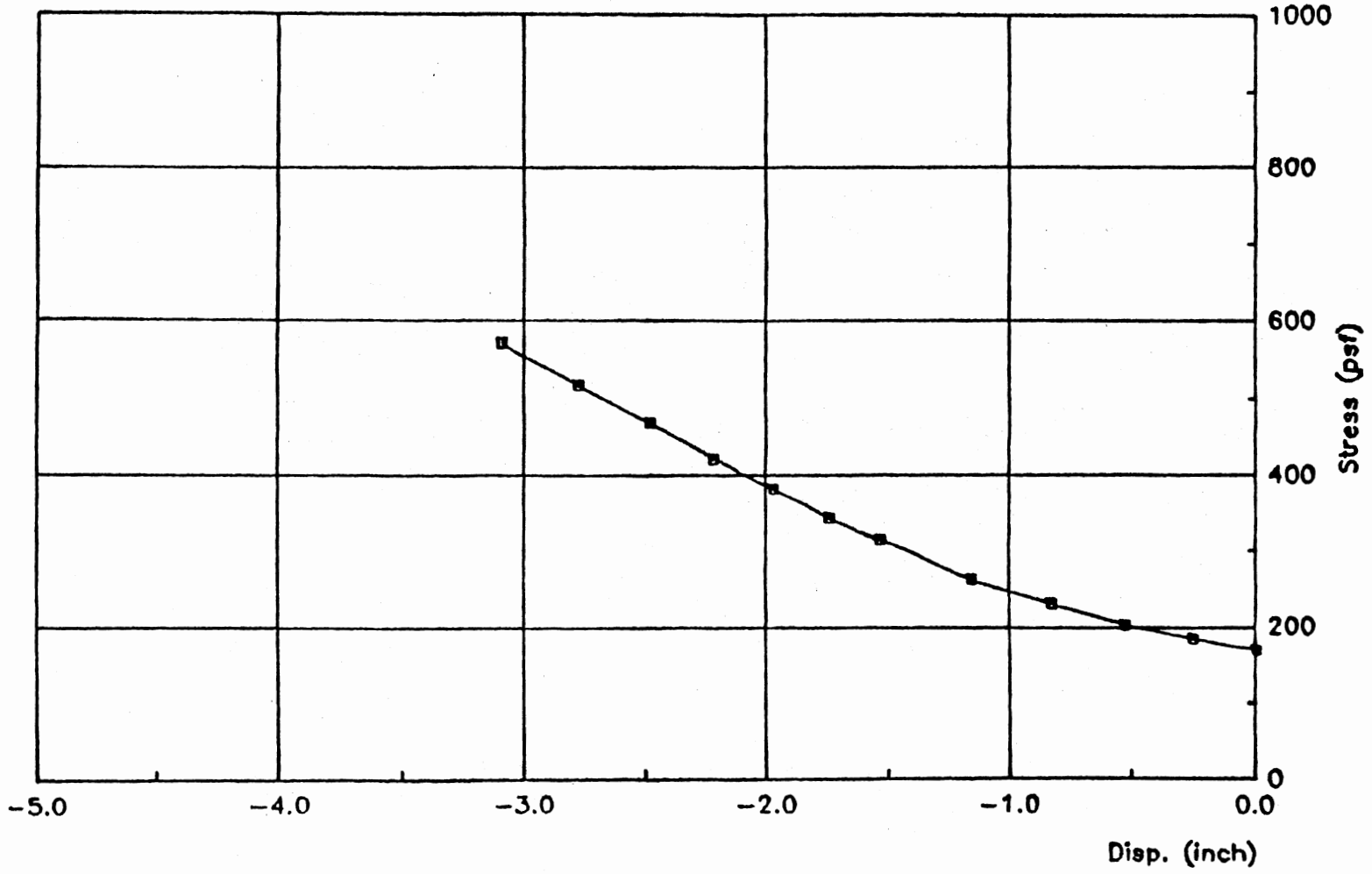

Figure 67(c). Soil-Response curve at 5 ft elevation, front side, medium strength profile, 30 ft pile penetration.

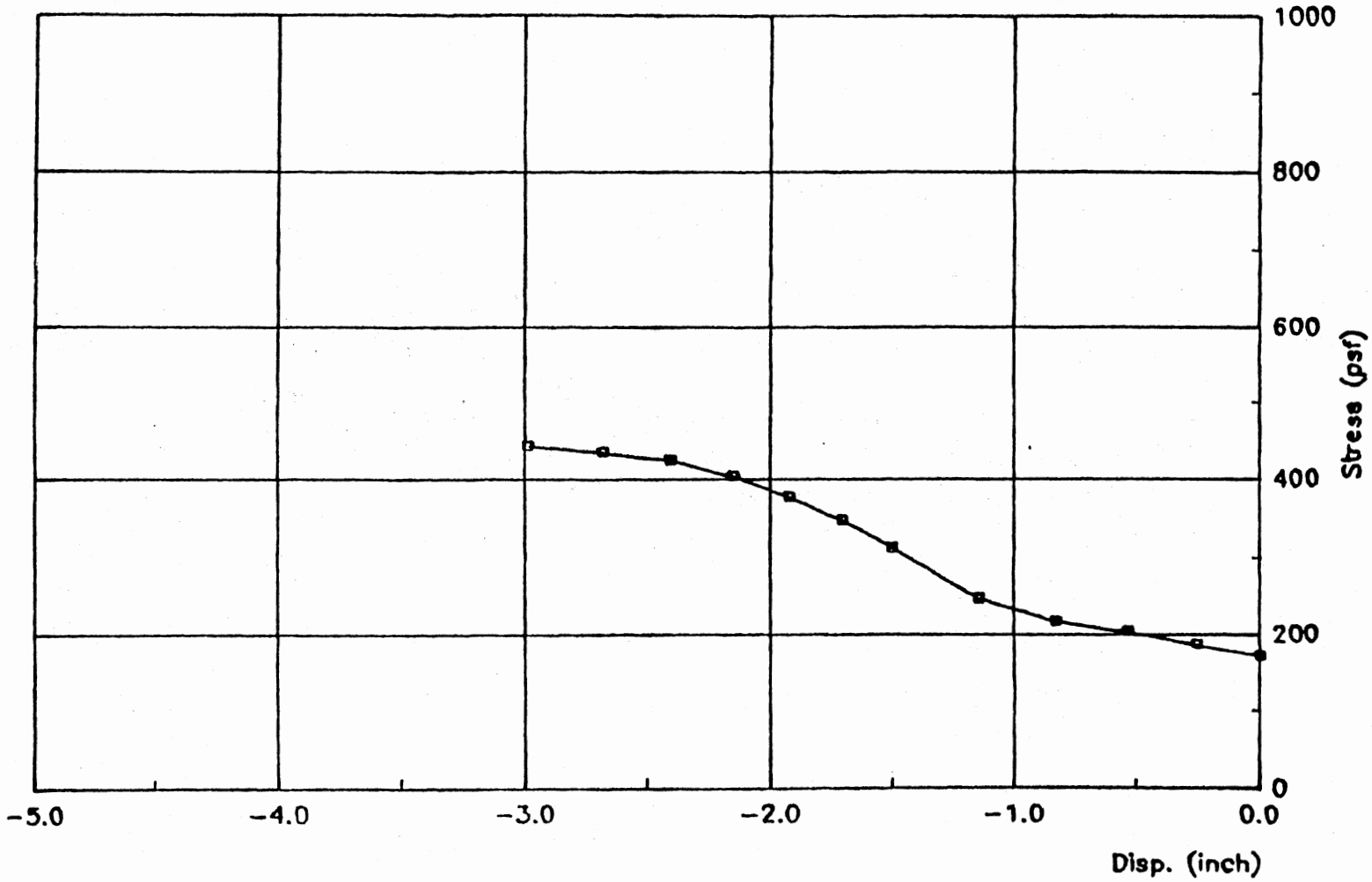

Figure 67(d). Soil-Response curve at 5 ft elevation, back side, medium strength profile, 10 ft pile penetration.

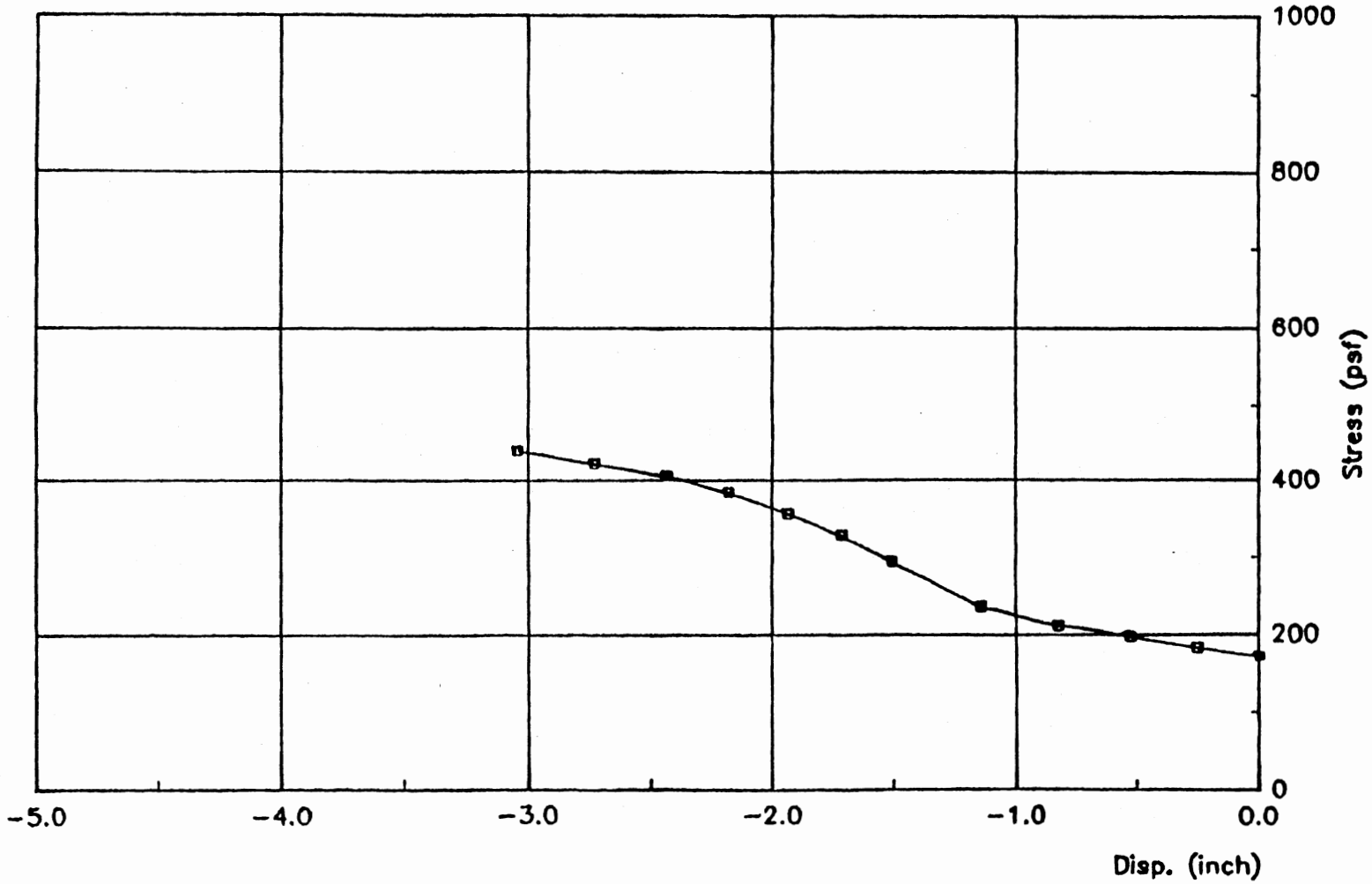

Figure 67(e). Soil-Response curve at 5 ft elevation, back side, medium strength profile, 20 ft pile penetration.

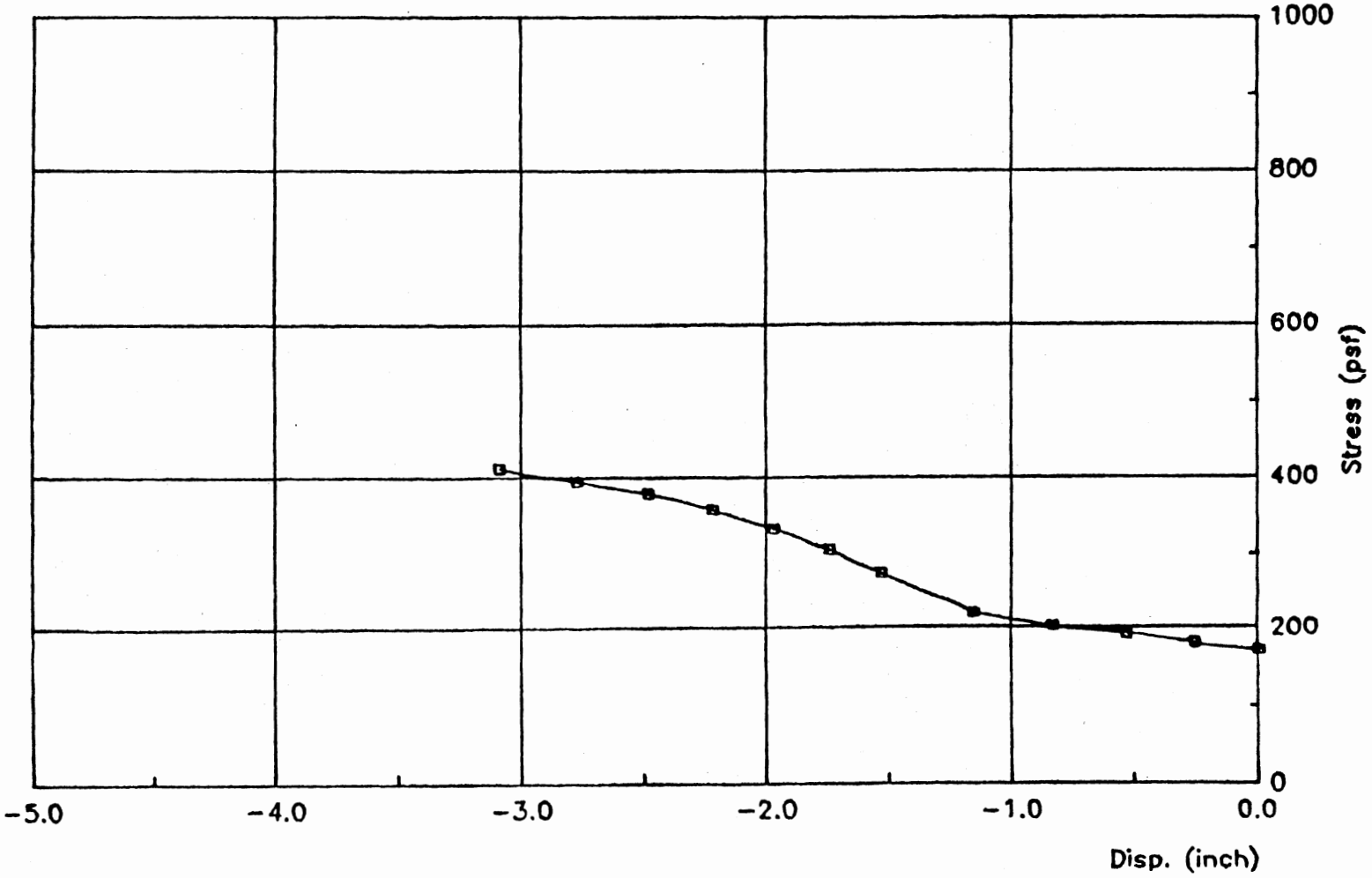

Figure 87(f). Soil-Response curve at 5 ft elevation, back side, medium strength profile, 30 ft pile penetration.

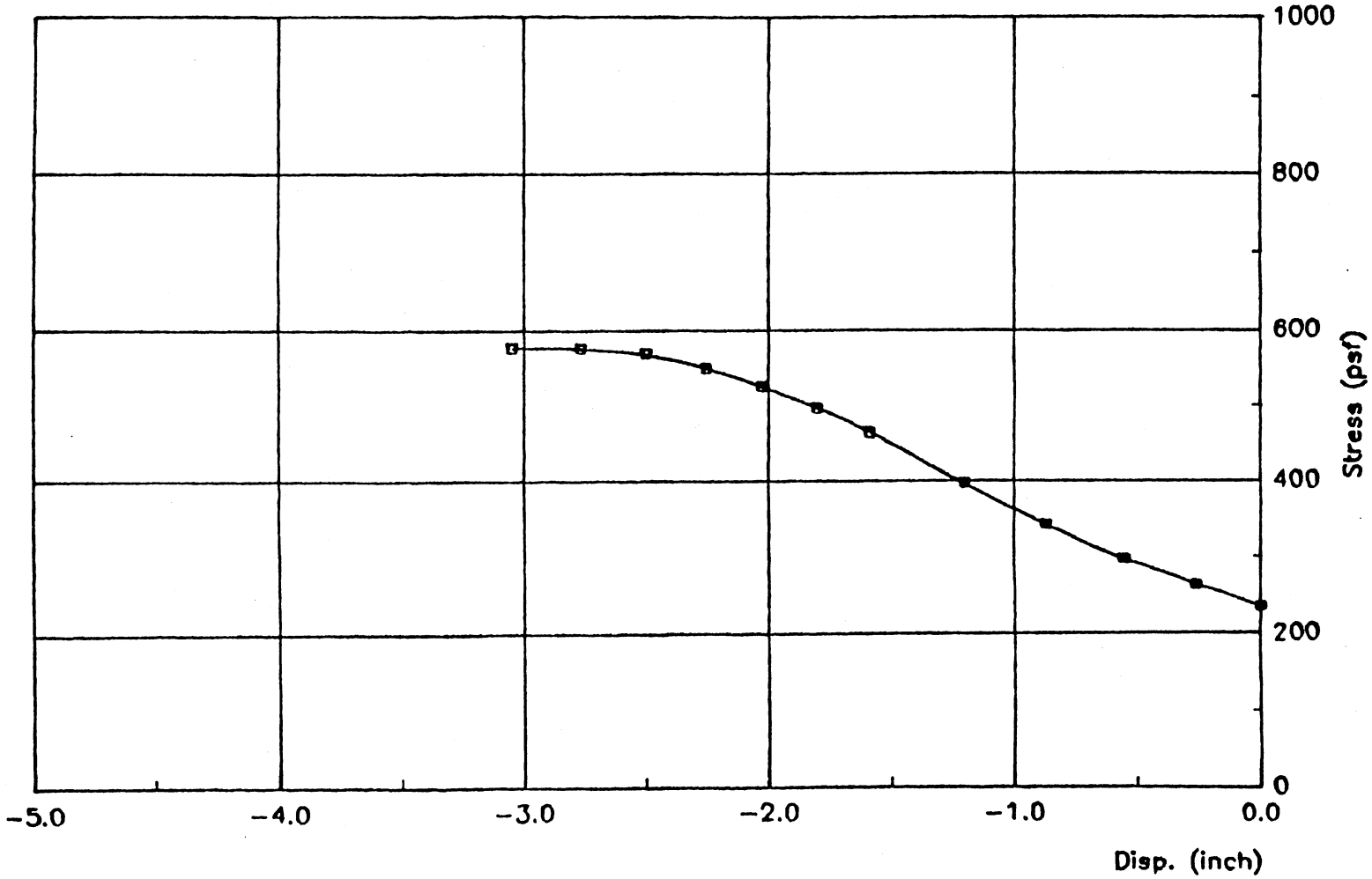

Figure 68(a). Soil-Response curve at 1 ft elevation, front side, medium strength profile, 10 ft pile penetration.

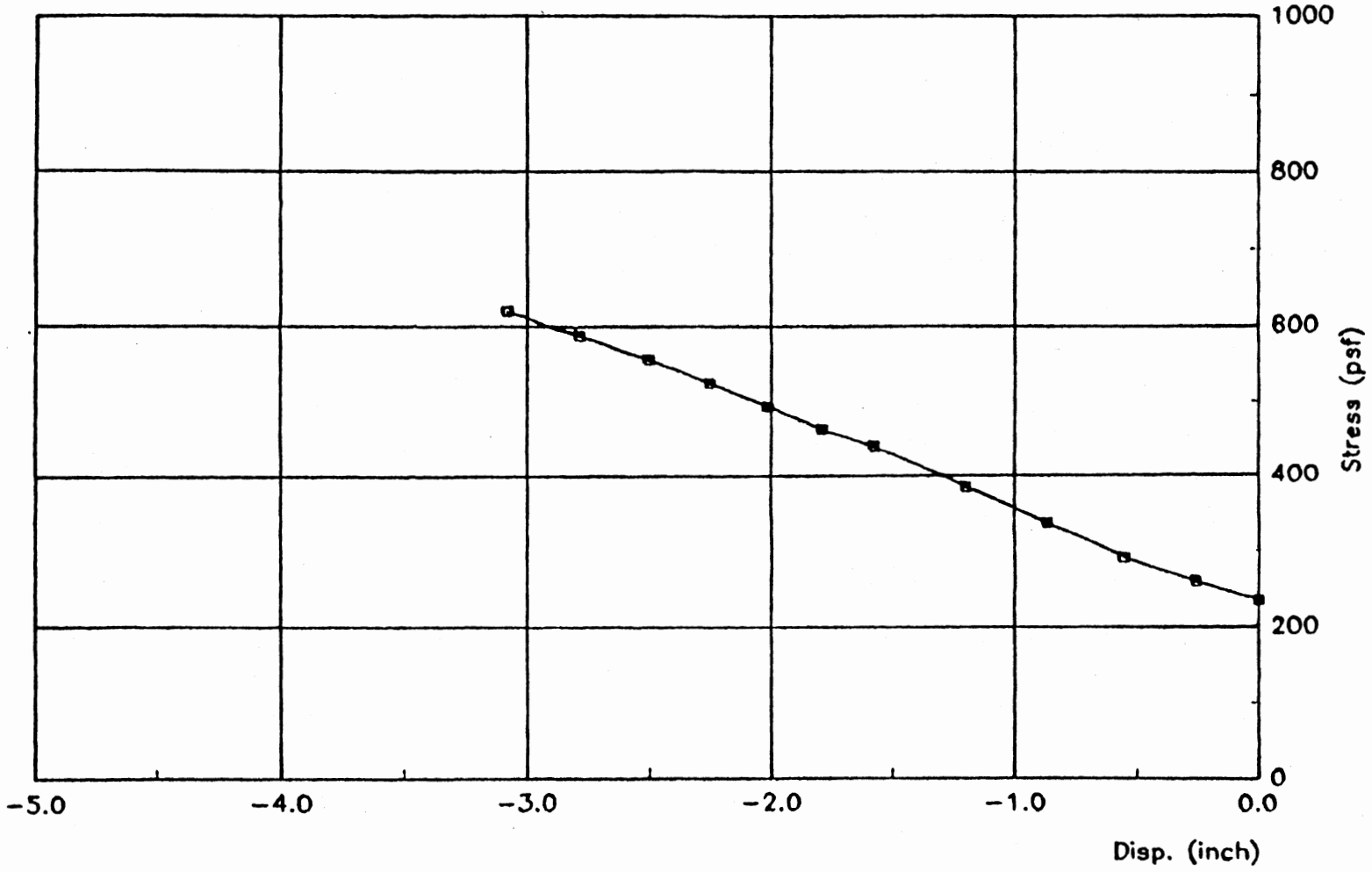

Figure 68(b). Soil-Response curve at 1 ft elevation, front side, medium strength profile, 20 ft pile penetration.

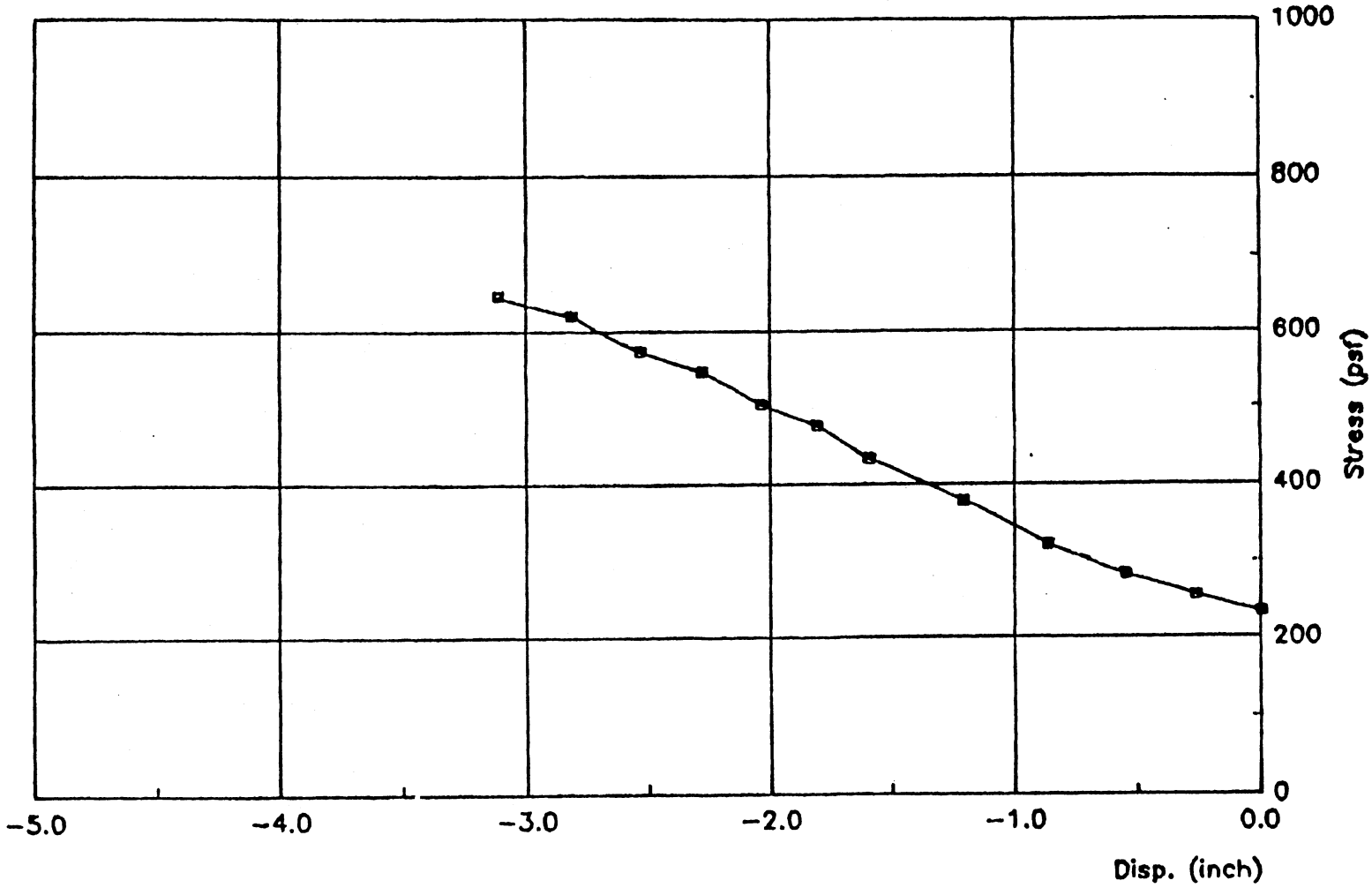

Figure 68(c). Soil-Response curve at 1 ft elevation, front side, medium strength profile, 30 ft pile penetration.

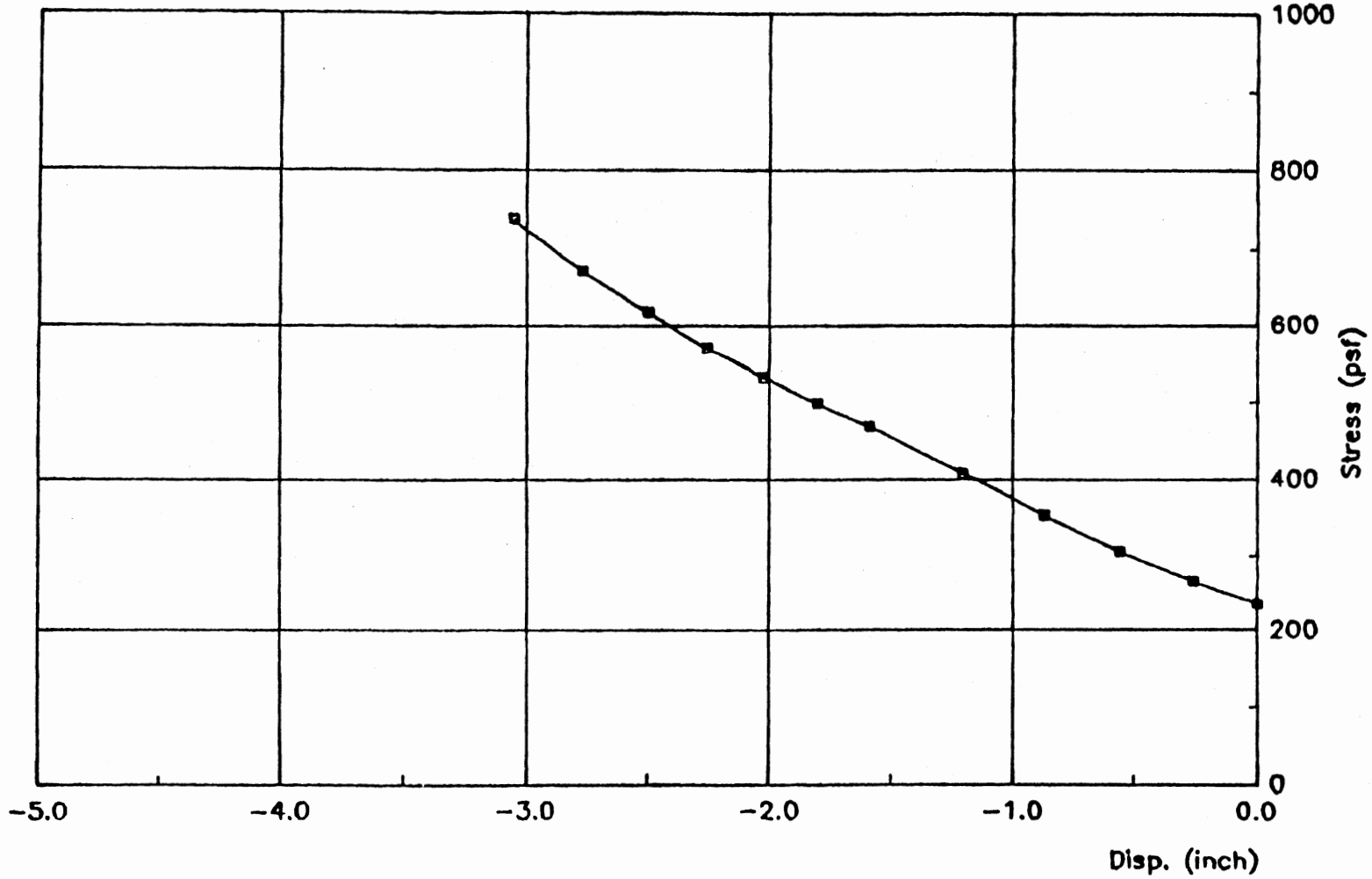

Figure 68(d). Soil-Response curve at 1 ft elevation, back side, medium strength profile, 10 ft pile penetration.

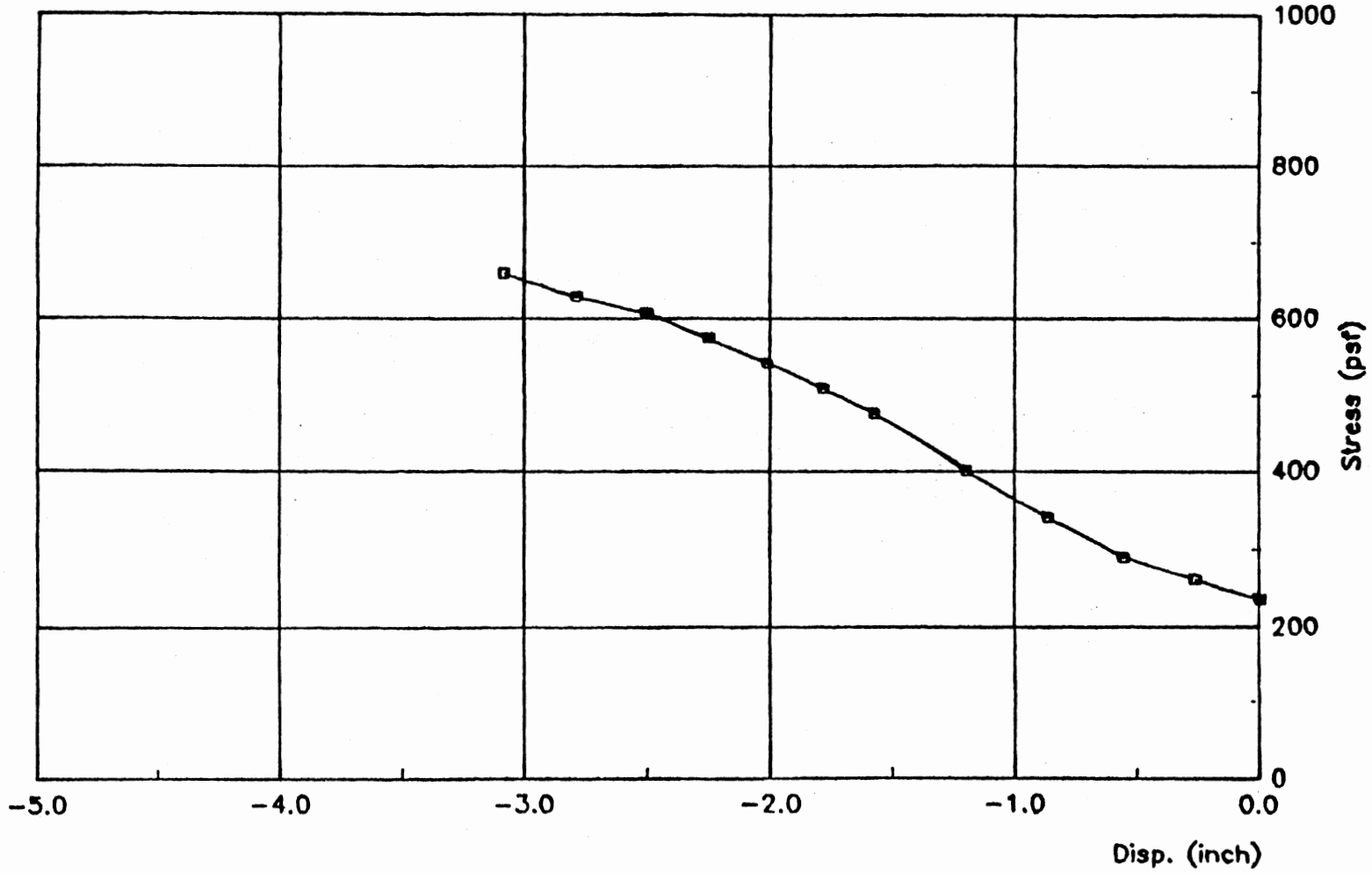

Figure 88(e). Soil-Response curve at 1 ft elevation, back side, medium strength profile, 20 ft pile penetration.

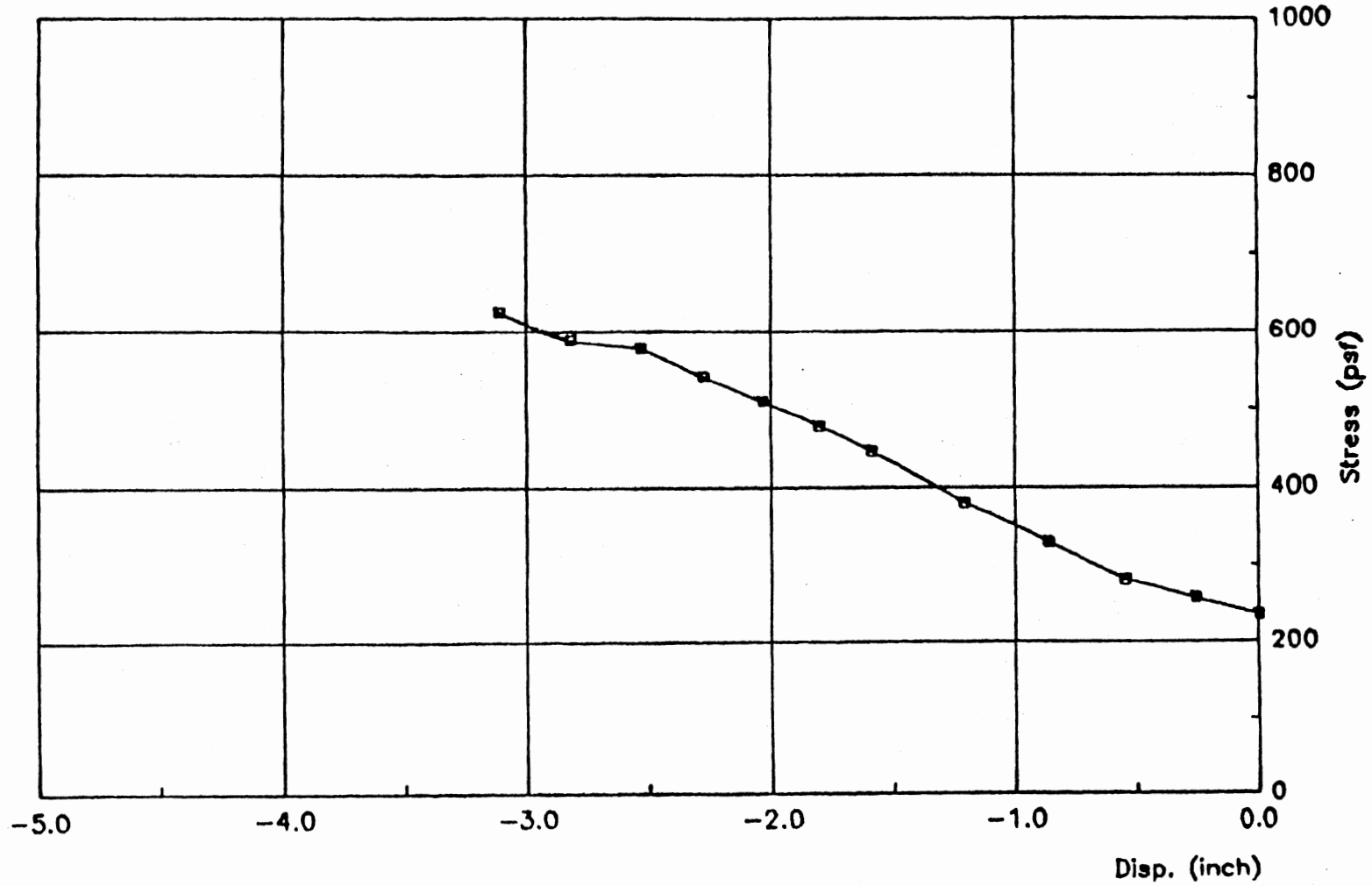

Figure 68(f). Soil-Response curve at 1 ft elevation, back side, medium strength profile, 30 ft pile penetration.

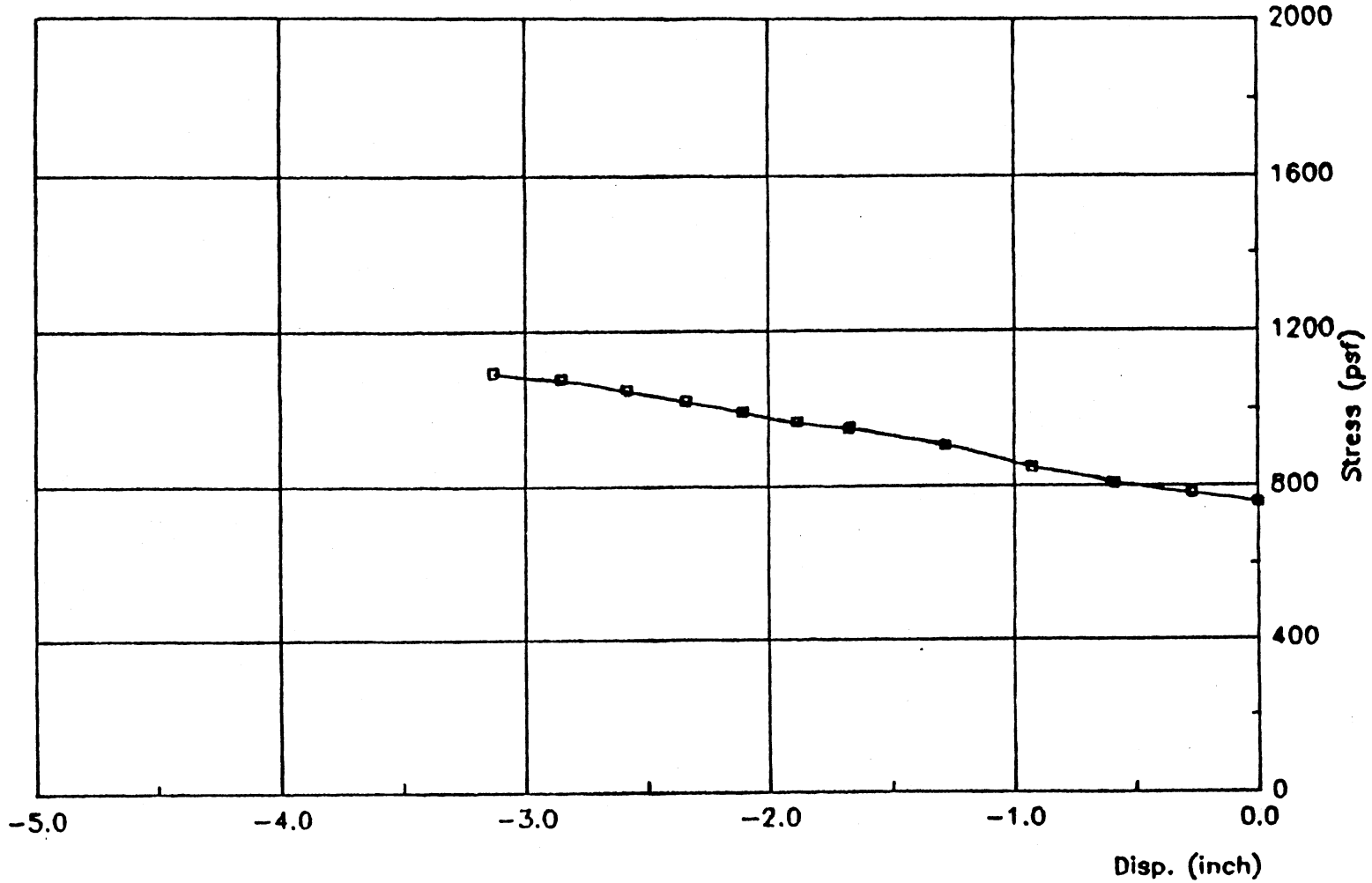

Figure 69(a). Soil-Response curve at -5 ft elevation, front side, medium strength profile, 20 ft pile penetration.

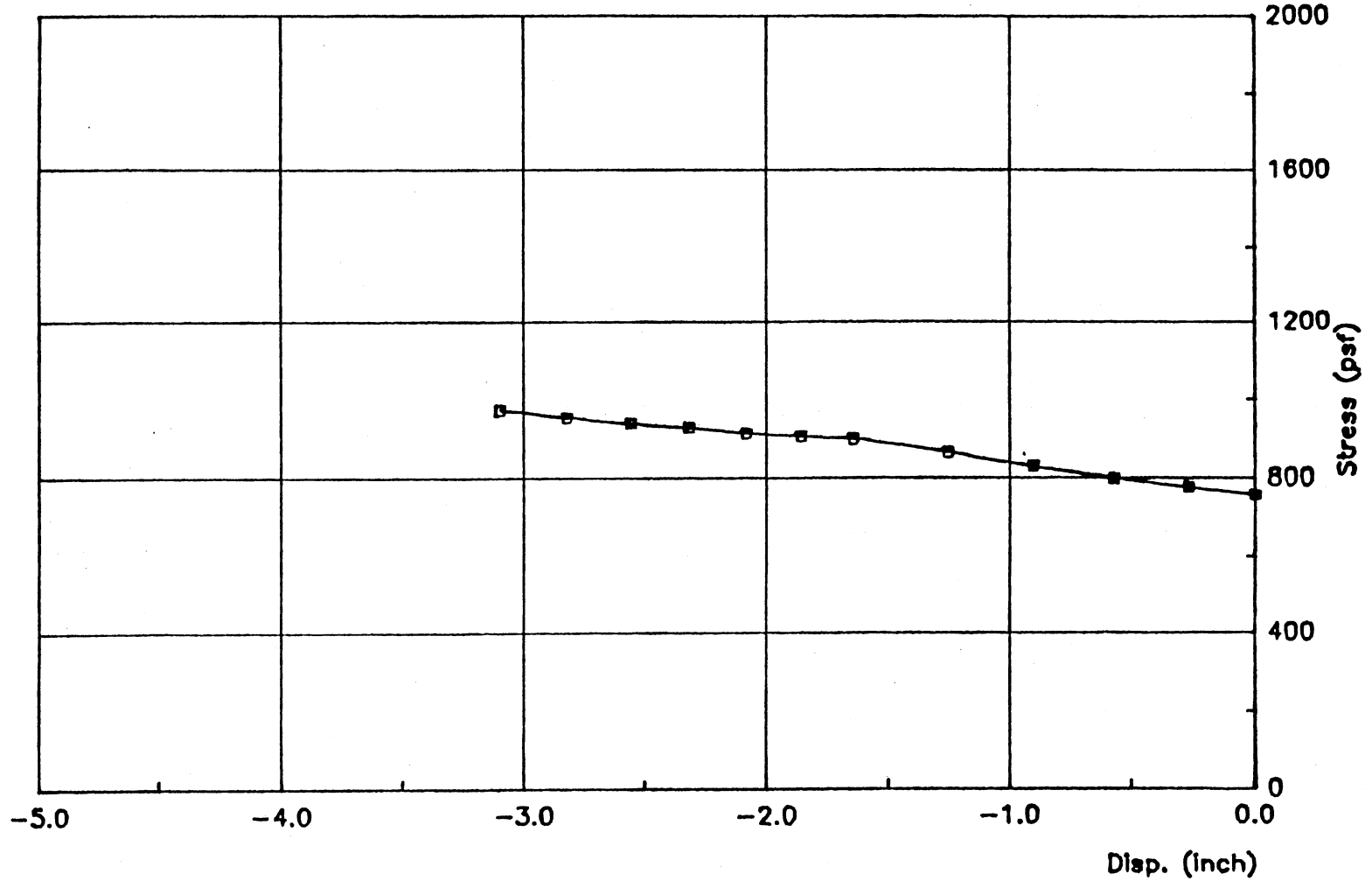

Figure 69(b). Soil-Response curve at -5 ft elevation, front side, medium strength profile, 30 ft pile penetration.

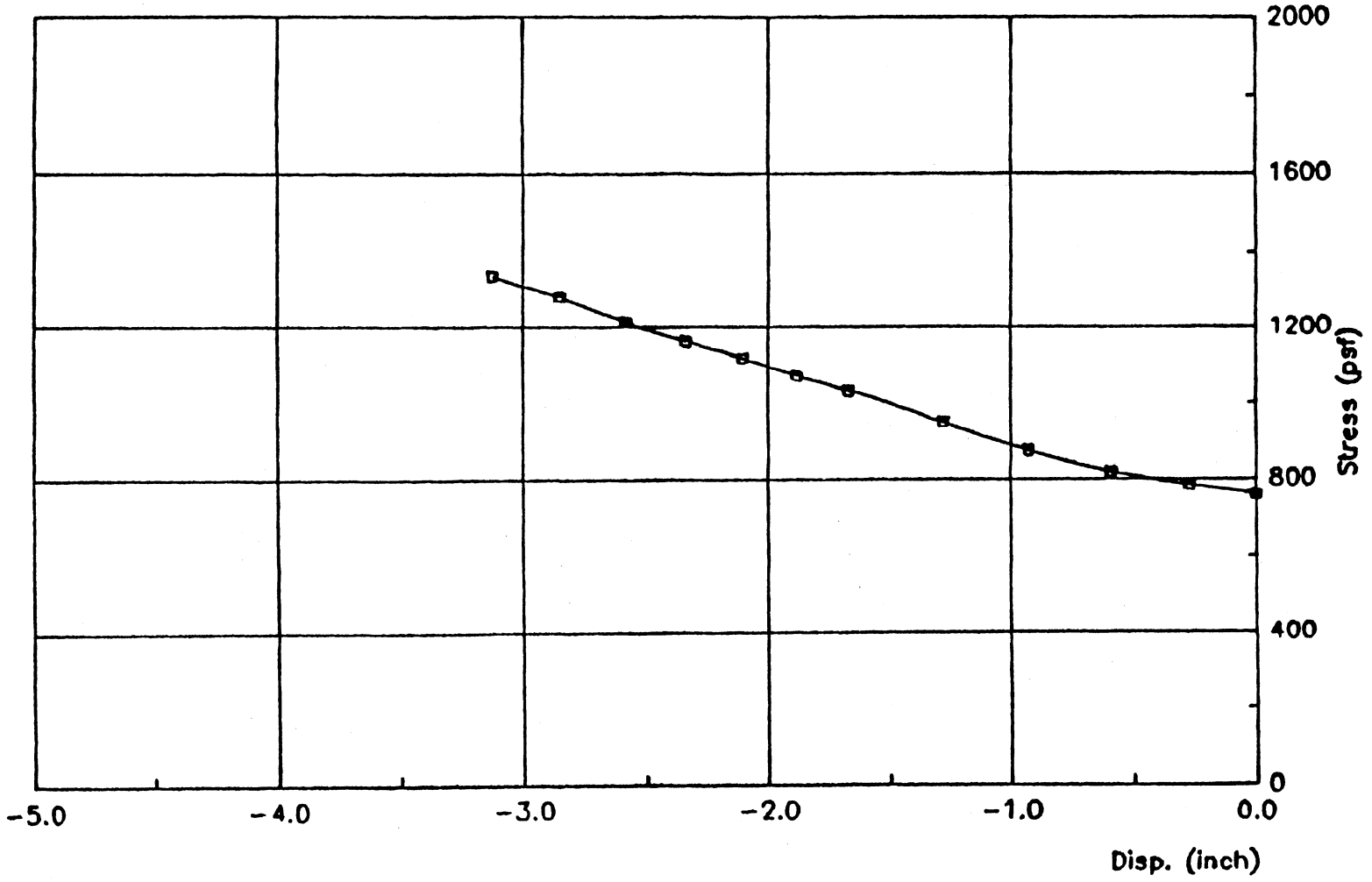

Figure 69(c). Soil-Response curve at -5 ft elevation, back side, medium strength profile, 20 ft pile penetration.

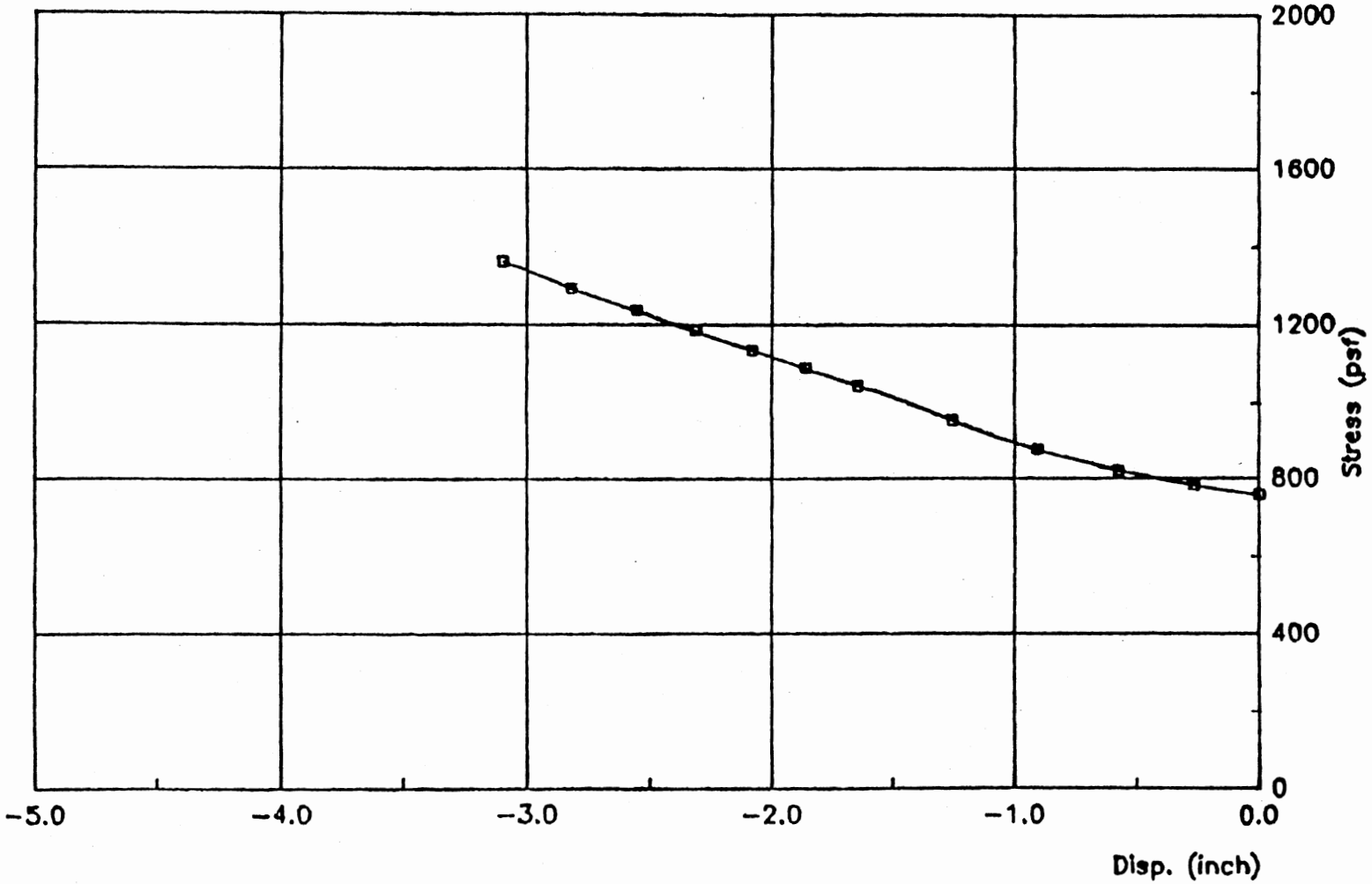

Figure 69(d). Soil-Response curve at -5 ft elevation, back side, medium strength profile, 30 ft pile penetration.

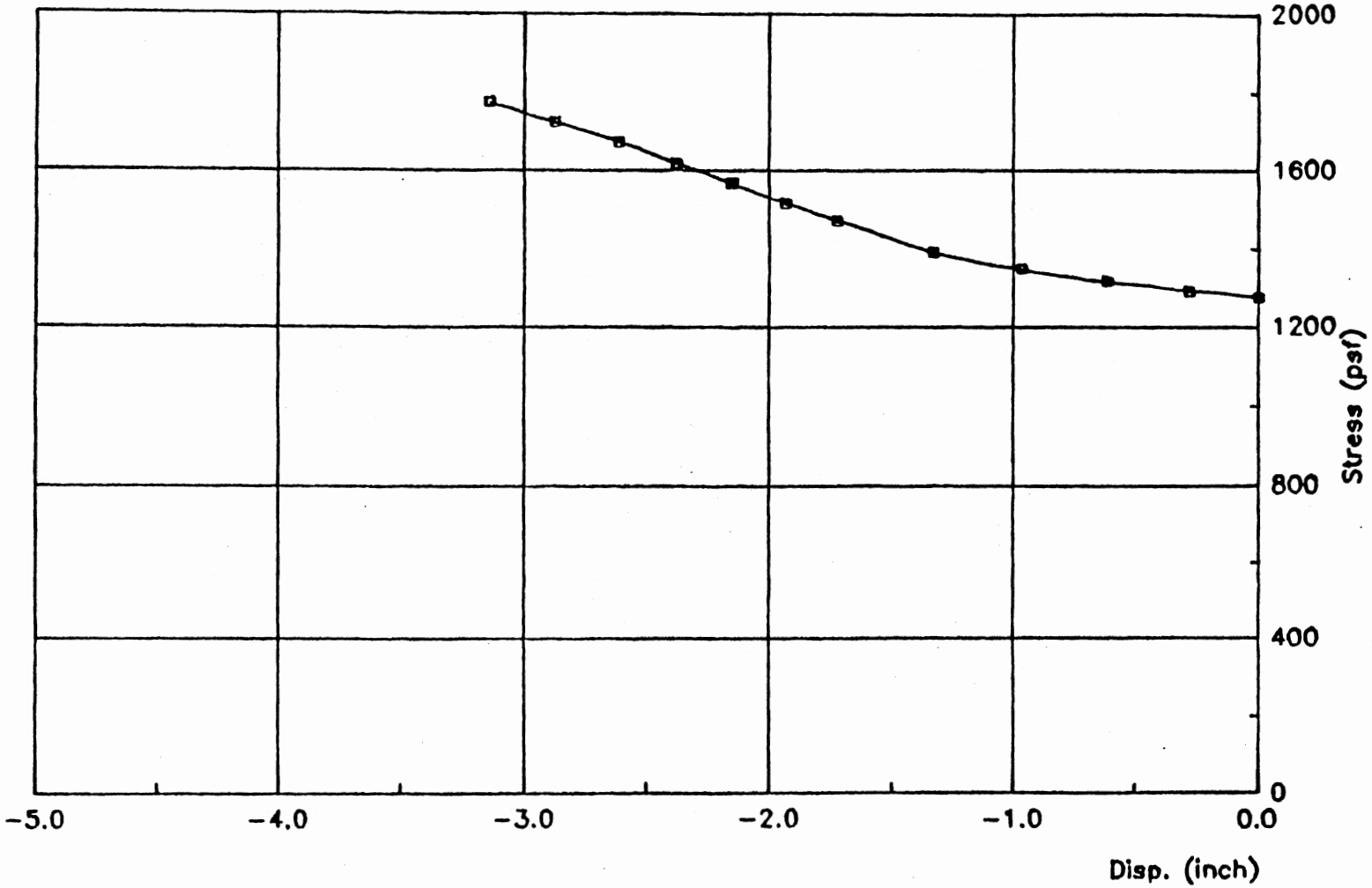

Figure 70(a). Soil-Response curve at -9 ft elevation, front side, medium strength profile, 20 ft pile penetration.

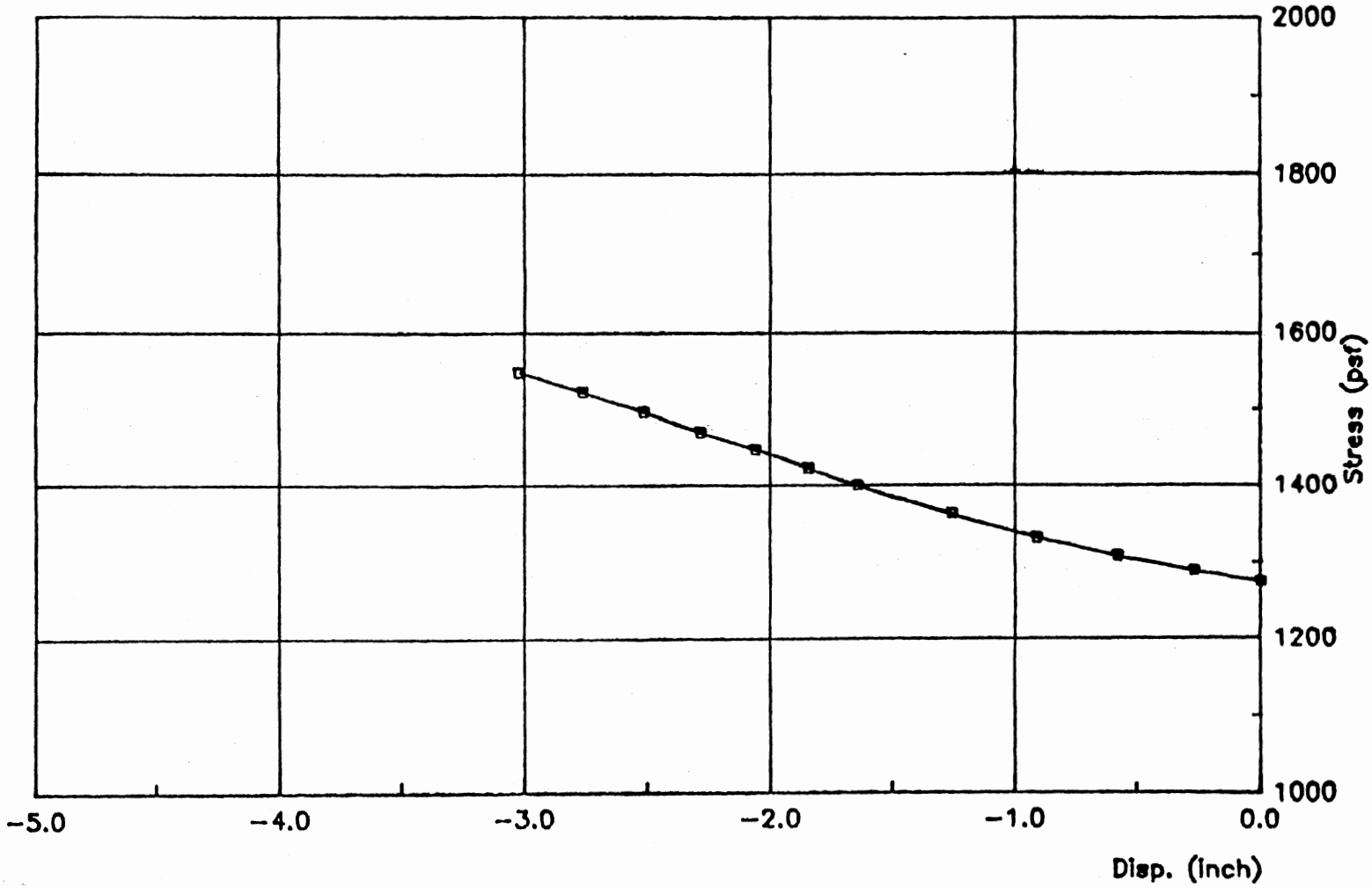

Figure 70(b). Soil-Response curve at -8 ft elevation, front side, medium strength profile, 30 ft pile penetration.

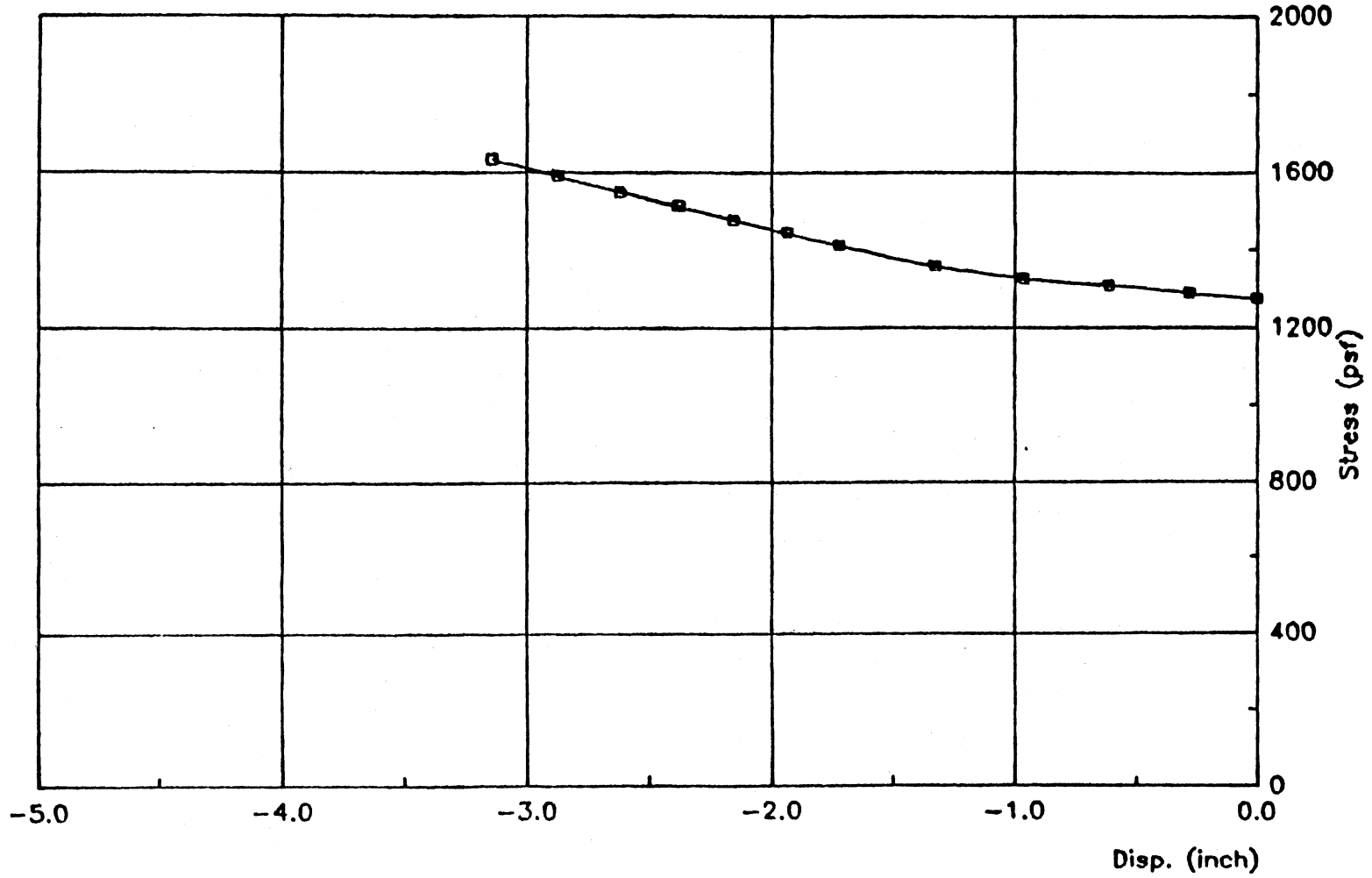

Figure 70(c). Soil-Response curve at -9 ft elevation, back side, medium strength profile, 20 ft pile penetration.

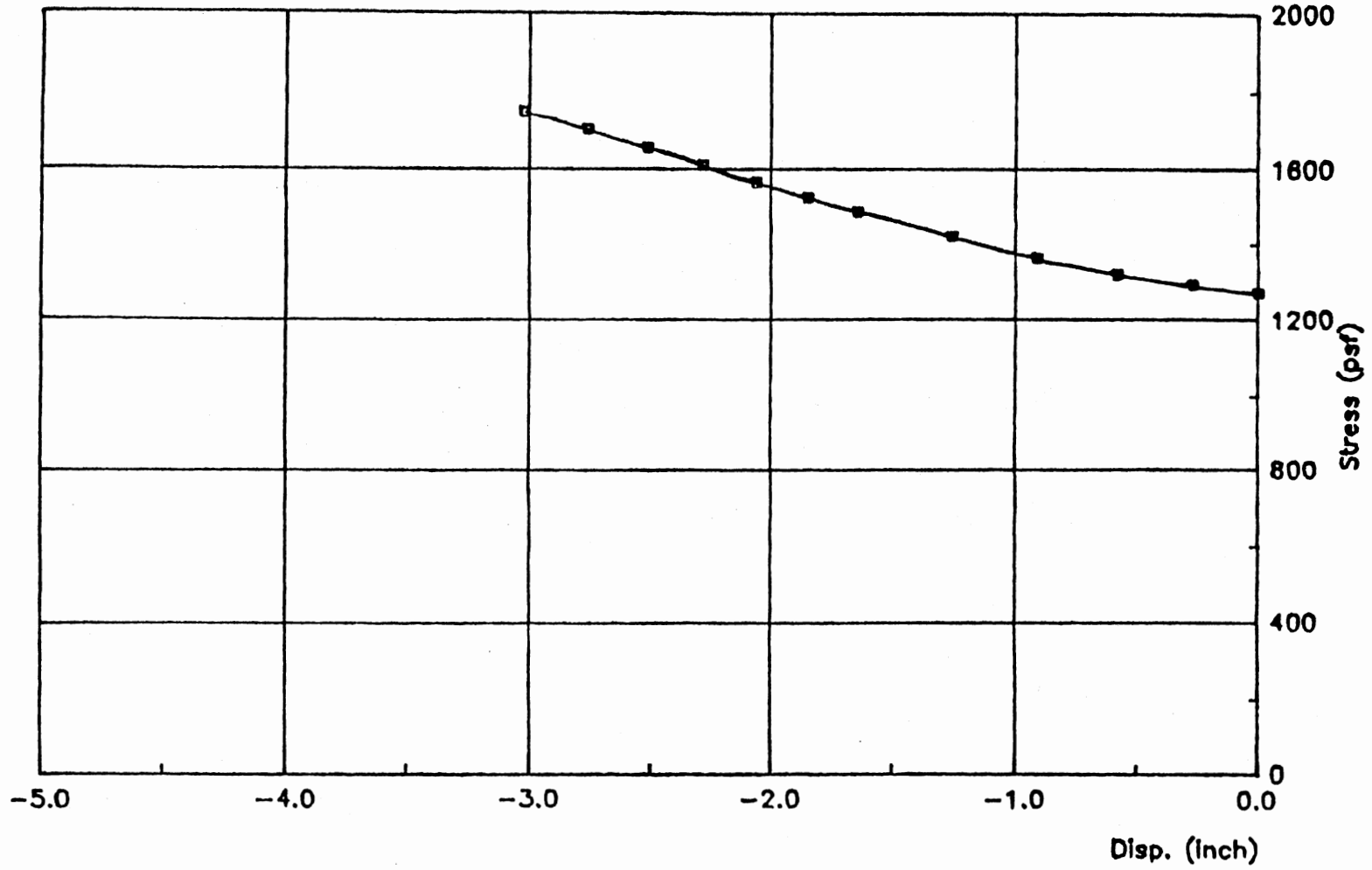

Figure 70(d). Soil-Response curve at -8 ft elevation, back side, medium strength profile, 30 ft pile penetration.

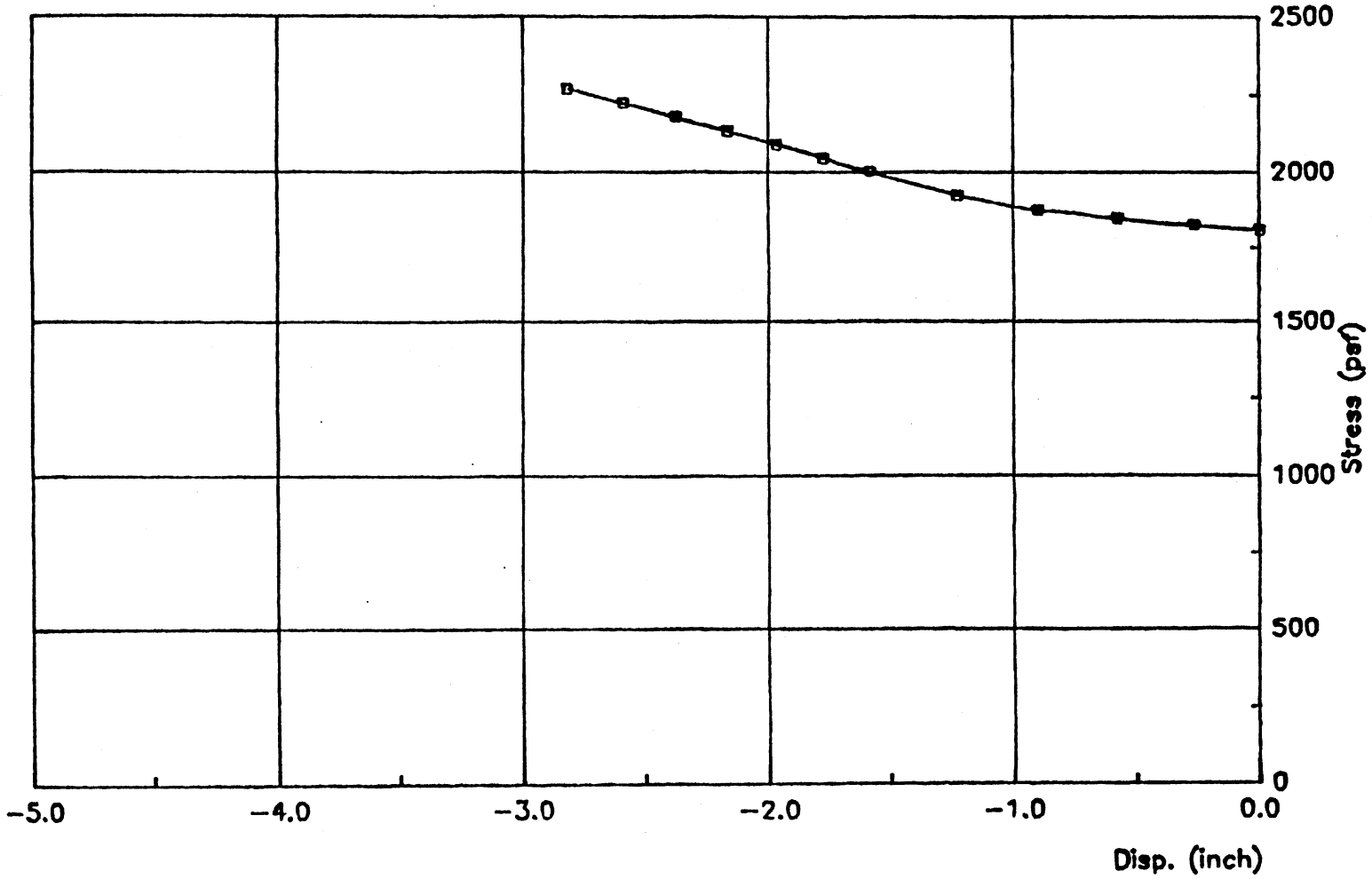

Figure 71(a). Soil-Response curve at -15 ft elevation, front side, medium strength profile, 30 ft pile penetration.

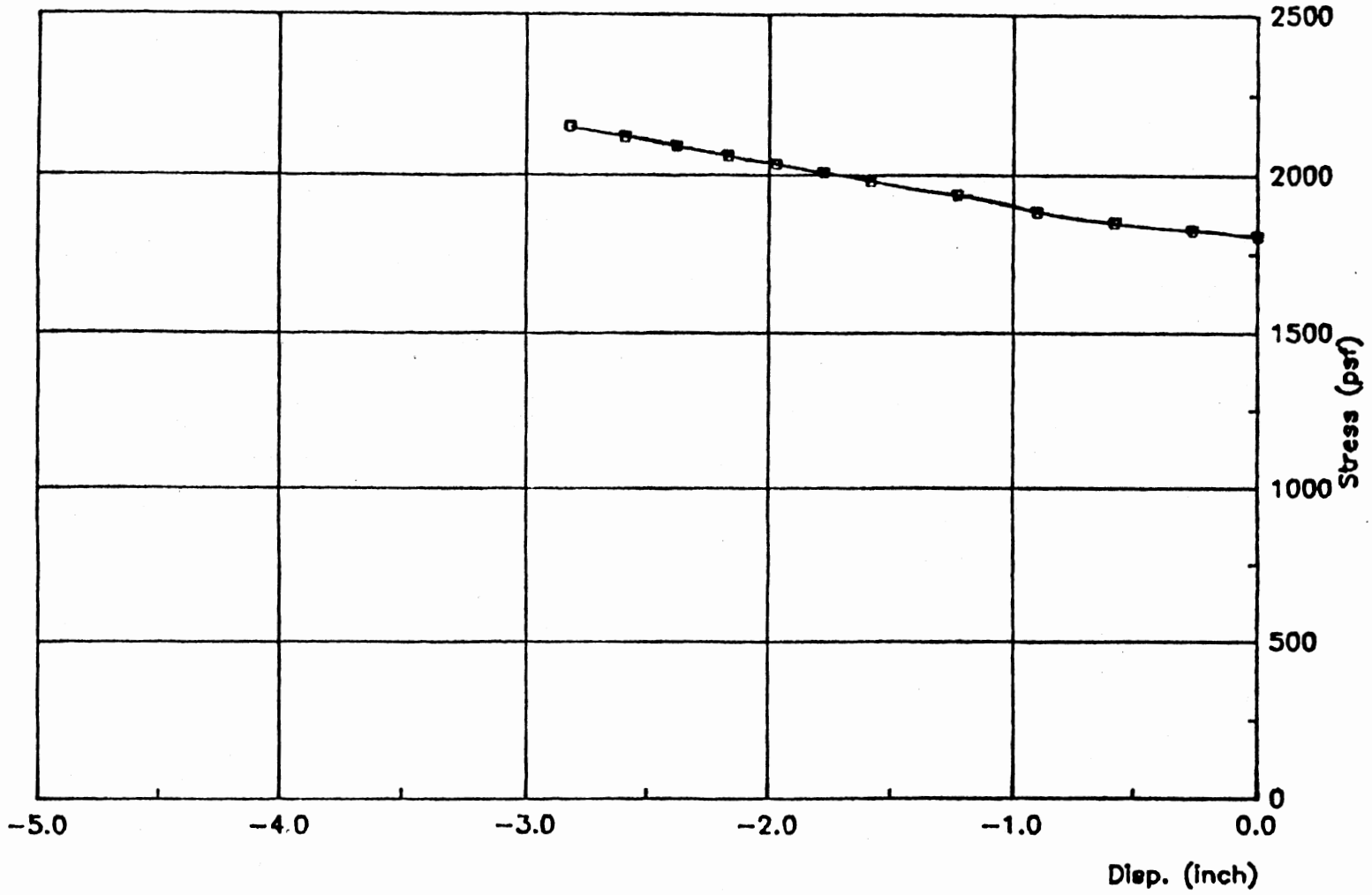

Figure 71(b). Soil-Response curve at -15 ft elevation, back side, medium strength profile, 30 ft pile penetration.

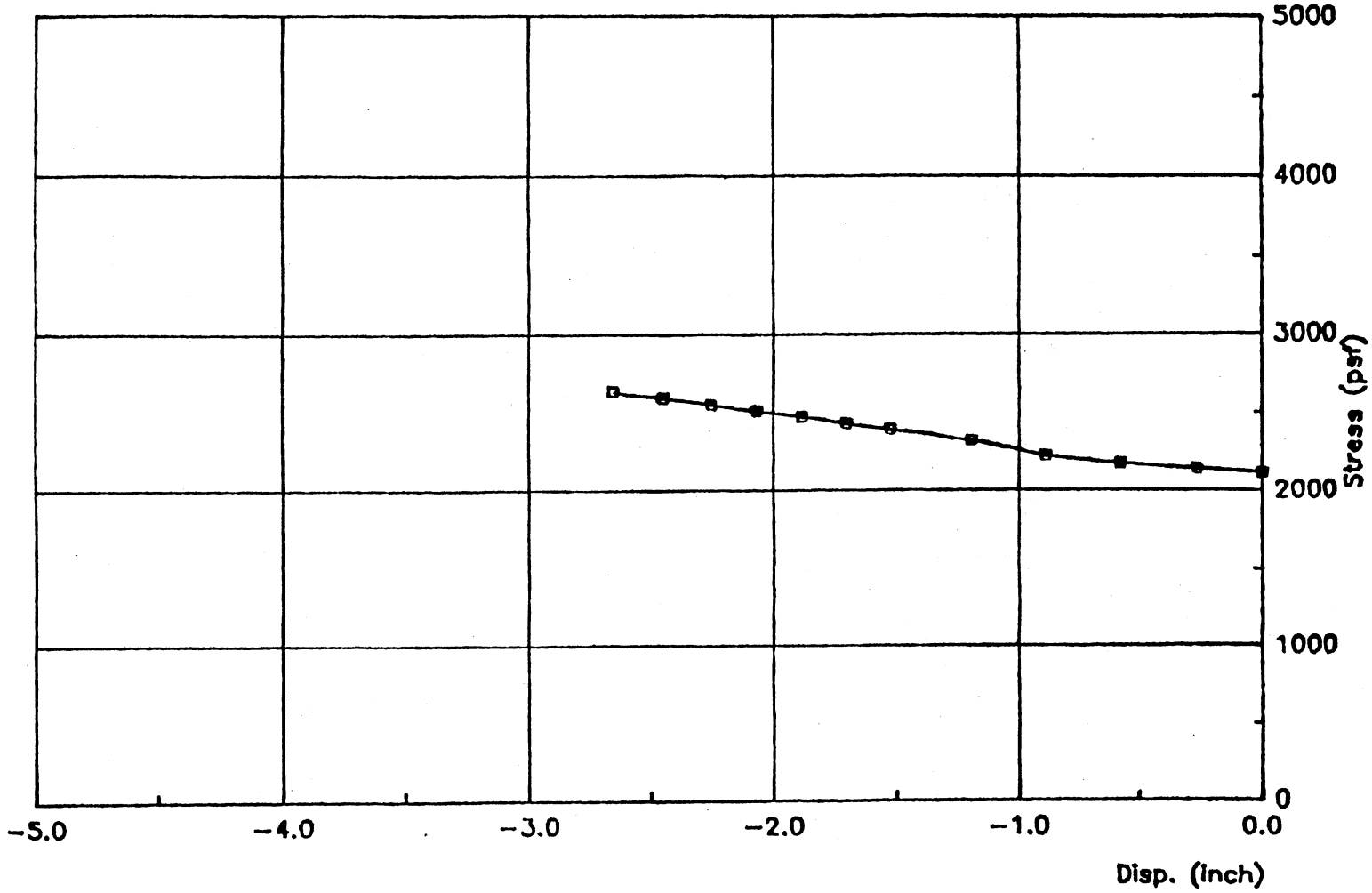

Figure 72(a). Soil-Response curve at -19 ft elevation, front side, medium strength profile, 30 ft pile penetration.

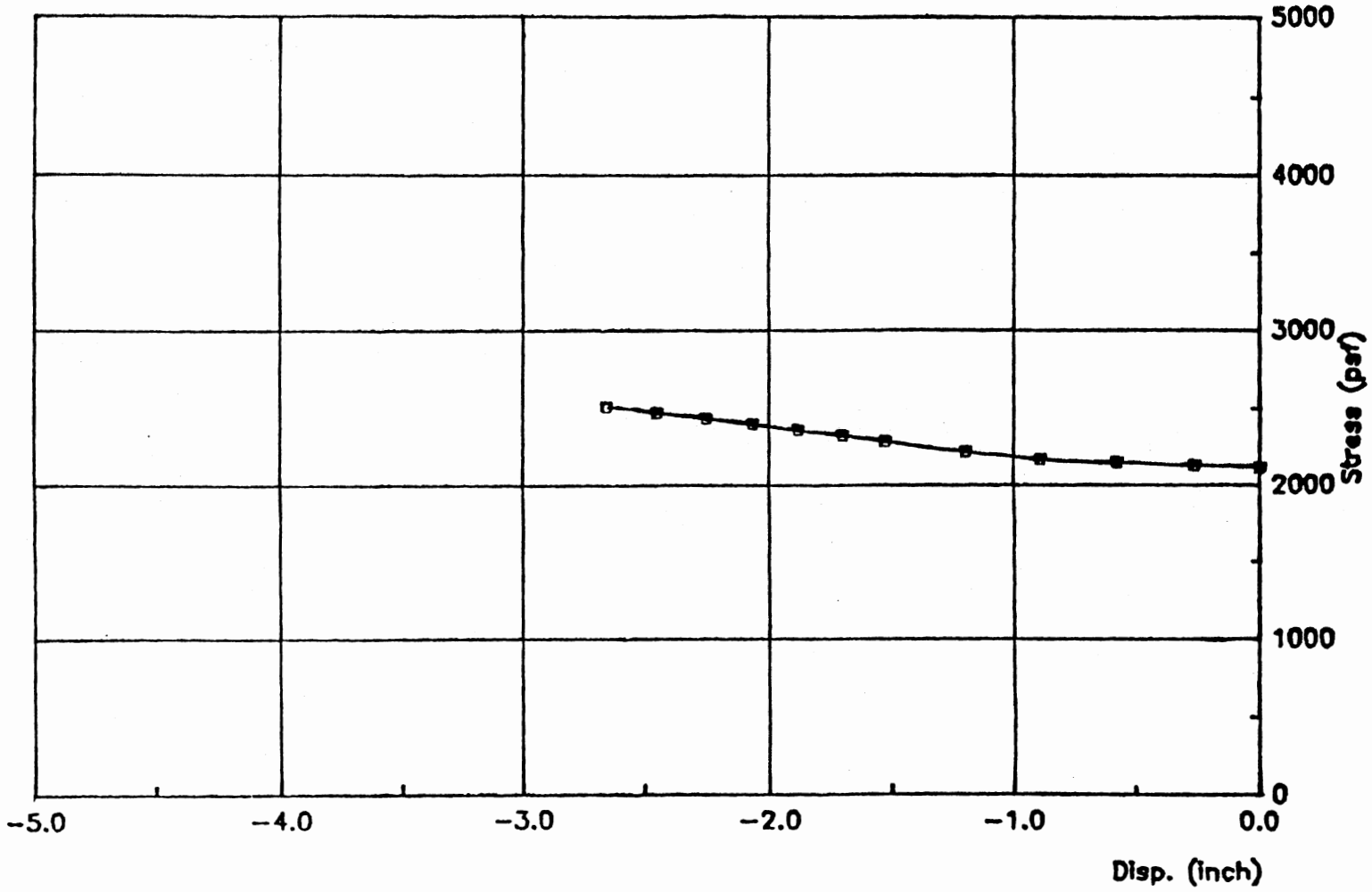

Figure 72(b). Soil-Response curve at -19 ft elevation, back side, medium strength profile, 30 ft pile penetration.

VITA

Issam Samih Hallal

Candidate for the Degree of

Doctor of Philosophy

Thesis: ANALYSIS OF THE NONLINEAR BEHAVIOR OF FLOODWALL STRUCTURES

Major Field: Civil Engineering

Biographical:

Personal Data: Born in Kuwait, Kuwait, October 28, 1959, the son of Mr. and Mrs. Samih F. Hallal.

Education: Graduated from Ramel Alzarif High School, Beirut, Lebanon, in June 1978; received the Bachelor of Science in Civil Engineering degree from Oklahoma State University in May, 1981; received the Master of Science degree in Civil Engineering from Oklahoma State University in December, 1982; completed the requirements for the Doctor of Philosophy degree at Oklahoma State University in July, 1988.

Professional Experience: Structural Engineer, Komati Design Office, Beirut, Lebanon, February, 1983, to July, 1983; Civil Engineer, Al-Mahir Construction Company, Jeddah, Saudi Arabia, August, 1983, to July, 1984; Teaching Assistant, Department of Civil Engineering, Oklahoma State University, January, 1986, to May, 1987; Staff Research Associate, Department of Civil Engineering, Oklahoma State University, June, 1987, to July, 1988.

Professional Organizations: Civil Engineering Honor Society (Chi Epsilon), Board of Engineers, Beirut, Lebanon.

Professional Registration: Registered Professional Engineer in Lebanon.